Transactions of the ASME, Journal of Heat Transfer (ISSN 0022-1481) is published monthly by The American Society of Mechanical Engineers, Three Park Avenue, New York, NY 10016. Periodicals postage paid at New York, NY and additional mailing offices. POSTMASTER: Send address changes to Transactions of the ASME, Journal of Heat Transfer, c/o THE AMERICAN SOCIETY OF MECHANICAL ENGINEERS, 22 Law Drive, Box 2300, Fairfield, NJ 07007-2300. **CHANGES OF ADDRESS** must be received at Society headquarters seven weeks before they are to be effective. Please send old label and new address. **STATEMENT from By-Laws.** The Society shall not be responsible for statements or opinions advanced in papers or ... printed in its publications (B7.1, Para. 3).

Journal of Heat Transfer

Published Monthly by ASME

VOLUME 128 • NUMBER 9 • SEPTEMBER 2006

RESEARCH PAPERS

TECHNICAL BRIEFS

(**Contents continued on inside back cover**)

This journal is printed on acid-free paper, which exceeds the ANSI Z39.48-1992 specification for permanence of paper and library materials. ♾™
♻ 85% recycled content, including 10% post-consumer fibers.

Journal of Heat Transfer **Volume 128, Number 9** **SEPTEMBER 2006**

ERRATUM

The ASME Journal of Heat Transfer is abstracted and indexed in the following:

Applied Science and Technology Index, Chemical Abstracts, Chemical Engineering and Biotechnology Abstracts (Electronic equivalent of Process and Chemical Engineering), Civil Engineering Abstracts, Compendex (The electronic equivalent of Engineering Index), Corrosion Abstracts, Current Contents, E & P Health, Safety, and Environment, Ei EncompassLit, Engineered Materials Abstracts, Engineering Index, Enviroline (The electronic equivalent of Environment Abstracts), Environment Abstracts, Environmental Engineering Abstracts, Environmental Science and Pollution Management, Fluidex, Fuel and Energy Abstracts, Index to Scientific Reviews, INSPEC, International Building Services Abstracts, Mechanical & Transportation Engineering Abstracts, Mechanical Engineering Abstracts, METADEX (The electronic equivalent of Metals Abstracts and Alloys Index), Petroleum Abstracts, Process and Chemical Engineering, Referativnyi Zhurnal, Science Citation Index, SciSearch (The electronic equivalent of Science Citation Index), Theoretical Chemical Engineering

Heat Transfer Enhancement by EHD-Induced Oscillatory Flows

F. C. Lai[1]
e-mail: flai@ou.edu

J. Mathew[2]
Graduate Research Assistant

School of Aerospace and Mechanical Engineering,
University of Oklahoma,
Norman, OK 73019

Prior numerical solutions of electrohydrodynamic (EHD) gas flows in a horizontal channel with a positive-corona discharged wire have revealed the existence of steady-periodic flows. It is speculated that heat transfer by forced convection may be greatly enhanced by taking advantage of this oscillatory flow phenomenon induced by electric field. To verify this speculation, computations have been performed for flows with Reynolds numbers varying from 0 to 4800 and the dimensionless EHD number (which signifies the effect of electric field) ranging from 0.05 to ∞. The results show that heat transfer enhancement increases with the applied voltage. For a given electric field, oscillation in the flow and temperature fields occurs at small Reynolds numbers. Due to the presence of oscillatory secondary flows, there is a significant enhancement in heat transfer.
[DOI: 10.1115/1.2241761]

Keywords: electric fields, enhancement, forced convection

Introduction

Enhancement of heat transfer using electrohydrodynamics (EHD) has been a subject of major interest for many decades. The mechanism for this heat transfer enhancement technique is generally attributed to the electrically induced secondary flow, which is also known as ionic wind or corona wind. The EHD-induced secondary flow can be thought of as a micro jet issued from the charged electrode to the grounded heat transfer surface. The net effect of this secondary flow is additional mixing of the fluid and destablization of the thermal boundary layer, thus leading to a substantial increase in the heat transfer coefficient. Due to the complications involved, previous studies were mostly conducted by experiments and had primarily emphasized the role of the electric body force in the creation of secondary flows [1–4]. While very limited numerical results have been reported on the interaction between the flow and electrostatic fields [5–10], numerical studies on heat transfer enhancement by electric field are even scarcer [11–14]. Since excellent reviews of the previous studies on this subject have been documented in the literature [1–4], they are not repeated here. For brevity, only those related to the present study are discussed below.

The first numerical study on EHD flows was reported by Ramadan and Soo [5] on the analysis of positive corona wind. Their results show that in the absence of any external flow, the electric body force creates a jet originating at the wire and streaming toward the ground plate. Yabe et al. [6] predicted similar results. In a more complete study of the interaction between corona wind and a superimposed external flow, Yamamoto and Velkoff [7] predicted steady EHD flows in a horizontal channel with single-wire and double-wire electrodes over a range of inlet velocities and applied voltages. Prior numerical characterizations of EHD flows have not considered the possibility of an oscillatory flow generated by electric field. It was not until more recently that the existence of EHD-induced oscillatory flows was revealed [8]. Since oscillatory flows produce additional mixing in fluid, it is expected that further heat transfer enhancement may be possible. Therefore, it is the purpose of this study to numerically investigate the possibility of further heat transfer enhancement due to EHD-induced oscillatory flows.

[1]Corresponding author.
[2]Presently at ClimateCraft, Oklahoma City, OK.
Contributed by the Heat Transfer Division of ASME for publication in the JOURNAL OF HEAT TRANSFER. Manuscript received June 2, 2005; final manuscript received March 1, 2006. Review conducted by Raj M. Manglik.

Formulation and Numerical Method

The geometry considered is a two-dimensional horizontal channel with electrode wire(s) charged with a dc high voltage being placed at the centerline (Fig. 1). The channel walls, which are maintained at a constant temperature T_w, are electrically grounded. Only positive corona discharge is considered in the present study. Since the positive corona discharge is uniformly distributed along the length of the wire, it permits a two-dimensional analysis. Air at a uniform velocity u_i and temperature T_i is introduced at the channel inlet. This channel, which has the exactly same dimensions as that of the previous study [7,8], is chosen so that the previously reported electric field data can be used for the present numerical calculations.

For the problem considered, the governing equations of the electrical field are given by [8]

$$\frac{\partial^2 V}{\partial x^2} + \frac{\partial^2 V}{\partial y^2} = -\frac{\rho_c}{\varepsilon_0} \tag{1}$$

$$\rho_c^2 = \varepsilon_0 \left(\frac{\partial \rho_c}{\partial x}\frac{\partial V}{\partial y} + \frac{\partial \rho_c}{\partial y}\frac{\partial V}{\partial x} \right) \tag{2}$$

with the boundary conditions given by

$$V = V_0, \quad \text{at the wire} \tag{3a}$$

$$V = 0, \quad \text{along the channel wall } (y = d) \tag{3b}$$

$$\frac{\partial V}{\partial y} = 0, \text{ along the horizontal centerline } (y = 0) \tag{3c}$$

$$\frac{\partial V}{\partial x} = 0, \text{ along the vertical centerline } (x = L/2) \tag{3d}$$

For parameters considered in the present study, the ion drift velocity is much higher than air velocity such that the contribution of convective flow to the current density can be neglected. Also, the electrodynamic and fluid dynamic equations can be uncoupled for the same reason. Thus, the solution of the electric field can be obtained independently of the flow equations. Although it has been accepted as a common practice, this so-called one-way coupling approach has been verified only recently [13].

For the flow and temperature fields, the dimensionless governing equations in terms of the stream function and vorticity are given by [13]

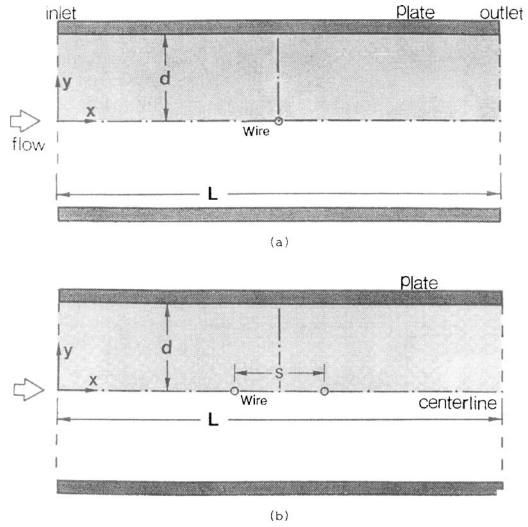

Fig. 1 A horizontal channel with (*a*) one wire electrode, (*b*) two wire electrodes (*d*=3 cm, *s*=4.8 cm, and *L*=25.8 cm)

$$\frac{\partial^2\Psi}{\partial X^2}+\frac{\partial^2\Psi}{\partial Y^2}=-\Omega \tag{4}$$

$$\frac{\partial\Omega}{\partial\tau}=\frac{\partial\Psi}{\partial X}\frac{\partial\Omega}{\partial Y}-\frac{\partial\Psi}{\partial Y}\frac{\partial\Omega}{\partial X}+\frac{1}{\mathrm{Re}_{\mathrm{EHD}}}\left(\frac{\partial^2\Omega}{\partial X^2}+\frac{\partial^2\Omega}{\partial Y^2}\right)+\left(\frac{\partial\overline{V}}{\partial Y}\frac{\partial\overline{\rho_c}}{\partial X}-\frac{\partial\overline{V}}{\partial X}\frac{\partial\overline{\rho_c}}{\partial Y}\right) \tag{5}$$

$$\frac{\partial\theta}{\partial\tau}=\frac{\partial\Psi}{\partial X}\frac{\partial\theta}{\partial Y}-\frac{\partial\Psi}{\partial Y}\frac{\partial\theta}{\partial X}+\frac{1}{\mathrm{Pe}_{\mathrm{EHD}}}\left(\frac{\partial^2\theta}{\partial X^2}+\frac{\partial^2\theta}{\partial Y^2}\right) \tag{6}$$

where $\mathrm{Re}_{\mathrm{EHD}}$ and $\mathrm{Pe}_{\mathrm{EHD}}$ are both based on the electric characteristic velocity u_e. The last term on the right-hand side of Eq. (5) represents the body force term due to the electrical field. For the geometry considered, the electric current involved is very small (on the order of 10^{-5} A based on the measurements of Yamamoto and Velkoff [7]) over the range of voltage applied, which justifies the neglect of Joule heating [14].

The boundary conditions for the flow and temperature fields are given by

$$X=0,\quad \Omega=0,\quad \Psi=\overline{u_i}Y,\quad \theta=0 \tag{7a}$$

$$X=\overline{L},\quad \frac{\partial\Omega}{\partial X}=0,\quad \frac{\partial\Psi}{\partial X}=0,\quad \frac{\partial\theta}{\partial X}=0 \tag{7b}$$

$$Y=1,\quad \Omega=\frac{\partial^2\Psi}{\partial Y^2},\quad \Psi=\overline{u_i},\quad \theta=1 \tag{7c}$$

$$Y=-1,\quad \Omega=\frac{\partial^2\Psi}{\partial Y^2},\quad \Psi=-\overline{u_i},\quad \theta=1 \tag{7d}$$

At the channel exit, gradients of stream function, vorticity, and temperature are set to zero. These boundary conditions are less restrictive and widely accepted. To make sure that the above exit boundary conditions do not impose any severe constraint on the numerical solutions obtained, calculations have been repeated for a longer channel. Only minimal difference in the streamline pattern is observed near the exit, the flow and temperature fields in the channel are otherwise the same.

For the solution of the electric field, the numerical procedure is identical to that used by Yamamoto and Velkoff [7]. Electric potential and space charge density are determined by iterations on

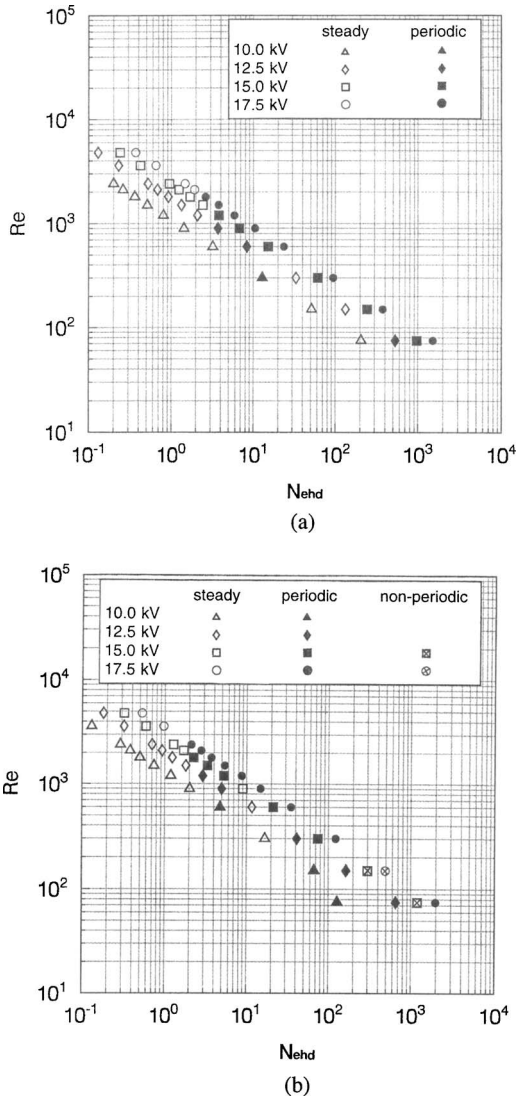

Fig. 2 Transition of flow fields under the influence of electric field (*a*) one wire electrode, (*b*) two wire electrodes

Eqs. (1) and (2) with an assumed value of space charge density at the wire (ρ_{c0}). The validity of the solution is checked by comparing the predicted total current with the measured current at the corresponding voltage. If the currents do not match, a new value of space charge density at the wire is assumed and the calculations are repeated. The accuracy of the electric field thus obtained has been tested against the results obtained by a different approach proposed by McDonald et al. [15] and Kalio and Stock [16], in which the electrical condition at the wire is estimated by the Peek's semiempirical formula [17] instead of an assumed value. It has been found that the agreement of results obtained by these two approaches is very good when the solutions converged. The solutions of the flow and temperature fields are obtained using the standard procedure for the stream function-vorticity formulation, which is well documented in most numerical textbooks and is omitted here for brevity.

The computational domain, which is the shaded area shown in Fig. 1, is one half of the flow channel due to the symmetry about the horizontal centerline. Accordingly, the boundary condition at the bottom wall, Eq. (7*d*), is replaced by the symmetric condition at the centerline. Since the radius of the electrode wire (10^{-4} m) is small as compared to the grid spacing used (9.375×10^{-4} m), it is appropriate to treat the wire as a nodal point. Numerical solution

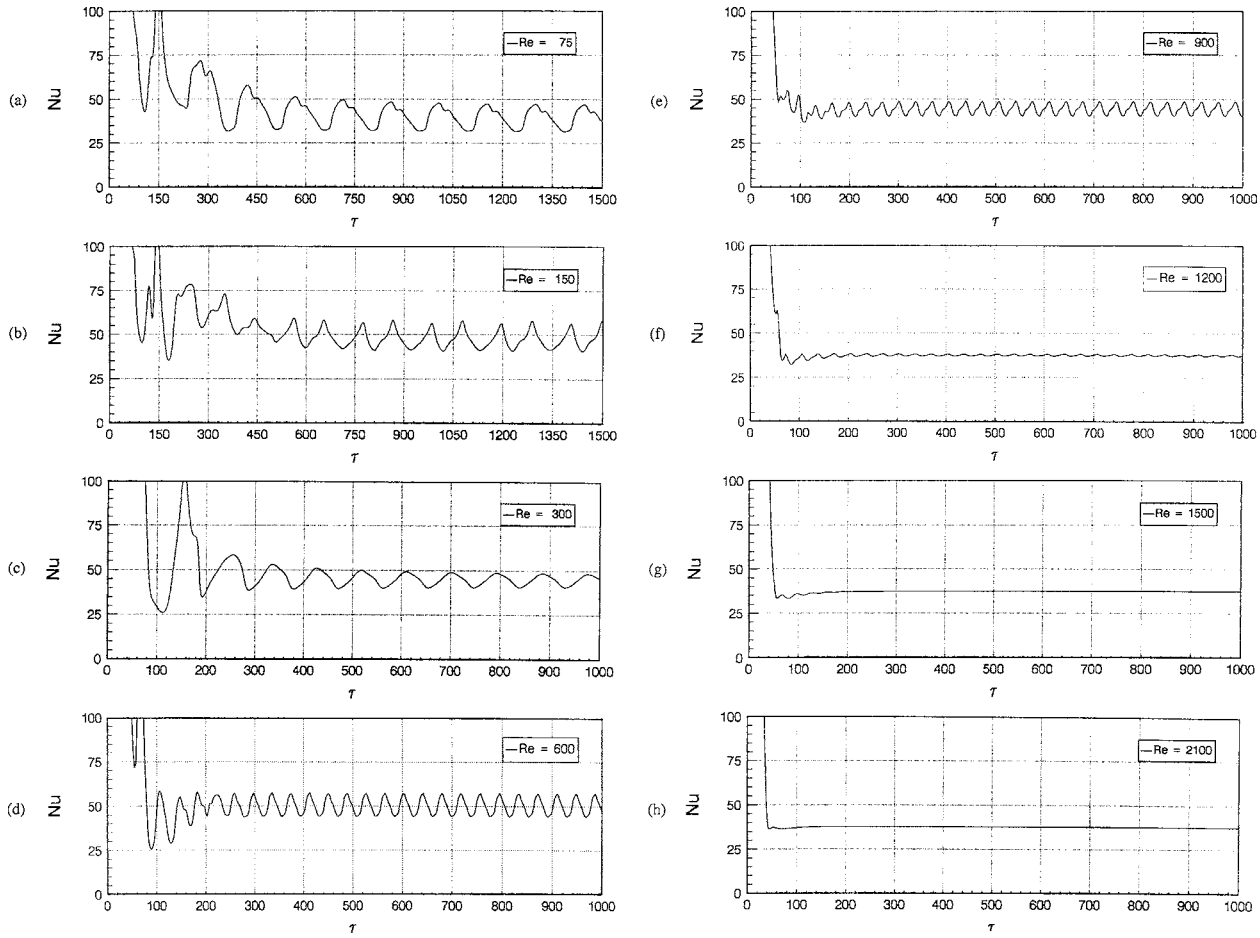

Fig. 3 Variation of Nusselt number with time (one electrode at V_0=15 kV): (*a*) Re=75 (N_{EHD}=969.57), (*b*) Re=150 (N_{EHD}=242.39), (*c*) Re=300 (N_{EHD}=60.60), (*d*) Re=600 (N_{EHD}=15.15), (*e*) Re=900 (N_{EHD}=6.73), (*f*) Re=1200 (N_{EHD}=3.79), (*g*) Re=1500 (N_{EHD}=2.42), (*h*) Re=2100 (N_{EHD}=1.24)

starts with the calculations of electric field, then is followed by solving the flow and temperature fields simultaneously. Since the test of grid dependence has been documented in the previous studies [7,8,13], there is no need to repeat it here. Uniform grids (225×33 for the single-wire case and 345×41 for the double-wire case) are used in the present study for consistency. The dimensionless time step chosen is 5×10^{-4} so as to guarantee numerical stability and accuracy. The stability criterion for the numerical scheme used is given by Jaluria and Torrance [18]

$$\Delta t \leqslant \frac{1}{2\nu\left[\frac{1}{(\Delta x)^2}+\frac{1}{(\Delta y)^2}\right]+\frac{|u|}{\Delta x}+\frac{|v|}{\Delta y}} \tag{8}$$

To verify that the observed oscillations are not due to numerical instability, the computation has been repeated with a reduced time step ($\Delta\tau=1\times10^{-4}$). The results obtained are identically the same with those using the time step of $\Delta\tau=5\times10^{-4}$. Calculations have covered a wide range of parameters ($10\leqslant V_o\leqslant17.5$ kV and $75\leqslant \mathrm{Re}\leqslant4800$) with particular attention being placed on the stability of the flow and temperature fields due to the added electric field. It should be mentioned that some of the flow conditions considered might have a Reynolds number exceeding the critical value that is commonly accepted (i.e., Re_{cr}=2300). However, there was no mention about turbulent flow from the experiment conducted by Yamamoto and Velkoff [7] for the same channel configuration and flow conditions, which implies that it is possible to have laminar flow for the Reynolds numbers considered in the present study. Another reason to consider these higher Reynolds number flows is that a better insight to the interaction between the flow inertia and electric body force can be obtained, which will be elaborated in the later sections. Also any turbulence generated from flow interactions with the wire electrode(s) was not observed in the flow field (and thus was not reported by Yamamoto and Velkoff [7]) because of the fine wire size and short channel length. As such, it is not considered in the present numerical analysis. To closely monitor the development of the flow and temperature fields, the computation is continued until a steady state or at least three complete cycles of oscillatory flow patterns are identified.

To examine the interaction between the flow and electric fields, it is convenient to use a parameter which can represent the ratio of electrical body force to flow inertia. For the present study, the parameter used is the EHD number proposed by Davidson and Shaughnessy [19], which is given by

$$N_{\mathrm{EHD}}=\frac{Id}{\rho u_i^2 bA} \tag{9}$$

where I is the total current and A is the surface area of the channel wall. A high EHD number thus implies that the flow field is dominated by electric body force. On the other hand, a small EHD number indicates that the flow field is controlled by flow inertia.

To evaluate the heat transfer performance, one needs to calculate the heat transfer coefficient. The local heat transfer coefficient in terms of the local Nusselt number is given by

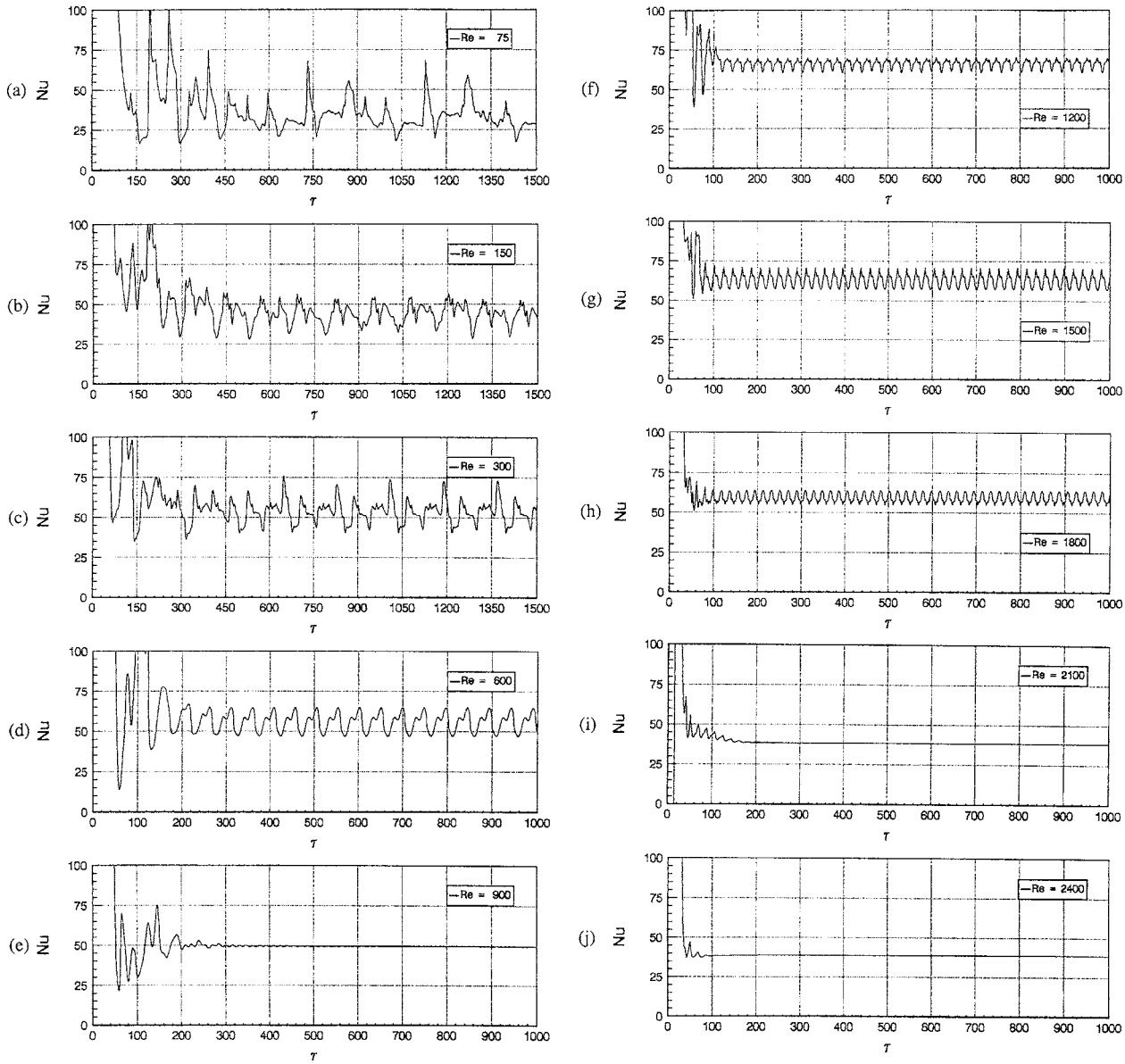

Fig. 4 Variation of Nusselt number with time (two electrodes at V_0=15 kV): (*a*) Re=75 (N_{EHD}=1191.85); (*b*) Re=150 (N_{EHD}=297.96), (*c*) Re=300 (N_{EHD}=74.49), (*d*) Re=600 (N_{EHD}=21.19), (*e*) Re=900 (N_{EHD}=9.01), (*f*) Re=1200 (N_{EHD}=5.30), (*g*) Re=1500 (N_{EHD}=3.30), (*h*) Re=1800 (N_{EHD}=2.25), (*i*) Re=2100 (N_{EHD}=1.70), (*j*) Re=2400 (N_{EHD}=1.28)

$$\mathrm{Nu}_x = \frac{hD_h}{k} = \frac{qD_h}{k(T_w - T_m)} = \frac{D_h(\partial T/\partial y)}{T_w - T_m} \tag{10}$$

In the above expression, D_h is the hydraulic diameter and T_m is the fluid bulk temperature at the given location. The average heat transfer coefficient can thus be determined from the overall Nusselt number which is given by

$$\mathrm{Nu} = \frac{\overline{hD_h}}{k} = \frac{1}{\overline{L}}\int_0^{\overline{L}} \mathrm{Nu}_x dX = \frac{4}{\overline{L}}\frac{\log(1/\theta_0)}{1-\theta_0}\int_0^{\overline{L}} \left.\frac{\partial\theta}{\partial Y}\right|_{Y=1} \mathrm{d}X \tag{11}$$

For periodic flows, the time-averaged Nusselt number is determined by averaging the Nusselt number over a period of oscillation and is given by

$$\overline{\mathrm{Nu}} = \frac{1}{\tau_P}\int_{\tau}^{\tau+\tau_P} \mathrm{Nu}\,\mathrm{d}\tau \tag{12}$$

while for nonperiodic flows, it is calculated by

$$\overline{\mathrm{Nu}} = \frac{1}{\tau_T}\int_0^{\tau_T} \mathrm{Nu}\,d\tau \tag{13}$$

where τ_P is the period of the oscillation, τ_T is the entire time span, and Nu is determined from Eq. (11) at each time step. It is observed that, as τ_T becomes sufficiently large, the average Nusselt number based on Eq. (13) approaches an asymptotic value.

Results and Discussion

In the absence of electrical field, the flow and temperature fields are all steady. It is noticed that the steady state is reached in a shorter period of time when the flow Reynolds number (Re $=2u_i d/\nu$) is higher. The results obtained for the average Nusselt number in general agree well with the empirical correlation reported by Shah and London [20]

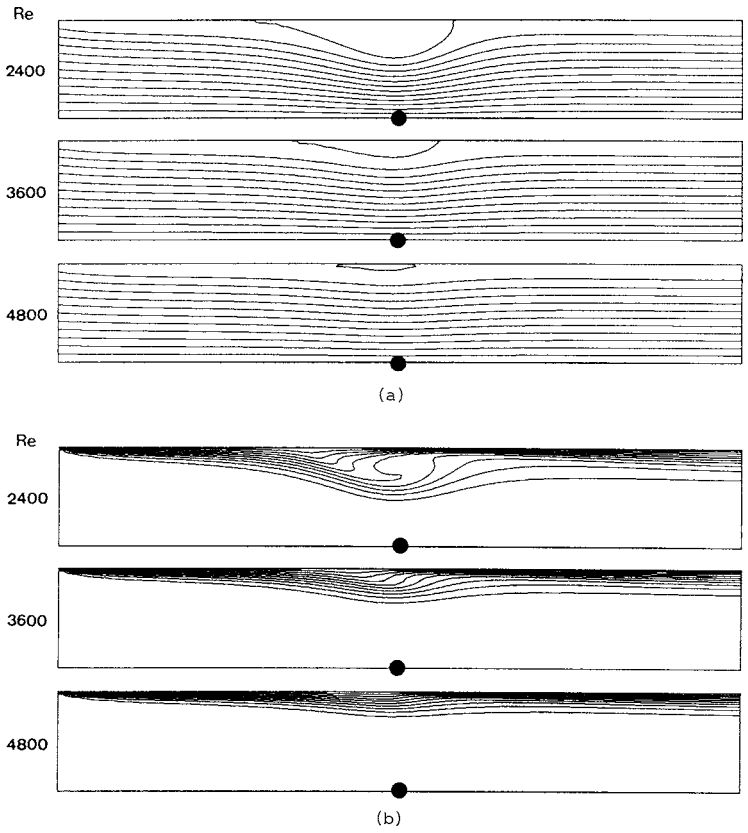

Fig. 5 Steady flow and temperature fields in a channel with one wire electrode at V_0=15 kV: (*a*) Stream functions ($\Delta\Psi$=0.015 for Re=2400, $\Delta\Psi$=0.02 for Re=3600, and $\Delta\Psi$=0.03 for Re=4800), (*b*) isotherms ($\Delta\theta$=0.1)

$$\mathrm{Nu}_0 = 7.55 + \frac{0.024(x^*)^{-1.14}}{1 + 0.0358(x^*)^{-0.64}\mathrm{Pr}^{0.17}}, \quad \text{where } x^* = \frac{x/D_h}{\mathrm{Re\,Pr}} \tag{14}$$

The discrepancy found varies from one to six percent, depending on the Reynolds number, which may be attributed to the neglect of axial diffusion in the formulation that led to the above empirical correlation.

In the presence of electrical field, the flow and temperature fields may not always reach a steady state due to their interaction with the corona wind. Although EHD-induced oscillatory flows were first observed in an experimental study by Takimoto et al. [21], detailed information about these oscillatory flows were not disclosed. From the present results, it is observed that flow and temperature fields may become oscillatory at a given electrical condition when the flow Reynolds number is small (i.e., a high EHD number). A steady state can only be reached when the flow Reynolds number becomes sufficiently large (i.e., a small EHD number). In fact, the transition of flow and temperature fields is a rather complicated function of EHD number as indicated in Fig. 2. As shown, the flow and temperature fields are always stable when $N_{\mathrm{ehd}}<2$ and become oscillatory when $N_{\mathrm{ehd}}>200$. No definite conclusion can be drawn on the flow stability when $2<N_{\mathrm{ehd}}<200$. For example, for an applied voltage at 10 and 12.5 kV, the flow and temperature fields may stabilize during this interval, but become oscillatory again if the EHD number is increased further. It is also interesting to note that the flow and temperature fields in a channel with one wire electrode can only become periodic oscillation when the EHD number increases, but can develop to periodic or nonperiodic oscillation with two wire electrodes. This probably can be best observed from the variation of Nusselt number with time as shown in Figs. 3 and 4 for an applied voltage at 15 kV. For channels with one wire electrode, the transition of flow and temperature fields is rather straightforward. They are in periodic oscillation at low Reynolds numbers ($\mathrm{Re}\leqslant 1200$) and become steady when Reynolds number is further increased (i.e., a further decrease in the EHD number). For channels with two wire electrodes, the transition of flow and temperature fields on the other hand becomes considerably complicated. As observed, the flow and temperature fields are initially nonperiodic at Re=75 and 150. With an increase in the Reynolds number, the flow and temperature fields first become steadily periodic at Re=300 and 600, then stabilized at Re=900. However, a further increase in the Reynolds number prompts the flow and temperature fields to become oscillatory again at Re=1200, and they do not stabilize until the Reynolds number is further increased to 2100. It is also noticed that the amplitude of oscillation in the first periodic flow regime ($300\leqslant \mathrm{Re}<600$) is larger than that of the second periodic flow regime ($1200\leqslant \mathrm{Re}<1800$). The frequency, on the other hand, shows an opposite trend. This observation also applies to other cases with a different applied voltage.

To better understand the origin of flow stability, one can examine the flow and temperature fields in contour plots at various operating conditions. At high Reynolds numbers, flow inertia overpowers the electric body force and leads to a steady flow field. The only effect produced by the electric body force is a weak recirculating cell directly above the wire electrode(s) (Figs. 5(*a*) and 6(*a*)). As the Reynolds number increases, the recirculation zone is confined to a smaller region, indicating the diminishing effect of electric body force. In the presence of recirculating flow, thermal boundary layer is perturbed near the wire(s), resulting in a significant change in the distribution of local heat flux (Figs. 5(*b*) and 6(*b*)). Although local heat transfer at the wall

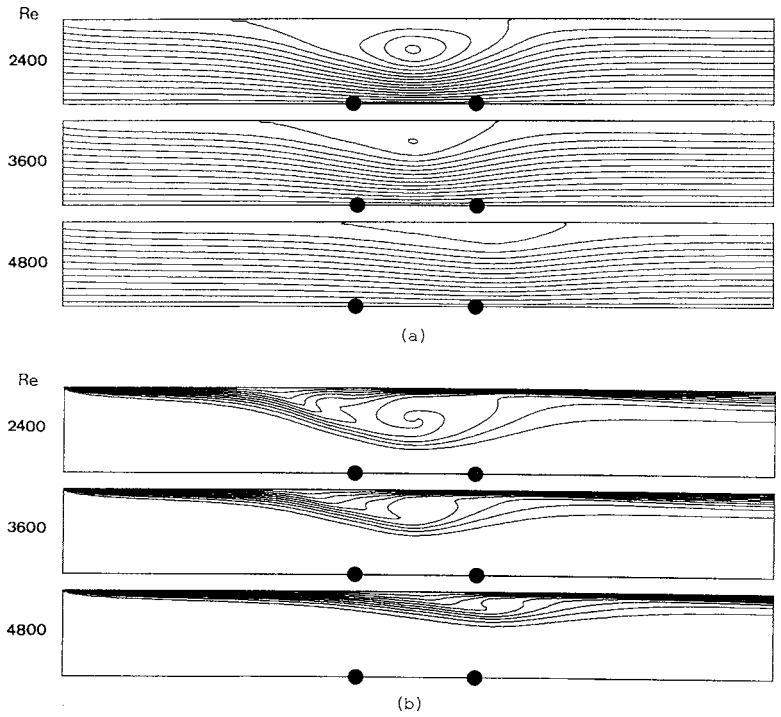

Fig. 6 Steady flow and temperature fields in a channel with two wire electrodes at V_0=15 kV: (*a*) Stream functions ($\Delta\Psi$=0.015 for Re=2400, $\Delta\Psi$=0.02 for Re=3600, and $\Delta\Psi$=0.03 for Re=4800), (*b*) isotherms ($\Delta\theta$=0.1)

immediately upstream the wire may suffer some reduction, the overall heat transfer is significantly enhanced by the increase of local heat transfer from the wall region near and downstream the wire(s). However, the modification of thermal boundary layer by electric body force becomes insignificant when the Reynolds number increases, which also implies that heat transfer enhancement by electric field is minimal under such condition.

At low Reynolds numbers, the electrical body force becomes more influential and may lead to oscillatory flow and temperature fields. Figures 7 and 8 show, respectively, an example of such oscillatory flow and temperature fields in a channel with a single electrode. At V_0=15 kV, the effect of electric body force is comparable with that of flow inertia. When interacting with the primary flow, corona wind produces a sizable recirculating cell directly above the wire (Fig. 7). As time advances, one notices that there is a slight change in the strength of the recirculating cell. Although the change may seem small, it produces visible effect on the thermal boundary layer downstream of the wire (Fig. 8). Because of the disruption of the thermal boundary layer development, there is an increase in the total heat transfer rate. However, the modification of the thermal boundary layer is limited to a region near the wire, one would expect that the resulting heat transfer enhancement may not be significant either. The flow field for a channel with double electrodes at the same operating conditions is characterized by the presence of multiple recirculating cells (Fig. 9). In this case, it is observed that the oscillation in the flow field is mainly due to the periodic generation and destruction of these multiple cells. The cell which is formed upstream of the first wire is charged to the maximum strength when it drifts down the stream to the region between two wires. Its strength is significantly reduced as soon as it leaves the region and drifts further down the stream. Along the way, it initiates the formation of another cell behind the second wire. The oscillatory flow observed here is somewhat similar to the vortex shedding from a cylinder. Correspondingly, the temperature field is distinguished by a wavelike appearance of the thermal boundary layer at the downstream of the wires (Fig. 10), which is very different from those shown in Fig. 6 for the steady-state cases. Because of these secondary flows, more mixing is realized which in turn leads to a significant increase in heat transfer.

Although the two cases presented above are both oscillatory, there is a fundamental difference in their flow structures. For the single-electrode channel, the flow field is characterized by a single recirculating cell while it is multiple-cell for the double-electrode

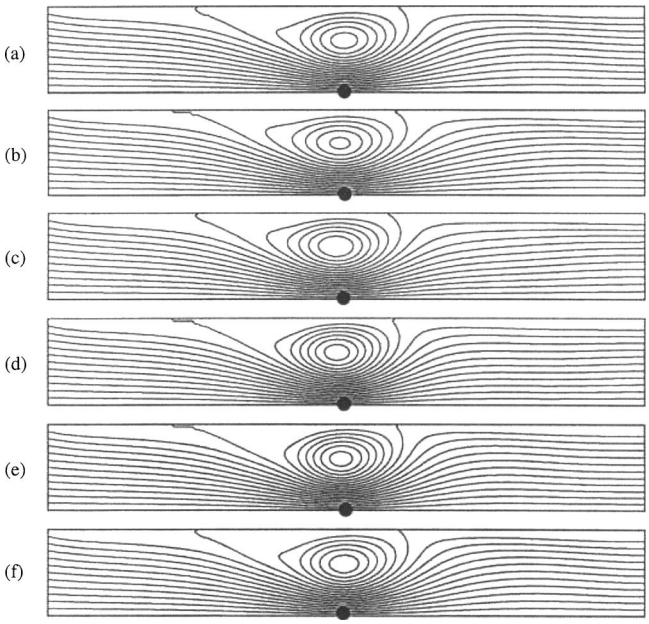

Fig. 7 Variation of flow field (stream functions) with time in a channel with one wire electrode (V_0=15 kV, Re=1200, $\Delta\Psi$=0.008): (*a*) τ=500, (*b*) τ=506.5, (*c*) τ=513, (*d*) τ=519.5, (*e*) τ=526, (*f*) τ=532.5

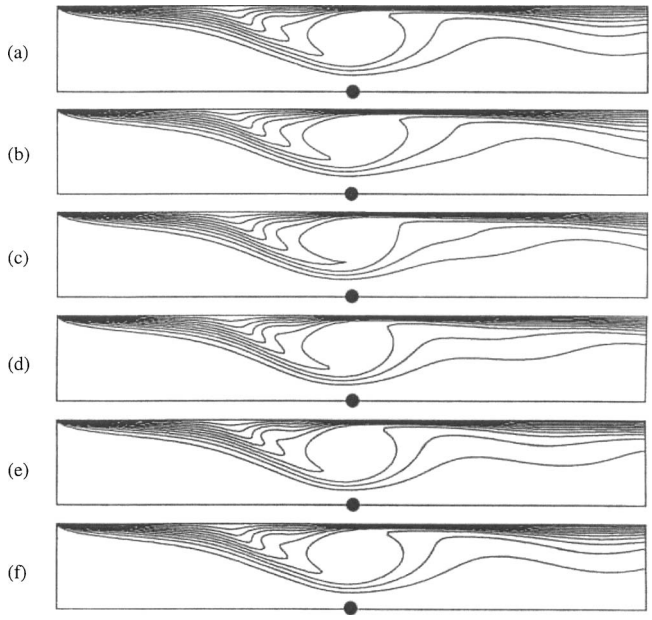

Fig. 8 Variation of temperature field (isotherms) with time in a channel with one wire electrode (V_0=15 kV, Re=1200, $\Delta\theta$=0.1): (*a*) τ=500, (*b*) τ=506.5, (*c*) τ=513, (*d*) τ=519.5, (*e*) τ=526, (*f*) τ=532.5

channel. As reported by Lai et al. [8], there is a strong connection between the periodicity of the oscillation and the flow structure (i.e., single cell or multiple cells). In this case, the period for oscillatory flow in the single electrode channel is found to be 32.5 dimensionless times and it is 45.5 dimensionless times for the double electrode channel. In addition, the single cell in the former case is mainly confined to a region near the wire. As such, its effect on the heat transfer enhancement may not be as significant as those multiple cells in the latter case, which have extended over the entire channel downstream of the wires. Thus, it is not surprising to find that heat transfer enhancement for the latter case is almost twice of that for the former case.

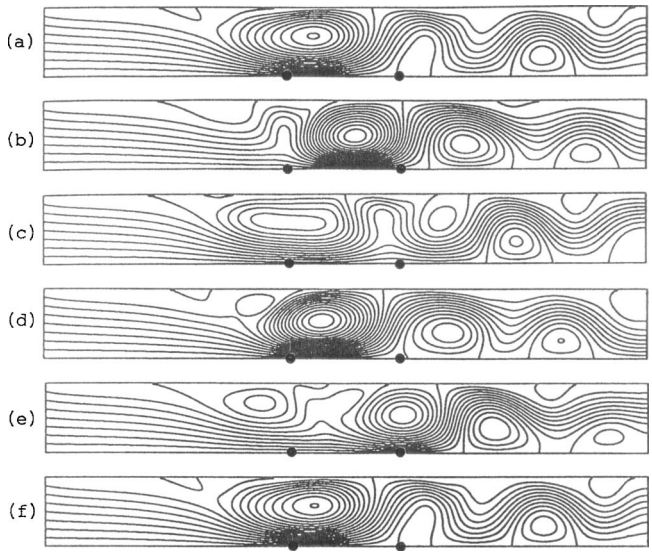

Fig. 9 Variation of flow field (stream functions) with time in a channel with two wire electrodes (V_0=15 kV, Re=1200, $\Delta\Psi$=0.012): (*a*) τ=400, (*b*) τ=409.1, (*c*) τ=418.2, (*d*) τ=427.3, (*e*) τ=436.4, (*f*) τ=445.5

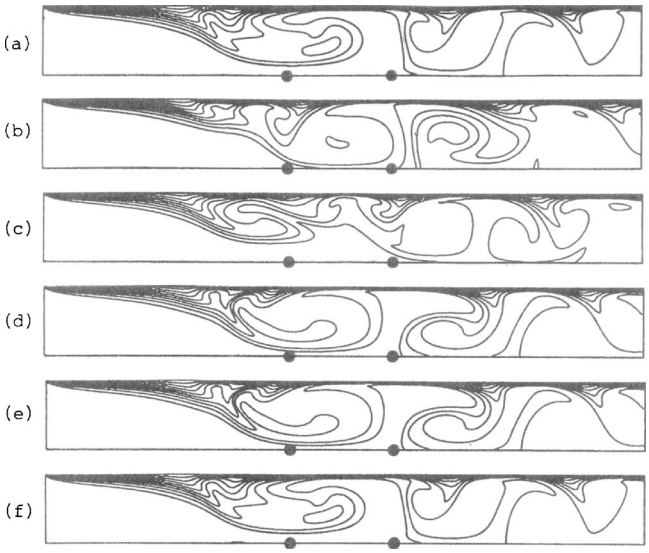

Fig. 10 Variation of temperature field (isotherms) with time in a channel with two wire electrodes (V_0=15 kV, Re=1200, $\Delta\theta$=0.1): (*a*) τ=400, (*b*) τ=409.1, (*c*) τ=418.2, (*d*) τ=427.3, (*e*) τ=436.4, (*f*) τ=445.5

To assess the enhancement in heat transfer, the Nusselt numbers obtained with the presence of electric field are compared with those without electric field and the results are presented in Fig. 11 as a function of the EHD number. For periodic flows, the average

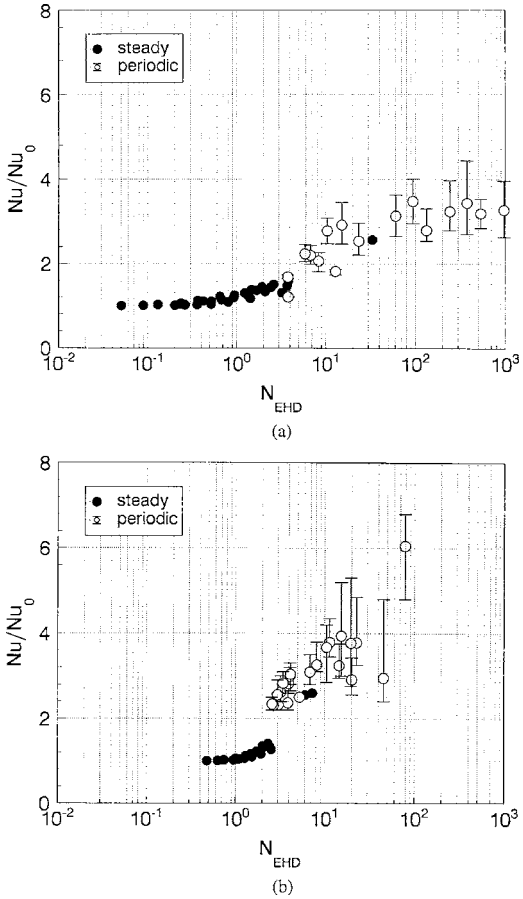

Fig. 11 Heat transfer enhancement by electric field, (*a*) one wire electrode, (*b*) two wire electrodes

Nusselt number is plotted along with its upper and lower bounds. At a given applied voltage, it is found that an increase in the flow velocity, which leads to a small EHD number, results in a reduction in the heat transfer enhancement. The reason for this reduction in heat transfer enhancement is due to the suppression of the EHD-induced secondary flow at a higher Reynolds number. The trend observed here is consistent with the experimental results reported by Takimoto et al. [21]. On the other hand, for a given inlet flow, it is observed that heat transfer enhancement increases with the applied voltage (i.e., the EHD number) for both single- and double-electrodes. As discussed earlier, flows tend to become oscillatory at a large EHD number. As such, one also notices that the heat transfer enhancement by oscillatory flows is usually higher than that by steady flows. It is interesting to note that heat transfer enhancement by steady flows is usually no more than two times of the forced convection alone while for oscillatory flows, it can be as high as four times. This finding implies that, to get the most out of the EHD-enhance heat transfer, one needs to operate the system in an oscillatory flow regime.

Conclusion

A numerical study has been conducted for forced convection in a horizontal channel under the influence of an electric field. The study has not only confirmed the effectiveness of using electric field in heat transfer enhancement, but also has successfully identified the possible mechanism for the dramatic heat transfer enhancement. The results have shown that the flow and temperature fields under the influence of an electric field may become steady, periodic or nonperiodic, depending on the flow Reynolds number and EHD number. When the flow inertia is weak (i.e., at a small flow Reynolds number or a high EHD number), the flow and temperature fields become oscillatory due to the presence of multiple secondary cells produced by the interaction between the primary flow and corona wind. On the other hand, when the flow inertia becomes dominant (i.e., at a high flow Reynolds number or a small EHD number), the EHD-induced recirculating flow is suppressed and the flow and temperature fields may be able to stabilize. It has been shown that an enhancement in heat transfer is possible due to the secondary flows produced by electric field. Depending on the operating conditions, the maximum enhancement in heat transfer by electric field can be more than double of that by forced convection alone.

While the present study has examined a fundamental problem in heat transfer enhancement using electric field, the results obtained have important implications for the realization of this technique. As the present results have indicated, the heat transfer enhancement by oscillatory flows is more effective than steady flows. To harvest from this heat transfer enhancement technique, one needs to operate the system in an EHD number range, usually $N_{\mathrm{EHD}} > 4$ based on the present results, to take advantage of oscillatory flows. The present results also show that heat transfer enhancement can be increased by using double (or multiple) electrodes. However, to make an efficient use of multiple electrodes, the system needs to be optimized (e.g., the location and spacing of the electrodes), which awaits further investigation in the future.

Nomenclature

A = surface area of channel wall, (m^2)
b = ion mobility of air, $b = 1.4311 \times 10^{-4}$ $m^2/V \cdot s$
d = distance between wire and plate, (m)
D_h = hydraulic diameter, (m)
g = acceleration due to gravity, (m/s^2)
h = local heat transfer coefficient, ($W/m^2 \cdot s$)
$\overline{h}$ = average heat transfer coefficient, ($W/m^2 \cdot s$)
I = total electric current, (A)
k = thermal conductivity of air, ($W/m \cdot s$)
$\overline{L}$ = dimensionless channel length, L/d
N_{EHD} = EHD number, defined in Eq. (12)
Nu = overall Nusselt number, $\overline{h}D_h/k$
$\overline{\mathrm{Nu}}$ = time-averaged Nusselt number
Nu_x = local Nusselt number, hD_h/k
Nu_0 = overall Nusselt number without the application of electric field, $\overline{h}D_h/k$
$\mathrm{Pe}_{\mathrm{EHD}}$ = Peclet number, $u_e d/\alpha$
Pr = Prandtl number, ν/α
Re = flow Reynolds number, $2u_i d/\nu$
$\mathrm{Re}_{\mathrm{EHD}}$ = EHD Reynolds number, $u_e d/\nu$
t = time, (s)
T_i = inlet air temperature, (K)
T_w = wall temperature, (K)
u = velocity in x-direction, (m/s)
u_e = characteristic velocity of ionic wind, $\sqrt{\rho_{c0} V_0/\rho}$, (m/s)
$\underline{u_i}$ = uniform velocity at the inlet, (m/s)
u_i = dimensionless inlet velocity of air, u_i/u_e
V = electric potential, (V)
$\overline{V}$ = normalized electrical potential, V/V_0
V_0 = electric potential at the wire, (V)
v = velocity in y-direction, (m/s)
X, Y = dimensionless Cartesian coordinates, $X = x/d$, and $Y = y/d$
x, y = Cartesian coordinates, (m)
α = thermal diffusivity, (m^2/s)
ε = permitivity of air, (F/m)
θ = dimensionless temperature, $(T - T_i)/(T_w - T_i)$
θ_0 = dimensionless mean outlet air temperature
ν = kinematic viscosity of air, (m^2/s)
ρ = density of air, (kg/m^3)
$\underline{\rho_c}$ = ionic space charge density, (C/m^3)
ρ_c = dimensionless space charge density, ρ_c/ρ_{c0}
ρ_{c0} = ionic space charge density at the wire, (C/m^3)
τ = dimensionless time, $u_e t/d$
Ψ = dimensionless stream function
Ω = dimensionless vorticity

References

[1] Jones, T. B., 1978, "Electrohydrodynamically Enhanced Heat Transfer in Liquids – A Review," *Advances in Heat Transfer*, Academic Press, New York, Vol. 14, pp. 107–148.
[2] Davidson, J. H., Kulacki, F. A., and Dunn, P. F., 1987, "Convective Heat Transfer with Electric and Magnetic Fields," *Handbook of Single-Phase Convective Heat Transfer*, edited by Kakac, S., et al., Wiley, New York.
[3] Yabe, A., Mori, Y., and Hijikata, K., 1996, "Active Heat Transfer Enhancement by Utilizing Electric Fields," Annu. Rev. Heat Transfer, **VII**, pp. 193–244.
[4] Seyed-Yagoobi, J., and Bryan, J. E., 1999, "Enhancement of Heat Transfer and Mass Transport in Single-Phase and Two-Phase Flows with Electrohydrodynamics," *Advances in Heat Transfer*, Academic Press, New York, Vol. 33, pp. 95–186.
[5] Ramadan, O. E., and Soo, S. L., 1969, "Electrohydrodynamic Secondary Flow," Phys. Fluids, **12**, pp. 1943–1945.
[6] Yabe, A., Mori, Y., and Nijikate, K., 1978, "EHD Study of the Corona Wind Between Wire and Plate Electrodes," AIAA J., **16**, pp. 340–345.
[7] Yamamoto, T., and Velkoff, H. R., 1981, "Electrohydrodynamics in an Electrostatic Precipitator," J. Fluid Mech., **108**, pp. 1–8.
[8] Lai, F. C., McKinney, P. J., and Davidson, J. H., 1995, "Oscillatory Electrohydrodynamic Gas Flows," J. Fluids Eng., **117**, pp. 491–497.
[9] Clover, G. M., and El-Khabiri, S., 1999, "Modeling of DC Corona Discharge Along an Electrically Conductive Flat Plate With Gas Flow," IEEE Trans. Ind. Appl., **35**, pp. 387–394.
[10] Yamamoto, T., Okuda, M., and Okubo, M., 2003, "Three-Dimensional Ionic Wind and Electrohydrodynamics of Tuft/Point Corona Electrostatic Precipitator," IEEE Trans. Ind. Appl., **39**, pp. 1602–1607.
[11] Lai, F. C., 1998, "Effects of Buoyancy on Electrohydrodynamic-Enhanced Forced Convection in a Horizontal Channel," J. Thermophys. Heat Transfer, **12**, pp. 431–436.
[12] Molki, M., Ohadi, M. M., Baumgarten, B., Hasegawa, M., and Yabe, A., 2000, "Heat Transfer Enhancement of Airflow in a Channel Using Corona Discharge," J. Enhanced Heat Transfer, **7**, pp. 411–425.
[13] Huang, M., and Lai, F. C., 2003, "Numerical Study of EHD-Enhanced Forced

Convection Using Two-Way Coupling," J. Heat Transfer, **125**, pp. 760–764.
[14] Huang, M., and Lai, F. C., 2006, "Effects of Joule Heating on EHD-Enhanced Natural Convection in an Enclosure," J. Thermophys. Heat Transfer, to be published.
[15] McDonald, J. R., Smith, W. B., Spencer, H. W., and Sparks, L. E., 1977, "A Mathematical Model for Calculating Electrical Conditions in Wire-Duct Electrostatic Precipitation Devices," J. Appl. Phys., **48**, pp. 2231–2243.
[16] Kallio, G. A., and Stock, D. E., 1985, "Computation of Electrical Conditions Inside Wire-Duct Electrostatic Precipitators Using a Combined Finite-Element, Finite-Difference Technique," J. Appl. Phys., **59**, pp. 999–1005.
[17] Peek, F. W., 1966, *Dielectric Phenomenon in High Voltage Engineering*, McGraw-Hill, New York.
[18] Jaluria, Y., and Torrance, K. E., 1986, *Computational Heat Transfer*, Hemisphere, New York.
[19] Davidson, J. H., and Shaughnessy, E. J., 1986, "Turbulence Generation by Electric Body Forces," Exp. Fluids, **4**, pp. 17–26.
[20] Shah, R. K., and London, A. L., 1978, "Laminar Flow Forced Convection in Ducts, Supplement 1," *Advances in Heat Transfer*, Academic Press, New York, 1978.
[21] Takimoto, A., Tada, Y., Yamada, K., and Hayashi, Y., 1988, "Heat Transfer Enhancement in a Convective Field With a Corona Discharge," Trans. Jpn. Soc. Mech. Eng., Ser. B, **54**, pp. 695–703.

Fluid Flow and Heat Transfer in Power-Law Fluids Across Circular Cylinders: Analytical Study

W. A. Khan[1]

J. R. Culham

M. M. Yovanovich

Microelectronics Heat Transfer Laboratory,
Department of Mechanical Engineering,
University of Waterloo,
Waterloo, ON, N2L 3G1, Canada

An integral approach of the boundary layer analysis is employed for the modeling of fluid flow around and heat transfer from infinite circular cylinders in power-law fluids. The Von Karman-Pohlhausen method is used to solve the momentum integral equation whereas the energy integral equation is solved for both isothermal and isoflux boundary conditions. A fourth-order velocity profile in the hydrodynamic boundary layer and a third-order temperature profile in the thermal boundary layer are used to solve both integral equations. Closed form expressions are obtained for the drag and heat transfer coefficients that can be used for a wide range of the power-law index, and generalized Reynolds and Prandtl numbers. It is found that pseudoplastic fluids offer less skin friction and higher heat transfer coefficients than dilatant fluids. As a result, the drag coefficients decrease and the heat transfer increases with the decrease in power-law index. Comparison of the analytical models with available experimental/numerical data proves the applicability of the integral approach for power-law fluids. [DOI: 10.1115/1.2241747]

Introduction

Many practical situations need a knowledge of fluid flow around and heat transfer from horizontal cylinders subjected to cross flow of non-Newtonian fluids. These fluids are classified by different authors in different ways. One important classification is the purely viscous fluids (Cho and Hartnett [1]). These fluids are further subdivided in to shear thinning (or pseudoplastic, e.g., glues, blood, and polymer melts), viscoplastic (or yield value, e.g., paints and concentrated suspensions) fluids, and shear thickening (or dilatant, e.g., wet sand, sugar, and borax solutions) fluids. In this study, fluid flow and heat transfer characteristics of these fluids across a circular cylinder are investigated using a power-law model. This model is based on the fact that both fluids exhibit a region of linear relationship between stress and strain rate when viewed on a log-log plot (Chhabra and Richardson [2]).

Literature Review

Fluid flow around and heat transfer from circular cylinders in cross flow to Newtonian fluids has been extensively studied theoretically, experimentally, and numerically by many researchers (Khan et al. [3]) but for non-Newtonian and especially for power-law fluids these types of studies are very limited. From a theoretical point of view, Acrivos et al. [4] were the first who investigated the forced convective heat transfer from an isothermal flat plate to power-law fluids using analytical-numerical approach. Later, Schowalter [5], Shah et al. [6], Acrivos et al. [7], and Lee and Ames [8] extended that work to solve 2-D boundary layer equations by using similarity transformations. Bizzell and Slattery [9] used the Von Karman-Pohlhausen integral method to analyze boundary layer on a sphere and calculated points of separation for different values of power-law index. However, no attempt was made to investigate heat transfer to power-law fluids. Wolf and Szewczyk [10] used Blasius series approach to investigate heat transfer from arbitrary cylinders to power-law fluids while Serth and Kiser [11] used Goertler series method to solve 2-D boundary layer equations for power-law fluids. Lin and Chern [12] and Kim et al. [13] presented laminar momentum boundary-layer analysis for non-Newtonian fluids by using the Merk-Chao expansion method. They obtained numerical and closed form solutions to the universal functions and then applied them to analyze the wedge flow and the flow over a circular cylinder and a sphere.

Mizushina and Usui [14] developed a theoretical framework for the laminar boundary heat transfer from a horizontal cylinder submerged in power-law fluids and expressed Nusselt number at the front stagnation point in the form

$$\mathrm{Nu}_D = 1.04n^{-0.4}\mathrm{Re}_{Dp}^{1/(n+1)}\mathrm{Pr}_p^{1/3} \tag{1}$$

Nakayama et al. [15], Shenoy and Nakayama [16], Nakayama [17], and Anderson [18] extended the Von Karman-Pohlhausen integral method to obtain solutions to both momentum and energy equations for power-law fluid flows past wedges, cones, and axisymmetric bodies.

From the experimental point of view, Shah et al. [6], Luikov et al. [19–21], James and Acosta [22], Takahashi et al. [23], Mizushina et al. [24], Mizushina and Usui [14], Kumar et al. [25], Ghosh et al. [26], Rao [27] measured local heat/mass transfer coefficients for the non-Newtonian fluids from a circular cylinder in cross flow and determined average heat transfer. Ghosh et al. [28] also reviewed the bulk of the literature on non-Newtonian fluids. Mizushina et al. [24] developed the following empirical correlation for the Nusselt number averaged over the circumference of the cylinder:

$$\mathrm{Nu}_D = 0.72n^{-0.4}\mathrm{Re}_{Dp}^{1/(n+1)}\mathrm{Pr}_p^{1/3} \tag{2}$$

whereas Ghosh et al. [26] developed the following empirical correlation for heat and mass transfer from a cylinder in cross flow to power-law fluids:

$$\mathrm{Nu}_D = 0.785\,\mathrm{Re}_{Dp}^{1/2}Pr_p^{1/3} \quad \text{for } 10 < \mathrm{Re}_{Dp} < 25{,}000 \tag{3}$$

Coelho and Pinho [29–31] performed a series of experiments to study the flow of non-Newtonian fluids around a cylinder. They measured shedding frequency, the formation length (l_f) and the pressure distribution around a cylinder and determined the shedding regimes and the drag coefficients.

D'Alessio and Pascal [32] investigated numerically the steady power-law flow around a circular cylinder at three different Reynolds numbers $\mathrm{Re}_{Dp}=5$, 20, and 40 using a first-order accurate difference method for a fixed blockage ratio. They found that the

[1]Corresponding author now at Department of Mathematics, COMSATS Information Technology Center, University Road, 22060, NWFP, Pakistan.

Contributed by the Heat Transfer Division of ASME for publication in the JOURNAL OF HEAT TRANSFER. Manuscript received May 31, 2005; final manuscript received February 17, 2006. Review conducted by Jay M. Khodadadi. Paper presented at the ASME 2005 International Mechanical Engineering Congress and Exposition.

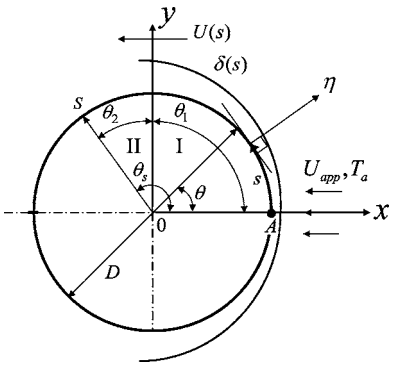

Fig. 1 Flow over circular cylinder

critical Reynolds number, wake length, separation angle, and drag coefficient depend on the power-law index. Chhabra et al. [33] extended that work by using a more accurate second-order finite difference method, more refined computational meshes, and greater blockage ratio and power-law index ranges in order to investigate the effect of blockage on drag coefficient, wake length, separation angle, and flow patterns over wide ranges of conditions. Agarwal et al. [34] investigated numerically the momentum and thermal boundary layers for power-law fluids over a thin needle under wide ranges of kinematic and physical conditions. They introduced a similarity variable and transformed the momentum and energy equations into ordinary differential equations. They reported extensive results on axial velocity profiles, shear stress, and skin friction distribution on the surface of the needle, temperature and local Nusselt number variation, and momentum and thermal boundary layer thicknesses in the following ranges of conditions: $0.2 \leqslant n \leqslant 1.6$, $1 \leqslant \mathrm{Pr} \leqslant 1000$, $\mathrm{Re} < 10^6$ and for three needle sizes.

In this study, an approximate method, based on the Karman-Pohlhausen integral momentum and energy equations, is used to study the fluid flow and heat transfer in power-law fluids across a single circular cylinder.

Analysis

Consider a uniform flow of a non-Newtonian (power-law) fluid past a fixed circular cylinder of diameter D, with vanishing circulation around it, as shown in Fig. 1. The approaching velocity of the fluid is U_{app} and the ambient temperature is assumed to be T_a. The surface temperature of the wall is $T_w (> T_a)$ in the case of the isothermal cylinder and the heat flux is q for the isoflux boundary condition. The flow is assumed to be laminar, steady, and two dimensional. The fluid is assumed to be incompressible with constant thermophysical and rheological properties. The potential flow velocity just outside the boundary layer is denoted by $U(s)$. Using an order-of-magnitude analysis (Khan [35]), the reduced equations of continuity, momentum, and energy in the curvilinear system of coordinates (Fig. 1) for a power-law fluid can be written as:

Continuity:

$$\frac{\partial u}{\partial s} + \frac{\partial v}{\partial \eta} = 0 \tag{4}$$

s-Momentum:

$$u\frac{\partial u}{\partial s} + v\frac{\partial u}{\partial \eta} = -\frac{1}{\rho}\frac{dP}{ds} + \frac{1}{\rho}\frac{\partial \tau_w}{\partial \eta} \tag{5}$$

η-Momentum:

$$\frac{dP}{d\eta} = 0 \tag{6}$$

Energy:

$$u\frac{\partial T}{\partial s} + v\frac{\partial T}{\partial \eta} = \alpha\frac{\partial^2 T}{\partial \eta^2} \tag{7}$$

with

$$-\frac{1}{\rho}\frac{dP}{ds} = U(s)\frac{dU(s)}{ds} \tag{8}$$

and

$$\tau_w = m\left(\frac{\partial u}{\partial \eta}\right)^n\bigg|_{\eta=0} \tag{9}$$

where m is a consistency index for non-Newtonian viscosity and n is called power-law index, that is <1 for pseudoplastic, $=1$ for Newtonian, and >1 for dilatant fluids.

Hydrodynamic Boundary Conditions

The assumptions of no slip boundary condition at the cylinder wall ($u=0$, at $\eta=0$), no mass flow through the cylinder wall ($v=0$ at $\eta=0$), and the potential flow just outside the boundary layer ($u=U(s)$ at $\eta=\delta(s)$) give the following complete set of hydrodynamic conditions:

(i) at the cylinder surface, i.e., at $\eta=0$

$$u = 0 \quad \frac{\partial^2 u}{\partial \eta^2} = -\frac{U(s)\dfrac{dU(s)}{ds}}{n\gamma\left(\dfrac{\partial u}{\partial \eta}\right)^{n-1}} \tag{10}$$

where $\gamma = m/\rho$,

(ii) at the edge of the boundary layer, i.e., at $\eta=\delta(s)$

$$u = U(s), \quad \frac{\partial u}{\partial \eta} = 0 \quad \frac{\partial^2 u}{\partial \eta^2} = 0 \tag{11}$$

These conditions will help in determining the velocity distribution inside the boundary layer.

Thermal Boundary Conditions

The assumptions of uniform wall temperature (UWT) and uniform wall flux (UWF) boundary conditions give the following complete set thermal conditions:

(i) at the cylinder surface, i.e., at $\eta=0$

$$\frac{\partial^2 T}{\partial \eta^2} = 0, \quad \begin{cases} T = T_w & \text{for UWT} \\ \dfrac{\partial T}{\partial \eta} = -\dfrac{q}{k_f} & \text{for UWF} \end{cases} \tag{12}$$

(ii) at the edge of thermal boundary layer, i.e., at $\eta=\delta_T$

$$T = T_a \quad \frac{\partial T}{\partial \eta} = 0 \tag{13}$$

Using these thermal conditions, the temperature distributions inside the thermal boundary layer can be determined.

Velocity Distribution

Assuming a thin hydrodynamic boundary layer around the cylinder, the velocity distribution inside the boundary layer, satisfying Eqs. (10) and (11), can be approximated by a fourth-order polynomial as suggested by Pohlhausen [36]:

$$\frac{u}{U(s)} = (2\eta_H - 2\eta_H^3 + \eta_H^4) + \frac{\lambda}{6}(\eta_H - 3\eta_H^2 + 3\eta_H^3 - \eta_H^4) \tag{14}$$

where $0 \leqslant \eta_H = \eta/\delta(s) \leqslant 1$ and λ is the pressure gradient parameter, given by

$$\lambda = \frac{\frac{dU(s)}{ds}\delta^{n+1}U(s)^{1-n}\left(2+\frac{\lambda}{6}\right)^{1-n}}{n\gamma} \tag{15}$$

With the help of velocity profiles, Schlichting [37] showed that the parameter λ is restricted to the range $-12 \leqslant \lambda \leqslant 12$.

Temperature Distribution

Assuming a thin thermal boundary layer around the cylinder, the temperature distribution in the thermal boundary layer, satisfying Eqs. (12) and (13), can be approximated, in terms of $\eta_T = \eta/\delta_T$, by a third-order polynomial

$$\frac{T-T_a}{T_w-T_a} = 1 - \frac{3}{2}\eta_T + \frac{1}{2}\eta_T^3 \tag{16}$$

for the isothermal boundary condition and

$$T - T_a = \frac{2q\delta_T}{3k_f}\left(1 - \frac{3}{2}\eta_T + \frac{1}{2}\eta_T^3\right) \tag{17}$$

for the isoflux boundary condition.

Boundary Layer Parameters

The momentum integral equation can be written as

$$U^2\frac{d\delta_2}{ds} + (2\delta_2 + \delta_1)U\frac{dU}{ds} = \frac{1}{\rho}\tau_w \tag{18}$$

where δ_1 and δ_2 are the displacement and momentum boundary layer thicknesses and are given by

$$\delta_1 = \delta\int_0^1\left[1 - \frac{u}{U(s)}\right]d\eta_H \tag{19}$$

and

$$\delta_2 = \delta\int_0^1\frac{u}{U(s)}\left[1 - \frac{u}{U(s)}\right]d\eta_H \tag{20}$$

Using velocity distribution from Eq. (14), Eqs. (19) and (20) can be written as

$$\delta_1 = \frac{\delta}{10}\left(3 - \frac{\lambda}{12}\right) \tag{21}$$

and

$$\delta_2 = \frac{\delta}{63}\left(\frac{37}{5} - \frac{\lambda}{15} - \frac{\lambda^2}{144}\right) \tag{22}$$

Simplifying and arranging the terms in Eq. (18), we get

$$\frac{U\delta_2^n}{\gamma U^{n-1}}\frac{d\delta_2}{ds} + \left(2+\frac{\delta_1}{\delta_2}\right)\frac{\delta_2^{n+1}U^{1-n}}{\gamma}\frac{dU}{ds} = \left(\frac{\delta_2}{\delta}\right)^n\left(2+\frac{\lambda}{6}\right)^n \tag{23}$$

Assuming

$$Z = \frac{\delta_2^{n+1}U^{1-n}}{\gamma} \qquad K = Z\frac{dU}{ds}$$

Eq. (23) can be reduced to a nonlinear differential equation of the first order for Z, which can be written as

$$\frac{dZ}{ds} = \frac{F}{U} \tag{24}$$

where

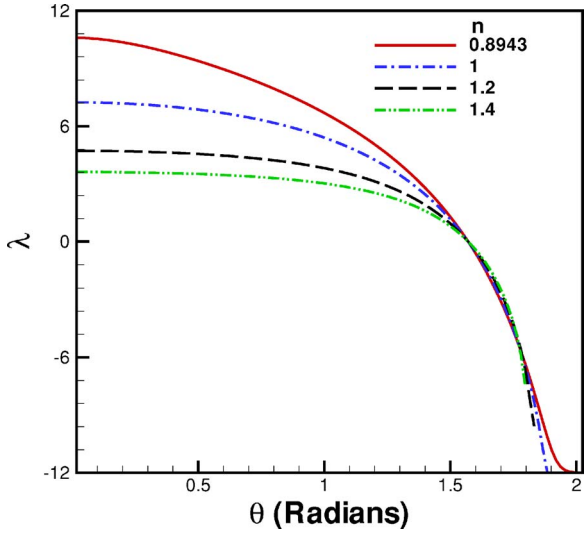

Fig. 2 Behavior of pressure gradient parameter for power-law fluids

$$F = \frac{K\left[\frac{(n+1)\left(2+\frac{\lambda}{6}\right)}{n} - (1+3n)\lambda\left(\frac{\delta_2}{\delta}\right) - (n+1)\lambda\left(\frac{\delta_1}{\delta}\right)\right]}{\lambda\left(\frac{\delta_2}{\delta}\right)} \tag{25}$$

At the stagnation point $s=0$, $U=0$. Since dZ/ds cannot be infinite, F must be zero at the stagnation point. Hence

$$\frac{(n+1)\left(2+\frac{\lambda}{6}\right)}{n} - (1+3n)\lambda\left(\frac{\delta_2}{\delta}\right) - (n+1)\lambda\left(\frac{\delta_1}{\delta}\right) = 0 \tag{26}$$

which gives the values of the pressure gradient parameter λ for different values of n at the stagnation point. Due to limitations of the method used in this study, no root of Eq. (26) could be found in the range $-12 \leqslant \lambda \leqslant 12$ for $n < 0.895$. Bizzell and Slattery [9] could calculate the roots for $0.7358 \leqslant n \leqslant 1.0$ only, whereas Mizushina and Usui [14] calculated the roots in the range $0.895 \leqslant n \leqslant 1.19$. In the present study, the values of λ are calculated for $n \geqslant 0.895$. These values are plotted in Fig. 2 as a function of n.

Following Walz [38], the function F can be approximated by a straight line

$$F = a - bK \tag{27}$$

where the constants a and b are determined for each power index n. From Eq. (25), the values of K and F are obtained for different values of lambda. Following the method of Walz [38] and Schlichting [37], straight lines are obtained between the point of maximum velocity ($K=0$) and the stagnation point ($F=0$) and then correlated to obtain

$$a = 0.45n^{-1.25}, \quad b = 6.2n^{0.8} \tag{28}$$

These correlations are valid between the stagnation point ($F=0$) and the point of maximum velocity ($K=0$). So Eq. (24) can be written as

$$U(s)\frac{dZ}{ds} = a - bK \tag{29}$$

Using potential flow velocity outside the boundary layer for a circular cylinder and rearranging the terms, Eq. (29) can be solved for the local dimensionless momentum thickness:

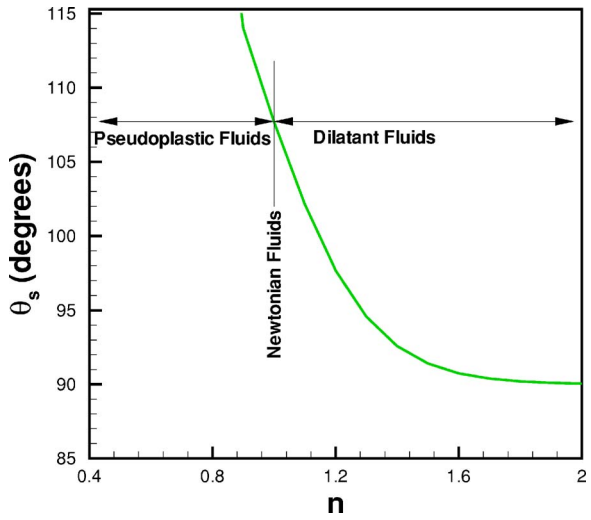

Fig. 3 Angles of separation for power-law fluids

$$\frac{\delta_2}{D} = \left[\frac{a(\sin\theta)^{1+b-n}}{2^{3-n}\mathrm{Re}_{Dp}} \cdot \int_0^{\theta} (\sin\zeta)^{b-1} d\zeta \right]^{1/(n+1)} \tag{30}$$

where ζ is a dummy variable and Re_{Dp} is the generalized Reynolds number for a power-law fluid and is defined as

$$\mathrm{Re}_{Dp} = \frac{D^n \rho U_{\mathrm{app}}^{2-n}}{m} \tag{31}$$

From Eq. (15), the dimensionless hydrodynamic boundary layer thickness can be written as

$$\frac{\delta}{D} = \left[\frac{1}{\mathrm{Re}_{Dp}} \cdot \frac{n\lambda \sin^n\theta}{2^{2-n}\sin 2\theta \left(2+\frac{\lambda}{6}\right)^{1-n}} \right]^{1/(n+1)} \tag{32}$$

Solving Eq. (22) with Eq. (32) and comparing the results with the numerical values obtained from Eq. (30), one can get the values of pressure gradient parameter λ for each position along the circumference of the cylinder. These values were fitted by the least-squares method for each power-law index n and are shown in Fig. 2 for pseudoplastic and dilatant fluids. It shows that the value of λ decreases with increasing n. Using the analytical definition of the point of separation, the angle of separation was determined which depends on the nature of the fluid (pseudoplastic or dilatant) as well as on the velocity distribution inside the boundary layer. The calculated angles of separation are plotted in Fig. 3 as a function of n. It shows that the separation angle decreases with the increase in power-law index n, which is in accordance with Serth and Kiser [11].

Fluid Flow

The first parameter of interest is fluid friction which manifests itself in the form of the drag force F_D, where F_D is the sum of the skin friction drag D_f and pressure drag D_p. Skin friction drag is due to viscous shear forces produced at the cylinder surface, predominantly in those regions where the boundary layer is attached. In dimensionless form, it can be written as

$$C_f = \frac{\tau_w}{\frac{1}{2}\rho U_{\mathrm{app}}^2} \tag{33}$$

Using Eqs. (9) and (14) and simplifying, we get

$$C_f = \frac{2}{\mathrm{Re}_{Dp}^{1/(n+1)}} \left[\frac{(\lambda+12)\sin\theta}{3} \right]^n \left[\frac{\sin 2\theta \left(2+\frac{\lambda}{6}\right)^{1-n}}{2^{n-2} n\lambda \sin^n\theta} \right]^{n/(n+1)} \tag{34}$$

The friction drag coefficient can be defined as

$$C_{Df} = \int_0^{\pi} C_f \sin\theta d\theta = \int_0^{\theta_s} C_f \sin\theta d\theta + \int_{\theta_s}^{\pi} C_f \sin\theta d\theta \tag{35}$$

Since the shear stress on the cylinder surface after boundary layer separation is very small, the second integral can be neglected and the friction drag coefficient can be written as

$$C_{Df} = \int_0^{\theta_s} C_f \sin\theta d\theta \tag{36}$$

The calculations were performed for different values of n and the results are correlated in terms of n and the generalized Reynolds number Re_{Dp} in to a single correlation

$$C_{Df} = \frac{5.786 n^{0.32}}{\mathrm{Re}_{Dp}^{1/(n+1)}} \tag{37}$$

which gives friction drag coefficient for the flow of a power-law fluid over a circular cylinder in an infinite medium. It is interesting to note here that for $n=1$, Eq. (37) gives the friction drag coefficient for the flow of Newtonian fluid over a circular cylinder (Khan et al. [3]).

Pressure drag is due to the unbalanced pressures which exist between the relatively high pressures on the upstream surfaces and the lower pressures on the downstream surfaces. In dimensionless form, it can be written as

$$C_{Dp} = \int_0^{\pi} C_p \cos\theta d\theta \tag{38}$$

where C_p is the pressure coefficient and can be defined as

$$C_p = \frac{\Delta P}{\frac{1}{2}\rho U_{\mathrm{app}}^2} \tag{39}$$

The pressure difference ΔP can be obtained by integrating θ-momentum equation with respect to θ. Following Shibu et al. [39], the θ-momentum equation, for power-law fluids, can be written as

$$u_r \frac{\partial u_\theta}{\partial r} + \frac{u_\theta}{r}\frac{\partial u_\theta}{\partial \theta} + \frac{u_r u_\theta}{r} = -\frac{1}{2r}\frac{\partial C_p}{\partial \theta} + \frac{2^n}{\mathrm{Re}_{Dp}} \cdot \left[\frac{1}{r^2}\frac{\partial}{\partial r}(r^2 \tau_{r\theta}) + \frac{1}{r}\frac{\partial \tau_{\theta\theta}}{\partial \theta} \right] \tag{40}$$

where

$$\tau_{r\theta} = 2\eta\epsilon_{r\theta} \quad \tau_{\theta\theta} = 2\eta\epsilon_{\theta\theta}$$

$$\eta = (2\Pi)^{(n-1)/2} \quad \epsilon_{r\theta} = \frac{1}{2}\left[r\frac{\partial}{\partial r}\left(\frac{u_\theta}{r}\right) + \frac{1}{r}\frac{\partial u_r}{\partial \theta} \right]$$

with

$$\epsilon_{\theta\theta} = \frac{1}{r}\frac{\partial u_\theta}{\partial \theta} + \frac{u_r}{r} \quad \Pi = \epsilon_{rr}^2 + \epsilon_{\theta\theta}^2 + 2\epsilon_{r\theta}^2$$

and

$$u_r = \cos\theta\left(1-\frac{1}{r^2}\right) \quad u_\theta = -\sin\theta\left(1+\frac{1}{r^2}\right)$$

In Eq. (40), Shibu et al. [39] scaled the velocity terms using U_{app}, pressure with $\frac{1}{2}\rho U_{\mathrm{app}}^2$, radial coordinate by the radius of the

cylinder R, the stress components by $m(U_{app}/R)^n$, and the second invariant of the rate of deformation tensor, Π, using $(U_{app}/R)^2$. Using derivatives of the velocity components and an order-of-magnitude analysis (Khan [35]), Eq. (40) can be reduced to

$$\frac{\partial C_p}{\partial \theta} = -4\sin 2\theta - \frac{2^{3n}}{\mathrm{Re}_{Dp}}\sin\theta \tag{41}$$

Integrating it with respect to θ, we get

$$C_p = 2(1-\cos 2\theta) + \frac{2^{3n}}{\mathrm{Re}_{Dp}}(1-\cos\theta) \tag{42}$$

Using Eq. (42) in Eq. (38), the pressure drag coefficients are calculated for different values of n up to the separation point and correlated in terms of n and Re_{Dp} to give

$$C_{Dp} = \frac{1.26n^{3.25}}{\mathrm{Re}_{Dp}} + 1.28[1-\exp(-2.4n)] \tag{43}$$

The total drag coefficient C_D can be written as the sum of both drag coefficients

$$C_D = \frac{5.786n^{0.32}}{\mathrm{Re}_{Dp}^{1/(n+1)}} + \frac{1.26n^{3.25}}{\mathrm{Re}_{Dp}} + 1.28[1-\exp(-2.4n)] \tag{44}$$

which agrees with the drag coefficient of a Newtonian fluid ($n=1$) over a circular cylinder (Khan et al. [3]).

Heat Transfer

The second parameter of interest is the dimensionless average heat transfer coefficient, Nu_D for large Prandtl numbers. This parameter is determined by integrating Eq. (7) from the cylinder surface to the thermal boundary layer edge. Assuming the presence of a thin thermal boundary layer δ_T along the cylinder surface, the energy integral equation for the isothermal boundary condition can be written as

$$\frac{d}{ds}\int_0^{\delta_T}(T-T_a)u\,d\eta = -\alpha\left.\frac{\partial T}{\partial \eta}\right|_{\eta=0} \tag{45}$$

Using velocity and temperature profiles Eqs. (14) and (16), and assuming $\zeta=\delta_T/\delta<1$, Eq. (45) can be simplified to

$$\delta_T\frac{d}{ds}[U(s)\delta_T\zeta(\lambda+12)] = 90\alpha \tag{46}$$

Heat transfer analysis is divided into two parts due to discontinuity at $\theta=\pi/2$. So Eq. (46) is rewritten separately for the two regions (Fig. 1), i.e.

$$\delta_T\frac{d}{ds}[U(s)\delta_T\zeta(\lambda_1+12)] = 90\alpha \tag{47}$$

for region I, and

$$\delta_T\frac{d}{ds}[U(s)\delta_T\zeta(\lambda_2+12)] = 90\alpha \tag{48}$$

for region II. Integrating Eqs. (47) and (48), in the respective regions, with respect to s, one can obtain local thermal boundary layer thicknesses

$$\left(\frac{\delta_T(\theta)}{D}\right)\cdot\mathrm{Re}_{Dp}^{1/(n+1)}\mathrm{Pr}_p^{1/3} = \begin{cases}\sqrt[3]{45F_1(n,\theta)} & \text{for region I}\\ \sqrt[3]{45F_2(n,\theta)} & \text{for region II}\end{cases} \tag{49}$$

where the Prandtl number, Pr_p, for a power-law fluid is defined as

$$\mathrm{Pr}_p = \frac{U_{app}D}{\alpha}\mathrm{Re}_{Dp}^{-2/(n+1)} \tag{50}$$

The functions $F_1(n,\theta)$ and $F_2(n,\theta)$ in Eq. (49) are given by

$$F_1(n,\theta) = \frac{f_1(\theta)}{\sin^2\theta(\lambda_1+12)^2}\left[\frac{2^{n-2}n\lambda_1\sin^n\theta}{\sin 2\theta\left(\frac{\lambda_1+12}{6}\right)^{1-n}}\right]^{1/(n+1)}$$
$$F_2(n,\theta) = \frac{f_3(\theta)}{\sin^2\theta}\left[\frac{2^{n-2}n\lambda_2\sin^n\theta}{\sin 2\theta\left(\frac{\lambda_2+12}{6}\right)^{1-n}}\right]^{1/(n+1)} \tag{51}$$

with

$$f_1(\theta) = \int_0^{\theta}\sin\theta(\lambda_1+12)d\theta$$
$$f_2(\theta) = \int_{\theta_1}^{\theta_s}\sin\theta(\lambda_2+12)d\theta \tag{52}$$
$$f_3(\theta) = \frac{f_1(\theta)}{\lambda_1+12} + \frac{f_2(\theta)}{\lambda_2+12}$$

The local heat transfer coefficients, for the isothermal boundary condition, in both the regions can be written as

$$h_1(\theta) = \frac{3k_f}{2\delta_{T_1}} \quad h_2(\theta) = \frac{3k_f}{2\delta_{T_2}} \tag{53}$$

Thus the dimensionless local heat transfer coefficients, for both regions, can be written as

$$\frac{\mathrm{Nu}_D(\theta)|_{\text{isothermal}}}{\mathrm{Re}_{Dp}^{1/(n+1)}Pr_p^{1/3}} = \frac{3}{2}\begin{cases}\sqrt[3]{\frac{1}{45F_1(n,\theta)}} & \text{for region I}\\ \sqrt[3]{\frac{1}{45F_2(n,\theta)}} & \text{for region II}\end{cases} \tag{54}$$

The average heat transfer coefficient is defined as

$$h = \frac{1}{\pi}\int_0^{\pi}h(\theta)d\theta = \frac{1}{\pi}\int_0^{\theta_s}h(\theta)d\theta + \frac{1}{\pi}\int_{\theta_s}^{\pi}h(\theta)d\theta \tag{55}$$

The first term on the right-hand side shows the heat transfer from the front stagnation point to the separation point and can be written as

$$\int_0^{\theta_s}h(\theta)d\theta = \int_0^{\theta_1}h(\theta)d\theta + \int_{\theta_1}^{\theta_s}h(\theta)d\theta \tag{56}$$

where θ_1 is the angle where the values of the pressure gradient parameter are zero. This angle is found to be very close to $\pi/2$ for all values of n. So, the dimensionless average heat transfer coefficient of the cylinder from the front stagnation point to the separation point can be obtained, using Eqs. (49)–(53), for different values of n and then correlated them to obtain a single expression in terms of Re_{Dp} and Pr_p. This expression is given by

$$\mathrm{Nu}_{D1} = 0.593n^{-0.17}\mathrm{Re}_{Dp}^{1/(n+1)}\mathrm{Pr}_p^{1/3} \tag{57}$$

The second term on the right-hand side of Eq. (55) gives the heat transfer from the separation point to the rear stagnation point. The integral analysis can predict only heat transfer values from the front stagnation point to the separation point. The experiments (Žukauskas and Žiugžda [40], Fand and Keswani [41], and Nakamura and Igarashi [42] among others for Newtonian fluids and Rao [27] for non-Newtonian fluids) show that the heat transfer from the rear portion of the cylinder increases with Reynolds number. For Newtonian fluids, Van der Hegge Zijnen [43] demonstrated that the average heat transferred from the rear portion of the cylinder can be determined from $\mathrm{Nu}_{D2}=0.001\,\mathrm{Re}_{Dp}$ that shows the weak dependence of average heat transfer from the rear portion of the cylinder on Reynolds number. The same weak depen-

dence can be observed from Rao [27] experiments for non-Newtonian fluids.

Thus, the total average dimensionless heat transfer, for isothermal boundary condition, can be written as

$$\mathrm{Nu}_D|_{\mathrm{isothermal}} = 0.593n^{-0.17}\mathrm{Re}_{Dp}^{1/(n+1)}\mathrm{Pr}_p^{1/3} + 0.001\,\mathrm{Re}_{Dp} \quad (58)$$

For the isoflux boundary condition, the energy integral equation can be written as

$$\frac{d}{ds}\int_0^{\delta_T}(T-T_a)ud\eta = \frac{q}{\rho c_p} \quad (59)$$

Assuming constant heat flux and thermophysical properties and using Eqs. (14) and (17), Eq. (58) can be simplified to

$$\frac{d}{ds}[U(s)\delta_T^2\zeta(\lambda+12)] = 90\frac{k_f}{\rho c_p} \quad (60)$$

Rewriting Eq. (60) for the two regions in the same way as Eq. (46), one can obtain local thermal boundary layer thicknesses δ_{T_1} and δ_{T_2} under isoflux boundary condition. The local surface temperatures for the two regions can then be obtained from temperature distribution

$$\Delta T_1(\theta) = \frac{2q\delta_{T_1}}{3k_f} \quad \Delta T_2(\theta) = \frac{2q\delta_{T_2}}{3k_f} \quad (61)$$

The local heat transfer coefficient can now be obtained from its definition as

$$h_1(\theta) = \frac{q}{\Delta T_1(\theta)} \quad h_2(\theta) = \frac{q}{\Delta T_2(\theta)} \quad (62)$$

which give the local Nusselt number for the cross flow over a cylinder with constant flux

$$\frac{\mathrm{Nu}_D(\theta)|_{\mathrm{isoflux}}}{\mathrm{Re}_{Dp}^{1/(n+1)}\mathrm{Pr}^{1/3}} = \frac{3}{2}\begin{cases}\sqrt[3]{\dfrac{2}{45G_1(n,\theta)}} & \text{for region I}\\ \sqrt[3]{\dfrac{2}{45G_2(n,\theta)}} & \text{for region II}\end{cases} \quad (63)$$

where

$$G_1(n,\theta) = \frac{\theta}{\sin\theta(\lambda_1+12)}\left[\frac{2^{n-2}n\lambda_1\sin^n\theta}{\sin 2\theta\left(\dfrac{\lambda_1+12}{6}\right)^{1-n}}\right]^{1/(n+1)}$$

$$G_2(n,\theta) = \frac{g(\theta)}{\sin\theta}\left[\frac{2^{n-2}n\lambda_2\sin^n\theta}{\sin 2\theta\left(\dfrac{\lambda_2+12}{6}\right)^{1-n}}\right]^{1/(n+1)} \quad (64)$$

with

$$g(\theta) = \left[\frac{\theta}{\lambda_1+12} + \frac{\theta-\pi/2}{\lambda_2+12}\right] \quad (65)$$

Following the same procedure for the average heat transfer coefficient as mentioned earlier, one can obtain the average Nusselt number for an isoflux cylinder as

$$\mathrm{Nu}_D|_{\mathrm{isoflux}} = 0.627n^{-0.19}\mathrm{Re}_{Dp}^{1/(n+1)}\mathrm{Pr}_p^{1/3} \quad (66)$$

Combining the results for both thermal boundary conditions, we have

$$\frac{\mathrm{Nu}_D}{\mathrm{Re}_{Dp}^{1/(n+1)}\mathrm{Pr}_p^{1/3}} = \begin{cases}0.593n^{-0.17} & \text{for UWT}\\ 0.627n^{-0.19} & \text{for UWF}\end{cases} \quad (67)$$

These correlations agree with the heat transfer coefficients for a Newtonian fluid ($n=1$) over a circular cylinder (Khan et al. [3]).

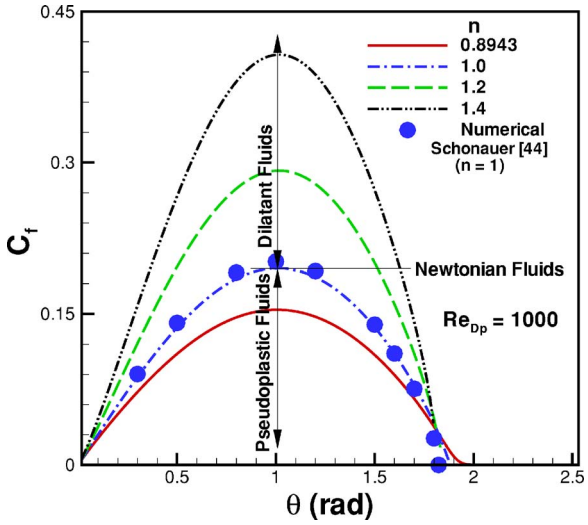

Fig. 4 Effect of power index *n* on skin friction for a circular cylinder

Results and Discussion

Flow Characteristics. The dimensionless local shear stress, C_f, is plotted in Fig. 4 for different power-law fluids. It shows that C_f is zero at the stagnation point for each fluid and reaches a maximum at $\theta \approx 58°$.

The increase in shear stress is caused by the deformation of the velocity profiles in the boundary layer, a higher velocity gradient at the wall, and a thicker boundary layer. In the region of decreasing C_f preceeding the separation point, the pressure gradient decreases further and finally C_f falls close to zero around the separation point, where boundary-layer separation occurs. Beyond this point, C_f remains close to zero up to the rear stagnation point. It also shows that the skin friction increases with the increase in power-law index n. Thus pseudoplastic (shear-thinning) fluids offer less skin friction than dilatant (shear-thickening) fluids, which is in accordance with the numerical results of Agarwal et al. [34]. The results of Newtonian fluids ($n=1$) are compared with the numerical data of Schönauer [44], which shows good agreement for the entire range.

The variation of the total drag coefficient C_D with the power-law index n for different Reynolds number is illustrated in Fig. 5.

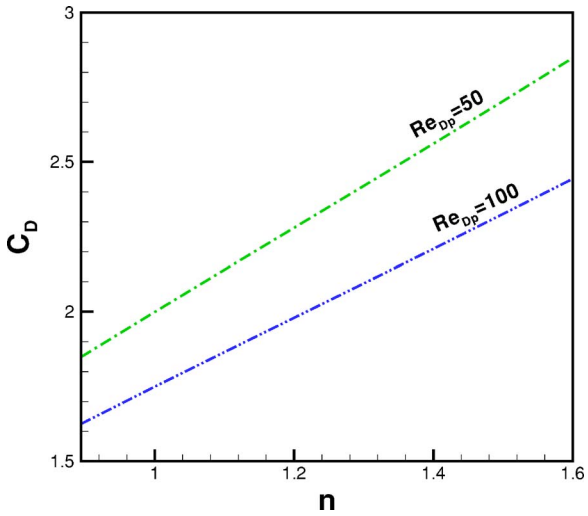

Fig. 5 Effect of *n* on drag coefficients for a circular cylinder

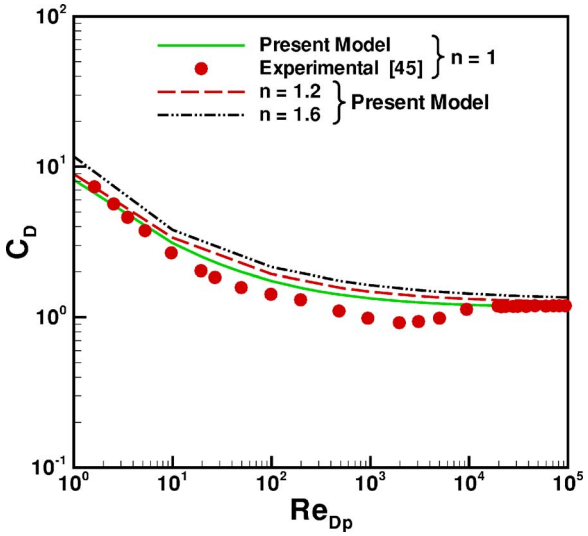

Fig. 6 Effect of Re_{Dp} on drag coefficients for a circular cylinder

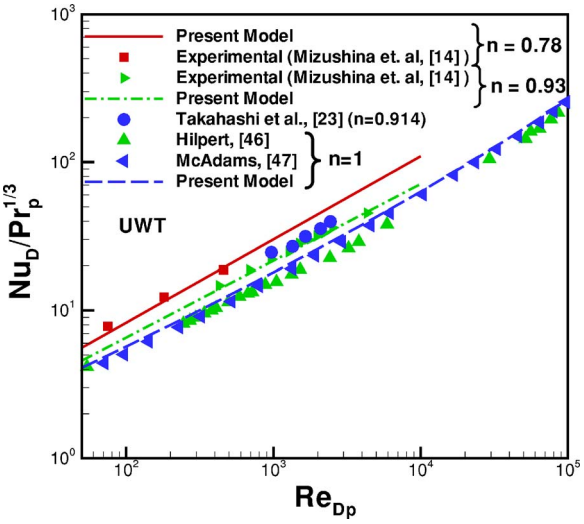

Fig. 8 Comparison of heat transfer coefficients from an isothermal circular cylinder

It shows that for a given Reynolds number, the drag coefficient C_D increases linearly with n and for a given fluid it decreases with the increase in Reynolds number. The drag coefficients for pseudoplastic fluids are found to be lower than dilatant fluids.

The effect of Reynolds number on the drag coefficients for different fluids is shown in Fig. 6. Since there are no other experimental/numerical results to compare with pseudoplastic/dilatant fluids, comparisons are made with the experimental results of Wieselsberger [45] for the air ($n=1$) only. The comparison shows good agreement with the Newtonian case.

Heat Transfer Characteristics. The heat transfer parameter (HTP) $Nu_D/Re_{Dp}^{1/(n+1)}Pr_p^{1/3}$ is presented in Fig. 7 for both the isothermal and isoflux boundary conditions. It shows that HTP decreases with the increase in the power law index n. Thus pseudoplastic fluids transfer more heat than dilatant fluids for the same thermal boundary condition. The isoflux boundary condition gives a higher heat transfer coefficient for both types of fluids.

Figure 8 shows the comparison of the average heat transfer coefficients $Nu_D/Pr_p^{1/3}$ versus Re_{Dp} for Newtonian fluids. Here, the experimental results of Hilpert [46] and McAdams [47] for air are compared with the present model for $n=1$. The average heat transfer coefficients are also presented for non-Newtonian fluids. Experimental results of Takahashi et al. [23] and Mizushina et al. [14] for different CMC (carboxy methyl cellulose) solutions are compared with the present models for isothermal boundary condition. The comparison is found to be in good agreement for all fluids.

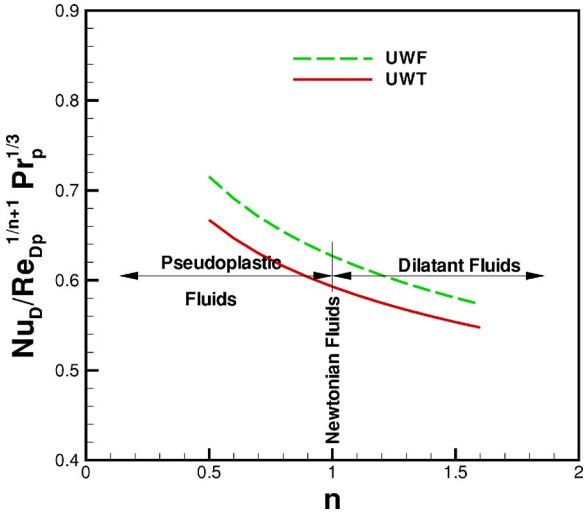

Fig. 7 Comparison of heat transfer parameters for isothermal and isoflux thermal boundary conditions

Conclusions

An integral approach is employed to investigate the fluid flow and heat transfer from an isolated circular cylinder submerged in power-law fluids. Closed form solutions are developed for both the drag and heat transfer coefficients in terms of generalized Reynolds and Prandtl numbers. The correlations of heat transfer are developed for both isothermal and isoflux boundary conditions. It is found that pseudoplastic fluids offer less skin friction and higher heat transfer coefficients than dilatant fluids. Furthermore, the drag coefficients decrease and the heat transfer increases with the decrease in power-law index. It is shown that the present results are in good agreement with the available suitable data for the full laminar range of Reynolds number in the absence of free stream turbulence and blockage effects.

Acknowledgment

The authors gratefully acknowledge the financial support of Natural Sciences and Engineering Research Council of Canada and the Center for Microelectronics Assembly and Packaging.

Nomenclature

C_D = total drag coefficient
C_{Df} = friction drag coefficient
C_{Dp} = pressure drag coefficient
C_f = skin friction coefficient $\equiv 2\tau_w/\rho U_{app}^2$
C_p = pressure coefficient $\equiv 2\Delta P/\rho U_{app}^2$
c_p = specific heat of the fluid (J/kg·K)
D = cylinder diameter (m)
k = thermal conductivity (W/m·K)
h = average heat transfer coefficient (W/m^2·K)
m = consistency index for non-Newtonian viscosity (Pa·s^n)
n = power-law index
Nu_D = average Nusselt number based on the diameter of the cylinder $\equiv hD/k_f$

Pr_p = Prandtl number for power-law fluids $\equiv (U_{\mathrm{app}} D/\alpha)\mathrm{Re}_{Dp}^{-2/(n+1)}$

P = pressure ($\mathrm{N/m^2}$)

q = heat flux ($\mathrm{W/m^2}$)

Re_{Dp} = generalized Reynolds number based on the diameter of the cylinder $\equiv D^n \rho U_{\mathrm{app}}^{2-n}/\mathrm{m}$

s = distance along the curved surface of the circular cylinder measured from the forward stagnation point (m)

T = temperature ($^{\circ}\mathrm{C}$)

U_{app} = approach velocity (m/s)

$U(s)$ = potential flow velocity just outside the boundary layer $\equiv 2U_{\mathrm{app}} \sin\theta$ (m/s)

u = s-component of velocity in the boundary layer (m/s)

v = η-component of velocity in the boundary layer (m/s)

Greek Symbols

α = thermal diffusivity ($\mathrm{m^2/s}$)

δ = hydrodynamic boundary-layer thickness (m)

δ_1 = displacement thickness (m)

δ_2 = momentum thickness (m)

δ_T = thermal boundary layer thickness (m)

η = distance normal to and measured from the surface of the circular cylinder (m)

λ = pressure gradient parameter

μ = absolute viscosity of the fluid ($\mathrm{Ns/m^2}$)

ν = kinematic viscosity of the fluid ($\mathrm{m^2/s}$)

ρ = density of the fluid ($\mathrm{kg/m^3}$)

τ = shear stress ($\mathrm{N/m^2}$)

θ = angle measured from front stagnation point (rad)

ζ = ratio of thermal and hydrodynamic boundary layers $\equiv \delta_T/\delta$

Subscripts

a = ambient

f = fluid or friction

H = hydrodynamic

p = pressure

s = separation

T = thermal or temperature

w = wall

References

[1] Cho, Y. I., and Hartnett, J. P., 1985, "Non-Newtonian Fluids," *Handbook of Heat Transfer Applications*, 2nd ed., McGraw-Hill, New York, Chap. 2.

[2] Chhabra, R. P., and Richardson, J. F., 1999, "Non-Newtonian Flow in the Process Industries: Fundamentals and Engineering Applications," Butterworth-Heinemann, London.

[3] Khan, W. A., Culham, J. R., and Yovanovich, M. M., 2005, "Fluid Flow Around and Heat Transfer From an Infinite Circular Cylinder," ASME J. Heat Transfer, **127**, pp. 785–790.

[4] Acrivos, A., Shah, M. J., and Petersen, E. E., 1960, "Momentum and Heat Transfer in Laminar Boundary-Layer Flows of Non-Newtonian Fluids Past External Surfaces," AIChE J., **6**, pp. 312–317.

[5] Schowalter, W. R., 1960, "Application of Boundary-Layer Theory to Power-Law Pseudo-Plastic Fluids: Similar Solutions," AIChE J., **6**, pp. 24–28.

[6] Shah, M. J., Petersen, E. E., and Acrivos, A., 1962, "Heat Transfer from a Cylinder to a Power-Law Non-Newtonian Fluid," AIChE J., **8**, pp. 542–549.

[7] Acrivos, A., Shah, M. J., and Petersen, E. E., 1965, "On Solution of Two-Dimensional Boundary-Layer Flow Equations for Non-Newtonian Power-Law Fluid," Chem. Eng. Sci., **20**, pp. 101–105.

[8] Lee, S. Y., and Ames, W. F., 1966, "Similarity Solutions for Non-Newtonian Fluids," AIChE J., **12**, pp. 700–708.

[9] Bizzell, G. D., and Slattery, J. C., 1962, "Non-Newtonian Boundary-Layer Flow," Chem. Eng. Sci., **17**, pp. 777–782.

[10] Wolf, C. J., and Szewczyk, A. A., 1966, "Laminar Heat Transfer to Non-Newtonian Fluids From Arbitrary Cylinders," *Proceedings of the Third IHTC*, Chicago, IL, August 7–12, Vol. 1.

[11] Serth, R. W., and Kiser, K. M., 1967, "A Solution of the Two-Dimensional Boundary-Layer Equations for an Ostwald-de Waele Fluid," Chem. Eng. Sci., **22**, pp. 945–956.

[12] Lin, F. N., and Chern, S. Y., 1979, "Laminar Boundary Layer Flow of Non-Newtonian Fluid," Int. J. Heat Mass Transfer, **22**, pp. 1323–1329.

[13] Kim, H. W., Jeng, D. R., and DeWitt, K. J., 1983, "Momentum and Heat Transfer in Power-Law Fluid Flow Over Two-Dimensional or Axisymmetrical Bodies," Int. J. Heat Mass Transfer, **26**, pp. 245–259.

[14] Mizushina, T., and Usui, H., 1978, "Approximate Solution of the Boundary Layer Equations for the Flow of a Non-Newtonian Fluid Around a Cylinder," Heat Transfer-Jpn. Res., **7**, pp. 83–92.

[15] Nakayama, A., Shenoy, A. V., and Koyama, H., 1986, "An Analysis for Forced Convection Heat Transfer From External Surfaces to Non-Newtonian Fluids," Warme-und Stoffubertragung, **20**, pp. 219–227.

[16] Shenoy, A. V., and Nakayam, A., 1986, "Forced Convection Heat Transfer for Axisymmetric Bodies to Non-Newtonian Fluids," Can. J. Chem. Eng., **64**, pp. 680–686.

[17] Nakayama, A., 1986, "Integral Methods for Forced Convection Heat Transfer in Power-Law Non-Newtonian Fluids," *Encyclopedia of Fluid Mechanics: Rheology and Non-Newtonian Flows*, Gulf, Houston, Vol. 7, pp. 305–339.

[18] Anderson, H. I., 1988, "The Nakayama-Koyama Approach to Laminar Forced Convection Heat Transfer to Power-Law Fluids," Int. J. Heat Fluid Flow, **9**, pp. 343–346.

[19] Luikov, A. V., Schulman, Z. P., and Berkovsky, B. M., 1966, "Heat and Mass Transfer in a Boundary Layer of Non-Newtonian Fluids," *Proceedings of the Third IHTC*, Chicago, IL, August 7–12, Vol. 1.

[20] Luikov, A. V., Schulman, Z. P., and Puris, B. I., 1969a, "Mass Transfer of Cylinder in Forced Flow of Non-Newtonian Viscoelastic Fluid," Heat Transfer-Sov. Res., **1**, pp. 121–132.

[21] Luikov, A. V., Schulman, Z. P., and Puris, B. I., 1969b, "External Convective Mass Transfer in Non-Newtonian Fluid," Int. J. Heat Mass Transfer, **12**, pp. 377–391.

[22] James, D. F., and Acosta, A. J., 1970, "The Laminar Flow of Dilute Polymer Solutions Around Circular Cylinders," J. Fluid Mech., **42**, pp. 269–288.

[23] Takashi, K., Maeda, M., and Ikai, S., 1977, "Experimental Study of Heat Transfer from a Cylinder Submerged in a Non-Newtonian Fluid," die dem Nahenungsansatz von K. Pohlhausen genugen, Lilenthal Bericht, **510**, pp. 335–339.

[24] Mizushina, T., Usui, H., Veno, K., and Kato, T., 1978, "Experiments of Pseudoplastic Fluid Cross Flow Around a Circular Cylinder," Heat Transfer-Jpn. Res., **7**, pp. 92–101.

[25] Kumar, S., Mall, B. K., and Upadhyay, S. N., 1980, "On the Mass Transfer in Non-Newtonian Fluids. II. Transfer From Cylinders to Power-Law Fluids," Lett. Heat Mass Transfer, **7**, pp. 55–64.

[26] Ghosh, U. K., Gupta, S. N., Kumar, S., and Upadhay, S. N., 1986, "Mass Transfer in Cross Flow of Non-Newtonian Fluid Around a Circular Cylinder," Int. J. Heat Mass Transfer, **29**, pp. 955–960.

[27] Rao, B. K., 2000, "Heat Transfer to Non-Newtonian Flows Over a Cylinder in Cross Flow," Int. J. Heat Fluid Flow, **21**, pp. 693–700.

[28] Ghosh, U. K., Upadhay, S. N., and Chhabra, R. P., 1994, "Heat and Mass Transfer From Immersed Bodies to Non-Newtonian Fluids," Adv. Heat Transfer, **25**, pp. 251–319.

[29] Coelho, P. M., and Pinho, F. T., 2003, "Vortex Shedding in Cylinder Flow of Shear-Thinning Fluids. I. Identification and Demarcation of Flow Regimes," J. Non-Newtonian Fluid Mech., **110**, pp. 143–176.

[30] Coelho, P. M., and Pinho, F. T., 2003, "Vortex Shedding in Cylinder Flow of Shear-Thinning Fluids: II. Flow Characteristics," J. Non-Newtonian Fluid Mech., **110**, pp. 177–193.

[31] Coelho, P. M., and Pinho, F. T., 2004, "Vortex Shedding in Cylinder Flow of Shear-Thinning Fluids: III. Pressure Characteristics," J. Non-Newtonian Fluid Mech., **121**, pp. 55–68.

[32] D'Alessio, S. J. D., and Pascal, J. P., 1996, "Steady Flow of a Power-Law Fluid Past a Cylinder," Acta Mech., **117**, pp. 87–100.

[33] Chhabra, R. P., Soares, A. A., and Ferreira, J. M., 2004, "Steady Non-Newtonian Flow Past a Circular Cylinder: A Numerical Study," Acta Mech., **172**, pp. 1–16.

[34] Agarwal, M., Chhabra, R. P., and Eswaran, V., 2002, "Laminar Momentum and Thermal Boundary Layers of Power-Law Fluids Over a Slender Cylinder," Chem. Eng. Sci., **57**, pp. 1331–1341.

[35] Khan, W. A., 2004, "Modeling of Fluid Flow and Heat Transfer for Optimization of Pin-Fin Heat Sinks," Ph.D. thesis, Department of Mechanical Engineering, University of Waterloo, Canada.

[36] Pohlhausen, K., 1921, "Zur Näherungsweise Integration der Differential Gleichung der Laminaren Reibungschicht," Z. Angew. Math. Mech., **1**, pp. 252–268.

[37] Schlichting, H., 1979, *Boundary Layer Theory*, 7th ed., McGraw-Hill, New York.

[38] Walz, A., 1941, "Ein neuer Ansatz für das Greschwindlig-keitsprofil der laminaren Reibungsschicht," Lilienthal-Bericht **141**, p. 8.

[39] Shibu, S., Chhabra, R. P., and Eswaran, V., 2001, "Power-Law Fluid Flow Over a Bundle of Cylinders at Intermediate Reynolds Numbers," Chem. Eng. Sci., **56**, pp. 5545–5554.
[40] Žukauskas, A., and Žiugžda, J., 1985, *Heat Transfer of a Cylinder in Crossflow*, Hemisphere, New York.
[41] Fand, R. M., and Keswani, K. K., 1972, "A Continuous Correlation Equation for Heat Transfer From Cylinders to Air in Crossflow for Reynolds Numbers From 10^{-2} to 2×10^{5}," Int. J. Heat Mass Transfer, **15**, pp. 559–562.
[42] Nakamura, H., and Igarashi, T., 2004, "Variation of Nusselt Number With Flow Regimes Behind a Circular Cylinder for Reynolds Numbers From 70-30000," Int. J. Heat Mass Transfer, **47**, pp. 5169–5173.
[43] Van der Hegge Zijnen, B. G., 1956, "Modified Correlation Formulae for Heat Transfer by Natural and Forced Convection From Horizontal Cylinders," Appl. Sci. Res., Sect. A, **6**, pp. 129–140.
[44] Schönauer, W., 1964, "Ein Differenzenverfahren zur Lösung der Grenzschichtgleichung für stationäre, laminare, inkompressible Strömung," Ing.-Arch., **33**, p. 173.
[45] Wieselsberger, C., 1921, "New Data on The Laws of Fluid Resistance," NASA TN No. 84.
[46] Hilpert, R., 1993, "Ẅarmeabgabe von Geheizten Drahten und Rohren," Forsch. Geb. Ingenieurwes., **4**, pp. 215–224.
[47] McAdams, W. H., 1942, *Heat Transmission*, 3rd ed., McGraw-Hill, New York.

Film Cooling Effectiveness on the Leading Edge Region of a Rotating Turbine Blade With Two Rows of Film Cooling Holes Using Pressure Sensitive Paint

Jaeyong Ahn

M. T. Schobeiri

Je-Chin Han
e-mail: jc-han@tamu.edu

Department of Mechanical Engineering,
Texas A&M University,
College Station, TX 77843-3123

Hee-Koo Moon
Solar Turbines Incorporated,
2200 Pacific Highway,
San Diego, CA 92101

Detailed film cooling effectiveness distributions are measured on the leading edge of a rotating gas turbine blade with two rows (pressure-side row and suction-side row from the stagnation line) of holes aligned to the radial axis using the pressure sensitive paint (PSP) technique. Film cooling effectiveness distributions are obtained by comparing the difference of the measured oxygen concentration distributions with air and nitrogen as film cooling gas respectively and by applying the mass transfer analogy. Measurements are conducted on the first-stage rotor blade of a three-stage axial turbine at 2400 rpm *(positive off-design),* 2550 rpm *(design), and* 3000 rpm *(negative off-design), respectively. The effect of three blowing ratios is also studied. The blade Reynolds number based on the axial chord length and the exit velocity is 200,000 and the total to exit pressure ratio was 1.12 for the first-stage rotor blade. The corresponding rotor blade inlet and outlet Mach numbers are 0.1 and 0.3, respectively. The film cooling effectiveness distributions are presented along with discussions on the influence of rotational speed (off design incidence angle), blowing ratio, and upstream nozzle wakes around the leading edge region. Results show that rotation has a significant impact on the leading edge film cooling distributions with the average film cooling effectiveness in the leading edge region decreasing with an increase in the rotational speed (negative incidence angle).* [DOI: 10.1115/1.2241945]

Keywords: gas turbine, film cooling, rotating blade, leading edge, pressure sensitive paint (PSP)

Introduction

The rotor blade inlet temperature of modern gas turbines has been increased to achieve higher thermal efficiency. However, the increased inlet temperature can result in material failure of the turbine blades due to the higher heat load and thermal stress. In order to overcome the hazard from the severe environment and prevent failure of turbine components, film cooling has been widely used as an active cooling method. In a film cooled blade, relatively cooler air from compressor is injected through several rows of discrete holes on the surface which provide a protective film between the hot mainstream gases and the turbine blade. This helps in maintaining the surface at an acceptable temperature level, thus protecting the turbine blade from failure. However, excessive use of a coolant can reduce the gain of a higher inlet temperature because the extraction of compressed air for film cooling and the resulting mixing losses between the hot mainstream flow and the film coolant, reduce the thermal efficiency of the entire system. Thus, many studies have been conducted to understand the physical phenomena regarding the film cooling process and to find better film-hole configurations that can provide more protection with minimal amount of coolant. A comprehensive compilation of the available cooling techniques used in the gas turbine industry has been presented by Han et al. [1] in their book.

Many investigations have been conducted on the turbine airfoil film cooling in a cascade environment. Nirmalan and Hylton [2] studied the effects of various operating parameters on film cooling in a turbine vane cascade whose conditions are similar to the ranges found in actual engines. Abuaf et al. [3] presented heat transfer coefficients and film effectiveness for a film cooled vane. The heat transfer coefficient on the pressure surface shows very little effect from film injection while the suction side heat transfer coefficient shows a significant increase. Cruse et al. [4] studied the effect of leading-edge shapes. They measured the film cooling effectiveness using an infrared camera with circular and elliptic leading edge geometries. They observed similar film cooling results for both leading edge geometries. Ekkad et al. [5] studied the combined effects of unsteady wake and free stream turbulence on the film cooling effectiveness and the heat transfer coefficient with air and CO_2 film injection. They found higher heat transfer coefficients and lower film cooling effectiveness compared to the individual effects. Cutbirth and Bogard [6] studied the effects of coolant density ratio on film cooling effectiveness in a simulated turbine vane model using an infrared camera.

More detailed investigations were performed in the leading edge region because it has the highest heat transfer level due to flow stagnation and it affects the heat transfer and aerodynamics over the entire blade. Luckey et al. [7] simulated the airfoil leading edge using a cylinder with several film cooling rows. The holes were located at angles of 20 deg, 30 deg, and 40 deg to the surface in the spanwise direction. The coolant to mainstream density ratio was 2.15, which is a typical engine condition. They correlated their results for the optimum blowing ratio in terms of coolant to mainstream velocity ratio and injection angle. Mick and Mayle [8] studied the effect of coolant blowing ratio and film

Contributed by the Heat Transfer Division of ASME for publication in the JOURNAL OF HEAT TRANSFER. Manuscript received October 30, 2005; final manuscript received April 22, 2006. Review conducted by Phillip M. Ligrani.

cooling-hole location on the stagnation region of a semicircular leading edge with a flat body. They presented heat transfer coefficient and film effectiveness results for two rows of holes at ±15 deg and ±44 deg from stagnation with the coolant blowing ratio from $M=0.38$ to 0.97. Karni and Goldstein [9] studied the effect of blowing ratio and injection location on the mass transfer coefficient using a cylindrical leading edge model. Mehendale et al. [10] and Mehendale and Han [11] investigated the effect of free stream turbulence on heat transfer and film cooling effectiveness using a cylindrical leading edge model. They showed that the coolant jet structures are maintained over a longer distance at lower free stream turbulence. Ou et al. [12] presented the effect of film-hole location and inclined film slots on the leading edge film cooling heat transfer using a cylindrical leading edge model. They showed that two-row injection performs better at a lower blowing ratio while, at higher blowing ratio, two-row injection and one-row injection film effectiveness distributions overlap. Mehendale and Han [13] studied the Reynolds number effect on leading edge film effectiveness and heat transfer coefficients. Their results showed that an increase in the Reynolds number increases both the heat transfer coefficients and film cooling effectiveness as the momentum of the flow near the wall is higher which causes more film deflection and attachment to surface. Salcudean et al. [14] investigated the effect of coolant to mainstream density ratio using air and CO_2 as coolant gases. They used the heat/mass transfer analogy to measure adiabatic wall effectiveness. Funazaki et al. [15] studied the effect of unsteady wake on the leading edge film cooling effectiveness. They used a spoked-wheel-type generator to simulate the periodic unsteady wake effect. They pointed out that the effect of length scale should be considered, and the presence of unsteady wakes may reduce film cooling effectiveness. Ekkad et al. [16] presented the effect of coolant density and free-stream turbulence on a cylindrical leading edge model using a transient liquid crystal technique to obtain the detailed heat transfer coefficient and film effectiveness distributions. They also used CO_2 and air as coolant gases to simulate the density ratio effect. They showed that the film cooling effectiveness values for air as the coolant are highest at low blowing ratios and decrease with an increase in the blowing ratio. In the meantime, for CO_2 as the coolant, the highest film cooling effectiveness is obtained at a blowing ratio of 0.8. Ou and Rivir [17] examined the effect of turbulence intensity, blowing ratio, and Reynolds number using a transient liquid crystal image method on a large scale symmetric circular leading edge. Their result showed similar trends with previous research and confirmed the heat flux reduction due to the film cooling. Many studies were also conducted on the effect of film-hole geometry. Reiss and Bölcs [18] and Kim and Kim [19] studied the effect of the injection hole shape using a cylindrical leading edge model and showed that holes with a laid back design and widened exits gave higher film cooling effectiveness compared to the cylindrical holes.

Despite the numerous studies on the film cooling effectiveness, most of them were performed in a cascade blade or in a wind tunnel using a flat plate or a cylindrical model. Only a few results on film cooling effectiveness under turbine rotating conditions are available in open literature due to the difficulty in conducting this type of experiments. Dring et al. [20] investigated film cooling performance in a low speed rotating facility. A film cooling hole was located on both the pressure and suction sides. They used ammonia and Ozalid paper to qualitatively observe the coolant trace while the quantitative tests were conducted using thermocouples. Their results show that the film coolant had only a small radial displacement, similar to flat plate results, on the suction side. On the pressure side, the film coolant trace had a large radial displacement toward the blade tip due to rotation. Takeishi et al. [21] also reported the film cooling effectiveness distributions on a low speed stator-rotor stage using a rotating rig with a one-stage turbine model. They simulated actual flow velocity triangles and pressure ratios of an actual heavy-duty gas turbine. The blowing ratios were similar to engine conditions ($M=0.6-1.0$) while the coolant to the mainstream density ratio was unity, whereas the coolant to the mainstream density ratio is 1.5–2.5 in real engine conditions. They sampled the cooling gas at several locations along the blade surface and analyzed them using gas chromatography. They also simulated similar conditions in a cascade and compared with the data from the rotating rig. The results showed that the film cooling effectiveness from the cascade and the rotating blade matched well on the suction side while the rotating film cooling data decreased more rapidly than the cascade data on the pressure side. They explained that this phenomenon is due to the radial flow and strong mixing on the pressure side under rotation conditions. They also noted that the overall value on the suction side is higher than that of the pressure side, and that strong lateral mixing plays a fundamentally different role on boundary layer stability on concave (pressure-side) and convex (suction-side) surfaces. Abhari and Epstein [22] investigated time-resolved measurements of heat transfer on a fully cooled transonic turbine stage. Using a short-duration blowdown turbine test facility, they simulated full engine operating parameters. The coolant was supplied through the film cooling holes on the pressure and the suction sides, but no film cooling holes were located on the leading edge region. They distributed several thin-film heat flux gages along the blade surface to measure the time-resolved heat flux distributions. Their results showed that the film injection has very little effect on the pressure side heat transfer level, while a strong effect of film injection is observed on the entire suction side surface.

This study is aimed to investigate the effects of the rotational speed on film cooling effectiveness as well as the effects of the blowing ratio on the coolant path in the leading edge region with two rows of showerhead holes aligned to the radial axis. This is the first paper available in open literature using the PSP method to determine the detailed film cooling effectiveness of a rotating blade. The rotational speed was controlled to be 2400 rpm (off design condition), 2550 rpm (design condition), and 3000 rpm (off design condition) and the averaged blowing ratio was controlled to be 0.5, 1.0, and 2.0, respectively. The experimental results of the detailed film effectiveness distributions on the rotating turbine blade leading edge region will be helpful in understanding the physical phenomena regarding the film injection and useful in designing more efficient film-cooled turbine blades.

In this study, the pressure sensitive paint (PSP) technique was used to measure the detailed film cooling effectiveness distributions in a rotating frame. Note that PSP technique is based on the mass transfer analogy. Thus, it is free from the heat conduction effects, which cannot be avoided using the standard heat transfer measurement methods. This technique was proposed by Zhang et al. [23]. In their study, the film cooling effectiveness distributions were measured on the flat plate using PSP technique, and the results were validated by the gas chromatography measurements. They also applied PSP technique to measure the film effectiveness distributions on a turbine vane end-wall region [24,25]. Ahn et al. [26] and Mhetras et al. [27] used the same PSP technique to obtain the local film cooling effectiveness distributions on the blade tip region, and on the squealer rim wall region, respectively, in a cascade. Wright et al. [28] conducted an assessment of steady state PSP, TSP (temperature sensitive paint), and IR (infrared) measurement techniques for flat plate film cooling. Gao et al. [29] compared the steady state PSP and transient IR measurement techniques for the nonrotating leading edge region film cooling. PSP works by sensing the partial pressure of oxygen on the test surface. By displacing the oxygen on the leading edge via nitrogen injection from the film cooling holes and by measuring the relative difference between air and nitrogen injection, the film cooling effectiveness can be calculated. Since no heating is involved, errors resulting from lateral heat conduction in the test surface are avoided resulting in a clean and well-defined coolant trace.

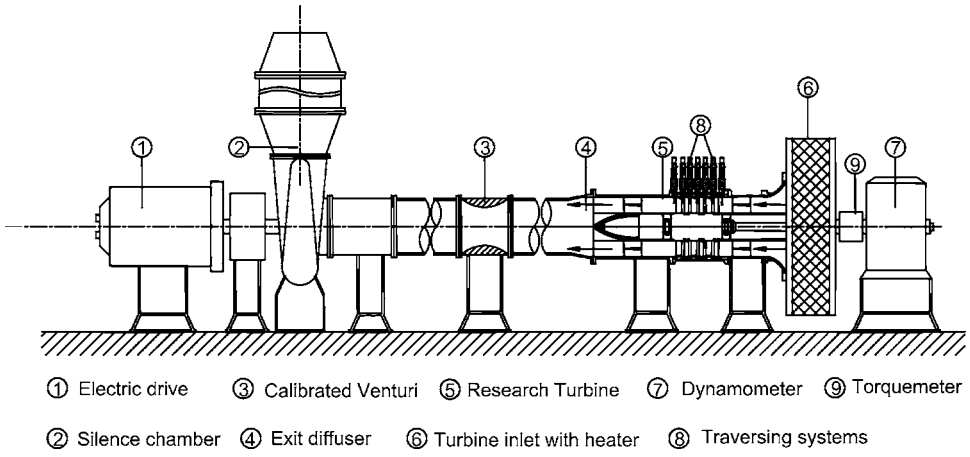

Fig. 1 Overall layout of TPFL-research turbine facility, from Schobeiri et al. [30]

Facilities and Testing

Research Type Turbine Facility. To address the major turbine efficiency, performance, heat transfer, and flow research issues, Schobeiri and his co-workers [30,31] developed and designed a state-of-the-art multipurpose turbine research facility with a versatile research turbine as its core component. The compressor and combustar stages of a gas turbine are not modeled. The modular structured design of the research turbine enables incorporation of up to four turbine stages. The stator and rotor blades may be of any arbitrary design, ranging from zero degree of reaction cylindrical blades to higher reaction 3D blades. Test blades of high, intermediate, or low pressure turbine units may be used. The facility is capable of accurately measuring the efficiency and performance of the entire turbine engine. In particular, the sophisticated inter-stage traversing system provides detailed flow and temperature profiles of the turbine stages.

The overall layout of the test facility is shown in Fig. 1. It consists of a 300 HP electric motor connected to a frequency controller which drives the compressor component. A three-stage centrifugal compressor supplies air with a maximum pressure difference of 55 kPa and a volume flow rate of 4 m^3/s. The compressor operates in suction mode and the pressure and volume flow can be varied by a frequency controller from 0 to 66 Hz. A pipe fitted with a transition piece connects the compressor to a Venturi mass flow meter which is used to measure the mass flow through the turbine component. An exit diffuser serves as a smooth transition piece between the turbine component and the Venturi. The three-stage turbine with a fully automated data acquisition system is the core component of the test facility. The turbine inlet has an integrated heater that prevents condensation of water from humid air expanding through the turbine during the test. The turbine shaft is connected through a flexible coupling with one end of a high precision torque meter. The accuracy of this torque meter is ±0.02% of full scale. The other end of the torque meter is coupled via a second flexible coupling with an eddy current low inertia dynamometer with the maximum power of 150 KW, a maximum torque of 500 Nm, and a rotational speed accuracy of ±1 rpm. The dynamometer is controlled by a Texcel V4-EC controller acquisition computer. Figure 2 shows a three-stage air turbine component with its dimensions and operating conditions specified in Table 1. For the current investigations, 2D blades are used. A conceptual view of each stage is shown in Fig. 3. The blades are mounted on the rotor cylinder, which is connected to the shaft via two locking mechanisms. Detailed flow characteristics of this turbine can be found in the study of Schobeiri et al. [30,31]. They used a five-hole probe to provide flow angles, loss characteristics, pressure contours at several sections, and other aerodynamic performance at design point and off-design conditions.

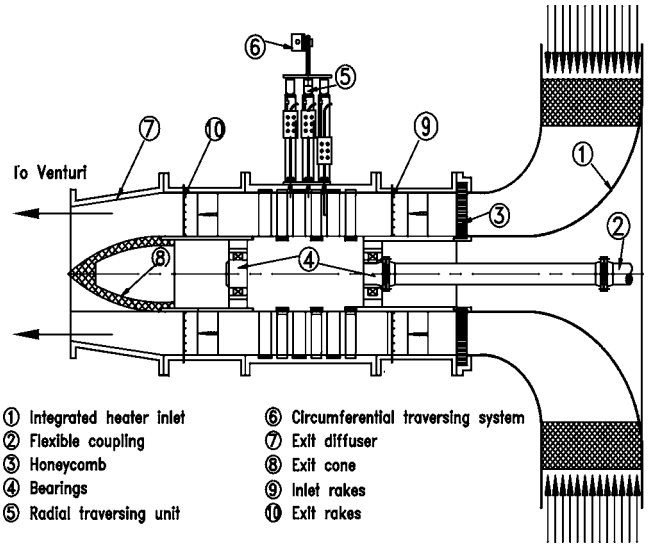

Fig. 2 Three-stage research turbine components, from Schobeiri et al. [30]

Modification on the Turbine. For film cooling heat transfer investigations, a module was added to the system to enable precise measurement of film cooling effectiveness on rotating blades using PSP as the measurement technique. To supply coolant to the blade, the rotor cylinder and turbine shafts were modified as shown in Fig. 4. Blue arrows show the coolant flow path while red arrows indicate the mainstream flow. A rotary seal was adapted to

Table 1 Turbine dimensions and operating conditions

Item	Specification	Item	Specification
Stage no.	$N=3$	Mass flow	$ms=3.728$ kg/s
Tip diameter	$D_t=685.8$ mm	Speed range	$n=1800-3000$ rpm
Hub diameter	$D_h=558.8$ mm	Design speed	$n_D=2550$ rpm
Blade height	$B_h=63.5$ mm	Current speed	$n=2400-3000$ rpm
Blade no.	Stator 1=58	Inlet pressure	$p_{in}=101.356$ kPa
Blade no.	Rotor 1=46	Exit pressure	$p_{ex}=71.708$ kPa
Blade no.	Stator 2=52	Blade no.	Stator 3=56
Blade no.	Rotor 2=40	Blade no.	Rotor 3=44
Power		$P=80.0-110.0$ kW	

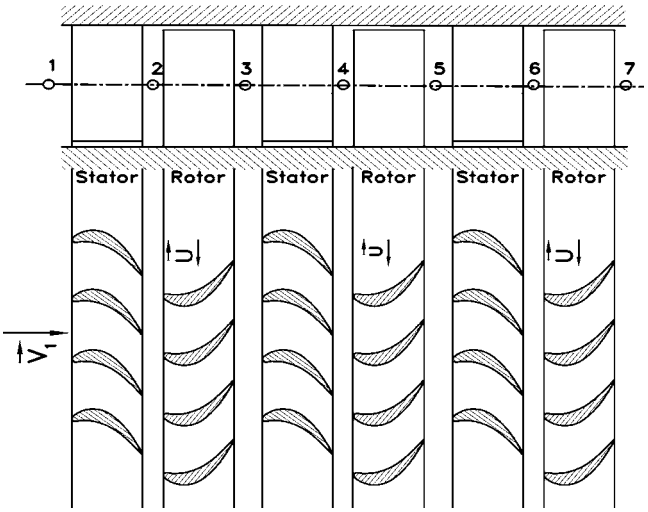

Fig. 3 Conceptual view of the three-stage turbine, from Schobeiri et al. [31]

prevent any leakage between rotating and nonrotating components. The coolant is supplied through the hollow shaft and fills inside of the rotor cylinder. Then, the coolant is injected into the blades through hollow bolts used to attach the blade to the cylinder.

Figure 5 shows the coolant path inside the blade at the first rotor stage. The blade consists of top and bottom pieces due to the manufacturing constraints and its total height and axial chord length are 63.5 and 38.1 mm, respectively. The coolant is injected into the leading edge plenum connected to a radial slot. This design was applied to ensure a uniform coolant discharge from the plenum to the film cooling holes. Then, the coolant gas is finally injected into the mainstream through the discrete holes on the leading edge.

There are 16 film cooling holes in two rows; pressure side row and suction side row from stagnation (Fig. 6). Each row has eight film cooling holes and those in the pressure side row are staggered to the holes in the suction side row. The distance between adjacent film cooling holes (p) in the spanwise direction is 7.1 mm for the film hole diameter (d) 1.19 mm ($p/d=5.97$). The distance between the pressure and suction side rows is 4.06 mm. The film cooling holes were oriented to the spanwise (radial) direction and inclined to the surface by 30 deg. In order to prevent any rotor imbalance, two modified film cooling blades were diametrically mounted.

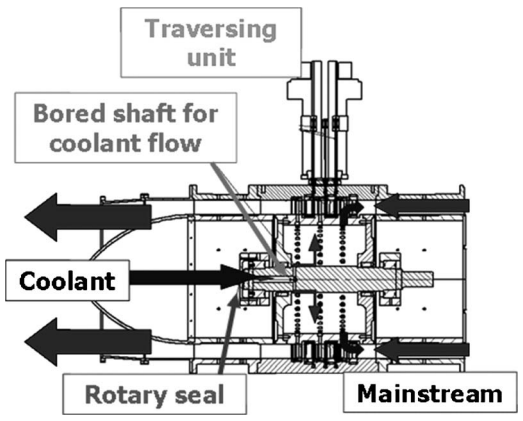

Fig. 4 Flow path of the coolant gas

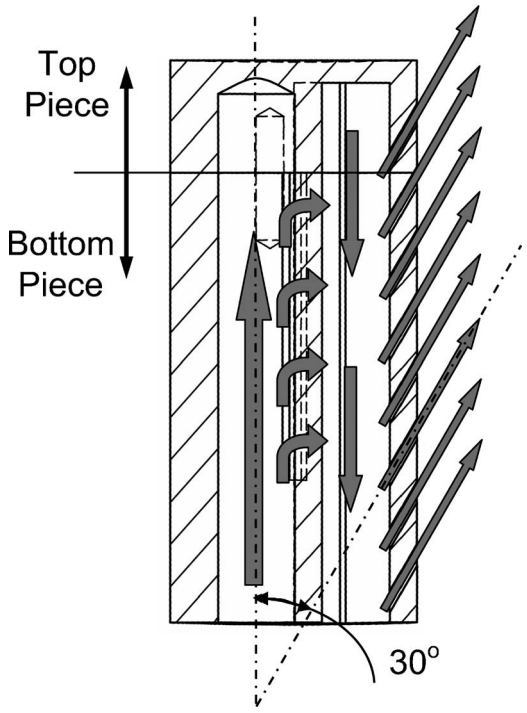

Fig. 5 Coolant path inside the blade

Film Cooling Effectiveness Measurement Using PSP Technique. As mentioned above, PSP is based on the mass transfer analogy and, thus, eliminate the effects of the heat conduction. Under rotating conditions, especially, this technique can avoid the difficulties of mounting heaters and thermocouples on the rotating blades. Thus, the PSP technique was utilized for this study. The accuracy of the PSP technique for measuring film-cooling effectiveness has been compared by Wright et al. [28] on a flat plate with compound angled ejection holes using steady-state infrared (IR) technique and steady-state temperature sensitive paint (TSP) technique. Results were obtained for a range of blowing ratios and show reasonable agreement with each other with IR, TSP as well as PSP giving effectiveness results within 15% of each other.

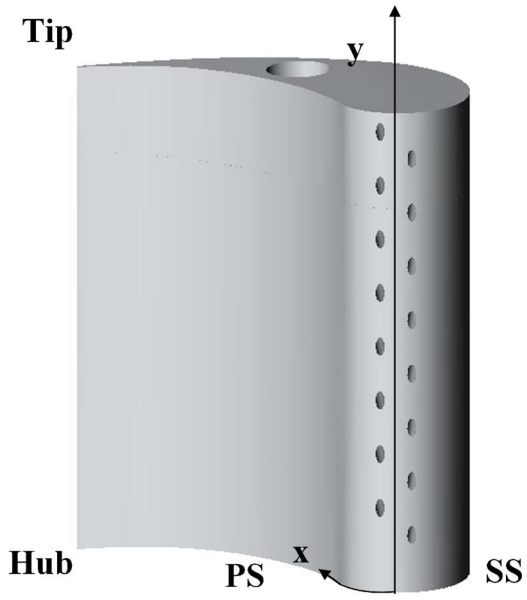

Fig. 6 Modified film cooling blade

Larger uncertainties for heat transfer techniques such as IR and TSP methods were observed due to lateral heat conduction in the flat plate as corrections for heat conduction were not included in the presented results.

PSP is a photo-luminescence material that changes emitting light intensity according to the surrounding partial pressure of oxygen. By comparing the intensity difference between with and without flow cases, we can obtain the oxygen partial pressure information from the following equation:

$$\frac{I_{\text{ref}} - I_{\text{blk}}}{I_{\text{air}} - I_{\text{blk}}} = f\left(\frac{(P_{O_2})_{\text{air}}}{(P_{O_2})_{\text{ref}}}\right) \tag{1}$$

We need to take three kinds of images to enables it; reference image, air image, and black image. The reference image ($\boldsymbol{I_{ref}}$) is taken without any air flow but with the coated surface illuminated. The pressure on the test surface $(\boldsymbol{P_{O_2}})_{\boldsymbol{ref}}$ is constant because there is no air flow. The air image ($\boldsymbol{I_{air}}$) is taken with the mainstream and coolant flow on and with the surface illuminated. Note that air is used for both mainstream and coolant. The black image ($\boldsymbol{I_{blk}}$) is taken without any flow or illumination in order to eliminate camera noise. If the function $\boldsymbol{f}$ is available after a proper calibration process (discussed in the following section), the only unknown variable $(\boldsymbol{P_{O_2}})_{\boldsymbol{air}}$ can be calculated. Most common applications of PSP are the static pressure measurements. Because the concentration of oxygen is constant ($\boldsymbol{P_{O_2}=0.21P}$) in the air, the oxygen partial pressure can be converted into the static pressure directly

$$\frac{(P_{O_2})_{\text{air}}}{(P_{O_2})_{\text{ref}}} = \frac{(0.21 \times P)_{\text{air}}}{(0.21 \times P)_{\text{ref}}} = \frac{P_{\text{air}}}{P_{\text{ref}}} \tag{2}$$

The film cooling effectiveness can be measured using PSP technique by replacing the coolant gas as nitrogen instead of air. In this case, the oxygen as the coolant is replaced with nitrogen and generate lower oxygen partial pressure distribution $(\boldsymbol{P_{O_2}})_{\boldsymbol{mix}}$. It can be obtained from the following equation by taking another image: Mixture image ($\boldsymbol{I_{mix}}$). It is taken with the mainstream, coolant flow (nitrogen) and with the surface illuminated

$$\frac{I_{\text{ref}} - I_{\text{blk}}}{I_{\text{mix}} - I_{\text{blk}}} = f\left(\frac{(P_{O_2})_{\text{mix}}}{(P_{O_2})_{\text{ref}}}\right) \tag{3}$$

The difference in molecular weight between air and nitrogen is assumed to be small enough to be neglected. Thus, if the pressure field generated by film injection is assumed to be same for the air and nitrogen injection cases, we can measure the effectiveness from the oxygen partial pressure difference. Note that the film-cooling effectiveness can be expressed by a ratio of oxygen concentrations in terms of mass transfer and can be re-written in terms of oxygen partial pressure

$$\eta = \frac{C_{\text{mix}} - C_{\text{air}}}{C_{N_2} - C_{\text{air}}} = \frac{C_{\text{air}} - C_{\text{mix}}}{C_{\text{air}}} = \frac{(P_{O_2})_{\text{air}} - (P_{O_2})_{\text{mix}}}{(P_{O_2})_{\text{air}}} \tag{4}$$

C_{air}, C_{mix}, and C_{N_2} are the oxygen concentrations of mainstream air, local mixed gas on the test surface, and coolant gas, respectively. The definition for film effectiveness in Eq. (4) based on mass transfer analogy is of similar form as that for adiabatic film cooling effectiveness given in Eq. (5)

$$\eta = \frac{T_{\text{mix}} - T_m}{T_c - T_m} \tag{5}$$

Optical Components Setup. Figure 7 is the schematic drawing of the optical components. A narrow gap exists between the first stage stator and rotor. For safety reasons, the rotating turbine is enclosed in a steel casing. Thus, in order to take images of the leading edge of the rotor blade, traditional camera lenses and lighting sources could not be used in the research turbine for data acquisition as an optical window could not be provided near the leading edge. Hence, a borescope was used to enable optical access to the blade leading edge region. It was inserted between the trailing edge of first stator and the leading edge of the first rotor and was confirmed to be rigid under load. It had a 90 deg direction of view and a ±45 deg field of view and its diameter was 5.77 mm. A 6 W Argon ion laser, whose wavelength was 488 nm, illuminated the PSP coated blade. Both the exciting light from the laser and the emitted light from the PSP coating were delivered through the borescope using separate paths of fiber optic cables embedded in the borescope. A 12-bit scientific grade CCD camera (High speed Sensicam with CCD temperature maintained at −15°C using two-stage peltier cooler) with an exposure time of 15 μs was employed to measure the emitting light intensity. A small exposure time was selected to minimize image blurring from rotor movement. At the given optical setup and exposure time, the averaged number of photons detected by a pixel is about 1500 e^- while the full-well capacity of the camera is 35,000 e^-. After averaging 200 images, it gives 0.2–0.4% shot noise error for given pressure range. The camera was triggered by a signal from an angular position sensor attached on the shaft. By detecting the same angular position, the images from the camera had the same view angle and were able to be averaged without blurring the information. In addition, a 600 nm long pass optical filter was placed between the camera and the borescope to block any reflected light and to record only the emitted light from the PSP. Spectral characteristics of the current PSP were also considered to choose the wavelengths for excitation (blue at 488 nm) and return (orange) signals for the PSP. The borescope is located upstream of the rotor blade leading edge between the first stage stator-rotor gap to capture images. It should be noted that the distance between the rotor blade leading edge and the borescope is about 10 mm due to the geometric restriction in this gap. The additional wake from the borescope may affect the film coolant distribution on the leading edge region. However, the response time of current PSP is about 0.3 s to the pressure variation. During 0.3 s, the film cooling blade travels 12–15 revolutions. Thus, at the instant at which an image of the test surface (15 μs) is captured, the PSP does not have sufficient reaction time to detect the effect of the wake from the borescope. Hence, the information from the PSP represents an averaged value over several revolutions and the effect of the additional wake from the borescope, which is present only at a particular position in time, can be neglected.

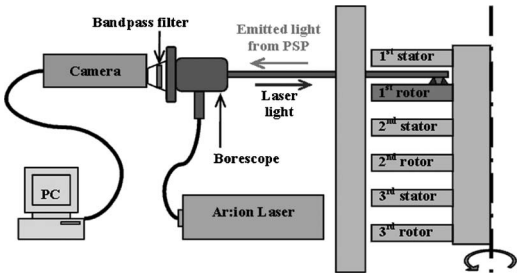

Fig. 7 Schematic drawing of the optical components

Calibration of PSP. Calibration for the PSP was conducted inside a vacuum chamber with same optical components and settings. Figure 8 shows the schematic of the calibration setup. Heated air was circulated until the temperatures of the test sample and the calibration chamber are at steady state at the desired temperature. Temperature dependence of PSP was avoided by performing all the experiments at this temperature corresponding to the first stage stator exit at steady state conditions. After that, the inlet of the air flow was blocked and the inside pressure was controlled using a vacuum pump from 0 to 1 atm. The intensity from the PSP coated test plate was recorded at different pressures. To validate the potential influence of the convex leading edge

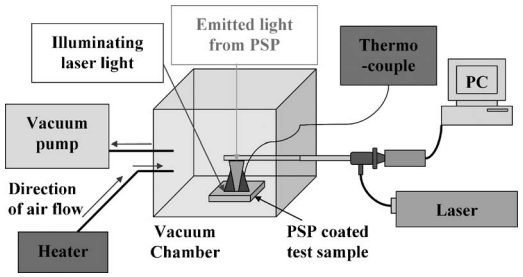

Fig. 8 Schematic calibration setup

shape or off-axis lighting/viewing, calibration was conducted on a cylinder, whose radius was similar to the curvature of the blade leading edge surface. The calibration result shows that the off-axis lighting/viewing does not affect the result up to ±50 deg. The view windows of the present experimental results are within the range. Figure 9 shows the calibration curve of intensity ratio versus pressure ratio, which is found to be linear except in the high vacuum range.

Experimental Procedure. For each kind of image, 200 pictures were taken and saved as TIF format to calculate the averaged intensity at each pixel. As the viewing angle for the borescope was not large enough to cover the entire leading edge, individual images for each hole were taken and then arranged together. The film cooling holes were used as position markers to align each picture. During tests, it was ensured that the temperature of the mainstream air, coolant and test section as well as the rotational speed, torque on the dynamometer and laser output power were in steady state conditions. Reference images were taken at 0 rpm, after the rotating main experiments. MATLAB and FORTRAN programs were used to convert the intensity information into the film cooling effectiveness data.

The uniformity of the temperature was considered. In general, the mainstream flow may have a temperature variation in radial direction. However, the mainstream flow is highly turbulent and film cooling flow interrupts the mainstream flow resulting in further mixing. Thus, the temperature difference should be less than a degree. In addition, the blade is made of aluminum. Due to its high thermal conductivity, the temperature difference of a few degrees can be absorbed. So, the error due to the nonuniform temperature distribution would be minimal.

The coolant flow rate for a certain blowing ratio was predetermined from the mainstream flow conditions at the rotor inlet. The flow rate was then set using a rotameter and then fed into an axial supply line through a rotary union placed downstream of the turbine rotor. The annular shaft was specifically designed for coolant transport which then fed the coolant through radial holes drilled in the shaft into the turbine disk plenum. The mating interfaces of the turbine assembly were lined with a sealant to prevent coolant leakage. A pressure test for the shaft and the turbine disk was also performed to ensure there was no leakage.

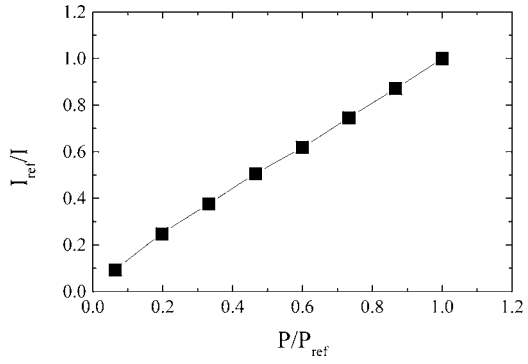

Fig. 9 Calibration curve of the PSP

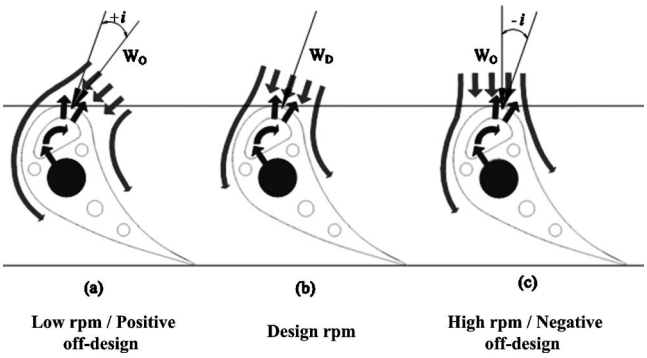

Fig. 10 Flow path inside and outside the blade for (*a*) positive off-design, (*b*) design, and (*c*) negative off-design conditions

Uncertainty Calculations. Uncertainty calculations were performed based on a confidence level of 95% and are based on the uncertainty analysis method of Coleman and Steele [32]. The uncertainty for effectiveness is estimated to be 7%, which arises due to an uncertainty of about 5% in the partial pressures of oxygen. This uncertainty is contributed by uncertainties in calibration (4%) and image capture (1%). Also, the level of the shot noise was estimated to be 0.4% [33]. However, the edge of each view window has larger error. Uncertainty for the blowing ratios is estimated to be 4%.

Discussion of Results

Effects of the Rotational Speed on the Film Cooling Effectiveness Level. In order to understand and interpret the film cooling effectiveness results, the following turbine aerodynamic aspects need to be discussed beforehand (for detailed discussion see Schobeiri et al. [30,31]). (a) Operating the turbine at an off-design point causes changes in incidence. If the rotational speed is lower than design point, the flow impinges on the rotor leading edge with a negative incidence that causes the stagnation line to shift toward the suction side. As a consequence, some of the film cooling jets stemming from the suction side holes are deflected toward the pressure surface. On the other hand, if the turbine is operated at higher rpm, the stagnation line shift toward the pressure side and the traces are deflected toward the suction surface. This phenomenon is graphically explained for positive, zero and negative incidence angle cases in Fig. 10. (b) The cylindrical blades are usually designed to operate at mid-height radius with an optimum efficiency at zero incidence-angle when operated at the design point. Thus, any deviation from that radius causes incidence that are associated with increased total pressure losses. The results of the film cooling effectiveness reflect these aerodynamic situations.

The results for film effectiveness trace patterns at 2400, 2550, and 3000 rpm are shown in Figs. 11–13, respectively. Based on the directions of the film traces, it can be clearly observed that the location of the stagnation line moves from the pressure side to the suction side as the rotational speed increases and changes the deflection angles of the traces. Note that the black lines in each contour represent the approximate stagnation line. In the 2400 rpm case, the stagnation line is located near the pressure side film cooling row and the coolant traces from the first three holes from the hub on the pressure side row are deflected to the suction side. In the mean time, the coolant from the upper five holes goes to the pressure side as expected. Based on the coolant flow direction of each hole, it seems that the stagnation line is slightly inclined because of the two-dimensional characteristics of the cylindrical blade. On the suction side, the coolant traces from the suction side row of holes go to the suction side beyond the flow

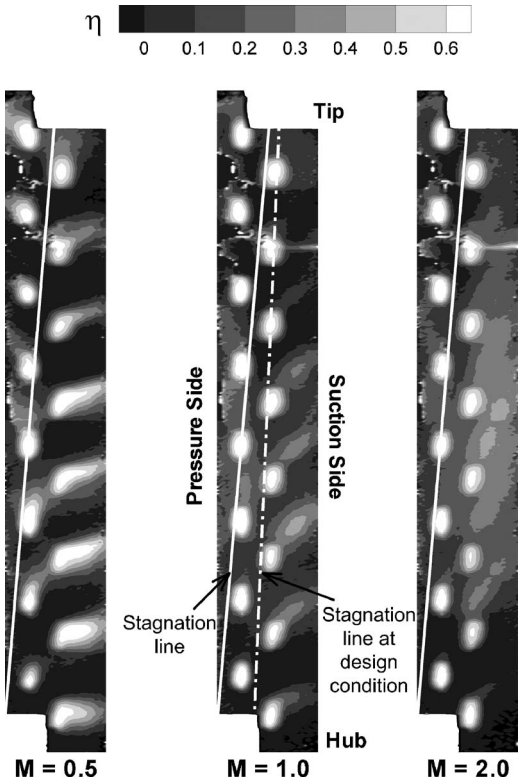

Fig. 11 Leading edge region film cooling effectiveness distribution at 2400 rpm, (*a*) *M*=0.5, (*b*) *M*=1.0, and (*c*) *M*=2.0

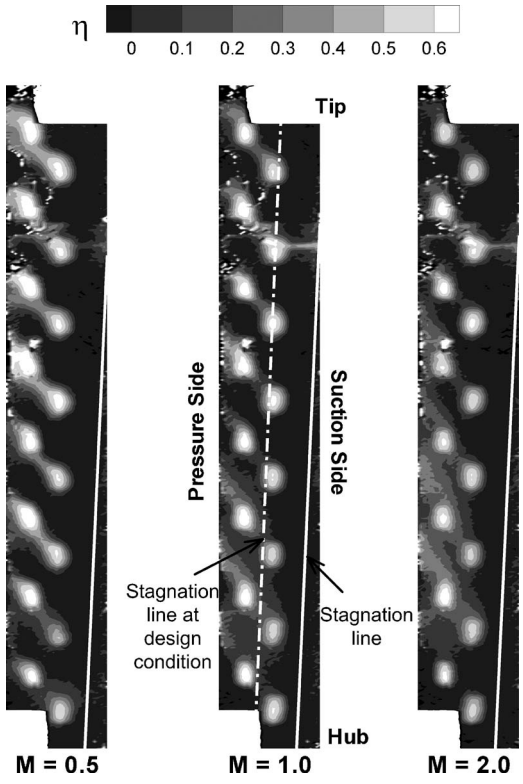

Fig. 13 Leading edge region film cooling effectiveness distribution at 3000 rpm (*a*) *M*=0.5, (*b*) *M*=1.0, and (*c*) *M*=2.0

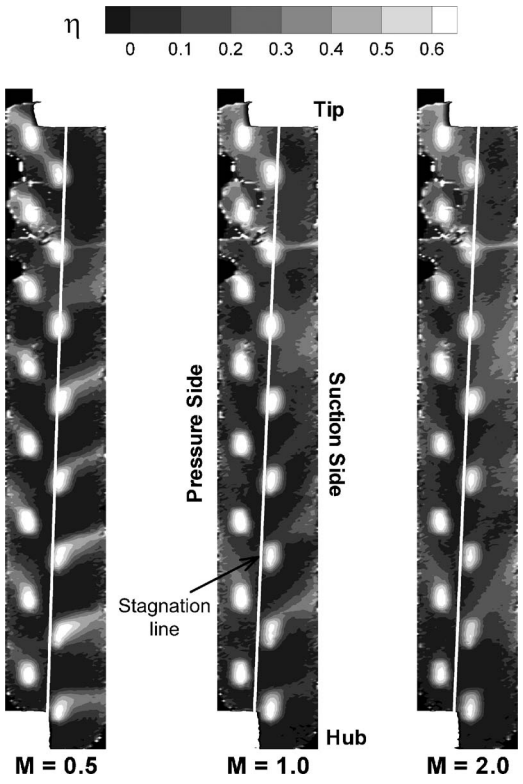

Fig. 12 Leading edge region film cooling effectiveness distribution at 2550 rpm, (*a*) *M*=0.5, (*b*) *M*=1.0, and (*c*) *M*=2.0

stagnation line and its degree of deflection reduces as the immersion ratio increases. For 2550 rpm case, which is the design point, the stagnation line generally is located between the pressure side and suction side film cooling holes rows. Thus, the film coverage on the pressure and suction side is comparable to each other. However, the area between the coolant-hole rows is not much protected except near the tip portion, and the coolant goes to both sides except those from the first two holes from the tip on the suction side row. Again, this is due to inclined stagnation line shown in the figure. In the 3000 rpm cases, the stagnation line moved to the suction side and all the traces go to the pressure side. In this case, the deviation from the design condition is three times compared to the 2400 rpm case. Thus, the stagnation line shifted much further to the suction side and the effects of rotational speed should be larger. As a result, none of the coolant ejecting from the suction side goes to the suction side.

The location of the stagnation line also seems to affect the local blowing ratio distribution. The static pressure on the stagnation line is the highest while the pressure inside the blade plenum can be assumed to be the same for every hole. As a consequence, the local blowing ratio is directly affected by the location of the stagnation line. The 2400 rpm cases show this phenomenon. The traces from the suction side row are generally stronger than those from the pressure side row, which is closer to the stagnation line. The overall film cooling effectiveness levels decrease as the rotational speed increases. The increase of rotational speed affects the film effectiveness level in two ways. One is that the blade experiences more wakes originating from the stator trailing edge for a given time. The other is that the effect of each wake is larger because the relative inlet velocity reduces as the rotational speed increase while the size of the wake remains same. Both these effects increase the wake Strouhal number. Thus, the leading edge portion experiences severe mixing due to the increased unsteady turbulent wake effect and the film cooling effectiveness level is lower as the rotational speed increases.

CFD was done by Yang et al. [34] confirmed the trend obtained

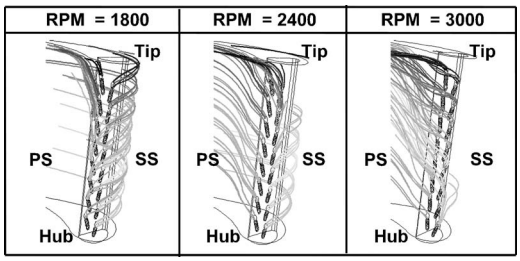

Fig. 14 Coolant path lines colored by particle number (Yang et al. [34])

from experimental film trace results (Fig. 14). The geometry of the CFD calculations was similar to the current turbine. A CFD software package FLUENT (version 6) was used in their calculation to calculate the pressure, heat transfer coefficient, and film cooling effectiveness distributions. It can be seen that the film trace comparison between the experiments and CFD is reasonable in terms of the effects of rotating speed on the film cooling flow direction, as explained in the above paragraph.

Effects of the Blowing Ratio. The averaged blowing ratio was controlled to be (a) 0.5, (b) 1.0, and (c) 2.0 for each rotating speed. As the blowing ratio increases, the directions of the coolant flows are closer to the radial or spanwise direction due to the higher momentum of coolant flows. The peak effectiveness levels are also affected by the momentum level of coolant flows. When $M=0.5$, coolant traces are stronger and more distinguishable from each other. However, the area covered by the coolant is limited. As the blowing ratio increases, the coolant covers more area although individual coolant traces are weaker and not very distinguishable from each other. In general, if the blowing ratio is higher than one, some of the coolant gas penetrates into the mainstream and lifts off from the surface. Thus, the strength of the coolant flow downstream of the film cooling hole is weaker compared to the low blowing ratio case. Possibly, the coolant gas has more interaction with the mainstream at higher blowing ratio and is distributed more uniformly. This study being the first investigation involving detailed film cooling measurements on a rotating blade, the present results cannot be compared against available data in open literature. However, tests performed under stationary conditions on simulated cylindrical leading edges indicate similar results for comparable blowing ratios. PSP measurements by Gao et al. [29] on a two row showerhead cylindrical leading edge model also gave stronger traces for $M=0.4$ whereas $M=1.2$ showed more spreading but weaker individual coolant traces. Similar trends were also obtained by Ekkad et al. [16] for air injection on the leading edge of a simulated semicylindrical leading edge in a low speed wind tunnel.

Effects of the Spanwise Location. In general, the film cooling effectiveness distributions show that the film coolant traces near the mid-section region is stronger than the other regions. Schobeiri et al. [31] showed that the losses are the lowest between $r^*=0.3$ and 0.6 (mid-section region) for the current cylindrical blades. Higher loss coefficient implies that there is more mixing and, as a result, lower film cooling effectiveness around the hub and tip. It also agrees with the flow structure because there are strong secondary vortices at the hub and tip regions. The results at the lower rotational speed show larger differences in the film effectiveness level between the mid-section and the hub and tip regions compared to the results at higher rotational speed.

Spanwise Averaged Film Cooling Effectiveness. Figures 15(*a*)–15(*c*) shows the spanwise averaged film cooling effectiveness at each rotational speed. It seems the blowing ratio does not affect the averaged results much. Considering the contour plots in Figs. 11–13, however, it does not mean that each blowing ratio case provides similar protections to the blade surface. At $M=0.5$, the traces from each holes are stronger while they covers only limited area. At $M=2.0$, the coolant films are distributed more uniformly and cover a larger area, although the traces themselves are weak and hardly distinguishable. As a result, the strength of the coolant film is compensated by the size of protected area and averaged results for each case are similar.

The spanwise averaged film cooling effectiveness results are

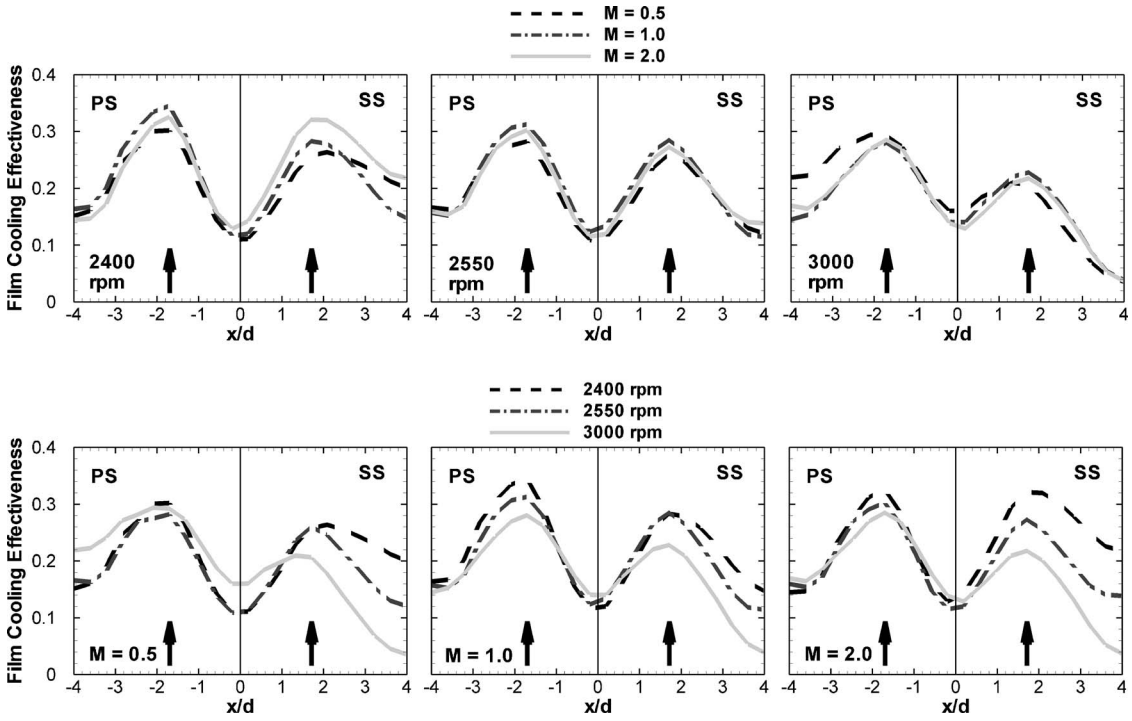

Fig. 15 Span-wise averaged film cooling effectiveness

re-arranged to see the effects of the rotational speed (Figs. 15(*d*)–15(*f*)). Generally, higher rotational speed reduces the effectiveness level due to the increased wake effects. The effectiveness level on the suction side is more sensitive to the rotational speed compared to the pressure side. As mentioned before, the coolant from the suction side row flows to the suction side at low rotational speed while it flows to the pressure side at a higher rotational speed. In that case, the area at the downstream of the suction side row ($2<x/d<4$) is not much protected by the coolant at higher rotational speed because most of the coolant traces are deflected towards the pressure side. The change in the rotational speed also affects the direction of the coolant traces from the pressure side row. However, those coolant traces generally head to the pressure side and their variation in this direction is smaller compared to that from the suction side row. Thus, the spanwise averaged effectiveness level near the pressure side row shows less dependency on the rotational speed. It should be noted that the spanwise averaged results mask the influence of the inclined stagnation line as shown in Figs. 11 and 12. The stagnation line orientation causes the coolant traces to reverse near the blade hub and tip for a few cases (2400 and 2550 rpm) causing the spanwise averaged results to be biased.

Conclusions

Detailed film cooling effectiveness distributions on the leading edge region of a rotating blade with two rows of radial-angle film cooling holes were measured by the PSP technique. The conclusions of this study are as follows:

(1) The rotational speed or the flow stagnation line incidence angle is the most important factor in determining the leading-edge region film cooling effectiveness distributions. Different rotational speed changes the incidence angle to the leading edge and affects the direction of the film coolant path to either side of the design condition stagnation line.
(2) For 2400 rpm (positive off-design condition), film cooling traces from both film cooling hole rows generally go to the suction side of the rotating blade, while they go to the pressure side at 3000 rpm (negative off-design condition). In the case of 2550 rpm design condition, the film cooling traces from the two rows are almost evenly distributed between pressure and suction side, from the stagnation line.
(3) In general, the average film cooling effectiveness decreases as the rotational speed increases from 2400 rpm (positive incidence angle) to 3000 rpm (negative incidence angle).
(4) As the blowing ratio increases, each coolant trace is weaker, but more uniformly distributed on the leading edge region.
(5) Overall averaged film cooling effectiveness decreases slightly as the blowing ratio increases at the 3000 rpm case. For 2400 and 2550 rpm, it is fairly insensitive with blowing ratio.

Acknowledgment

This work was prepared with the support of Solar Turbines, Inc. The authors appreciate their help and support. The authors also thank our co-worker, Burak Ozturk for the helpful discussions and comments.

Nomenclature

C = oxygen concentration
d = diameter of film-cooling holes (1.19 mm)
I = pixel intensity for an image
M = average blowing ratio ($=\rho_c V_c/\rho_m V_m$)
P_{O_2} = partial pressure of oxygen
P = static pressure
p = spanwise distance between film cooling holes
PS = blade pressure-side
r^* = immersion ratio, $(r-r_{hub})/(r_{tip}-r_{hub})$
SS = blade suction-side
T = temperature (°C)
x = streamwise distance measured from midway between the two rows of holes
η = local film-cooling effectiveness

Subscripts

c = coolant
m = mainstream
air = mainstream air with air as coolant
mix = mainstream air with nitrogen as coolant
ref = reference image with no mainstream and coolant flow
blk = image without illumination (black)

References

[1] Han, J. C., Dutta, S., and Ekkad, S. V., 2000, *Gas Turbine Heat Transfer and Cooling Technology*, Taylor and Francis, New York.
[2] Nirmalan, N. V., and Hylton, L. D., 1990, "An Experimental Study of Turbine Vane Heat Transfer With Leading Edge and Downstream Film Cooling," ASME J. Turbomach., **112**, pp. 477–487.
[3] Abuaf, N., Bunker, R., and Lee, C. P., 1997, "Heat Transfer and Film Cooling Effectiveness in a Linear Airfoil Cascade," ASME J. Turbomach., **119**, pp. 302–309.
[4] Cruse, M. W., Yuki, U. M., and Bogard, D. G., 1997, "Investigation of Various Parametric Influences on Leading Edge Film Cooling," ASME Paper No. 97-GT-296.
[5] Ekkad, S. V., Mehendale, A. B., Han, J. C., and Lee, C. P., 1997, "Combined Effect of Grid Turbulence and Unsteady Wake on Film Effectiveness and Heat Transfer Coefficient of a Gas Turbine Blade With Air and CO_2 Film Injection," ASME J. Turbomach., **119**, pp. 594–600.
[6] Cutbirth, J. M., and Bogard, D. G., 2003, "Effects of Coolant Density Ratio on Film Cooling Performance on a Vane," *Proceedings of ASME Turbo Expo 2003*, Atlanta, GA, June, Paper No. GT2003-38582.
[7] Luckey, D. W., Winstanley, D. K., Hames, G. J., and L'Ecuyer, M. R., 1977, "Stagnation Region Gas Film Cooling for Turbine Blade Leading-Edge Applications," AIAA J., **14**, pp. 494–501.
[8] Mick, W. J., and Mayle, R. E., 1988, "Stagnation Film Cooling and Heat Transfer Including Its Effect Within the Hole Pattern," ASME J. Turbomach., **110**, pp. 66–72.
[9] Karni, J., and Goldstein, R. J., 1990, "Surface Injection Effect on Mass Transfer From a Cylinder in Crossflow: A Simulation of Film Cooling in the Leading Edge Region of a Turbine Blade," ASME J. Turbomach., **112**, pp. 418–427.
[10] Mehendale, A. B., Han, J. C., and Ou, S., 1991, "Influence of High Mainstream Turbulence on Leading Edge Heat Transfer," ASME J. Heat Transfer, **113**, pp. 843–850.
[11] Mehendale, A. B., and Han, J. C., 1992, "Influence of High Mainstream Turbulence on Leading Edge Film Cooling Heat Transfer," ASME J. Turbomach., **114**, pp. 707–715.
[12] Ou, S., Mehendale, A. B., and Han, J. C., 1992, "Influence of High Mainstream Turbulence on Leading Edge Film Cooling Heat Transfer: Effect of Film Hole Row Location," ASME J. Turbomach., **114**, pp. 716–723.
[13] Mehendale, A. B., and Han, J. C., 1993, "Reynolds Number Effect on Leading Edge Film Effectiveness and Heat Transfer Coefficient," Int. J. Heat Mass Transfer, **36**(15), pp. 3723–3730.
[14] Salcudean, M., Gartshore, I., Zhang, K., and Barnea, Y., 1994, "Leading Edge Film Cooling of a Turbine Blade Model Through Single and Double Row Injection: Effects of Coolant Density," ASME Paper No. 94-GT-2.
[15] Funazaki, K., Yokota, M., and Yamawaki, K., 1997, "The Effect of Periodic Wake Passing on Film Effectiveness of Discrete Holes Around the Leading Edge of a Blunt Body," ASME J. Turbomach., **119**, pp. 292–301.
[16] Ekkad, S. V., Han, J. C., and Du, H., 1998, "Detailed Film Cooling Measurements on a Cylindrical Leading Edge Model: Effect of Free-Stream Turbulence and Coolant Density," ASME J. Turbomach., **120**, pp. 799–807.
[17] Ou, S., and Rivir, R. B., 2001, "Leading Edge Film Cooling Heat Transfer With High Free Stream Turbulence Using a Transient Liquid Crystal Image Method," Int. J. Heat Mass Transfer, **22**, pp. 614–623.
[18] Reiss, H., and Bölcs, A., 2000, "Experimental Study of Showerhead Cooling on a Cylinder Comparing Several Configurations Using Cylindrical and Shaped Holes," ASME J. Turbomach., **122**, pp. 161–169.
[19] Kim, Y. J., and Kim, S. M., 2004, "Influence of Shaped Injection Holes on Turbine Blade Leading Edge Film Cooling," Int. J. Heat Mass Transfer, **47**, pp. 245–256.
[20] Dring, R. P., Blair, M. F., and Hoslyn, H. D., 1980, "An Experimental Investigation of Film Cooling on a Turbine Rotor Blade," ASME J. Eng. Power, **102**, pp. 81–87.

[21] Takeishi, K., Matsuura, M., Aoki, S., and Sato, T., 1990, "An Experimental Study of Heat Transfer and Film Cooling on Low Aspect Ratio Turbine Nozzles," ASME J. Turbomach., **112**, pp. 488–496.
[22] Abhari, R. S., and Epstein, A. H., 1994, "An Experimental Study of Film Cooling in a Rotating Transonic Turbine," ASME J. Turbomach., **116**, pp. 63–70.
[23] Zhang, L. J., and Fox, M., 1999, "Flat Plate Film Cooling Measurement Using PSP and Gas Chromatography Techniques," *Proc. Fifth ASME/JSME Joint Thermal Engineering Conference*, San Diego, CA.
[24] Zhang, L. J., Baltz, M., Pudupatty, R., and Fox, M., 1999, "Turbine Nozzle Film Cooling Study Using the Pressure Sensitive Paint (PSP) Technique," ASME Paper No. 99-GT-196.
[25] Zhang, L. J., and Jaiswal, R. S., 2001, "Turbine Nozzle Endwall Film Cooling Study Using Pressure-Sensitive Paint," ASME J. Turbomach., **123**, pp. 730–738.
[26] Ahn, J., Mhetras, S., and Han, J. C., 2004, "Film-Cooling Effectiveness on a Gas Turbine Blade Tip Using Pressure Sensitive Paint," *Proceedings of ASME Turbo Expo 2004*, Paper No. GT-2004-53249.
[27] Mhetras, S., Yang, H., Gao, Z., and Han, J. C., 2005, "Film-Cooling Effectiveness on Squealer Rim Walls and Squealer Cavity Floor of a Gas Turbine Blade Tip Using Pressure Sensitive Paint," *Proceedings of ASME Turbo Expo 2005*, Paper No. GT 2005-68387.
[28] Wright, L. M., Gao, Z., Varvel, T. A., and Han, J. C., 2005, "Assessment of Steady State PSP, TSP, and IR Measurement Techniques for Flat Plate Film Cooling," *Proceedings of 2005 ASME Summer Heat Transfer Conference*, Paper No. HT 2005-72363.
[29] Gao, Z., Wright, L. M., and Han, J. C., 2005, "Assessment of Steady PSP and Transient IR Measurement Techniques for Leading Edge Film Cooling," *Proceedings of 2005 ASME IMECE Congress and Exposition*, Paper No. IMECE2005-80146.
[30] Schobeiri, M. T., Gillaranz, J. L., and Johansen, E. S., 2000, "Aerodynamic and Performance Studies of a Three Stage High Pressure Research Turbine With 3D Blades, Design Points and Off-Design Experimental Investigations," *Proceedings of ASME Turbo Expo 2000*, Paper No. 2000-GT-484.
[31] Schobeiri, M. T., Suryanarayanan, A., Jermann, C., and Neuenschwander, T., 2004, "A Comparative Aerodynamic and Performance Study of a Three-Stage High Pressure Turbine With 3D Bowed Blades and Cylindrical Blades," ASME Paper No. GT2004-53650.
[32] Coleman, H. W., and Steele, W. G., 1989, *Experimentation and Uncertainty Analysis for Engineers*, Wiley, New York.
[33] Liu, T., Guille, M., and Sullivan, J. P., 2001, "Accuracy of Pressure Sensitive Paint," AIAA J., **39**(1), pp. 103–112.
[34] Yang, H., Chen, H. C., Han, J. C., and Moon, H. K., 2005, "Numerical Prediction of Film Cooling and Heat Transfer on the Leading Edge of a Rotor Blade With Two Rows Holes in a 1-1/2 Turbine Stage, At and Off Design Conditions," *Proceedings of ASME Turbo Expo 2005*, Paper No. GT-2005-68355.

K. C. Ng
e-mail: mpengkc@nus.edu.sg

M. A. Sai

A. Chakraborty

Mechanical Engineering Department,
National University of Singapore,
10 Kent Ridge Crescent,
Singapore 119260

B. B. Saha
e-mail: bidyutb@cm.kyushu-u.ac.jp

S. Koyama
e-mail: koyama@cm.kyushu-u.ac.jp

Interdisciplinary Graduate School
of Engineering Sciences,
Kyushu University,
Kasuga-koen, 6-1, Kasuga-shi,
Fukuoka 816-8580, Japan

The Electro-Adsorption Chiller: Performance Rating of a Novel Miniaturized Cooling Cycle for Electronics Cooling

The paper describes the successful amalgamation of the thermoelectric and the adsorption cycles into a combined electro-adsorption chiller (EAC). The symbiotic union produces an efficiency or COP (coefficient of performance) more than threefold when compared with their individual cycles. The experiments conducted on the bench-scale prototype show that it can meet high cooling loads, typically 120 W with an evaporator foot print of 25 cm^2, that is 5 W/cm^2 at the heated surface temperature of 22°C, which is well below that of the room temperature. The COPs of the EAC chiller vary from 0.7 to 0.8, which is comparable to the theoretical maximum of about 1.1 at the same operating conditions. With a copper-foam cladded evaporator, the high cooling rates have been achieved with a low temperature difference. In addition to meeting high cooling rates, the EAC is unique as (i) it has almost no moving parts and hence has silent operation, (ii) it is environmentally friendly as it uses a nonharmful adsorbent (silica gel), and (iii) water is used as the refrigerant. [DOI: 10.1115/1.2241786]

Keywords: electro-adsorption cycle, electronic cooling, miniaturized chiller, silica gel-water adsorption cycle

Introduction

The advent of high clocking-speed processors of computers or CPUs has generated a "crisis state" in its thermal management because the convective fins/fan cooling can no longer remove sufficiently all the heat generated. This is attributed to the current trends in packaging a large number of integrated circuits (ICs) within the available CPU's footprint. When the encasement surface temperature of the CPUs reaches its thermal design point (TDP) [1], the on-board thermal management software would automatically curtail the clocking speed to reduce heat generation. Given the constraints of finite area of fins and low power electric fans, major CPU manufacturers have resorted to using two or more processors or the multicore design on an enlarged footprint, distributing the heat generation of CPU to a larger encasement. A plot of the surface temperature of CPU encasement with the power intensity is shown in Fig. 1 where the TDP of 73°C has frequently been breached when the clock speeds of the CPUs exceeded 3.0 GHz.

One of the most promising methods to resolve the heat dissipation problem of CPUs is the development of a novel, high cooling density, and low maintenance cooling cycle that could be scaled in a manner that a miniaturized chiller could fit onto the desk-top PCs or server systems. New generations of CPU coolers aim to maintain the casement temperature no more than a few degrees above the ambient temperature, which is not possible by the constraints of fins-fan systems. A survey of the literature [2,3] shows that there are two categories of cooling devices: (i) the passive-type cooling devices in which the load-surface temperatures are operated well above the ambient temperature and these devices include forced-convective air cooling, liquid immersion cooling, heat pipe, and thermo-syphon cooling, and (ii) the active-type cooling device where electricity or power is consumed. For example, a scale-down vapor-compression refrigeration system has the capability of lowering the load surface temperature below the ambient temperature. However, the efficiency of such a vapor-compression-type cooler decreases rapidly when its physical dimensions are miniaturized as the dissipative losses of the refrigeration cycle could not be reduced accordingly [4]. The surface and fluid friction of the refrigeration cycle increase relatively with reduced volume of devices. In addition, mechanical devices have high maintenance cost.

The simplest method is the forced air convection [5] with the option of an extended heat sink that increases the heat source surface area of heat exchanger and/or incorporates the flow barriers on the surfaces to be cooled to increase air turbulence for better heat dissipation. This method is adequate for many types of current microelectronic cooling application. These methods, although feasible, may cease to satisfy the constraint of compactness for future generations of CPUs as cooling power may increase to the order of 200 to 300 W.

Passive thermo-syphons [6] are similar low-maintenance-type devices where they involve virtually no moving parts except with the cooling fans for the condenser. Such devices, however, are orientation dependent as they rely on gravity and elevation differential for condensate return from the condenser to the evaporator. Thermo-syphons equipped with one or more mini pump have also been proposed [7]. Instead of relying on gravity, the condensate is pumped from the condenser to the evaporator, which provides for orientation independency. It also allows for the possibilities of forced convective boiling, spraying of condensate, or jet impingement of condensate at the evaporator, which will effectively enhance boiling characteristics and therefore cooling performance.

Laid-out heat pipes [8,9] have found applications in laptop and desktop computers. The evaporating ends of the miniaturized heat pipes are judiciously arranged over the CPU while the condensing ends are arranged to increase the surface area of the heat sink.

Mini vapor compression chillers [10] have also found applications in the cooling of CPUs. In one design, the evaporator is

Contributed by the Heat Transfer Division of ASME for publication in the JOURNAL OF HEAT TRANSFER. Manuscript received June 26, 2005; final manuscript received February 7, 2006. Review conducted by Suresh V. Garimella. Paper presented at the 2005 ASME Heat Transfer Summer Conference (HT2005), July 15–22, 2005, San Francisco, California, USA.

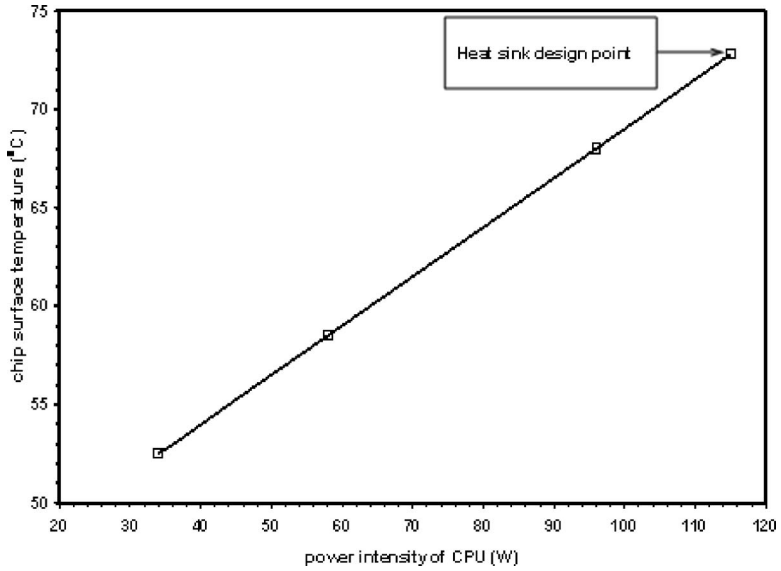

Fig. 1 The dependence of the chip surface temperature versus the power intensity of CPU with a convective fins-fan system

placed over the heat source surface while the mini condensing unit is positioned remote from the heat source. Although the vapor compression chillers may be efficient at macro dimensions, the miniaturized versions of the macro counterparts suffer high friction and heat losses when miniaturized as the ratio of surface area to volume increases. With many moving parts in the compressors, the cost of maintenance is known to be high.

Thermoelectric chillers [11,12] are also used in CPU cooling, but they suffer from inherently low COP (typically in the range of 0.1–0.3 for the temperature differentials of microelectronic applications) and high cost. The low efficiency implies that the increase in cooling rates requires unacceptably high electrical power input and, thus, compounds the problem of heat rejection to the environment. Thermoelectric chillers, on the other hand, are compact and they have no moving parts other than the cooling fans.

Adsorption chillers [13,14] are known to have the potential for miniaturization [15]. This is because adsorption and desorption processes of refrigerant onto the adsorbent are primarily surface rather than bulk processes. Micro-scale reactors could be designed to comprise the micro-channel cavities containing the adsorbents where the molecular adsorbates are attached during the processes. The technology of coupling a thermoelectric device (Peltier device) to an adsorber and a desorber has been reported previously [16,17], but their applications have been confined to humidification, dehumidification, gas purification, and gas detection. Recently, Ng et al. [18,19] patented a miniaturized and yet modular cooling device, called the electro-adsorption chiller (EAC). It is a hybrid cooling cycle that amalgamates all the virtues of thermoelectrics and the silica gel-water adsorption cycles. It exploits not only the ease of thermoelectric operation but, when symbiotically combined with the adsorption cycle, the EAC amplifies the system COP many-fold over. The increased performance is attributed to both the heating and cooling fluxes from the thermoelectrics being concomitantly regenerated and reutilized by the batch operation of the adsorption cycle.

A prototype EAC has been tailored to the required cooling of CPUs and other electronic components, for example, an encasement surface temperature of a CPU with an area of 5×5 cm^2 totaling a heat release of 120 W. A comparison of heat rejection rates of present day CPUs in relation to operating temperatures of cooling methods is shown in Fig. 2. The EAC is found to give the lowest encasement temperature (as opposed to the temperature within the silicon wafer) at heat fluxes higher than 3 W/cm^2—a region that could be reached by the conventional methods without increasing the encasement temperature.

In this paper, the authors describe a detailed construction and testing of a prototype bench-scale EAC for an assorted range of heat fluxes and surface temperatures. The experiments demonstrate the effectiveness of the hybrid cycles at high cooling densities and, yet, yield a low cooling surface temperature at the evaporator. High boiling heat fluxes are realized by the use of a copper-foam evaporator, in which there is intense boiling within the pores of a copper-foam metal operating with a small temperature differential between the metal surface and the saturated liquid [20,21]. The rating tests on the EAC span across an assorted range of conditions for the thermoelectric power, cooling and chilling water temperatures within the designated adsorber and the evaporator, the cycle, and switching time intervals of the adsorption cycle.

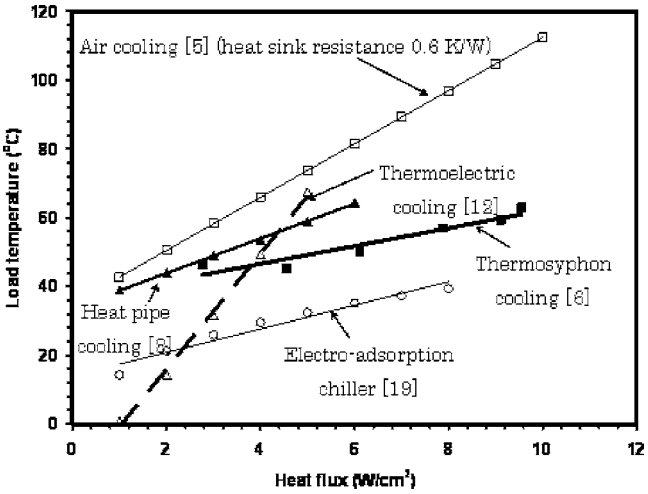

Fig. 2 A comparison of the simulated results of the electro-adsorption chiller (PEAC) versus the conventional methods of cooling the computer's CPU

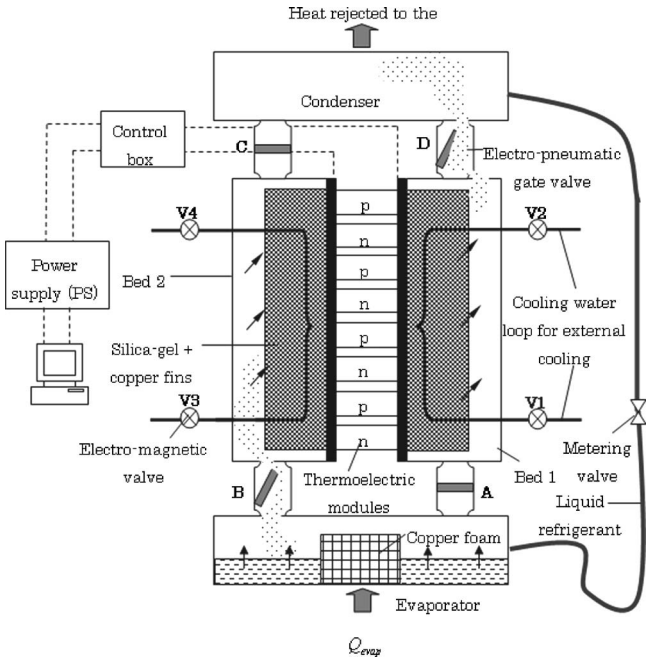

Fig. 3 A schematic of the electro-adsorption chiller (EAC)

Electro-Adsorption Chiller (EAC) Cycle

The schematic of the electro-adsorption chiller (EAC) is shown in Fig. 3. It comprises an evaporator, a condenser, two reactors or beds containing the adsorbent, and an array of nine thermoelectric (TE) modules per bed. Both water and silica gel are used in the hybrid cycles and thus the EAC is environmental friendly. The prototype EAC combines the heating and cooling behaviors of the TEs in a batch-operated adsorption cycle. Two time intervals are activated in series for the operation of an EAC, namely a short switching interval of about 100 s and the half-cycle interval, which could be varied up to 700 s. The electrical power supply (either in a forward and a reverse polarity mode) to the EAC operates the TEs, producing both the hot and cold surfaces on the heat exchangers of desorber and adsorber. The heated desorber would drive-off the vapor from the adsorbent (silica gel) into the condenser. At the same time, the adsorber draws vapor from the evaporator and cooling of the adsorber is achieved by the cold junction of the TE as well as assistance from external cooling. The batch operation of the EAC is controlled by the coordinated opening and closure of the electro-pneumatic valves that are positioned along the tubing between the beds, the evaporator, and the condenser, and the detailed sequence of operation is tabulated in Table 1.

Heat rejection to the ambient from the EAC is via an air-cooled condenser that simultaneously condenses the desorbed vapor within the tubes. The condensate (refrigerant) is refluxed back to the evaporator via a pressure reducing valve. Pool boiling in the evaporator is sustained by the continued vapor uptake of the designated adsorber and completes the refrigeration flow cycle. The alternating roles of the beds (containing the adsorbent) are continuously refreshed by the batch-operated processes. This is achieved simply by reversing the direction of the dc power supply (current flow direction is reversed): what was formerly the cold junction becomes the hot junction and vice versa. Concomitantly, the external coolant cooling is also switched to the designated adsorber and, similarly, the valves linking the evaporator and condenser are also switched to the respective adsorber and desorber. During the switching interval, no mass transfers occur between the hot bed and the condenser or the cold bed and the adsorber.

Experiments

An assembled, bench-size prototype EAC with major dimensions is shown in Fig. 4. Based on these dimensions, the nominal cooling capacity is about 120 W. Each reactor is sized to hold 0.3 kg of silica gel (Fuji Davison type "RD") and the surface areas of the reactors, evaporator, and condenser are respectively 169, 50, and 80 cm^2. The reactors are connected to the evaporator and condenser via on-off control valves (electro-pneumatic gate-valve). Nine pieces of thermoelectric modules (Melcor, UT8-12-40-F1), arranged in three series and three parallel, are placed be-

Table 1 Energy utilization schedule of an electro-adsorption chiller (valve notations are referred to Fig. 3)

Cycle 1					
R-1	SW	DES→ADS	V1, V2→ON	A, B, C, D CLOSED	PS ON
R-2	SW	ADS→DES	V3, V4→ OFF		VPS 1
R-1	OP	ADS	V1, V2→ON	A,C→OPEN	PS ON
R-2	OP	DES	V3, V4→ OFF	B,D→ CLOSED	VPS 1
DELAY 1 Second, A, B, C, D Closed					PS OFF
Cycle 2					
R-1	SW	ADS→DES	V1, V2→ OFF	A, B, C, D	PS ON
R-2	SW	DES→ADS	V3, V4→ON	CLOSED	VPS 2
R-1	OP	DES	V1,V2→ OFF	A,C→CLOSE	PS ON
R-2	OP	ADS	V3, V4→ON	B,D→OPEN	VPS 2

continue

Notations:

ADS: adsorption stage, dES: desorption stage
SW: switching period (100 s), OP: operation period (400 to 700 s)
half-cycle time=switching time+operation time
R-1: Reactor 1 or bed 1, R-2: Reactor 2 or bed 2
PS: power supply, VPS: voltage polarity switching
A, B, C, D: electro-pneumatic gate valve (OFF/ON control)
V1, V2, V3, V4: electro-magnetic valve (OFF/ON control)

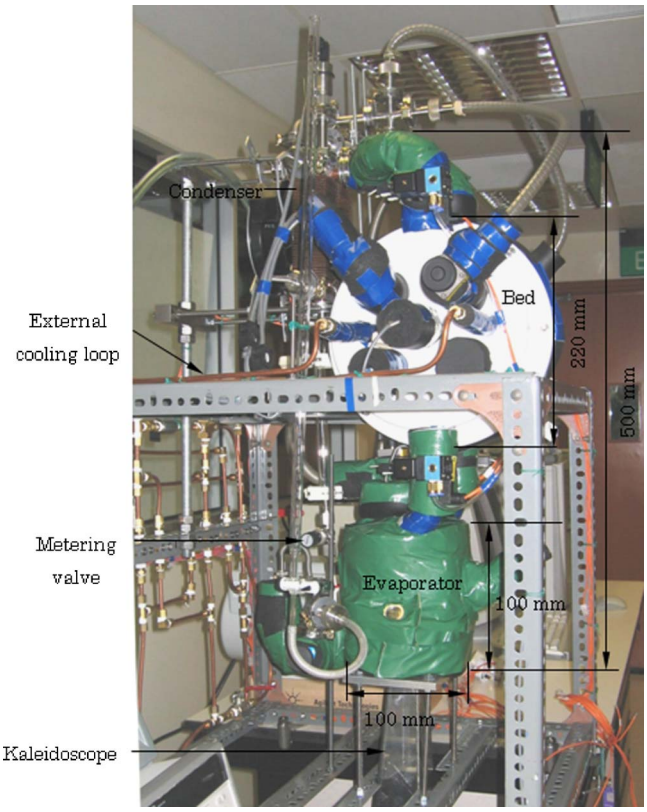

Fig. 4 A pictorial view of the assembled bench-size electro-adsorption chiller (EAC)

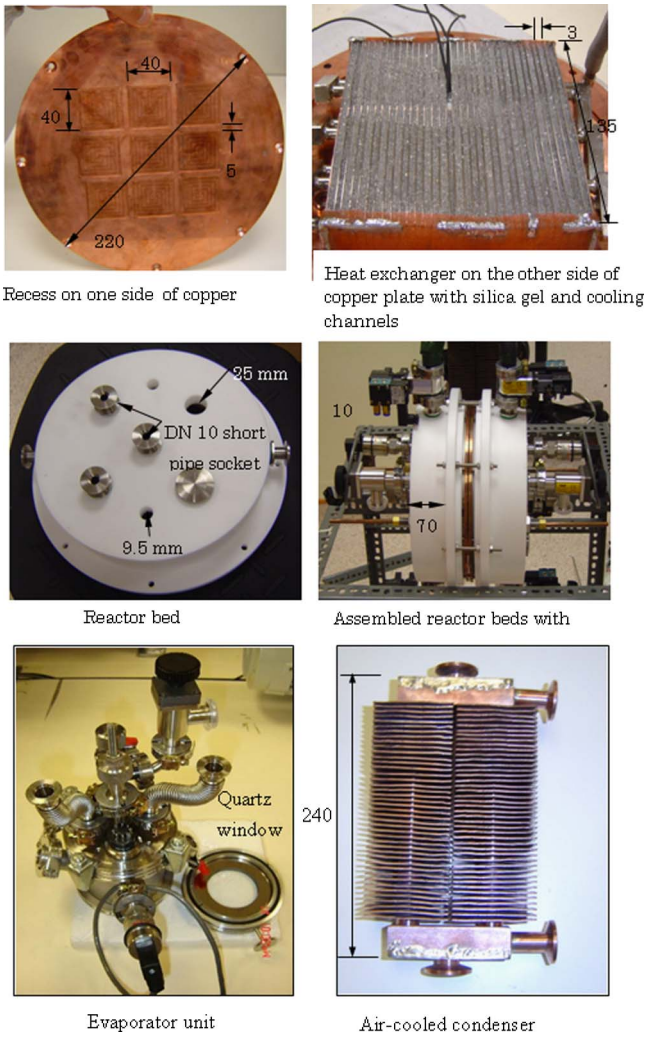

Fig. 5 Pictures of the key components of EAC prior to its assembly (all dimensions are in mm)

tween the two reactors. The major components of a reactor or bed are (i) two circular copper plates, (ii) a heat exchanger with fins and tubes, and (iii) the PTFE enclosures. Locating the TEs is performed by a 3×3 recess (each has a width = 40 mm, length = 40 mm with a depth 1 mm), while the opposite surface (which is evacuated) has a square recess (width: 135 mm, length: 135 mm with a depth of 1 mm), machined into the copper plate to hold the base of the heat exchanger bed. The heat exchanger block has a total of 34 fins (each 1 mm thick), uniformly spaced at 4 mm pitch, and the silica gel (nominal diameter is 0.7 mm) is closely packed into the slot spaces and the exterior surfaces of the heat exchanger are enclosed by fine copper mesh (16 meshes per cm).

Temperatures of silica gel of the reactor bed are measured with four RTD probes (uncertainty ±0.1°C) at different depths and the output signals are to taken out in the vacuum chambers via an electrical feed through (eight pins, TL8K25, Edwards). The whole heat exchanger (containing the silica gel) is fastened to the inner side of the copper plate to minimize the contact resistance. A PTFE enclosure (low thermal conductivity) is used as the cover for the adsorber or desorber bed. Five short pipe sockets (DN 10, stainless steel), with a viton "O" ring for vacuum sealing, link the condenser and the evaporator. Two ports (9 mm diameter) made of copper tubes are inserted via the cover, designed to carry external coolant to cool the beds. On one surface of the chamber's copper flange, a circular groove (250 mm diameter, 3 mm wide, and 4 mm deep) for the location of a centering ring (DN 200 for vacuum rating) is machined. Lastly, thermoelectric modules (three series and three parallel connections) are placed at the outer surface of the reactor, sandwiched by the two reactors that are held together by four sets of studs-and-nuts fixtures.

A finned tube air-cooled condenser has two finned-tube bundles, a vapor and a condensate collection tube. A 30 LPM fan forces air through the fins of condenser. Two YSI (0.1% accuracy) thermisters are used to measure the temperatures of refrigerant at the inlet and outlet of the condenser, and pressure is continuously monitored by a strain gauge type transducer (±2% full scale). The evaporator chamber consists of a NW 100 stainless steel tube body and two NW 100 flanges (S.S. blanking flange and a quartz view port) fitted for vacuum rating. Two glass view ports are made on the tube body of the evaporator to observe the pool boiling and the level of refrigerant. Four ports (14 mm diameter) and one big port (25 mm diameter) are provided at the top plate (NW 100, S.S., 12 mm thickness) where four short pipe sockets (DN 10) are welded. The electrical lead through (TL8K25, eight pins EDWARDS) is placed with the viton O ring. Two short pipe sockets are connected to the reactors via electro-pneumatic gate valves (DN 16) and flexible hoses. The third one is connected with a temperature sensor (±0.1°C; 100 Ω) and the fourth is connected to a pressure transducer (±0.2% full scale) with compression fittings.

A predetermined amount of water (refrigerant) is charged into the evaporator chamber by a diaphragm vacuum valve, and the pressure difference between the condenser and evaporator is throttled by a needle-type valve, allowing the condensate to reflux back to the evaporator. Pool boiling enhancement in the evaporator is achieved using a copper-foam base (50 pores per inch or PPI), giving an excellent capillary effect for liquid and enhancing boiling within foam surfaces. Figure 5 shows the pictorial views of major parts of the EAC prior to its assembly.

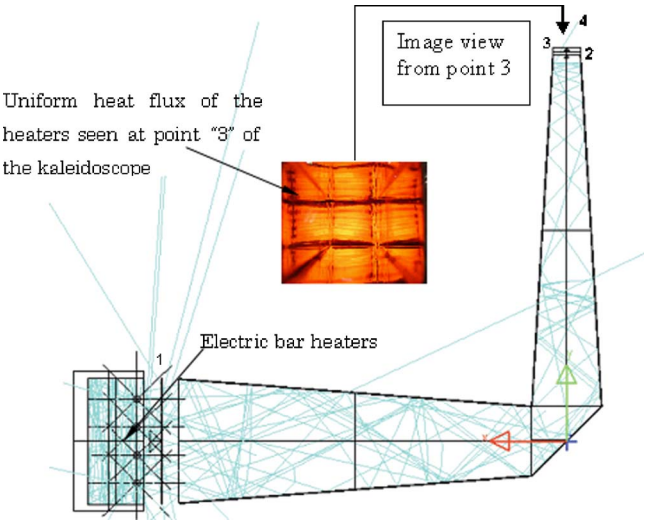

Fig. 6 A schematic of the IR electric heaters with a kaleidoscope for uniform heat flux delivery at the evaporator

An infrared radiant heater with a tapered homogenizer (kaleidoscope's reflectivity 0.94) is used to provide uniform radiation heat transfer to the copper foam in the evaporator via the quartz (wavelength up to 2500 nm) window opening. Uniform heat flux delivery is ensured by the kaleidoscope, as shown in Fig. 6. The insert in the figure shows the electric bar heaters, which are seen at the center while the surround "heaters" are the images formed by the sides of the kaleidoscope. The connections between the evaporator and the reactors, as well as those between the condenser and the reactors, are performed by the flexible hose (DN 10, vacuum rating) and electro-pneumatic gate valves (normally closed, 240 V). An Edwards rotary vane pump is used to vacuum and to purge any noncondensable gas in the EAC.

Power input to the thermoelectric modules is provided by a dc power supply (0–60 V, 0–50 A, 1200 W, GBIP auto ranging, uncertainty: voltage 0.035% or ±40 mV and current 0.2% or ±85 mA). In this experiment, the data acquisition unit accurately captures the temperatures and pressures at the evaporator, reactors, and condenser. All sensors are calibrated with traceability to national standards. A computer program (HPVEE) is used for the controls of the EAC such as (i) control the opening and closing of electro-pneumatic valves and electromagnetic valves at different time intervals in a batch cycle, (ii) reverse the polarity of the voltage supplied to the thermoelectric so that the role of the adsorber and desorber reversed after each batch cycle, and (iii) record the power supplied to the thermoelectric modules so that the performance of the electro-adsorption chiller can be computed.

Prior to experiment, the test facility is first evacuated by a two-stage rotary vane vacuum pump with a water vapor pumping rate of 315×10^{-6} $m^3\,s^{-1}$, and back migration of oil mist into the test apparatus is prevented by an alumina-packed foreline trap. During evacuation, power is applied to the infrared radiant heaters and thermoelectric modules to heat up the copper foam and silica gel to remove moisture and air from the beds and the evaporator. Evacuation is repeated until a satisfactory vacuum pressure is attained with negligible amount of noncondensable residual gas. The required amount of refrigerant water (about 300 cc) is then charged into the evaporator via a refrigerant charging unit. Prior to charging, the test facility is initially evacuated and maintained at room temperature.

Testing on the system is fully automatic under the control of a computer program. Two time intervals of the EAC are activated and they comprise (i) the switching time for the purpose of preheating or precooling the beds and (ii) operation time. Water vapor is generated in the evaporator chamber by vapor uptake to the designated adsorber and the IR radiant heating via the quartz window maintains the system pressure. Through the control program, the dc power supply and all electro-pneumatic valves (off/on control) are timed to operate in accordance to the schedule sequences.

COP of the Electro-Adsorption Chiller

The cycle-average coefficient of performance (COP) of the electro-adsorption chiller is expressed in terms of the cycle-average cooling rate of the overall device, i.e., the rate of heat extraction at the evaporator (Q_{evap}) and the power input from the thermoelectric device (P_{in}). The overall or net COP is

$$\mathrm{COP} = \frac{Q_{evap}}{P_{in}} = \frac{q'_{\mathrm{flux}} A_{evap}}{V\left[\int_0^{t_{cycle}} I(t)dt/t_{\mathrm{cycle}}\right]},$$

where V is the fixed terminal voltage of the thermoelectric modules, I is the direct current drawn by the thermoelectric modules, q'_{flux} is the externally delivered infrared radiant (IR) heat flux, A_{evap} is the area exposed to the IR heat flux, and t_{cycle} indicates the required cycle time.

Results and Discussion

The infrared (IR) radiant heater and the kaleidoscope provide a uniform heat flux to the window aperture of the evaporator up to 5 W/cm^2. The heat flux at the quartz window is calibrated by using a water cooled heat flux meter (Transducer type: circular foil heat flux meter, model 1000-0 with amp 11 Vatell, sensor emissivity: 0.94 at 2 μm and 3% uncertainty). The calibrated results as shown in Table 2 exhibit the amount of heat delivered or cooling power at the evaporator. As IR energy is received by the copper foam directly through the quartz window, pool boiling of liquid occurs within the evaporator. Figure 7 shows the typical temperature traces of the quartz surface, foam center, and saturated vapor of the evaporator with time at steady-state conditions. Owing to the higher wetted area for heat transfer of the foam, the overall temperature difference between the heated surface and the saturated vapor is measured less than 6 K at a heat flux of 5 W/cm^2.

Focusing on the performance of the EAC, the temperature distributions for a "cold" start of the batch-operated chiller is shown in Fig. 8. The initial temperatures of the condenser, evaporator, adsorber, and desorber beds are 32°C, 26°C, 41°C, and 50°C, respectively. In the first 100 s, the EAC undergoes a switching period where all valves linking between the condenser or evaporator to the designated beds are closed. Concomitantly, the adsorber and desorber beds undergo a precooling or preheating schedule. As the IR heating is applied from the quartz window, the temperatures of the evaporator and copper foam increase. The heating rates are substantially higher in the designated desorber than the cooling rates of the adsorber and the mal-distribution of heat rates is attributed to the performance characteristics of the thermoelectric (TE), where the forward voltage behavior tends to be better than the case when the voltages are reversed.

After the switching period, the EAC enters into a normal operating half-cycle where the continued heating and cooling from both sides of TE generate a large temperature lift across the designated desorber and adsorber beds. To compensate for the poorer cooling of TE, additional coolant cooling is supplied to the adsorber by injecting coolant through the heat exchanger. When the valves linking (i) the evaporator to the adsorption bed and (ii) the condenser to the desorber are opened, rapid vapor uptake by the silica gel occurs, promoting pool boiling within the evaporator and lowering the saturation temperature from the initial 26 to 20°C, while the foam surface temperature (although heated by IR) reduces to 25°C. Air cooling in the condenser permits the desorbed vapor from the desorber bed to be condensed.

Table 2 Heat flux calibration table (points are shown in Fig. 6)

Input from variable transformer (V)	Sensor output (uncertainty 3%) (mv)[a]		Power output (uncertainty 3%) (W/cm^2)		
	Near IR heater point 1	Quartz window point 2	Near IR heater point 1	Before quartz window point 2	Power at the evaporator $Q_{evap}=A_{evap}\times q''_{flux}$ (W)
164	3.6	1.01	4.49	1.22	31.5
175	4.85	1.27	6.97	1.95	50.3
185	5.3	1.45	8.86	2.35	60.6
196	5.72	1.65	9.68	2.78	71.7
207	6.3	1.85	11.07	3.25	83.6
218	7.2	2.03	13.3	3.75	96.8
229	8.1	2.35	15.55	4.51	116.4
234	8.5	2.42	16.47	4.7	120.0
240	8.9	2.52	17.54	4.97	128.2

[a]Conversion factor $x(\text{mv})=2.4438x\text{-}1.2189\ W/cm^2$.

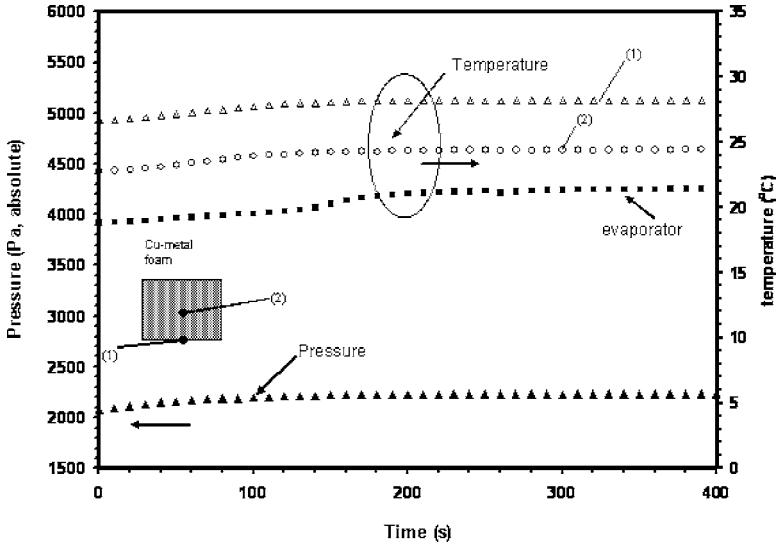

Fig. 7 Temperature traces of the copper-foam cladded evaporator and the saturated vapor

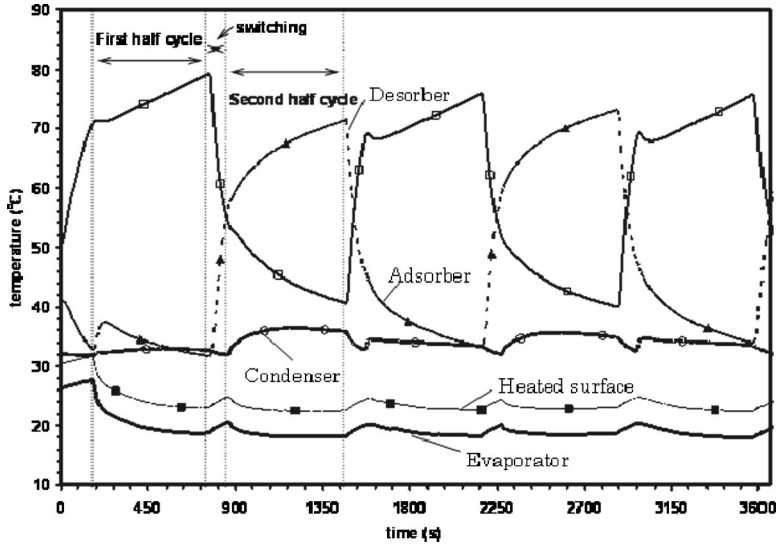

Fig. 8 The experimentally measured temporal history of the electro-adsorption chiller at a fixed cooling power of 120 W: □ defines the temperature of reactor 1; ▲ indicates the silica gel temperature of reactor 2; ∘ shows the condenser temperature; ■ represents the load surface (quartz) temperature and ——— is the evaporator temperature. Hence the switching and cycle time intervals are 100s and 600s, respectively.

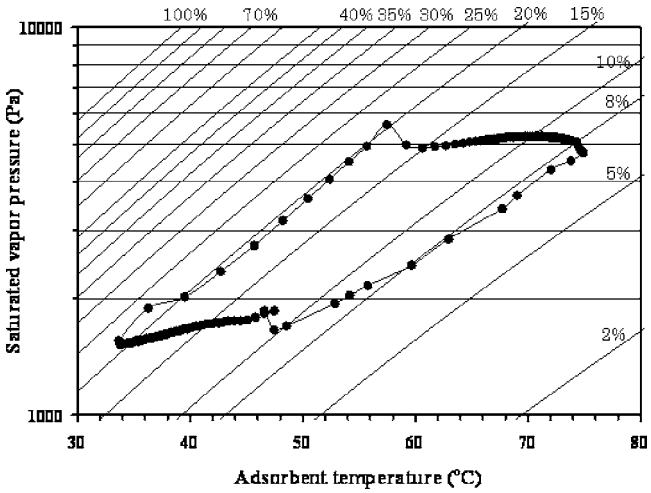

Fig. 9 Dühring diagram of the electro-adsorption chiller (EAC)

At the end of the half-cycle, the EAC enters into a switching period again where preheating and precooling processes commenced. This is followed by the next half-cycle, marked by the reversal of roles of the beds: The saturated adsorbent is now being heated for desorption and the unsaturated adsorbent is cooled for vapor uptake. Cyclic steady state of the EAC can be attained in just three to four half-cycles: The lowest possible condenser temperature reached is about 36°C, and the evaporator attains a low temperature of 18.2°C, corresponding to a delivered heat flux of 4.7 W/cm^2 or total heat input of 120 W.

Figure 9 shows the Dühring diagram of the electro-adsorption chiller with cycle time 600 s, having the fixed cooling capacity of 120 W. At 600 s, the difference in the vapor uptake and off-take is about 12% and the pressure of the adsorption bed goes down 1600 Pa. From the Dühring diagram, one observes the cold-to-hot thermal swing of the bed, causing momentary desorption at the beginning of operation and maintaining the pressure in the hot

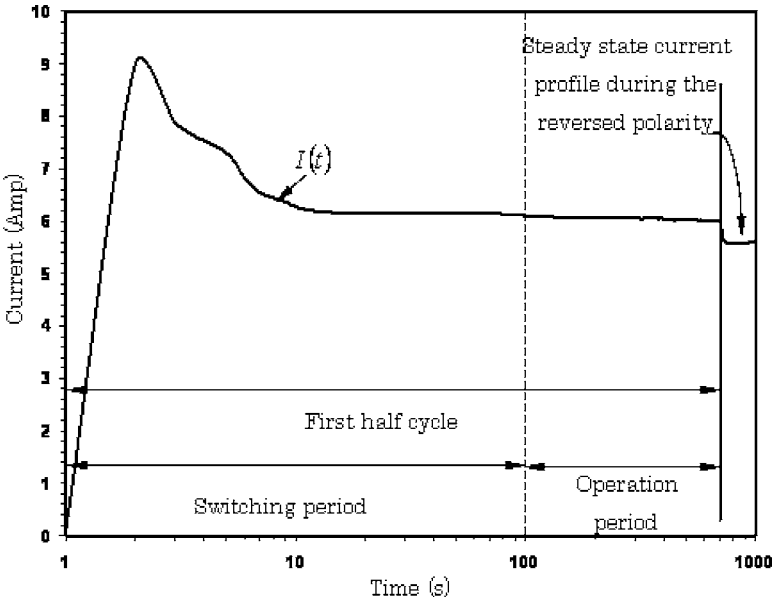

Fig. 10 The dc profile of the EAC for a fixed terminal voltage of 23 V of the thermoelectric modules. The current profiles for the forward polarity (switching and operation or the first half cycle) and the reversed polarity (very small time scale 700 to 1000 s including switching and operation periods or the next cycle) are shown here.

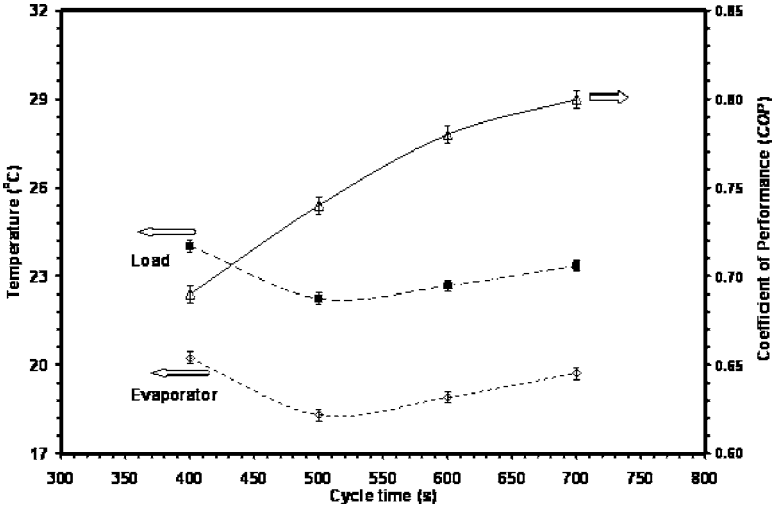

Fig. 11 Effects of cycle time on average load surface (quartz) temperature, evaporator temperature, and cycle average net COP. The constants used in this experiment are the heat flux q''_{flux}4.7 W/cm^2 and the terminal voltage of thermoelectric modules V=24 V.

reactor and the condenser. On the other hand, during hot-to-cold thermal swing of the bed, there is a sudden rise in the bed pressure at the end of the switching phase, causing momentary adsorption in the bed.

From experimental investigation, a sharp rise in temperature of the desorber bed during the switching interval is attributed due to the excellent heat regeneration within the beds. The thermoelectric modules draw heat from the adjacent bed and this results in a sharp rise in the dc flow during switching period. Figure 10 shows the current profile during a half-cycle operation of the electro-adsorption chiller. The thermal mass absorbs a relatively large amount of heat at the transient period and causes an additional heat pumping effect. The current is thus slightly lowered. After a long operating period the current becomes constant. The current decreases abruptly at the end of switching. The value of $I(t)$ increases during the switching operation, because of the presence of regenerative heat transfer occurring across the junctions of thermo-electrics.

For a 4.7 W/cm^2 heat flux in the evaporator, Fig. 11 shows the compiled experimental results of EAC as function of cycle time, the COP, and the temperatures of evaporator (T_{evap}) as well as the heated copper-foam (T_{load}). It is observed that there exist minima for both the T_{load} and T_{evap} at a cycle time (T_{cycle}) of 500 s and the measured COP (uncertainty of 0.03) is about 0.74. Increasing half-cycle time to 800 s, the temperatures of the evaporator and heated surface also increase monotonically, but the COP rises monotonically to 0.8. The high COP of the EAC reflects the unique advantages of amalgamating the TE with the adsorption cycles. It demonstrates also high cooling densities from the foam-cladded evaporator that meet the requirements of CPU cooling at low encasement temperature—a cooling regime that hitherto cannot be achieved by the conventional cooling devices.

Conclusions

The experiments show that the bench-scale electro-adsorption chiller (EAC) has been successfully designed, commissioned, and tested. Experimental results at assorted heat fluxes and half-cycle operation time intervals show that the EAC has a broad range of COP, from 0.7 to 0.8. With a suitable copper foam-cladded evaporator, it is capable of achieving cooling flux density up to 5 W/cm^2, corresponding to cooling capacity up to 125 W that is needed for a processor unit. More importantly, the cooling performed by the EAC is achieved at a low encasement temperature that is below or just at ambient—a region of CPU cooling that hitherto has yet to be reached by all passive methods.

Besides having high cooling densities, the EAC has almost no major moving parts except the fan of the condenser and it permits quiet operation as compared with other active coolers. The rating tests of the EAC show the resilience of the chiller by having a broad range of operating parameters that could be tuned to meet its cooling capacity CPUs operating at full or part loads. As both the adsorption (physio-sorption of vapor molecules) and TE (electrons flow) cycles are scale independent, the authors believe that the components of the bench-scale EAC could be further miniaturized without excessive loss of system efficiency.

Acknowledgment

The authors are grateful to the financial support given by ASTAR (Singapore) under Project No. 022 101 003 and for the use of the MSTI laboratory of the Mechanical Engineering Department, National University of Singapore.

References

[1] McGlen, R., Jachuck, R., and Lin, S., 2004, "Integrated Thermal Management Techniques for High Power Electronic Devices," Appl. Therm. Eng., **24**, pp. 1143–1156.
[2] Chu, R. C., Simons, R. E., Ellsworth, M. J., Schmidt, R., and Cozzolino, V., 2004, "Review of Cooling Technologies for Computer Products," IEEE Trans. Device Mater. Reliab., **4**, pp. 568–585.
[3] Phelan, P. E., Chiriac, V. A., and Lee, T. T., 2002, "Current and Future Miniature Refrigeration Cooling Technologies for High Power Microelectronics," IEEE Trans. Compon. Packag. Technol., **25**, pp. 356–365.
[4] Gordon, J. M., and Ng, K. C., 2000, *Cool Thermodynamics*, Cambridge International Science, Cambridge.
[5] Yu, X., Feng, J., Feng, Q., and Wang, Q., 2005, "Development of a Plate-fin Heat Sink and its Performance Comparisons with a Plate-fin Heat Sink," Appl. Therm. Eng., **25**, pp. 173–182.
[6] Haider, S. I., Joshi, Y. K., and Nakayama, W., 2002, "A Natural Circulation Model of the Closed Loop Two Phase Thermosyphon for Electronics Cooling," ASME J. Heat Transfer, **124**, pp. 881–890.
[7] Drost, K., Friedrich, M., Martin, C., Martin, J., and Hanna, B., 1999, "Mesoscopic Heat-actuated Heat Pump Development," *ASME IMECE Conf.*, Nashville, TN, November 14–19, ASME, New York.
[8] Yeh, L. T., 1995, "Review of Heat Transfer Technologies in Electronic Equipment," ASME J. Electron. Packag., **117**, pp. 333–339.
[9] Kim, K. S., Won, M. H., Kim, J. W., and Back, B. J., 2003, "Heat Pipe Cooling Technology for Desktop PC CPU," Appl. Therm. Eng., **23**, pp. 1137–1144.
[10] Schmidt, R., 2000, "Electronics Cooling the Current Resources for the Practitioners," IBM Corporation.
[11] Goldsmid, H. J., and Douglas, R. W., 1954, "The Use of Semiconductors in Thermoelectric Refrigeration," Br. J. Appl. Phys., **5**, pp. 386–390.
[12] Rowe, D. M., 1995, *CRC Handbook of Thermoelectrics*, CRC, Boca Raton, FL.
[13] Saha, B. B., Koyama, S., Kashiwagi, T., Akisawa, A., Ng, K. C., and Chua, H. T., 2003, "Waste Heat Driven Dual-Mode, Multi-Stage, Multi-Bed Regenerative Adsorption System," Int. J. Refrig., **26**, pp. 749–757.
[14] Saha, B. B., Koyama, S., Lee, J. B., Kuwahara, K., Alam, K. C. A., Hamamoto, Y., Akisawa, A., and Kashiwagi, T., 2003, "Performance Evaluation of a Low-Temperature Waste Heat Driven Multi-Bed Adsorption Chiller," Int. J. Multiphase Flow, **29**, pp. 1249–1263.
[15] Viswanathan, V. V., Wegeng, R., and Drost, K., 2002, Microscale Adsorption for Energy and Chemical Systems, Pacific Northwest National Laboratory (http://www.pnl.gov/microcats/aboutus/research/adsorption.html), date of access: 6 Feb. 2006.
[16] Edward, G., 1970, "Thermoelectric Adsorber," US Patent No. 3,734,793. March 4.
[17] Bonnissel, M. P., Luo, L., and Tondeur, D., 2001, "Rapid Thermal Swing Adsorption," Ind. Eng. Chem. Res., **40**, pp. 2322–2334.
[18] Ng, K. C., Gordon, J. M., Chua, H. T., and Chakraborty, A., 2002, "Electro-adsorption Chiller: A Miniaturized Cooling Cycle with Applications from Microelectronics to Conventional Air-conditioning," US Patent No. 6,434,955.
[19] Ng, K. C., Wang, X. L., Gao, L. Z., Chakraborty, A., and Sai, M. A., 2005, "Experimental Investigation of an Electro-adsorption Chiller," *Proc. ASME Heat Transfer Conf. Summer Heat Transfer Conf., July 17–22*, Westin St. Francis, San Francisco, CA.
[20] Chakraborty, A., 2005, "Thermoelectric Cooling Devices: Thermodynamic Modelling and their Application in Adsorption Cooling Cycles," Ph.D. thesis, Department of Mechanical Engineering, National University of Singapore.
[21] Ng, K. C., Chakraborty, A., Sai, M. A., and Wang, X. L., 2006, "New Pool Boiling Data for Water with Copper Foam-Metal at Sub-atmospheric Pressures: Experiments and Correlation," Appl. Therm. Eng., **26**, pp. 1286–1290.

Electronic Cooling Using Synthetic Jet Impingement

Anna Pavlova

Michael Amitay[1]
e-mail: amitam@rpi.edu

Mechanical, Aerospace and Nuclear Engineering Department,
Rensselaer Polytechnic Institute,
Troy, NY 12180

The efficiency and mechanisms of cooling a constant heat flux surface by impinging synthetic jets were investigated experimentally and compared to cooling with continuous jets. Effects of jet formation frequency and Reynolds number at different nozzle-to-surface distances (H/d) were investigated. High formation frequency ($f=1200$ Hz) synthetic jets were found to remove heat better than low frequency ($f=420$ Hz) jets for small H/d, while low frequency jets are more effective at larger H/d. Moreover, synthetic jets are about three times more effective in cooling than continuous jets at the same Reynolds number. Using particle image velocimetry, it was shown that the higher formation frequency jets are associated with breakdown and merging of vortices before they impinge on the surface. For the lower frequency jets, the wavelength between coherent structures is larger such that vortex rings impinge on the surface separately.
[DOI: 10.1115/1.2241889]

Keywords: synthetic jets, impingement cooling, coherent structures, operating frequencies, large-scale mixing

1 Introduction

Current trends in electronic components show continuously increasing needs for efficient heat removal in closely packed systems, and this need is predicted to continue to grow in the foreseeable future [1]. The current method of heat removal, involving extended surfaces and fan arrays, frequently used in electronics is clearly insufficient, especially as the electronic components become more and more powerful, dissipating more heat, whereas the space around these components continues to be reduced due to miniaturization trends. On the other hand, impinging jet cooling, which is the focus of the present paper, is much better at heat removal from electronic components.

A large number of investigations have been carried out in the area of jet impingement heat transfer over the years. Most of the earlier works have focused on optimizing the transport processes associated with continuous impinging jets. In that context, parameters such as the spacing between the jet outlet and the impingement surface, the magnitude of the jet velocities (i.e., Reynolds number), turbulence intensity, and the angle of impingement have been extensively studied. Much of this early research is summarized by Martin [2].

Some researchers have looked into potentially enhancing jet impingement heat transfer by exciting coherent structures in the jet flow. In 1961, Nevins and Ball [3] were among the first who looked into pulsed air jet impingement. They investigated spatially and temporally averaged heat transfer for an impinging pulsating circular air jet with nozzle-to-plate distance of 8–32 nozzle diameters, Reynolds numbers ranging between 1200 and 120,000 and Strouhal numbers ranging between 10^{-4} and 10^{-2} and concluded that no heat transfer enhancement resulted from the pulsations in the flow. More than two decades later, the issue of flow excitation with pulses was revisited. In 1987, Kataoka and Suguro [4] used a statistical technique with conditional sampling and found that secondary flow structures help enhance heat transfer from the surface, showing that the stagnation point heat transfer for axisymmetric submerged jets is enhanced by large-scale structures that impinge on the surface. In 1993, Eibeck et al. [5] used experiments and computations to identify secondary flow structures that were enhanced by pulsations introduced into the flow and found heat transfer enhancement in excess of 100%, attributing this to the intermittent vortex rings impinging on the surface. Heat transfer enhancement nearly by a factor of 2 due to pulsed impinging jets was also documented by Zumbrunnen and Aziz [6], who used water as their working fluid.

In 1999, Sailor et al. [7] used a square wave form signal to excite the jet and focused on the effect of the duty cycle (the ratio of pulse cycle on-time to total cycle time), in addition to the traditionally investigated parameters, such as jet to plate spacing, Reynolds number, and pulse frequency. They found the duty cycle to be a contributing factor to heat transfer enhancement in that the lower duty cycle resulted in better heat transfer results, especially at intermediate frequencies and high flow rates. Zulkifli et al. [8] carried out experiments to study the effect of pulsation on local and average heat transfer characteristics of a heated air jet. They considered excitation frequencies of 10–80 Hz with corresponding Strouhal numbers of 0.008 to 0.123, for Reynolds numbers between 16,000 and 32,000 at a fixed nozzle-to-plate distance and a duty cycle of 33%. They found that for most pulsation frequencies heat transfer was enhanced, attributing this to increased turbulence intensity induced by the pulsations.

In 2001, Hwang et al. [9] experimentally investigated the flow and heat transfer characteristics of an impinging jet, controlled by vortex pairing in pulsed jets. They showed that depending on how the flow is excited, heat transfer may be either hindered or improved. In a subsequent experimental study in 2003, Hwang and Cho [10] showed that the frequency and excitation level of acoustically excited impinging jets are both important in heat transfer enhancement.

Recently, Chaniotis et al. [11] carried out a numerical investigation of pulsation on single and dual continuous slot impinging jets on a constant heat flux surface with a focus on the influence of frequency, amplitude, and phase difference between the jets and comparing dual jets to an equivalent mass flux single continuous jet. They concluded that the strong aerodynamic and thermal interaction exhibits a nonlinear system response, with an intermittency of structures that is responsible for heat transfer enhancement.

Haneda et al. [12] considered the effects of a small cylinder suspended in the jet stream on the cooling efficiency of a two-

[1]Corresponding author.
Contributed by the Heat Transfer Division of ASME for publication in the JOURNAL OF HEAT TRANSFER. Manuscript received September 14, 2005; final manuscript received February 20, 2006. Review conducted by Yogendra Joshi. Paper presented at the 2005 ASME Heat Transfer Summer Conference (HT2005), July 15–22, 2005, San Francisco, CA.

dimensional impinging jet. They found that the insertion of a rigidly suspended cylinder degrades heat transfer around the stagnation region, while enhancing heat transfer outside that region, which is due to vortex shedding from the cylinder. Heat transfer from the entire surface was enhanced when the cylinder was mounted with springs, allowing it to oscillate. Camci and Herr [13] conducted an experimental investigation of a self-oscillating impinging jet. They showed that the flapping motion of the jet enhances the heat transfer from the surface as well as the area covered by the impingement zone, compared to a stationary impinging jet. These works indicate that there is potentially a great benefit in introducing coherent structures into the flow field by applying controlled excitation to impinging jets for heat transfer enhancement. However, jet impingement cooling requires rather complicated plumbing, which is not always convenient.

Recently, synthetic jets have been investigated for electronic component cooling, because synthetic jets require no plumbing associated with traditional continuous jets as they use ambient air, and, when properly designed, can be much more efficient. For example, in 2001, Vukasinovic and Glezer [14] investigated experimentally the performance of a low-profile radial countercurrent heat sink, driven by a synthetic jet actuator at 80 Hz normally impinging on an extended surface with a power dissipation of 50 W. Flow measurements using particle image velocimetry (PIV) and temperature measurements on a test die were carried out at several distances between the synthetic jet and the test die. The findings of their study show that synthetic jets may present a viable option for the cooling of electronics where space and volume are limited. In 2003, Kercher et al. [15] demonstrated the potential use of a synthetic microjet in conjunction with a fan, impinging on a heated surface for thermal management of electronics. More recently, Mahalingam et al. [16] also investigated synthetic jets for thermal management, using a two-dimensional synthetic jet to drive air through a rectangular channel and illustrating its potential usefulness.

The motivation of the present work is to further explore the efficiency of synthetic jet impingement cooling and understand the mechanisms by which heat is removed from a constant heat flux surface. The effects of jet formation frequency and Reynolds number at different nozzle-to-surface distances are investigated and compared to continuous jet impingement cooling. The heat transfer characteristics and flow structures are explored experimentally using thermocouples and PIV, respectively, to gain an understanding of the underlying physics of flow and heat transfer interactions in surface cooling with impinging synthetic jets.

2 Experimental Setup

The experiments were conducted in a special facility that was designed to house different configurations of synthetic jets impinging on a heated surface within an enclosure having clear walls and ceiling panels, such that both heat transfer and fluid dynamics measurements could be performed in the same enclosure (Fig. 1(*a*)). The enclosure features a 275 mm $\times$ 335 mm $\times$ 335 mm volume mounted on an optical table, facilitating precise mounting of associated optical hardware. A cooling module was designed, which is comprised of a heated surface and synthetic jet (Fig. 1(*b*)), mounted such that the jet orifice to surface distance can be controlled easily using a fine pitch traversing mechanism. The heater was constructed from oxygen-free copper disk (12.7 mm in diameter and 6 mm in thickness), which was heated by a round, flexible, commercially available kapton heater attached underneath. The copper heater was centrally mounted into a block of nylon insulation (150 $\times$ 150 $\times$ 55 mm) to minimize heat losses through the sides and bottom. In the present experiments the heat flux generated by the heater was $\sim$1 W/cm^2.

Heat losses through the sides and the bottom of the insulation were estimated assuming the copper heater is a disk at the surface of a semi-infinite insulation solid at T_∞ [17]. The surface temperature of the heater was found experimentally by insulating its top.

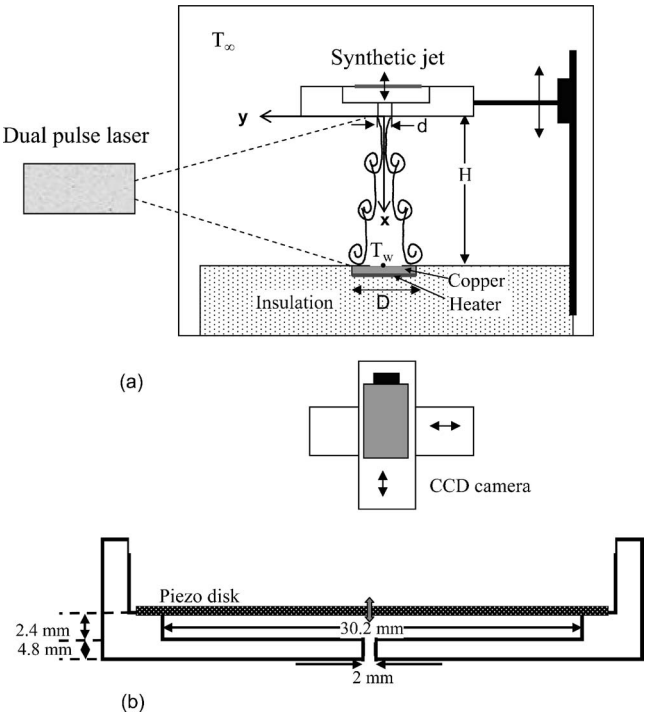

Fig. 1 (*a*) Experimental setup and (*b*) detailed drawing of the synthetic jet

In this manner, the losses through the sides and the bottom were found to be 20% of the power input. Because of low temperatures involved in this experiment, heat loss from the surface due to radiation transfer was neglected, as it was calculated to be less than 3% of the power input for all cases, which is within the resolution of the measurements. The heater surface provides a constant heat flux, as the driving power input is constant, and the flexible heater is specifically designed to provide a constant heat flux output. The Biot number for the copper disk in the thickness direction was calculated and found to be at most O(10^{-3}), which indicates that the conduction from the bottom surface, where the power is introduced, to the top surface happens on a much faster time scale than the convection from the surface.

The surface temperature was measured with a T-type thermocouple, 0.127 mm in diameter that was placed at the center of the copper disk just below the surface, 0.8 mm from the top surface, thus providing a spatially averaged heat transfer measurement over the exposed surface of the copper heater. An identical thermocouple was stationed inside the enclosure away from the heated surface for ambient air temperature monitoring. The thermocouples were calibrated with respect to one another at room temperature prior to the experiments. The control of the heat flux provided by the heater and the temperature data acquisition were carried out using LabVIEW.

The flow features associated with an isolated synthetic jet impinging on the surface were investigated using highly resolved spatial and temporal measurements via PIV, complemented with hot-wire anemometry. The facility was equipped with a computer-controlled traversing mechanism for the hot-wire anemometry and the PIV system. In this setup, the PIV system allows full-resolution measurements within domains that are as small as 10 $\times$ 10 mm. The PIV system is based on the commercial LaVision hardware and software, which utilizes two 120 mJ Nd:yttrium-aluminum-garnet (YAG) lasers and a 1376 $\times$ 1040 pixel resolution thermoelectrically cooled 12-bit charged coupled device (CCD) camera. The flow within the enclosure was seeded using incense smoke particles that had a diameter of O(1 μm). Four hundred image pairs were acquired for the time-averaged fields, while 200

image pairs were used to obtain the phase-averaged data. The streamwise and cross-stream velocity components (U,V) were computed from the crosscorrelation of pairs of successive images with 50% overlap between interrogation domains. The images were processed using an advanced multipass technique, where the initial and final correlation passes were 32×32 pixels and 16×16 pixels (two passes), respectively. The spatial resolution of the resulting vector fields is 0.2 mm.

2.1 Impinging Synthetic Jets. A synthetic jet is a jet that is synthesized at the edge of an orifice by a periodic motion of a diaphragm mounted on one (or more) walls of a sealed cavity. In the data presented here, the synthetic jet was driven by a single commercially available 32 mm diameter piezoelectric disk having the nominal resonant frequency of 1000 Hz, with a 2 mm circular orifice (Fig. 1(*b*)). When the diaphragm moves toward the orifice, a vortex ring is formed at the edge of the orifice, and it moves away with its own self-induced velocity such that when the diaphragm moves away from the orifice, the vortex ring is far enough away and is not affected by the fluid drawn into the cavity. Therefore, a synthetic jet has a zero-net-mass-flux per cycle of actuation but allows momentum transfer to the flow. With a proper design, the diaphragm and the cavity are driven at resonance; thus, only small electrical power input is needed, making the synthetic jet a very efficient and attractive actuator for flow and heat transfer control applications. Another advantage of the synthetic jet is that no plumbing or mechanical complexities are needed.

In the setup of the present experiments two operating frequencies, 420 and 1200 Hz, were the most effective in cooling (at the same Reynolds number) in terms of heat removal improvement. Furthermore, at the range of jet-to-heater distances discussed in the present paper these driving frequencies result in flow fields which affect the heat transfer differently, as discussed in Sec. 3. Hence, the data associated with synthetic jet cooling at these two operating frequencies are presented and discussed. The parameters of the jet that were varied in the experiments include $140<\mathrm{Re}_{U_0}<740$ (with a corresponding Re_{U_p} of 438–2306), $1.9<H/d<38.1$, and $0.18<\mathrm{St}<2.17$. Here, Re_{u_0} is defined based on the work of Smith and Glezer [18]

$$\mathrm{Re}_{U_0}=\frac{U_0 d}{\nu} \tag{1}$$

where d is the orifice diameter, ν is the kinematic viscosity, and U_0 is the average orifice velocity during the blowing portion of the actuation cycle defined as

$$U_0=\frac{L_0}{\tau}, \tag{2}$$

and L_0 is the jet's stroke length defined as

$$L_0=\int_0^{\tau/2} u(t)dt, \tag{3}$$

The synthetic jets were driven by an amplified sinusoidal signal from function generator, thus allowing for a straightforward calculation of the power required to operate the jet from the voltage, the current, and the phase difference between the two. The Reynolds number for synthetic jets was varied by changing the voltage of the input signal, which changes the U_0. The calibration of the synthetic jet for the different driving frequencies and amplitudes was conducted using a miniature hot-wire sensor (5 μm tungsten). Hot-wire measurements along the centerline of synthetic jets were used to verify the velocity data obtained with PIV.

Continuous jets for comparison purposes were produced using a special module, geometrically identical to the synthetic jet module on the outside, where the piezodisk cavity was replaced with a stainless steel tube having the inner diameter of 2 mm, through which compressed air was passed to create a jet whose Reynolds number was matched to that of the synthetic jets.

2.2 Measurement Uncertainties. In all experiments, the measured temperature difference (between the surface and ambient) was at least 20°C with an uncertainly of 2.5%. The uncertainty of the power supplied to the copper heater, assumed to be the same as the uncertainty of the heat flux out of the heater, was at most 5%. The uncertainty in the thermal conductivity of air, given the small temperature fluctuations, was estimated to be less than 3%, and the uncertainty of the heater diameter is approximately 0.1%. Assuming that errors are independent, it is reasonable to estimate the overall uncertainty of Nusselt number calculations based on the method of Kline and McClintock [19], which results in calculated Nusselt number uncertainty of less than 13% for all heat transfer experiments presented in this paper. The uncertainty of velocity and vorticity, based on the specifications of the PIV system used, are within 3% and 5%, respectively.

3 Result and Discussion

The effectiveness of synthetic jet impingement for cooling a constant heat flux surface was investigated experimentally using thermocouples and PIV. In the this section, heat transfer enhancement using synthetic jets is presented first, followed by a discussion on the flow field coherent structures that are responsible for the enhanced heat removal.

3.1 Heat Transfer Measurements. The effect of synthetic jet impingement cooling was investigated by measuring the surface and ambient temperatures for different synthetic jet operating frequencies and Reynolds numbers for a constant power of 1.15 W supplied to the heater.

The enhancement of the stagnation Nusselt number, compared to that achieved with free convection, as a function of H/d for operating frequencies of 420 and 1200 Hz and at different Reynolds numbers is presented in Figs. 2(*a*) and 2(*b*), respectively. Here $\Delta\mathrm{Nu}$ is the change in Nusselt number between the forced and free convection cases for the same conditions, and Nu_f is the free convection Nusselt number. Note that because the metal used in the heater is highly conductive copper, the stagnation Nusselt number resulting from temperature measurements is essentially the average Nusselt number across the heater surface, making it a reasonable parameter to assess the space-averaged heat transfer from the surface. As expected, for both frequencies, increasing the synthetic jet's Reynolds number results in greater heat transfer enhancement. When the synthetic jet is operated at a frequency of 420 Hz (Fig. 2(*a*)) the improvement of the stagnation Nusselt number (with respect to free convection) is up to 78%, with optimal cooling occurring for H/d of 6–18 for all Reynolds numbers. For $H/d>18$, the performance degrades, as it does for normalized distances below 6. At a higher operating frequency ($f=1200$ Hz), the enhancement in Nu_s is up to 113%, where the best cooling performance is obtained for H/d in the range of 3–11. Outside of this range, the cooling effectiveness decreases. The data show that the H/d range corresponding to better cooling at the higher frequency of synthetic jet is closer to the surface, compared to the lower frequency jet. This will be discussed in more details in Sec. 3.2

The effect of the operating frequency of the synthetic jet on the cooling effectiveness is further demonstrated in Fig. 3 for $f=420$ and 1200 Hz, both at the Reynolds number of 445 and is compared to the performance of a continuous jet at the same Reynolds number (represented by the dashed line). Note that the matching of the synthetic jet and the continuous jet was done based on the work of Smith and Swift [20] where the synthetic jet's orifice velocity, U_0, is the same as the averaged velocity of the continuous jet at the jet exit plane, U_{av_0}. This figure shows that both high and low frequency synthetic jets cool the surface better than the corresponding continuous jet over the range of H/d tested (for example, at $H/d=4.75$ the synthetic jet operated at 1200 Hz improved the heat transfer by a factor of 2.6, compared to the continuous jet). That, in itself, is very significant, as it illustrates

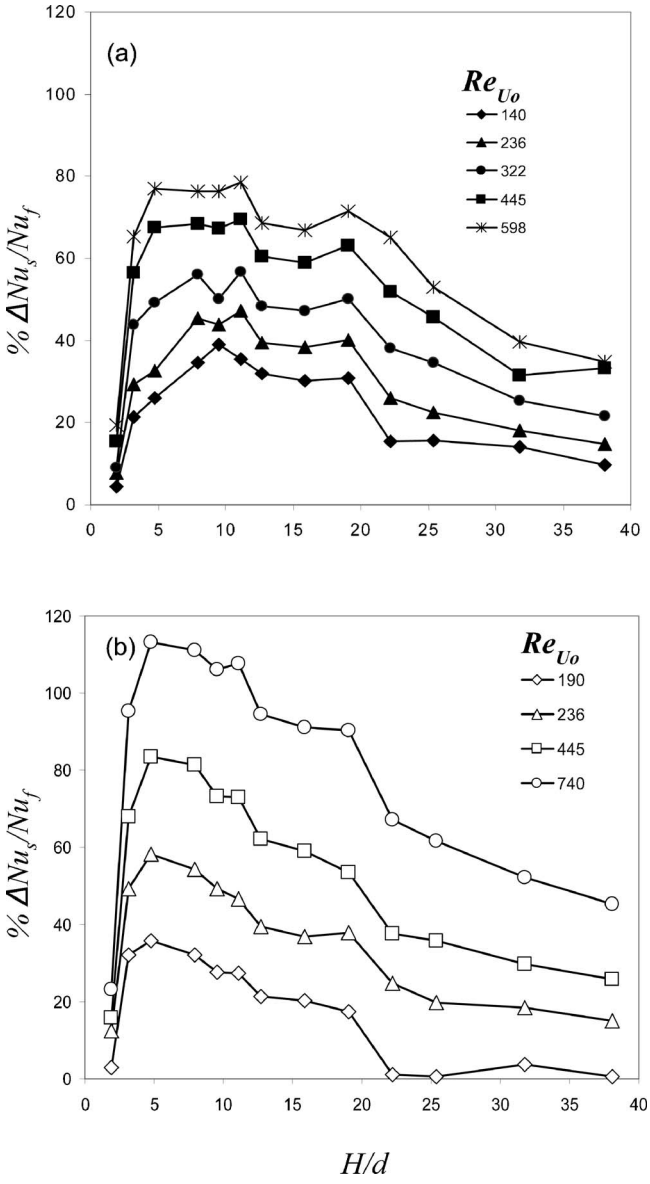

Fig. 2 The change in the stagnation Nusselt number (with respect to free convection) as a function of the normalized distance, *H*/*d*, for different Reynolds numbers: (*a*) *f*=420 Hz and (*b*) *f*=1200 Hz

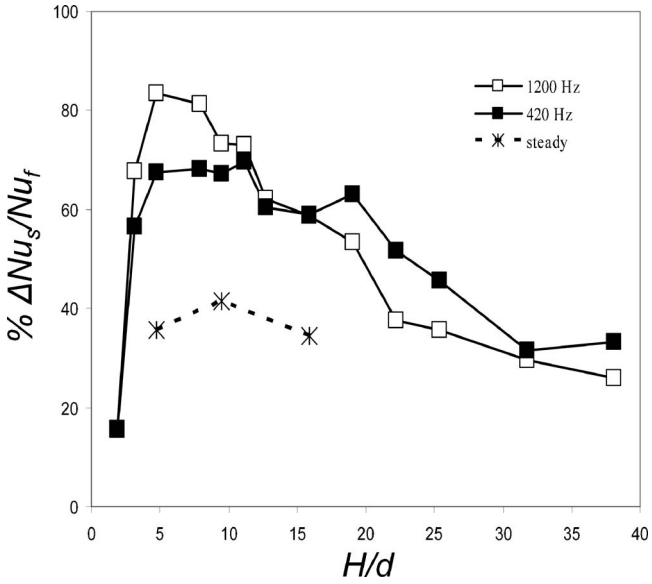

Fig. 3 The change in stagnation Nusselt number (with respect to free convection) as a function of the normalized distance, *H*/*d*, for Re_{U_0}=445

that synthetic jets provide an impressive heat removal improvement over continuous jets, in addition to the advantages of not requiring additional plumbing, as well as low energy consumption. This can be attributed to two major mechanisms: (1) as was shown by Smith and Swift [20], for the same Reynolds number synthetic jets are wider, slower, and have more momentum than similar continuous jets (due to enhanced entrainment), thus more heat is removed and (2) synthetic jets consist of a train of vortex rings (as will be shown is Sec. 3.2), which further enhance the heat removal, compared to continuous jets. Figure 3 also shows the difference in trend of cooling performance between synthetic jets of high and low formation frequency at different distances. The high frequency synthetic jet removes heat better than the low frequency jet for smaller distances, whereas the low frequency jet is more effective at larger distances up to $H/d \sim 28$, with the two having the same performance for H/d of 12.5– $\sim$16. This behavior is related to the wavelength of the coherent structures associated with the synthetic jets, which is discussed in detail in the following section. Note that similar behavior was obtained for different jet Reynolds numbers.

The efficiency of synthetic jet cooling for the matching Reynolds number jets at 420 and 1200 Hz as a function of H/d is presented in Fig. 4. The efficiency is defined as the ratio of the heat removed (compared to free convection), ΔP, to the input power to the synthetic jet, P_j. For a Reynolds number of 445 the 420 Hz synthetic jet the efficiency is up to 1000%, and is fairly consistent for H/d of 6–18, while the 1200 Hz synthetic jet reaches an efficiency of more than 1300% at H/d=4.75, which is very impressive. Here, we see the same trend as Fig. 3, illustrating that Nusselt number enhancement is closely tied to synthetic jet efficiency. The high efficiency is attributed to the fact that the synthetic jets are designed to operate near resonance conditions (i.e., where the piezodisk frequency and the Helmholtz frequency of the cavity are matched); thus, very small electrical power is needed.

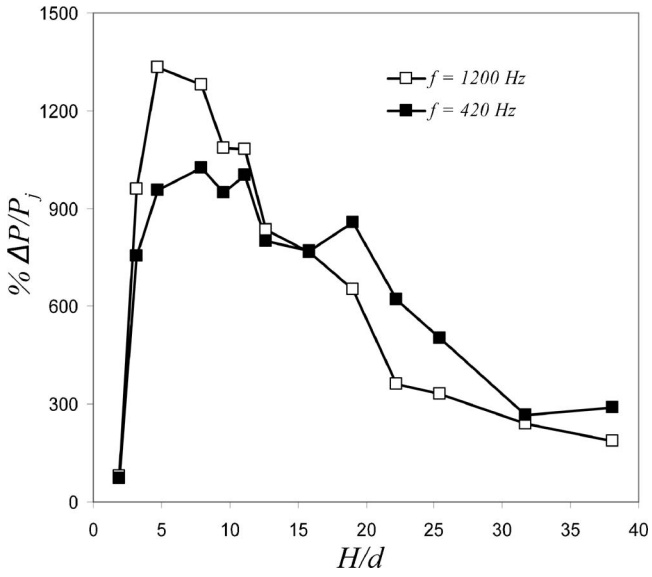

Fig. 4 Synthetic jet efficiency as a function of the normalized distance, *H*/*d*, for Re_{U_0}=445

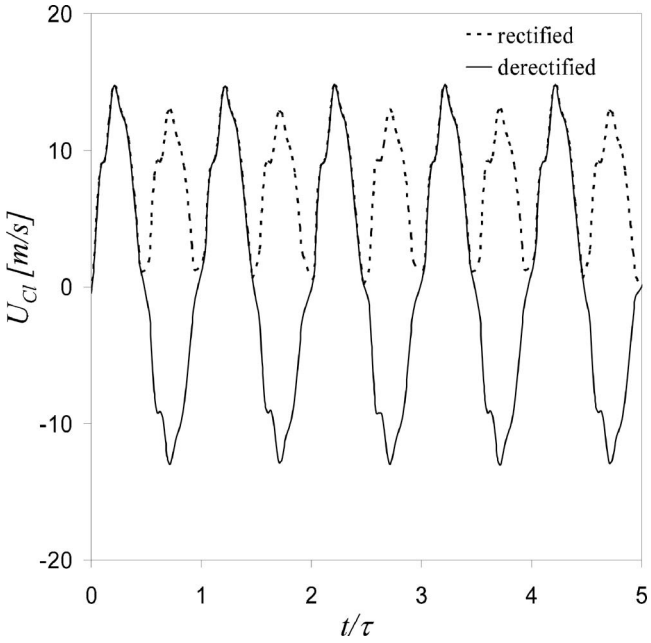

Fig. 5 Time trace of the velocity at the synthetic jet exit plane. Rectified (dashed line) and derectified (solid line). $Re_{U_0}=445$.

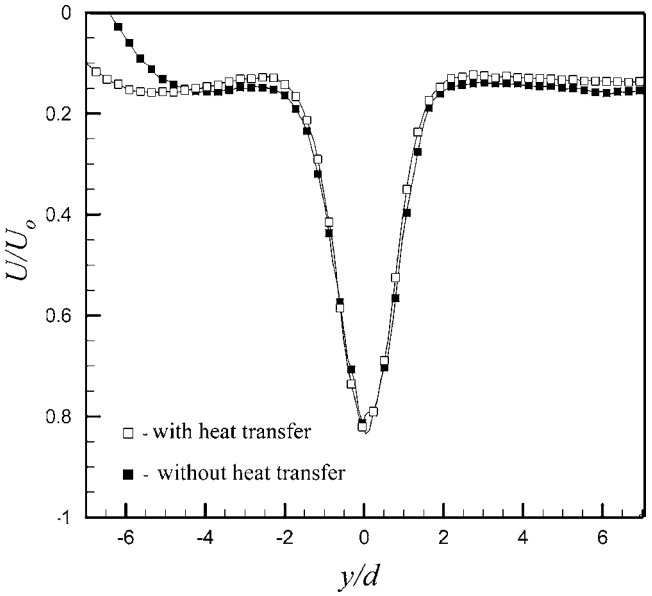

Fig. 6 Cross-stream distributions of the normalized time-averaged streamwise velocity component at $x/d=7.7$. $Re_{U_0}=190$, $f=1200$ Hz, and $H/d=9.5$.

3.2 Flow Measurements. In order to understand the mechanisms associated with synthetic jet impingement cooling and to explore the effect of the operating frequency on the cooling effectiveness, the flow field of the synthetic jet above the surface was investigated using PIV. As a first step, the synthetic jets were calibrated using single hot-wire anemometry, with which the centerline velocity was measured at the exit plane of the jet (i.e., the center of the orifice). Since the hot-wire probe is based on a Wheatstone bridge, it infers the velocity from temperature measurements and provides only the magnitude, but not the direction of the air flow. Therefore, the resulting signal is rectified, with the sense of velocity always positive (the dashed line in Fig. 5). This is not representative of the true velocity profile in the orifice of a synthetic jet, which roughly corresponds to a sinusoidal signal, where the air is periodically expelled out of the orifice and drawn into the cavity. Thus, the signal must be derectified, where the peaks corresponding to suction are essentially flipped over, as represented by the solid line in Fig. 5.

The velocity and vorticity plots presented in the following figures were acquired without the presence of heat transfer (i.e., the heater was turned off). The assumption was that at the conditions used in the present work the effect of buoyancy, due to the heated surface, does not significantly affect velocity. In order to validate this assumption, the velocity vector fields, without and with heat transfer, were measured and compared. Figure 6 presents the cross-stream distribution of the normalized streamwise velocity, U/U_0, at $x/d=7.7$ for $f=1200$ Hz at $H/d=9.5$ and a Reynolds number of 190, which corresponds to a synthetic jet weaker than any jets that are presented in this paper. It can be observed that the velocity distributions are almost identical, thus validating our assumption. Furthermore, the $\mathrm{Gr}/\mathrm{Re}_{U_0}^2$ for this case was also calculated and found to be 1.4×10^{-9}, suggesting that the buoyancy effect is negligible, which is consistent with the velocity profiles shown in Fig. 6. Note that since the streamwise velocity distribution (and the cross-stream velocity, not shown) at this low Reynolds number is not altered by the heat transfer, the rest of the velocity data presented in this paper, where stronger jets are used at the same power supplied to the heater, are also not affected.

First, normalized time-averaged streamwise velocity component distributions, U/U_0, of the impinging synthetic jet are presented in Fig. 7. These are shown at two streamwise locations of $x/d=5$ and 7.7 in Figs. 7(*a*)–7(*f*) for jet operating frequencies of 420 and 1200 Hz, respectively, where the distance between the jet and the surface is $H/d=9.5$. For each frequency, measurements at three Reynolds numbers were taken ($\mathrm{Re}_{U_0}=322$, 445, and, 598 for the 420 Hz jet, Figs. 7(*a*)–7(*c*), respectively, and $\mathrm{Re}_{U_0}=236$, 445, and 740, for the 1200 Hz jet, Figs. 7(*d*)–7(*f*), respectively). At the operating frequency of 420 Hz the velocity profiles exhibit a single peak distribution for all Reynolds numbers at both locations (Figs. 7(*a*)–7(*c*)). As x/d increases, the jet widens and the peak velocity increases. Moreover, the normalized maximum velocity decreases and the jet's width increases with increasing Reynolds number. This may be due to enhanced mixing at higher Reynolds numbers.

The cross-stream distributions of the streamwise velocity component for the higher operating frequency jet ($f=1200$ Hz, Figs. 7(*d*)–7(*f*)) exhibit a single peak distribution at $x/d=5$ for all three Reynolds numbers. However, farther downstream at $x/d=7.7$, as the jet is approaching the surface, there is a double peak distribution due to breakdown and merging of vortices, as will be discussed in conjunction with Figs. 8 and 9.

The effect of the operating frequency on the flow field near the impingement surface can be assessed by comparing Figs. 7(*b*) and 7(*e*), where the Reynolds number is the same ($\mathrm{Re}_{U_0}=445$) for $f=420$ and 1200 Hz, respectively. Here, different flow fields result in a similar enhancement of the stagnation Nusselt number. This will be discussed in detail with respect to Fig. 9. Interestingly, even where the Reynolds number is different ($\mathrm{Re}_{U_0}=322$ at $f=420$ Hz, Fig. 7(*a*) and $\mathrm{Re}_{U_0}=236$ at $f=1200$ Hz, Fig. 7(*d*)), the stagnation Nusselt number is the same in spite of the markedly different velocity distributions near the surface. The behavior of the flow and the corresponding cooling effectiveness of the synthetic jet at the two frequencies are intimately related and will be discussed at length later.

In order to further explore the flow characteristics of the impinging synthetic jet, mean vorticity fields were calculated from the velocity fields and are presented in Figs. 8(*a*)–8(*f*). Note that negative vorticity contours are represented by dashed lines. The difference between the two frequencies is apparent in these figures. For the $f=420$ Hz jet (Figs. 8(*a*)–8(*c*)), there are two regions of vorticity, positive on the right and negative on the left. These

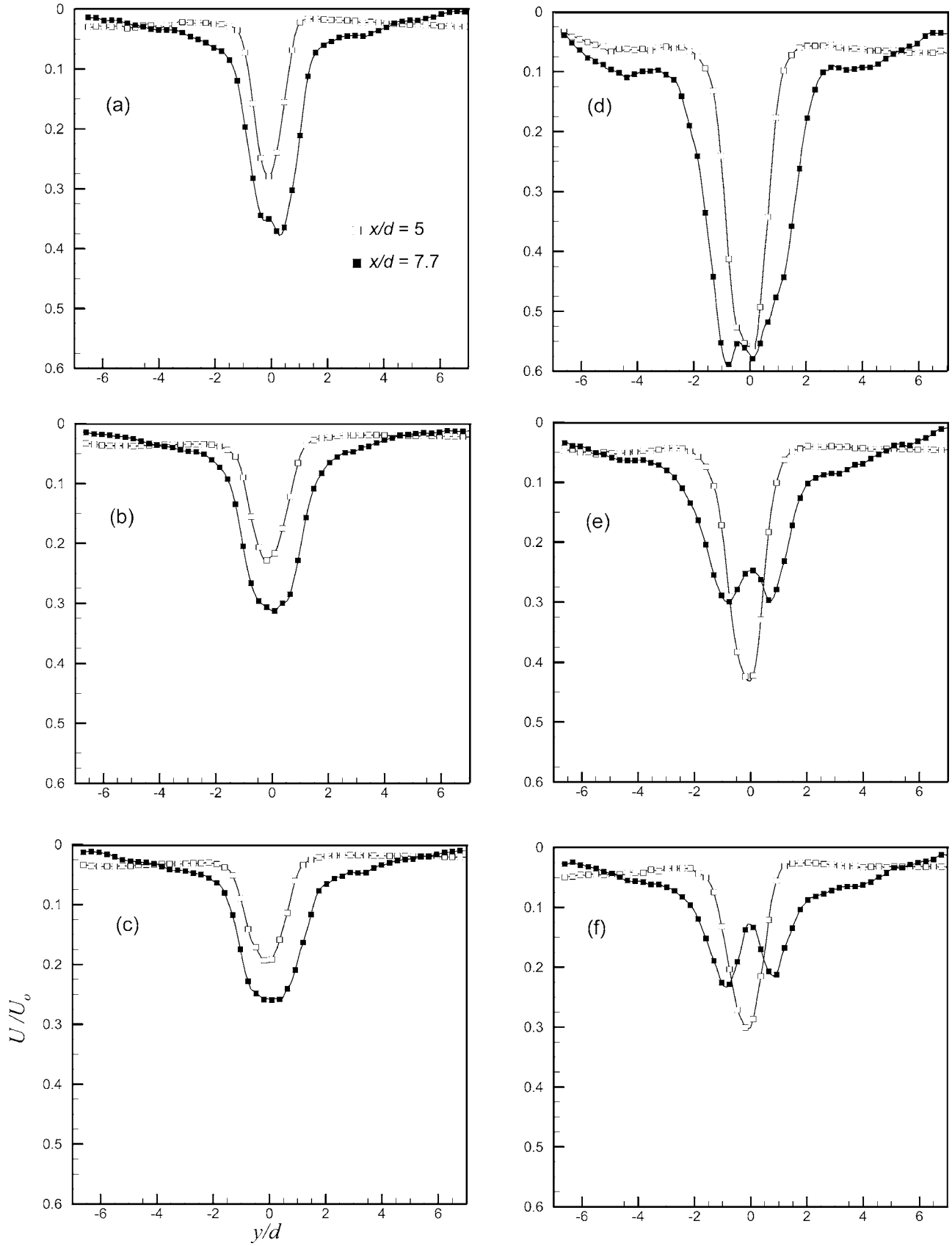

Fig. 7 Cross-stream distributions of the normalized time-averaged streamwise velocity component at $x/d=5$ and 7.7. (*a*)–(*c*) and (*d*)–(*f*) for jet operating frequencies of 420 and 1200 Hz, respectively. $Re_{U_0}=322$ (*a*), 445 (*b*), and 598 (*c*) for the 420 Hz jet, and $Re_{U_0}=236$ (*d*), 445 (*e*), and 740 (*f*) for the 1200 Hz jet; $H/d=9.5$.

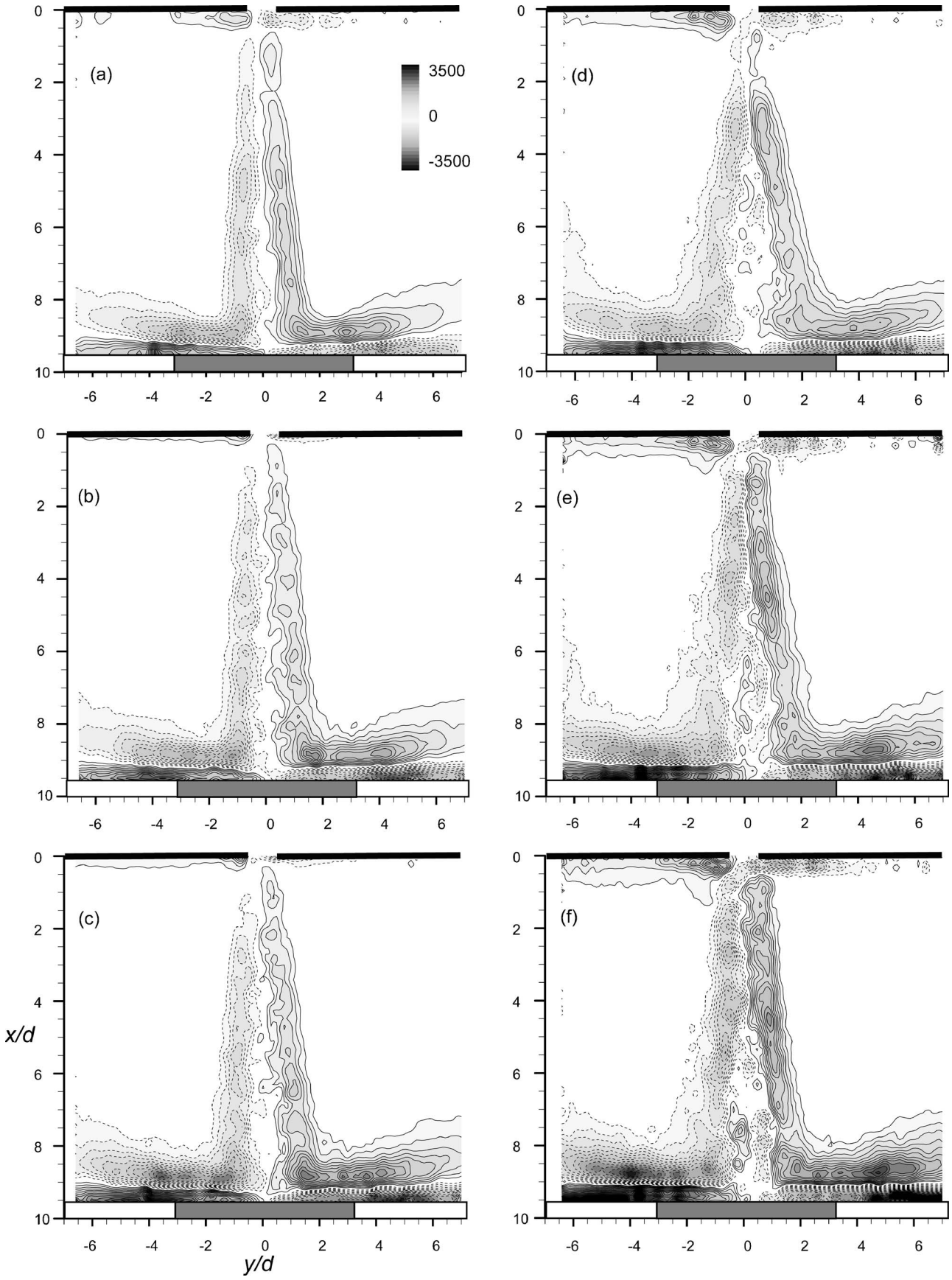

Fig. 8 Time-averaged spanwise vorticity fields for $f=420$ Hz ((*a*)–(*c*)) and $f=1200$ ((*d*)–(*f*)). $Re_{U_0}=322$ (*a*), 445 (*b*), and 598 (*c*) for the 420 Hz jet, and $Re_{U_0}=236$ (*d*), 445 (*e*), and 740 (*f*) for the 1200 Hz jet. $H/d=9.5$

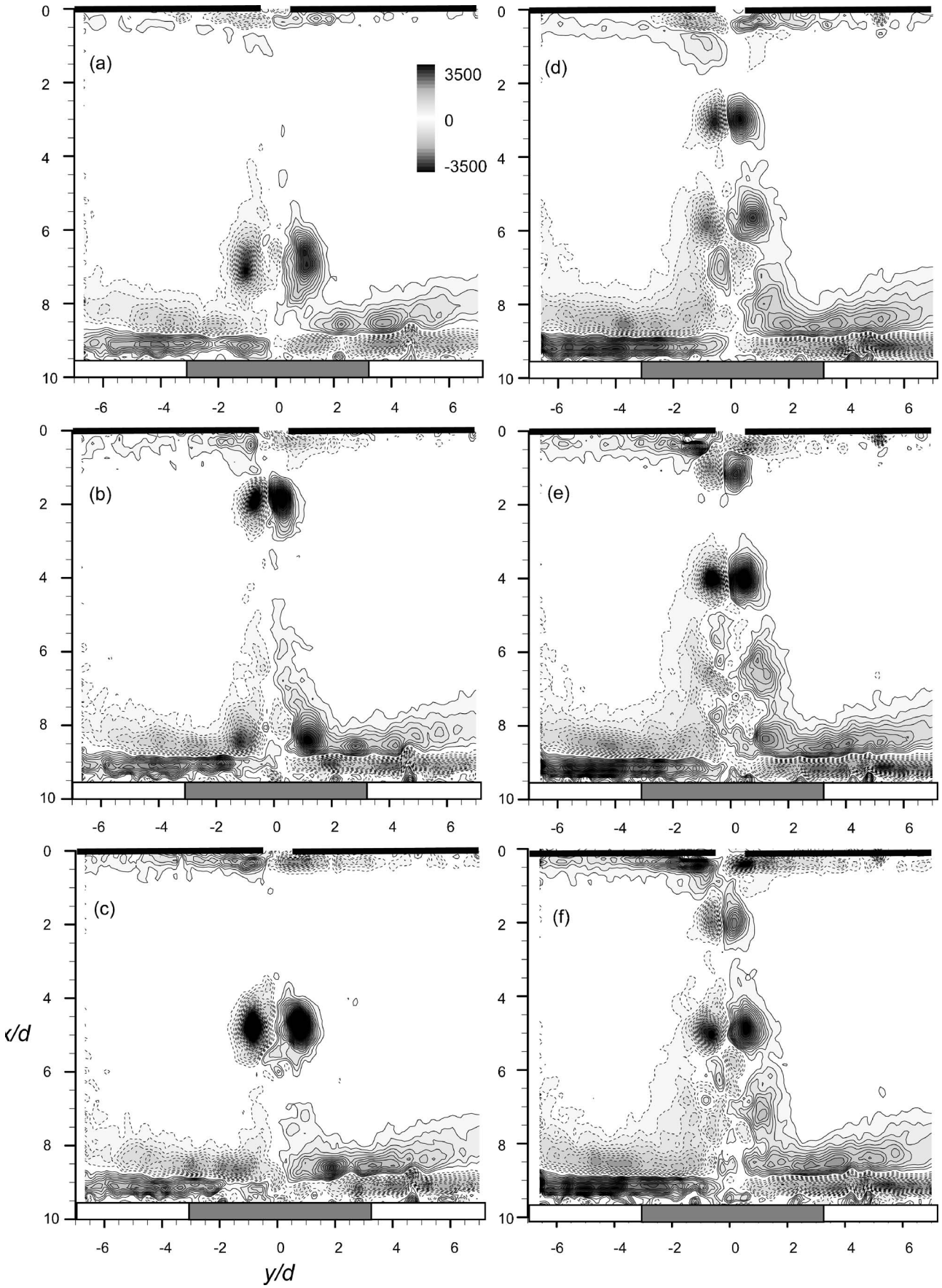

Fig. 9 Phase-averaged spanwise vorticity fields for f=420 Hz ((*a*)–(*c*)) and f=1200 ((*d*)–(*f*)). ϕ=0 deg ((*a*) and (*d*)), 120 deg ((*b*) and (*e*)), and 240 deg ((*c*) and (*f*)). Re_{U_0}=445 and H/d=9.5.

concentrations correspond to the shear layer of the vortex rings that are advected downstream and impinge on the surface of the heater. For the higher frequency jet (Figs. 8(*d*)–8(*f*)), the vorticity maps show that the vortex rings break up and form secondary structures before they hit the surface. This occurs at $x/d=4$ for the weakest jet at 1200 Hz (Fig. 8(*d*)) and is delayed until farther downstream for the higher Reynolds number jets (Figs. 8(*e*) and 8(*f*)). However, the smaller structures that result from the breakup of vortex rings are clearly visible in all three cases. The vortex ring breakup and formation of secondary structures are responsible for the decrease in the streamwise velocity at the center of the flow, which was observed in Figs. 7(*d*)–7(*f*) at $x/d=7.7$. Clearly, the heat removal mechanisms are different for the two frequencies. When the synthetic jet is driven at the low operating frequency, the vortex rings impinge on the surface individually; thus, these large-scale coherent structures are responsible for the enhanced heat removal (compared to continuous jet). At the high operating frequency, the vortex rings merge and break into smaller secondary structures before reaching the surface; hence, the heat removal is enhanced by mixing of smaller scale structures.

To further explore the flow field of the impinging synthetic jets and the formation of the coherent structures at both operating frequencies, phase-locked velocity fields were measured. The phase-locked spanwise vorticity contour maps of the jet for $H/d=9.5$ are presented in Figs. 9(*a*)–9(*f*) (for $f=420$ and 1200 Hz, respectively, at three phases along the actuation cycle). Both jets have the same Reynolds number of 445, which, at this H/d, results in a similar heat transfer enhancement of ~70% (Fig. 3).

For the 420 Hz synthetic jet, at the beginning of the blowing portion of the cycle ($\phi=0$ deg, Fig. 9(*a*)) a vortex ring is starting to emerge from the orifice, while the vortex ring from the previous cycle is located at $x/d=7.2$. Also, vortex rings formed in preceding cycles that already impinged on the surface and broke into smaller vortices are clearly visible. As the cycle continues ($\phi=120$ and 240 deg, Figs. 9(*b*) and 9(*c*), respectively), the vortex ring, formed at the edge of the orifice, moves downstream toward the impingement surface, such that near the end of the blowing cycle ($\phi=120$ deg, Fig. 9(*b*)) the vortex ring is at $x/d=2$. During this time, the previous vortex ring impinges on the surface and breaks up into smaller vortex rings that roll outward along the surface into the wall jet region.

The phase-locked vorticity field at the higher formation frequency, ($f=1200$ Hz, Figs. 9(*d*)–9(*f*)) exhibits a notably different behavior. Here, the vortex ring that is formed at the edge of the orifice moves downstream (Figs. 9(*d*) and 9(*e*)), and it is located at $x/d=1.1$ at $\phi=120$ deg (Fig. 9(*b*)). Note that the vortex ring for the lower frequency jet is located at $x/d=2$ at $\phi=120$ deg (Fig. 9(*b*)) due to the larger wavelength. Furthermore, while at the lower formation frequency the vortex rings impact the surface individually, at the higher formation frequency vortex rings merge and break into smaller vortical structures with opposite sense *before* they impinge on the surface.

The different formation and advection of the coherent structures shown in Fig. 9 can explain the effect of the formation frequency on the synthetic jet cooling at other H/d, as illustrated in Fig. 3 above. When the high frequency jet is used, it is more effective at small H/d because of accumulation of vortices that impact the surface as they gain strength and break into smaller structures. At large H/d the vortex rings merge, lose their coherence, and breakdown into a quasi-steady jet (see Smith and Glezer [18]), thus the additional heat removal capabilities due to the enhanced mixing by the coherent structures are reduced. The low frequency jet is more effective at large H/d, due to the larger wavelength that results in merging of the vortices (similar to the high frequency jet at low H/d), while at low H/d, each vortex ring impinges on the surface individually, which is not as effective.

The mechanisms associated with the enhanced heat removal at the two operating frequencies were also examined by comparing the turbulent quantities. Figures 10(*a*)–10(*d*) show the three turbulent quantities at Reynolds number of 445, with operating frequencies of 420 and 1200 Hz, respectively. The contour plots of the normalized streamwise normal stress, u'^2/U_0^2, at operating frequencies of 420 and 1200 Hz and $H/d=9.5$ are presented in Figs. 10(*a*) and 10(*c*), respectively. At the low operating frequency ($f=420$ Hz, Fig. 10(*a*)) there is high concentration of u'^2/U_0^2 along two cross-stream regions (one on each side of the centerline at $y/d=\pm1$), corresponding to the shear layers of the vortex ring, where the highest concentration is slightly above the surface at $x/d\approx8.5$.

At the higher operating frequency ($f=1200$ Hz, Fig. 10(*c*)) there are two distinct peaks in the cross-stream distribution only near the orifice (at $x/d\approx1$). Farther downstream, the double peak distribution becomes a single peak distribution due to the merging of vortex rings that break into smaller structures, as was shown in Fig. 9. At this operating frequency, the highest streamwise normal stress values are concentrated in a narrow region (at $y/d=\pm0.5$) right above the point of impingement, while at the 420 Hz case, the highest normal stresses are concentrated in two regions. This, again, supports our previous conclusion that if the vortex rings do not merge (as in the 420 Hz case), the heat removal is associated with large-scale mixing, while merging of vortex rings (which accelerates their breakdown into smaller less coherent vortices, as in the 1200 Hz case) results in a smaller-scale mixing. This can explain the similar heat removal enhancement of the low and high frequency jets at this height (see Fig. 3), as the 420 Hz jet has lower streamwise mixing that covers a larger area of the heater, while the 1200 Hz jet has higher streamwise mixing that covers a smaller portion of the heater.

Figures 10(*b*) and 10(*d*) show the normalized cross-stream normal stress, v'^2/U_0^2, for the lower and higher frequency jets, respectively. Figure 10(*b*) illustrates that there is no double peak in the distribution of the cross-stream normal stress, where the highest values appear to be right above the impingement surface. The distribution of the cross-stream normal stress for a synthetic jet with an operating frequency of 1200 Hz (Fig. 10(*d*)) is a similar to that of the 420 Hz case. However, the highest magnitude of the normal stresses expands along a larger streamwise region (from x/d of about 4.5 to the impingement surface), and throughout the flow the magnitudes of v'^2/U_0^2 are larger for the higher frequency case.

4 Conclusions

The efficiency of synthetic jet impingement cooling and the mechanisms associated with the removal of heat from a constant heat flux surface were investigated experimentally using thermocouples and particle image velocimetry. The effects of jet formation frequency and Reynolds number at different nozzle-to-surface distances were investigated and compared to continuous impingement jet cooling.

In the experiments, the synthetic jet was operated at two separate frequencies, 420 and 1200 Hz, which were found to be the most effective (for the Reynolds number range used) in terms of the heat removal improvement. The jet parameters that were varied in the experiments include $140<\mathrm{Re}_{U_0}<740$, $1.9<H/d<38.1$, and $0.18<\mathrm{St}<2.17$.

It was found that synthetic jet cooling presents a very efficient means of heat removal from the surface and is up to three times better than continuous jet cooling at the same Reynolds numbers. This is attributed to the coherent vortex rings that are formed by the synthetic jet, which enhance the mixing and thus the heat removal from the surface. For small distances between the synthetic jet and the heated surface, the high formation frequency ($f=1200$ Hz) synthetic jet removes heat better than the low frequency ($f=420$ Hz) jet, whereas the low frequency jet is more effective at larger distances.

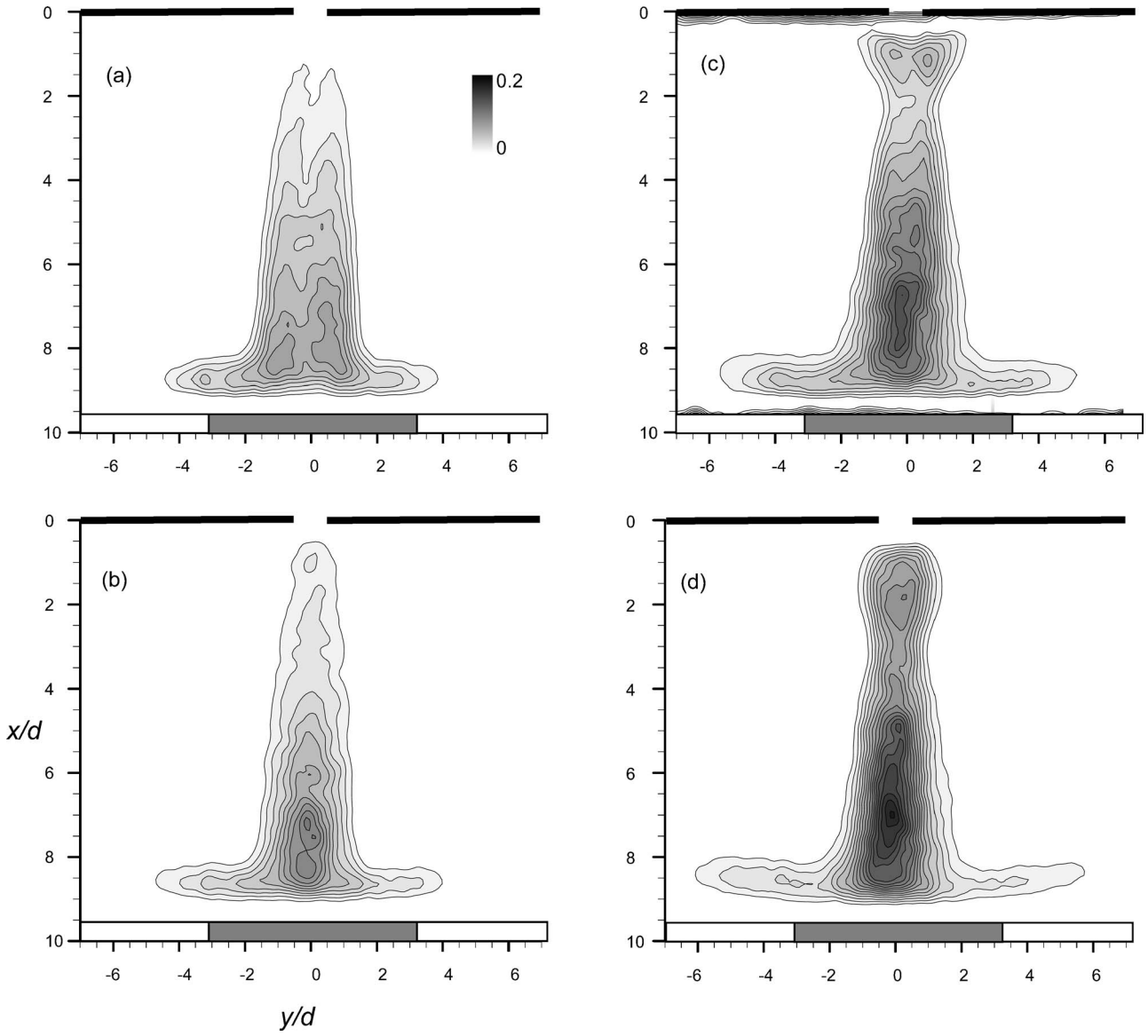

Fig. 10 Contour maps of time-averaged u'^2/U_0^2 ((*a*) and (*c*)) and v'^2/U_0^2 ((*b*) and (*d*)) for $f=420$ Hz ((*a*) and (*b*)) and $f=1200$ ((*c*) and (*d*)). $\mathrm{Re}_{U_0}=445$ and $H/d=9.5$

PIV measurements of the synthetic jet velocity fields were conducted in order to understand the different flow mechanisms associated with heat removal from the surface by synthetic jets at the two operating frequencies. The data indicate at small distances between the synthetic jet and the heated surface, the higher formation frequency jet is associated with accumulation of vortex rings and breakup to smaller structures before they impinge on the surface. When the lower frequency jet is used, the wavelength between coherent structures is larger, and each vortex ring impinges on the surface separately.

Acknowledgment

This work was supported by internal funding provided by Rensselaer Polytechnic Institute. The help of Nolin Borrero in the design and fabrication of the experimental facility is greatly appreciated.

Nomenclature

A_h = area of the heater
D = diameter of the heater
d = jet's orifice diameter
f = jet's formation frequency
g = acceleration due to gravity
Gr = Grashof number, $\mathrm{Gr}=g\beta(T_w-T_\infty)D^3/\nu^2$
H = distance between jet's orifice and heated surface
h = convection heat transfer coefficient, $h=Q/A_h(T_w-T_\infty)$
k = thermal conductivity
Nu_s = stagnation Nusselt number, $\mathrm{Nu}_s=hD/k$
P = power
Q = power of the heater
Re_{U_0} = Reynolds number based on average orifice velocity, $\mathrm{Re}_{U_0}=U_0d/\nu$
Re_{U_p} = Reynolds number based on peak velocity, $\mathrm{Re}_{U_p}=U_pd/\nu$
St = Strouhal number, $\mathrm{St}=f\cdot d/U_0$,
T_w = temperature of the heated surface
T_∞ = ambient temperature
t = time

U = jet velocity in the x-direction
U_{av_0} = average velocity of the continuous jet at the orifice plane
U_{cl} = centerline velocity at the jet exit plane
U_0 = average orifice velocity, $U_0 = L_0/\tau$
U_p = peak orifice velocity
u'^2/U_0^2 = normalized streamwise normal stress
V = jet velocity in the y-direction
ν'^2/U_0^2 = normalized cross-stream normal stress
x = jet's streamwise direction
y = jet's cross-stream direction

Greek Symbols

β = coefficient of thermal expansion
Δ = change in
ϕ = phase along the cycle (deg)
τ = cycle period in sec $\tau = 1/f$

Subscripts

j = jet
h = heater
f = free convection
0 = orifice
∞ = ambient

References

[1] Electronics Cooling Magazine, January 2005.
[2] Martin, H., 1977, "Heat and Mass Transfer between Impinging Gas Jets and Solid Surfaces," Adv. Heat Transfer, **13**, pp. 1–60.
[3] Nevins, R. G., and Ball, H. D., 1961, "Heat Transfer Between a Flat Plate and a Pulsating Impinging Jet," *Proc. of the National Heat Transfer Conference*, Boulder, CO, Vol. 60, pp. 510–516.
[4] Kataoka, K., Suguro, M., Degawa, H., Maruo, K., and Mihata, I., 1987, "The Effect of Surface Renewal Due to Large-Scale Eddies on Jet impingement Heat Transfer," Int. J. Heat Mass Transfer, **30**, pp. 559–567.
[5] Eibeck, P. A., Keller, J. O., Bramlette, T. T., and Sailor, D. J., 1993, "Pulse Combustion: Impinging Jet Heat Transfer Enhancement," Combust. Sci. Technol., **94**, pp. 147–165.
[6] Zumbrunnen, D. A., and Aziz, M., 1993, "Convective Heat Transfer Enhancement Due to Intermittency in an Impinging," ASME J. Heat Transfer, **115**, pp. 91–97.
[7] Sailor, D. J., Rohli, D. J., and Fu, Q., 1999, "Effect of Variable Duty Cycle Flow Pulsations on Heat Transfer Enhancement for an Impinging Air Jet," Int. J. Heat Fluid Flow, **20**, pp. 574–580.
[8] Zulkifli, R., Benard, E., Raghunathan, S., and Linton, A., 2004, "Effect of Pulse Jet Frequency on Impingement Heat Transfer," AIAA Paper No. 2004–1343.
[9] Hwang, S. D., Lee, C. H., and Cho, H. H., 2001, "Heat Transfer and Flow Structures in Axisymmetric Impinging Jet Controlled by Vortex Pairing," Int. J. Heat Fluid Flow, **22**, pp. 293–300.
[10] Hwang, S. D., and Cho, H. H., 2002, "Effects of Acoustic Excitation Positions on Heat Transfer and Flow in Axisymmetric Impinging Jet: Main Jet Excitation and Shear Layer Excitation," Int. J. Heat Fluid Flow, **24**, pp. 199–209.
[11] Chaniotis, A. K., Poulikakos, D., and Ventikos, Y., 2003, "Dual Pulsating Slot Jet Cooling of a Constant Flux Surface," ASME J. Heat Transfer, **125**, pp. 575–586.
[12] Haneda, Y., Tsuchiya, Y., Nakabe, K., and Suzuki, K., 1998, "Enhancement of Impinging Jet Heat Transfer by Making Use of Mechano-Fluid Interactive Flow Oscillation," Int. J. Heat Fluid Flow, **19**, pp. 115–124.
[13] Camci, C., and Herr, F., 2002, "Forced Convection Heat Transfer Enhancement Using a Self-Oscillating Impinging Planar Jet," ASME J. Heat Transfer, **124**, pp. 770–782.
[14] Vukasinovic, J., and Glezer, A., 2001, "An Active Radial Countercurrent Heat Sink," *Proceedings of IMECE 2001: 2001 International Mechanical Engineering Congress and Exposition*, EEP-6AI-2.
[15] Kercher, D. S., Lee, J.-B., Brand, O., Allen, M. G., and Glezer, A., 2003, "Microjet Cooling Devices for Thermal Management of Electronics," J. Chem. Theory Comput., **26**(2), pp. 359–366.
[16] Mahalingam, R., Rumigny, N., and Glezer, A., 2004, "Thermal Management Using Synthetic Jet Ejectors," J. Chem. Theory Comput., **27**(3), pp. 439–444.
[17] Incorpera, F. P., and DeWitt, D. P., 1996, *Fundamentals of Heat and Mass Transfer*, 4th ed., Wiley, New York, p. 171.
[18] Smith, B., and Glezer, A., 1998, "The Formation and Evolution of Synthetic Jets," Phys. Fluids, **31**, pp. 2281–2297.
[19] Kline, S. J., and McClintock, F. A., 1953, "Describing Uncertainties in Single Sample Experiments," Mech. Eng. (Am. Soc. Mech. Eng.), **75**, pp. 3–8.
[20] Smith, B. L., and Swift, G. W., 2001, "Synthetic Jets at Large Reynolds Numbers and Comparison to Continuous Jets," AIAA J. Paper No. 2001–3030.

Heat and Moisture Transport Through the Microclimate Air Annulus of the Clothing-Skin System Under Periodic Motion

K. Ghali
Department of Mechanical Engineering,
Beirut Arab University,
Beirut, Lebanon

N. Ghaddar[1]
ASME Fellow
e-mail: farah@aub.edu.lb

E. Jaroudi

Department of Mechanical Engineering,
American University of Beirut,
P.O. Box 11-0236,
Beirut 1107-2020, Lebanon

*The study is concerned with the heat and moisture transport in a ventilated fabric-skin system composed of a microclimate air annulus that separates an outer cylindrical fabric boundary and an inner oscillating cylinder representing human skin boundary for open and closed aperture settings at the ends of the cylindrical system. The cylinder ventilation model of Ghaddar et al. (2005, Int. J. Heat Mass Transfer, **48**(15), pp. 3151–3166) is modified to incorporate the heat and moisture transport from the skin when contact with fabric occurs at repetitive finite intervals during the motion cycle. During fabric skin contact, the heat and moisture transports are modeled based on the fabric dry and evaporative resistances at the localized touch regions at the top and bottom of points of the cylinder. Experiments were conducted to measure the mass transfer coefficient at the skin to the air annulus under periodic ventilation and to measure the sensible heat loss from the inner cylinder for the two cases of fabric-skin contact and no contact. The model predictions of time-averaged steady-periodic sensible heat loss agreed well with the experimentally measured values at different frequencies. The model results showed that the rate of heat loss increased with increased ventilation frequency at fixed (=amplitude/mean annular spacing). At amplitude factor of 1.4, the latent heat loss in the contact region increased by almost 40% compared to the loss at amplitude factor of 0.8 due to the increase in fabric temperature during contact. The sensible heat loss decreased slightly between 3% at $f=60$ rpm and 5% at $f=25$ rpm in the contact region due to higher air temperature and lack of heat loss by radiation when fabric and skin are in touch. The presence of an open aperture has a limited effect on increasing the total heat loss. For an open aperture system at amplitude factor of 1.4, the increase in heat loss over the closed apertures is 4.4%, 2.8%, and 2.2% at $f=25$, 40, and 60 rpm, respectively.* [DOI: 10.1115/1.2241811]

Keywords: ventilation of the micro-climate within clothing, modulated microclimate air layer annulus, steady periodic heat transfer in clothing, ventilation rates due to periodic motion of fabric

Introduction

The heat and moisture transport processes from the human skin are enhanced by the ventilating motion of air through the fabric initiated by the human relative motion with respect to the environment. The size of the air spacing between the skin and the fabric varies continuously in time depending on activity level and location, thus inducing variable airflow in and out of the fabric [1,2]. Microclimate ventilation refers to air exchange between clothing microclimate (air within the environment of the clothing assembly) and the ambient air. Herter et al. [3] reported that the microclimate ventilation rate was mainly influenced by the walking velocity with a relatively small effect of external wind at normal or rapid walking speeds. For the past two decades, the so-called pumping or bellows effect has been studied, and its importance on the heat and mass transfer of the human body has often been discussed [4–6]. In order to describe the dynamic behavior, Jones et al. [7,8] described a model of the transient response of clothing systems, which took into account the sorption behavior of fibers, but assumed local thermal equilibrium with the surrounding air. Ghali et al. [9,10] studied the effect of ventilation on heat and mass transport through a fibrous material and reported transport coefficients in a cotton fibrous medium. Ghali et al. [9] developed a thermal model and reported experimental data on sensible and latent heat transport initiated by sinusoidal motion of a fabric plane above a sweating isothermal hot plate placed in a controlled environment. Their model predicted the heat loss from the wet boundary and agreed fairly well with the experimentally measured values.

Periodic ventilation models of fibrous media of Ghali et al. [9,10] and Lotens [4] considered the impact of normal airflow. However, the Lotens model is based on empirical equations that restricted its use. The Ghali et al. [9] ventilation model is valid for normal airflow through the fabric, but is not applicable for parts of the body where parallel airflow to the fabric exists at the sleeve and neck openings. Ghaddar et al. [11] developed further the Ghali et al. ventilation model to account for the presence of open apertures using a locally governed Womersley flow in the direction parallel to the fabric [11,12].

In real application, three-dimensional motion of trapped air exists between the cylindrical shaped body parts and the surrounding clothing. Air motion takes place in the angular direction and hence reduces further the normal flow rate in and out of the fabric due to gap height asymmetry. Ghaddar et al. [1] developed from first

[1]Corresponding author.

Contributed by the Heat Transfer Division of ASME for publication in the JOURNAL OF HEAT TRANSFER. Manuscript received July 12, 2005; final manuscript received February 10, 2006. Review conducted by Raj M. Manglik. Paper presented at the 2005 ASME Heat Transfer Summer Conference (HT2005), July 15–22, 2005, San Francisco, California, USA.

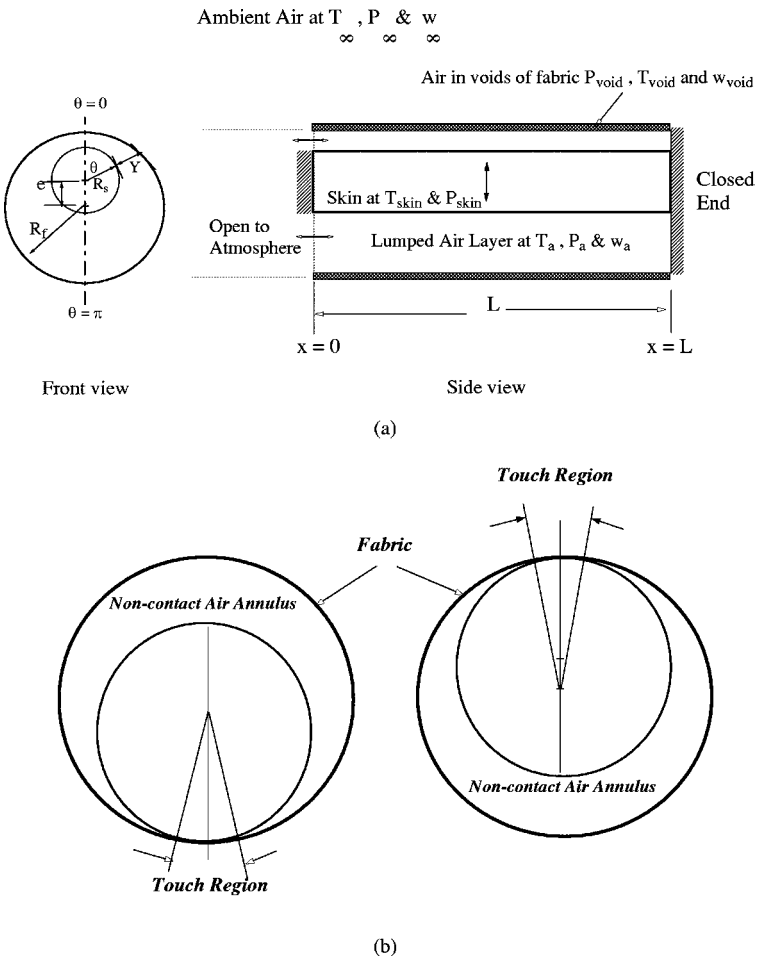

Fig. 1 Schematic of the physical domain of the fabric-air layer-skin system when (*a*) fabric does not touch the inner cylinder and (*b*) fabric is in contact with the inner cylinder at θ=0 deg and θ=180 deg

principles a realistic 3-D model that can be used to predict air exchange rates within the internal air layer of a walking human at any speed in a loose-fitting one-layer ensemble with the clothing apertures open and closed. The model predicted the ventilation radial airflow through the fabric, the angular airflow and the axial airflow induced by the motion of the inner cylinder, and the losses associated with the presence of an opening to the atmosphere at one end of the annulus. The predicted ventilation flow rates agreed well with their experimental measurements of total renewal rates for closed and open aperture. The agreement improved at higher frequencies of ventilation [1].

The objective of the current work is to extend the cylinder model of Ghaddar et al. [1] of ventilated fabric-skin system to simulate the periodic fabric-skin boundary contact during the motion cycle. The second objective of the work is to perform experiments to measure the film coefficients from an inner oscillating body cylinder to the trapped air layer and validate the predictions of sensible heat losses of the ventilation model for the two cases when fabric is in contact with the skin surface and when no contact is present. The third objective is to perform a parametric study to predict sensible and latent heat losses from the system by ventilation at different frequencies, amplitudes of motion, and aperture setting.

Model Mathematical Formulation

Figure 1(*a*) depicts the schematic of the physical domain of a cylindrical air-layer-fabric system where an enclosed incompressible air layer annulus of length L and thickness Y separates the fabric boundary and the human skin. The skin inner boundary moves in a sinusoidal up and down motion, inducing air movement through the fabric. One end of the air layer physical domain at $x=0$ is open to ambient air, resembling the presence of a clothing open aperture, and the other end at $x=L$ is impermeable to flow (closed). The radial airflow is induced through the fabric material by the pressure difference between the internal air layer pressure and that of the environment. The airflow in the angular direction is driven by the pressure differential due to variation of the internal air gap length $Y(\theta,t)$. The airflow in the axial direction is driven by the pressure differential due to the presence of the opening [1]. The angular flow is modeled as a flow between eccentric cylinders, where the flow in the narrow gap between the fixed outer cylinder (fabric) of radius R_f and a slightly smaller, off-set, inner cylinder (skin) of radius R_s is moving up and down in sinusoidal motion. The mean spacing between the cylinders is $Y_m(=R_f-R_s)$ and the amplitude of oscillation is ΔY. A dimensionless amplitude parameter ζ is defined as

$$\zeta = \frac{\Delta Y}{Y_m} \tag{1}$$

The eccentricity e_c of the cylinders is time dependent and relates to the oscillation frequency ω and amplitude ΔY by

$$e_c = \Delta Y \sin(\omega t) \quad \text{when no skin-fabric contact is present} \tag{2a}$$

$$e_c = Y_m \quad \text{during skin fabric contact} \tag{2b}$$

Some elementary geometry shows that the width of the gap width Y between the two circular cylinders can be approximated by

$$Y(\theta,t) = Y_m - \Delta Y \sin(\omega t)\cos(\theta) \tag{3a}$$

when no skin-fabric contact is present

$$Y(\theta,t) = Y_m[1-\cos(\theta)] \quad \text{during skin-fabric contact} \tag{3b}$$

When the amplitude ratio is smaller than unity ($\zeta<1$), no skin fabric contact is present during the motion, while contact is locally present when the amplitude ratio is greater than or equal to unity ($\zeta\geq 1$). The sinusoidal motion is an approximate model of the periodic change of air spacing layer thickness for a walking person. Human gait analysis shows repeated periodic pattern of limbs motion as a function of walking speed that can be represented by a sinusoidal pattern [13]. The frequency of the oscillating motion of the fabric is generally proportional to the activity level of the walking human.

While walking, the clothed parts of the body such as arms or trunks with no openings at the sleeve or neck (closed apertures clothing) lose heat and moisture by ventilation of air through radial flow through the fabric and angular flow convection to the skin and fabric. The induced flow in the angular direction exhibits periodic motion due to the periodic change in the annulus thickness. The formulation of the periodic micro-climate ventilation problem is solved using the 3-D cylinder model of Ghaddar et al. [1] in the presence of an open aperture for amplitudes of motion $\Delta Y<Y_m(\zeta<1)$. The ventilation model of the microclimate air layer takes into account the flow inertia in the angular direction due to the periodic motion and flow reversal during the walking cycle. For amplitude $\Delta Y\geq Y_m$, the ventilation model [1] requires additional modifications to incorporate the region of contact. In this section the microclimate ventilation mass and energy balances are presented for the periodic motion effect of the cylindrical geometry when $\zeta<1$.

Microclimate Air Annulus Mass and Heat Transport Model ($\zeta<1$). The angular flow in the annulus exhibits periodic motion due to the periodic change of the gap angular thickness within the motion cycle. The radial airflow passing through the fabric layer during ventilation has also an obvious effect on the heat and mass transport from the skin. A general air layer mass balance performed on an element of height Y and thickness $R_f d\theta$ is given by

$$\frac{\partial(\rho_a Y)}{\partial t} = -\dot{m}_{ay} - \frac{\partial(Y\dot{m}_{ax})}{\partial x} - \frac{\partial(Y\dot{m}_{a\theta})}{R_f\,\partial\theta} \tag{4a}$$

$$\dot{m}_{a\theta}(x,\theta=0,t) = 0 \tag{4b}$$

$$\dot{m}_{a\theta}(x,\theta=\pi,t) = 0 \tag{4c}$$

$$\dot{m}_{ax}(x=0,\theta,t) = C_D\left(\frac{2\rho_a}{|P_L-P_\infty|}\right)^{1/2}[P_\infty - P_L] \tag{4d}$$

$$\dot{m}_{ax}(x=L,\theta,t) = 0 \tag{4e}$$

where $\dot{m}_{a\theta}$ is the mass flux in the angular direction, $\dot{m}_{ax}$ is the mass flux in the axial direction, and $\dot{m}_{ay}$ is the radial airflow rate. Equation (4*e*) is derived from the pressure drop at the opening by applying Bernoulli's equation from P_∞ in the far environment ($x\rightarrow-\infty$) to the opening at $x=0$, and C_D is the discharge loss coefficient at the aperture of the domain dependent on the discharge area ratio of the aperture to the air layer thickness Y. The flow rate in the radial direction is governed by the pressure differential across the fabric and is dependent on the fabric permeability [2]. The permeability is affected by the type of yarn, tightness of twist in yarns, yarn count, and fabric structure. The analysis of the airflow through the fabric boundary of the physical domain is based on the single lumped fabric layer of the three-node adsorption model described in detail by Ghali et al. [10] and will not be repeated here. The modified fabric internal transport coefficients of Ghaddar et al. [11] are used in this work. The mass flow rate in the θ direction is solved in terms of the driving pressure gradient using 1-D Womersley flow model [1]. The Womersley flow model has simplified the analysis by assuming quasi-parallel flow in the angular direction within the annulus [1]. The microclimate ventilation model details can be found in Ref. [1], where the mass conservation equation for the air layer is transformed into a pressure equation that can be solved for the pressure distribution $P(x,\theta,t)$ in the system while lumping the air layer of thickness Y in the radial direction.

Once the pressure and mass flow rates of the air layer are determined, the water vapor mass balance is performed. The radial airflow through the fabric depends on the air layer pressure compared to the environment pressure. The air from the environment will pass through the fabric void at $\dot{m}_{ay}$ into the air layer when the pressure in the air layer is $P_a<P_\infty$ and the air in the air layer will pass at $\dot{m}_{ay}$ through the fabric void space to the environment when $P_a\geq P_\infty$. The airflow into the air spacing layer coming from the air void node of the fabric will have the same humidity ratio as the air in the void space of the fabric while the airflow out of the air layer into the fabric void will carry the same humidity of the air layer. The water vapor mass balance for the air spacing layer is given by

$$\begin{aligned}\frac{\partial(\rho_a Y w_a)}{\partial t} &= h_{m(\text{skin-air})}(P_{sk}-P_a) - \dot{m}_{ay}w_p - \frac{\partial(Y\dot{m}_{ax}w_a)}{\partial x} \\ &\quad - \frac{\partial(Y\dot{m}_{a\theta}w_a)}{R_f\,\partial\theta} + D\frac{\rho_a(w_{\text{void}}-w_a)}{t_f/2} + \frac{D}{R_f^2}\frac{\partial}{\partial\theta}\left(Y\frac{\partial w_a}{\partial\theta}\right) \\ &\quad + DY\frac{\partial^2 w_a}{\partial x^2} + h_{m(o\text{-air})}(P_o-P_a)\end{aligned}$$

$$\text{where } w_p = \begin{cases} w_{\text{void}} & P_a(x,\theta,t) < P_\infty \\ w_a & P_a(x,\theta,t) \geq P_\infty \end{cases} \tag{5}$$

where $h_{m(\text{skin-air})}$ is the mass transfer coefficient between the skin and the air layer, which will be experimentally determined as will be explained in Sec. 4.1 of this paper, P_a is the water vapor pressure in the air layer, w_a is the humidity ratio of the air layer, P_{sk} is the vapor pressure at the skin solid boundary, w_{void} is the humidity ratio of the air void, e_f is the fabric thickness, and D is the diffusion coefficient of water vapor in air. The terms on the right-hand side of Eqs. (5) are explained as follows: the first term represents the mass transfer from the skin to the trapped air layer; the second term is the convective mass flow passing through the fabric voids, the third and fourth terms represent the net flux in the axial and angular directions, the fifth term is the vapor diffusion from the void space, the sixth and seventh terms represent the vapor diffusion in angular and axial directions, respectively, and the last term is the water vapor convective term from the air layer to the fabric outer node.

An energy balance on the air layer expresses the rate of change of the air-vapor mixture energy in the air layer in terms of (1) the external work done by the environment on the air layer, (2) the evaporative heat transfer from the moist skin, (3) the dry convective heat transfer from the skin, (4) the heat flow to or from the air layer associated with $\dot{m}_{ay}$, $\dot{m}_{a\theta}$, and $\dot{m}_{ax}$, (5) the heat diffusion from void air of the thin fabric to the air layer, and (6) the angular conduction and water vapor diffusion in the air layer. The energy balance of the air layer is given by

$$\frac{\partial}{\partial t}[\rho_a Y(C_v T_a + w_a h_{fg})] + P_a \frac{\partial Y}{\partial t}$$
$$= h_{m(\text{skin-air})} h_{fg}(P_{sk} - P_a) + h_{c(\text{skin-air})}(T_{sk} - T_a) - \dot{m}_{ay} H_p$$
$$- \frac{\partial Y[\dot{m}_{ax}(C_p T_a + w_a h_{fg})]}{\partial x} - \frac{\partial[Y\dot{m}_{a\theta}(C_p T_a + w_a h_{fg})]}{R_f \partial \theta}$$
$$+ \frac{Dh_{fg}}{R_f^2}\frac{\partial}{\partial \theta}\left(Y\frac{\partial w_a}{\partial \theta}\right) + Dh_{fg} Y\frac{\partial^2 w_a}{\partial x^2} + h_{m(o\text{-air})} h_{fg}(P_o - P_a)$$
$$+ \frac{k_a}{R_f^2}\frac{\partial}{\partial \theta}\left(Y\frac{\partial T_a}{\partial \theta}\right) + k_a Y\frac{\partial^2 T_a}{\partial x^2} + h_{c(o\text{-air})}(T_o - T_a)$$
$$+ k_a\frac{(T_{void} - T_a)}{e_f/2} + Dh_{fg}\frac{\rho_a(w_{\text{void}} - w_a)}{e_f/2} \tag{6a}$$

where H_p is the enthalpy of airflow into or from the air layer defined by

$$H_p = \begin{matrix} C_p T_{\text{void}} + w_{\text{void}} h_{fg} & P_a(x,\theta,t) < P_\infty \\ C_p T_a + w_a h_{fg} & P_a(x,\theta,t) \geq P_\infty \end{matrix} \tag{6b}$$

where $h_{c(o\text{-air})}$ is the convection coefficient from the fabric to air, and $h_{m(o\text{-air})}$ is the mass transport coefficient from the fabric to air, and k_a is the thermal conductivity of air. Since the fabric void thickness is very small, conduction of heat from the fabric void air to the trapped air layer follows the law of the wall as given in the last two terms of Eq. (6*a*). The inner cylinder skin condition can be specified at either constant skin temperature and humidity ratio (P_{sk} and T_{sk} are known), or constant flux condition at the surface. The fabric void air, outer node, and inner node mass, and energy balances can similarly be derived as found in the work of Ghali et al. [10].

Heat Transport during Fabric-Skin Contact ($\zeta > 1$). It is assumed that when the fabric cylinder is in contact with the solid cylinder (skin) at the top ($\theta = 0$ deg) or the bottom ($\theta = 180$ deg), both the fabric and the skin remain in touch at zero velocity for an interval of time until the reversal in motion takes place. The contact is not a point contact and is represented by a length of contact l_c of the fabric spanning about 10 deg around the cylinder surface at ($\theta = 0$ deg) or ($\theta = 180$ deg) due to flattening that takes place in the fabric at the contact area as observed in the experiments. The dimensionless air layer thickness Y' is defined as

$$Y' = \frac{Y(t)}{Y_m} = [1 - \zeta \sin(\omega t)] \tag{7}$$

If $Y' < 0$, then Y' is taken as zero for the contact interval within the cycle. During touch period Y' is frozen to the value of Y' at the time when touch starts in the motion cycle. As the fabric approaches the skin boundary, the radial ventilation flow rate decreases to a point where diffusion mechanism dominates the transport of heat and moisture [11]. The fabric three-node model of Ghali et al. [9] is used with the modified internal fabric transport coefficients of Ghaddar et al. [11] to model the heat and moisture transport by diffusion.

The modeling will cover two regions. The first region is the fabric-skin contact and the second region is a noncontact air layer region that separates the fabric from the skin as shown in Fig. 1(*b*). When contact takes place and through the duration of contact, the heat and mass transport problem in the fabric contact region I is solved as a transient diffusion problem of a thin fabric with one surface is suddenly exposed to a step change in temperature. The contact takes place at the skin with both the fabric outer node and the air void temperatures are at a lower temperature than the skin surface. The weighted fabric temperature and fabric total regain are defined, respectively as

$$T_f = \frac{(1-\varepsilon_f)\rho_s C_s[\gamma T_o + (1-\gamma)T_i] + \varepsilon_f \rho_a C_a T_{\text{void}}}{(1-\varepsilon_f)\rho_s C_s + \varepsilon_f \rho_a C_a} \tag{8a}$$

$$R = \gamma R_o + (1-\gamma) R_i \tag{8b}$$

where ε_f is the fabric porosity, γ is the mass fraction of the fabric in the outer node, T_i is the fabric inner node temperature, T_o is the fabric outer node temperature, T_{void} is the temperature of the air void space in the fabric, R_i is the fabric inner node regain, and R_o is the fabric outer node regain. The lumping of the fabric inner, outer, and void nodes into one fabric node has permitted the use of the experimentally established properties of the fabric dry and evaporative resistances to estimate the heat and moisture diffusion during the touch period [1]. The mass and energy balances of the lumped fabric in the contact region yield

$$\frac{\partial R}{\partial t} = \frac{1}{\rho_f e_f} * \left[\frac{(P_{sk} - P_f)}{(R_E/2) * h_{fg}} + \frac{(P_\infty - P_f)}{(R_E/2) * h_{fg} + 1/h_{m(f\text{-}\infty)}} + D_a\left(\frac{1}{R_f^2}\frac{\partial^2 R}{\partial \theta^2} + \frac{\partial^2 R}{\partial x^2}\right)\right] \tag{9}$$

$$\frac{\partial T_f}{\partial t} = \frac{\partial R}{\partial t} * \frac{h_{ad}}{C_{pf}} + \frac{1}{\rho_f e_f C_{pf}} * \left[\frac{(T_{sk} - T_f)}{R_D/2} + \frac{(T_{\text{aim}} - T_{\text{fabric}})}{R_D/2 + 1/(h_r + h_{c(f\text{-}\infty)})} + k_a\left(\frac{1}{R_f^2}\frac{\partial^2 T_f}{\partial \theta^2} + \frac{\partial^2 T_f}{\partial x^2}\right)\right] \tag{10}$$

where R is the fabric regain (kg of H_2O/kg of fabric), R_D is the fabric dry resistance, which is equal to 0.029 $m^2 \cdot K/W$ for cotton fabric, R_E is the fabric evaporative resistance equal to 0.0055 $m^2 \cdot kPa/W$ for cotton fabric, and $h_{c(f\text{-}\infty)}$ and $h_{m(f\text{-}\infty)}$ are the external heat and mass transfer coefficients with the environment, respectively. The value of $h_{c(f\text{-}\infty)}$ is taken as 4 $W/m^2 \cdot K$ [2], while $h_{m(f\text{-}\infty)}$ is derived from Lewis relation for air-water vapor mixtures as $h_{c(f\text{-}\infty)} = h_{m(f\text{-}\infty)} h_{fg}/16.5$ [1]. When the fabric departs from the skin boundary after contact, the fabric inner node, outer node, and void space will be in thermal and mass concentration equilibrium at T_f and R, respectively.

In the noncontact air layer region the mass and energy balances are modeled as follows:

$$\frac{\partial}{\partial t}(\rho_a Y w_a) = h_{m(\text{skin-air})}(P_{sk} - P_a) + h_{m(o\text{-air})}(P_o - P_a) + \frac{D}{R_f^2}\frac{\partial}{\partial \theta}\left(Y\frac{\partial w_a}{\partial \theta}\right) + DY\frac{\partial^2 w_a}{\partial x^2} \tag{11a}$$

$$\frac{\partial}{\partial t}[\rho_a Y(C_a T_a + h_{fg} w_a)] = h_{c(\text{skin-air})}(T_{sk} - T_a) + h_{c(o\text{-air})}(T_o - T_a) + h_{m(\text{skin-air})} h_{fg}(P_{sk} - P_a) + h_{m(o\text{-air})} h_{fg}(P_o - P_a) + k_a\frac{T_{\text{void}} - T_a}{e_f/2} + Dh_{fg}\frac{P_{\text{void}} - P_a}{e_f/2} + \frac{k_a}{R_f^2}\frac{\partial}{\partial \theta}\left(Y\frac{\partial T_a}{\partial \theta}\right) + h_{fg}\frac{D}{R_f^2}\frac{\partial}{\partial \theta}\left(Y\frac{\partial w_a}{\partial \theta}\right) + k_a Y\frac{\partial^2 T_a}{\partial x^2} + h_{fg} DY\frac{\partial^2 w_a}{\partial x^2} \tag{11b}$$

The terms that appear in the energy balance include convective energy transport to the fabric outer node by heat and mass diffusion from the fabric void space, and diffusion of heat and moisture in angular and axial directions of the air layer. The energy balances on outer nodes and inner nodes of the fabric remain the same as previously reported in the modified fabric three-node model of Ghali et al. [10]. The heat and moisture transport is

assumed to occur by diffusion in the fabric air void connecting the fabric nodes in touch with the skin and fabric nodes not in contact with skin. During the contact interval, the sensible heat loss q_s and latent heat losses q_L from the skin are given in the touch and the nontouch regions, respectively, by

$$\text{contact region} \quad q_s = \frac{T_{sk} - T_f}{R_D/2} \tag{12a}$$

$$q_L = \frac{P_{sk} - P_f}{R_E h_{fg}/2} h_{fg} \tag{12b}$$

noncontact air layer region

$$q_s = h_{c(\text{skin-air})}(T_{sk} - T_a) + h_r(T_{sk} - T_o) \tag{13a}$$

$$q_l = h_{m(\text{skin-air})} h_{fg}(P_{sk} - P_a) \tag{13b}$$

The modeled cotton fabric has an effective thermal conductivity of 0.042 $\text{W/m}\cdot\text{K}$ and thickness of 1 mm. The Biot number is equal to 0.095 at a convection coefficient of 4 $\text{W/m}^2\cdot\text{K}$ that justifies the use of a lumped approach as was also used by other researchers [14,15]. The contact model assumes that no wicking is present.

Numerical Procedure

The control volume methodology is used to divide the air layer into grids of size Δx, $R_f \Delta\theta$, and height $Y(\theta,t)$. Each grid volume contains a lumped adsorption system of fibrous inner and outer nodes and air void as the upper boundary [1]. The discrete model for the air mass balance of Eq. (4) and the incorporation of boundary conditions are given in detail in Ref. [1] and will not be repeated here. The numerical solution of the air annulus mass balance model equations will result in predicting the internal pressure at all grids of the domain. The air mass flow rates in the radial, angular, and axial directions are determined from the solution of the pressure equation. The temporal and spatial pressure distribution and determined airflow rates are used as direct input to the water vapor mass balance and the energy balance of the air layer, and of the fabric nodes and void space. These equations are integrated numerically using the first-order Euler-Forward scheme in time and control volume methodology in space with central differencing for the second-order angular derivatives. The solution was started from the initial thermal conditions of ambient air and of a fabric in thermal equilibrium with the surroundings. The vapor pressure of the flowing air in the air layer annulus or in the fabric voids is related to the air relative humidity, RH, and temperature and is calculated using the psychometric formulas of Hyland and Wexler [16] to predict the saturation water-vapor pressure and hence the vapor pressure at the specified relative humidity. The regain R of the cotton material has a definite relation to the relative humidity of the water vapor through a property curve of regain versus relative humidity [17].

The numerical model predicts the values of temperature and humidity ratio of the air annulus, the fabric inner and outer nodes, and the void node as a function of time and angular position. The mean steady periodic time and space-averaged values of the mass flow rates are also calculated. The net ventilation rate (inflow/outflow) of the microclimate air layer through the open aperture during one period of motion is defined by

$$\overline{\dot{m}_o} = \frac{2}{\tau\pi} \int_0^{\pi/2} \int_{-\pi/2}^{\pi/2} \dot{m}_o \, d\theta \, dt \quad \text{kg/s}\cdot\text{m}^2 \tag{14}$$

The total ventilation rate is the sum of the aperture ventilation rate and the radial ventilation rate through the fabric. The instantaneous sensible and latent heat losses from the inner cylinder are calculated. When a steady periodic solution is attained for temperature and humidity, time-space-averaged heat losses are calculated for the system over the oscillation cycle.

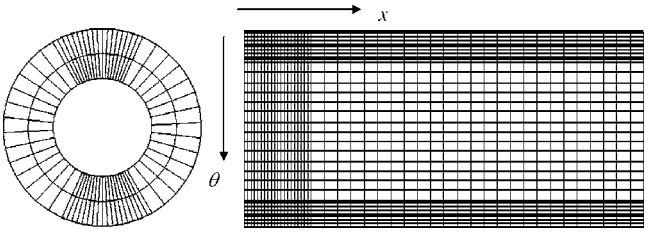

Fig. 2 The computational grid

Numerical Accuracy and Stability. Numerical tests were performed to assure a grid-independent, stable, and accurate solution for a domain of length $L=50$ cm, $R_f=7.56$ cm, $R_s=3.75$ cm, $C_D=1$, $Y_m=38.1$ mm, and $\Delta Y=0.635$ mm at $f=25$ rpm using different mesh sizes to get a grid-independent solution in the angular and axial directions. A nonuniform grid is used with the finer mesh implemented in the fabric touch region and near the opening as shown in Fig. 2. The size of the time step was taken at 0.005 and 0.001 s dictated by the period of oscillation of 2.4 s over a total integration time of 3600 s. The time step and the grid size are dictated by the second-order diffusion term.

Experimental Methodology and Validation of Model

Estimation of the Film Coefficients. The film coefficients at the skin are needed for the model simulation. Transport coefficients from skin to environment or clothing were reported in literature as a function of an effective wind velocity based on empirical work [5,18,19]. Such correlation would not be applicable for estimating the film coefficients in an enclosed air subject to an oscillatory flow. Ghaddar et al. [20] have empirically derived correlations of the evaporative and dry convective heat transport coefficients from the skin to the lumped air layer as a function of ventilation frequency for planar fabric motion of 1-D normal flow. No literature is present for cylindrical geometry on the value of the transport coefficients from the skin to the air annulus under periodic ventilation. For this reason, experiments were conducted to measure the mass transfer coefficient at the skin to the air layer and then using the Lewis relationship to estimate the heat transfer coefficient from the skin to the air layer.

Investigations were carried out in a climatic chamber where temperature and humidity were maintained at $T_\infty=24°\text{C}$ and RH $=50\%$, respectively. The precision in the set conditions of the climatic chamber temperature was $\pm 0.5°\text{C}$ and chamber relative humidity was $\pm 2\%$. Untreated cotton was chosen as a representative of a most common worn fabric to use in the ventilation tests. The cotton was obtained from Test Fabrics Inc. (Middlesex, NJ 08846) and is made of unmercerized cotton duck, style no. 466 of thickness of 1 mm.

Figure 3 shows a schematic of the experimental setup that consisted of (i) a hollow PVC inner cylinder (arm) 7.8 cm in diameter and 60 cm long; (ii) an outer 60 cm long cylinder (sleeve) of 13 cm diameter made of a thin metallic screen of 2 cm open squares where the cotton fabric was wrapped around and fitted; (iii) a power screw mechanism for up and down motion that includes two power screws, two sliders, two guides, electric dc motor, relays for reversing motor direction of rotation, and chain drive; (iv) support platform; and (v) flexible impermeable plastic membranes. The inner cylinder was connected to the sliders of the power screw mechanism where it was subjected to an up and down motion driven by the gear and chain mechanism connected to the dc motor. The dc motor rotational speed was controlled by a variable power supply to obtain different motion frequencies. The outer sleeve cylinder was fixed to the platform frame and was capped at both ends with a flexible impermeable plastic mem-

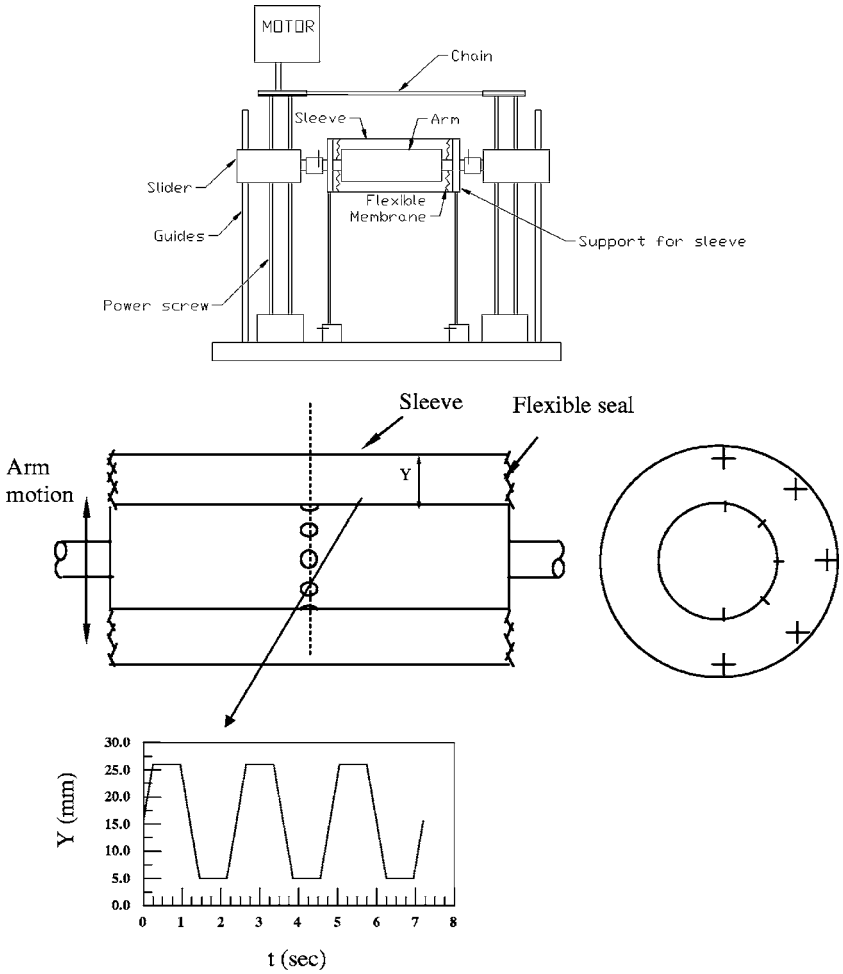

Fig. 3 A schematic of the experimental setup

brane to prevent air leaks in the axial direction. The periodic motion was not exactly a sinusoid where the inner cylinder moves up at constant speed to reach the maximum height and then the relay reverses direction to start the downward motion of the cycle as shown in Fig. 3. The amplitude of oscillations tested was 21 mm corresponding to amplitude ratios of $\zeta=0.8$. The selection of the amplitude of oscillation was selected to represent cases of medium to loose clothing situations. Experiments were conducted for gear motor frequencies of 30 and 60 rpm. In the plane above the fabric cylinder, a fan was positioned to provide sufficient circulation of air (0.7 m/s) for maintaining the constant chamber ambient conditions around the fabric. In addition, the inner cylinder was filled with Styrofoam insulation material.

The experimental setup was placed in the environmental chamber where constant climatic conditions were maintained for a period of 24 hours before the start of the experiments. At the beginning, the inner cylinder was wrapped with a saturated fabric sample (skin) and was weighed. The weight loss of moisture was monitored every half an hour for a total of 4 h from the onset of oscillations of the inner cylinder. So, every half hour, the wet fabric sample was quickly removed and placed inside a plastic bag for weighing using a sensitive scale of accuracy ±0.01 g. The temperature of the wetted cotton surface was monitored by a thermistor, while the temperature measurement of the air layer was taken by radiation-shielded thermistor. One thermistor was placed on the lower surface of the wet cotton sample while the other thermistor was placed in the enclosed air spacing between the oscillating fabric and the wet cotton surface. The accuracy of the temperature readings was ±0.1°C. Knowing the amount of water evaporated from the fabric, the temperature of the cotton wet sample, and the temperature of the air layer, the skin mass transfer coefficient can be estimated as

$$\dot{m}_s = h_{m(\text{skin-air})} A_{sk} (P_{sk} - P_a) \tag{15}$$

where $\dot{m}_s$ is the measured mass flux in g/s, P_a is the vapor pressure of the air in kPa, P_{sk} is the vapor pressure at the skin in kPa, and A_{sk} is the area of the fabric in m^2. The vapor pressure at the skin is estimated from the equilibrium vapor pressure at the skin temperature. The air layer temperature was measured. The wet bulb temperature of the air layer was taken as that of the saturated skin temperature since the setup was similar to an adiabatic saturator for the enclosed air. The measured temperature of the wet skin sample did not change since the sample was wet during the time of the experiment.

Figure 4 shows the measured temperature results with time of the skin and air layer at 60 and 80 rpm. The measured evaporation rates became steady starting from the second hour of onset of the measurements. In the initial transient period, the fabric was wet and possibly had some wicking present at the lower frequency when the weighing process took place at the first half hour. This effect was not present after a longer period of time when the fabric had no wicking. This effect was not very pronounced at the higher frequency due to the shorter transient period and faster evaporation taking place within that transient period. Table 1 summarizes the measured evaporation rate, temperatures of skin and air layer, the calculated mean mass transfer coefficient $h_{m(\text{skin-air})}$, and the corresponding heat transport coefficient from the skin to

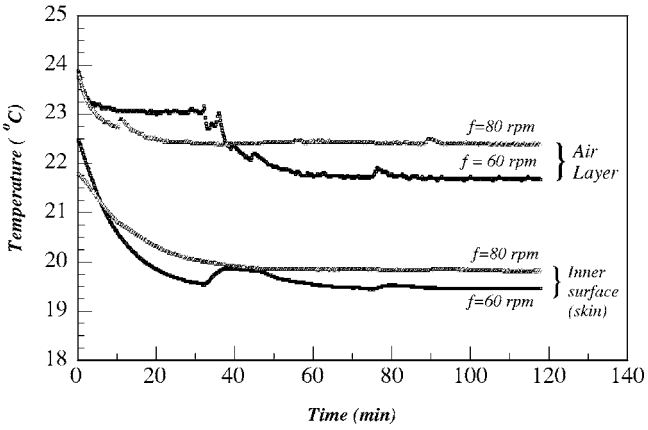

Fig. 4 The measured space-averaged temperatures with time of the skin and air layer at 60 and 80 rpm

the lumped air layer $h_{c(\text{skin-air})}$ using the Lewis relation for air-water vapor mixtures [17]. The mean transport coefficients for a cylindrical geometry are 29% lower than the planner normal periodic flow coefficients reported by Ghaddar et al. [20]. This is expected due to the reduced radial ventilation rate and increased angular motion parallel to the inner surface within the annulus. In addition, the results fall within a sound range of real subjects' experiments for different clothing ensembles where the present experimental findings of convection coefficients are within 5.2% from the findings of Lotens [4] at the walking speed of 0.2 m/s and at 7.7% from the findings of Havenith et al. [6] at 0.3 m/s walking speed.

Experimental Testing of the Thermal Behavior of a Heated Inner Cylinder Subjected to Periodic Motion. The aim of the experiment is to measure the time- and space-averaged skin and air layer temperatures at different frequencies and validate predictions of the theoretical model dry heat loss for closed aperture setting. The effect of modulation of the internal cylinder on the thermal system behavior was tested on heat transport from the inner cylinder surface to the environment when no contact took place between the inner and outer cylinder ($\zeta<1$) and when the outer cylinder touched the inner cylinder for part of the cycle ($\zeta>1$). Dry experiments were performed while subjecting the inner cylinder to a fixed heat flux boundary condition.

The same experimental setup shown in Fig. 3 was used. Metallic resistance heaters Omega-KH-1012 were placed on the inner conducting hollow cylinder surface to produce constant heat flux conditions in a climatic chamber at 24.5°C and RH at 50%. The heat flux was regulated at 80 W/m^2 and was verified by measuring the power input to the heaters. Thermistors of type Omega-44133 were placed in small microgrooves in the inner cylinder surface for three angular locations of top ($\theta=0$ deg), side ($\theta=90$ deg) and bottom ($\theta=180$ deg). Other radiation-shielded thermistors were placed within the air gap and about 0.5 cm from the outer circumference toward the center at $\theta=0$ deg, $\theta=90$ deg, and $\theta=180$ deg. The accuracy of the temperature readings was ±0.1°C. The thermistors' readings and the climatic chamber conditions are monitored in time by a data acquisition system of national instruments SCXI 1121 and by labview software version 7. The temperature was sampled at 10 reading/second and is averaged and recorded every 10 s.

Table 1 Film coefficients experiment: measured evaporation rate, measured skin and mean air layer temperatures, and corresponding calculated mass and heat transfer coefficients

Frequency	60 rpm	80 rpm
Measured evaporation rate $\dot{m}_s$(g/h)	6	5.8
Measured skin temperature (°C)	19.6±0.1	19.4±0.1
Measured mean air layer temperature (°C)	22.4±0.1	21.7±0.1
Mass transfer coefficient, $h_{m(\text{skin-air})}$ ($kg/s\cdot m^2\cdot kPa$)	6.4×10^{-5}	7.54×10^{-5}
Heat transfer coefficient using Lewis relation $h_{c(\text{skin-air})}$ ($W/m^2\cdot K$)	9.4	11.05

In the first set of experiments no contact was permitted between the cylinders, and the inner cylinder was operated at the frequencies of 25, 33, and 40 rpm for an amplitude of oscillations of 21 mm corresponding to an amplitude ratio of $\zeta=0.8$. Measurements were taken after the system reached the steady periodic state in 1 1/2 h after the onset of the experiment. The steady periodic state was assumed when no further change in measured temperature between one period and the next was observed within 0.1°C. The time for steady periodic solution in the dry experiments was around 20 min at 60 rpm and 15 min at 80 rpm, respectively. The higher frequency has a shorter transient period due to the fast renewal of air and corresponding dissipation of heat. In the second set of experiments a special relay was attached to the control circuit of the motor to stop the motion once the inner cylinder touched the outer cylinder, and to prevent the inner cylinder from further motion. Due to the contact that takes place between the inner cylinder and the fabric at the top ($\theta=0$ deg), and bottom ($\theta=180$ deg), only measurements of skin temperature were recorded at those positions. At the side where $\theta=90$ deg, the skin temperature and the air layer temperature are recorded. The experiments were performed at the frequencies of 25, 33, and 40 rpm for an amplitude of oscillations of 36.5 mm corresponding to an amplitude ratio of $\zeta=1.4$. It was not possible with the current contact mechanism between the cylinders to perform the experiments at the higher frequencies of 60 and 80 rpm.

Results and Discussion

Experimental Validation of the Cylinder-Fabric Model Heat Transport. The time- and space-averaged temperatures of the skin and the air layer will be presented for both sets of experiments at $\zeta=0.8$ and $\zeta=1.4$. The heat flux elements on the surface are thermally conducting. This has resulted in a closely uniform inner surface temperature and the maximum measured skin temperature difference between the three positions was 0.8°C at 25 rpm and 0.5°C at 80 rpm for $\zeta=0.8$ and 0.1 to 0.2°C at all frequencies for $\zeta=1.4$. The experimental results are used then to validate the 2-D cylinder model predictions.

The simulation program is run using the dimensions of the inner and outer cylinder at the dry isothermal condition of the skin as obtained in the experiments to predict the inner cylinder heat loss as a function of the periodic motion frequencies at $\zeta=0.8$ and $\zeta=1.4$. Figure 5 shows the predicted and measured time- and space-averaged skin and air layer temperatures as a function of the ventilation frequency at $\zeta=0.8$. Good agreement exists between the model predictions and experiment. At $\zeta=0.8$, the air layer temperature decreased with the increase in ventilation frequency and the predicted model values approach the experimental values as the frequency increases. Since constant heat flux is imposed, the skin temperature is expected to decrease with the decrease in air temperature at high frequency as seen by the model predictions. The mean error of the measurements of the skin temperatures compared with the predicted values of the model at sensible heat flux of 80 W/m^2 were less than 0.8°C. The difference between the predicted and measured values increased at high frequency due to the possible lower ventilation rates caused by the bellow effect of the capped plastic ends of the cylinder. The effect of natural convection present in the air layer, which induces slightly cooler skin temperature at the bottom of the cylinder than the top, could be responsible for the difference in the air layer temperature at low frequency. Note that the comparison is based

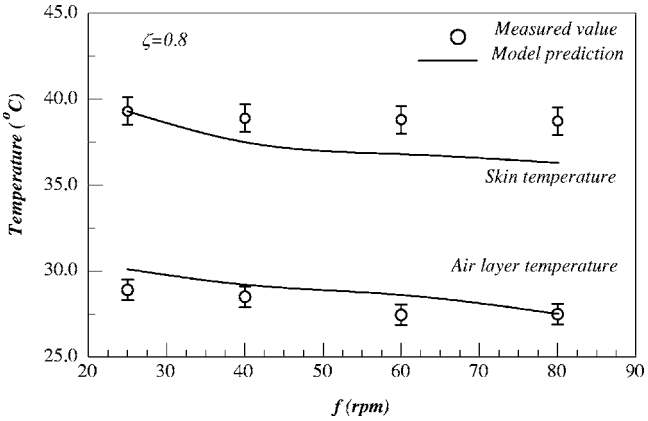

Fig. 5 The predicted and measured time- and space-averaged skin and air layer temperature as a function of the ventilation frequency at $\zeta=0.8$

on space-averaged temperature values.

Figure 6 shows the predicted and measured time- and space-averaged skin and air layer temperatures as a function of the ventilation frequency at $\zeta=1.4$. The agreement between experimental measurements and model predictions of skin temperature is good given a relative error of less than 5% while the air layer temperature has shown a relative error of 10%. This is expected since the model of the air layer is a lumped model, while measurements of air layer were taken at local points in the air annulus where the thermocouple was placed at 0.5 cm away from the outer surface.

Closed Aperture Air Annulus Mass and Heat Transport Model Results. The results of the 2-D radial and angular flow model are presented for ambient conditions at 25°C and 50% RH and at an inner cylinder isothermal skin condition of 35°C and 100% relative humidity. Simulations are performed for a domain mean spacing $Y_m=2.6$ cm at different frequencies and amplitude ratios for $R_f=6.5$ cm and $R_s=3.9$ cm. The numerical simulation results of the model predicts the transient steady periodic mass flow rates in the radial and angular directions, the fabric regain, the internal air layer temperature and humidity ratio, the fabric temperature, and the skin surface temperature.

Figure 7 shows the variation of (*a*) the steady periodic time-averaged lumped air layer temperature and (*b*) steady periodic time-averaged fabric temperature as a function of the angular position θ for the ventilation frequencies of 25, 40, and 60 rpm at $\zeta=0.8$ and 1.4. Note that when contact takes place, the air layer

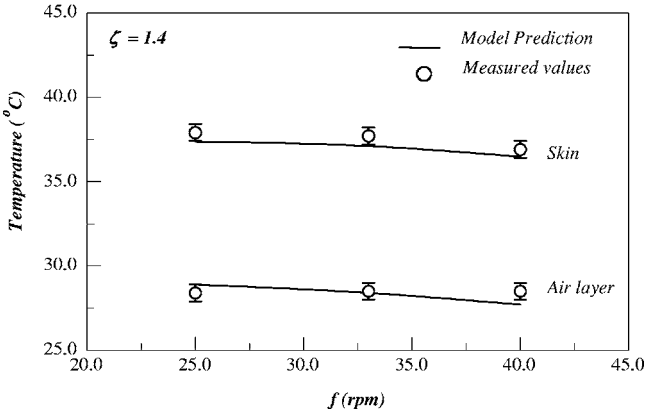

Fig. 6 The predicted and measured time- and space-averaged skin and air layer temperature as a function of the ventilation frequency at $\zeta=1.4$

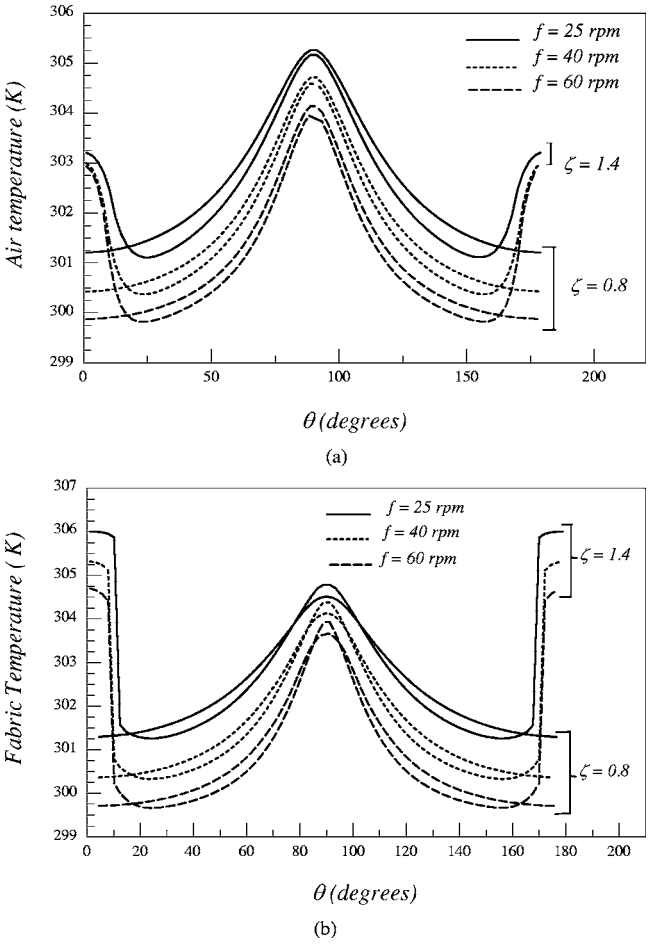

Fig. 7 The variation of (*a*) the steady periodic time-averaged lumped air layer temperature and (*b*) steady periodic time-averaged fabric temperature as a function of the angular position θ for the ventilation frequencies of 25, 40, and 60 rpm at $\zeta=0.8$ and 1.4

temperature is meaningless at those positions and its value is taken at the average of the skin and fabric void node temperatures. The fabric temperature at the contact region ($\theta=0$ and $\theta=\pi$) is the highest due to the contact with the hotter skin temperature. In addition, the calculated total regain is smaller in the contact region since fabric adsorption decreases with increased temperature. The air temperature and the fabric temperature at $\zeta=0.8$ are slightly higher than their values at $\zeta=1.4$ for the noncontact region due to the higher air renewal rate associated with the larger amplitude at $\zeta=1.4$.

Figure 8 shows the variation of the steady periodic time-averaged (*a*) sensible and (*b*) latent heat loss as a function of the angular position θ for the ventilation frequencies of 25, 40, and 60 rpm at $\zeta=0.8$ and $\zeta=1.4$. The sensible heat loss at $\zeta=0.8$ is slightly smaller than $\zeta=1.4$ due to the higher air temperature in the noncontact region. In the contact region the sensible heat loss is higher for $\zeta=0.8$. This is attributed to the higher fabric temperature associated with the contact region and the absence of heat loss by radiation in that region. The maximum sensible heat loss for $\zeta=0.8$ and 1.4 takes place in the contact region at $\theta=0$ and $\theta=\pi$ since that region has the highest ventilation rates until fabric contact takes place that results in a sudden increase of heat loss. The minimum heat loss is at $\theta=\pi/2$ since that region has the lowest radial ventilation. The latent heat loss at $\zeta=0.8$ is slightly smaller than $\zeta=1.4$ due to the higher dry air renewal in the noncontact region at $\zeta=1.4$. The latent heat loss increases signifi-

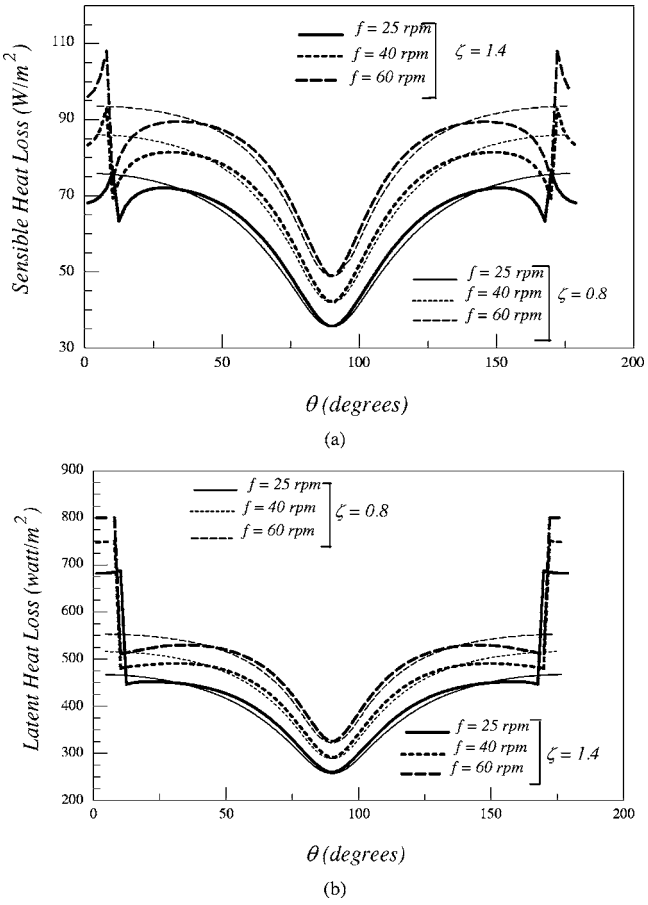

Fig. 8 The variation of the steady periodic time-averaged (*a*) sensible and (*b*) latent heat loss as a function of the angular position θ for the ventilation frequencies of 25, 40, and 60 rpm at $\zeta=0.8$ and $\zeta=1.4$

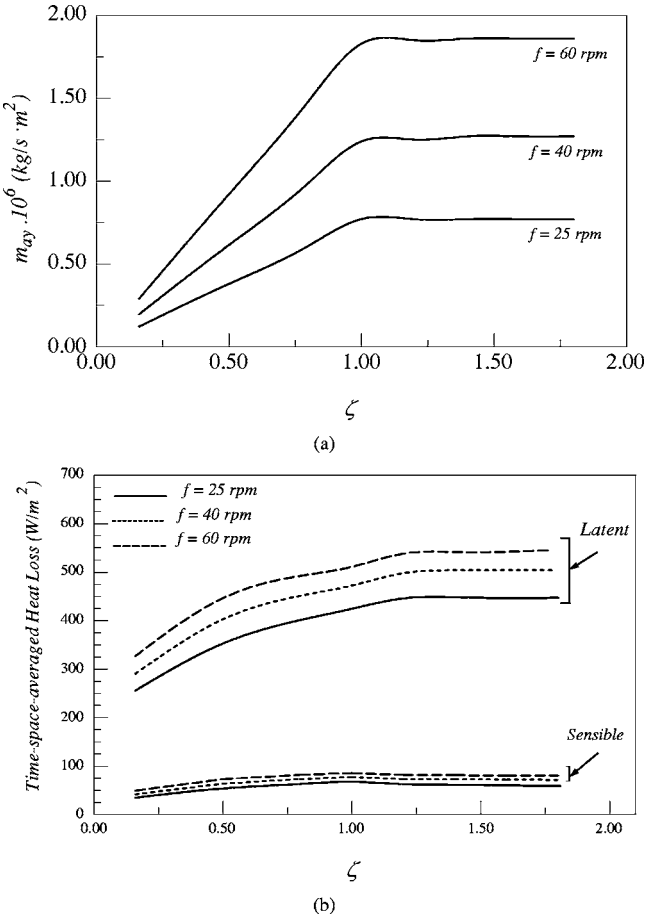

Fig. 9 The 2-D ventilation model predictions as a function of the amplitude ratio ζ of (*a*) the time-space-averaged total ventilation rate in the microclimate and (*b*) the time-space-averaged sensible and latent heat loss in W/m² at $f=25$, 40, and 60 rpm

cantly in the contact region compared to the no-contact region and to the case of $\zeta=0.8$. The fabric temperature is significantly higher after the contact with the hot skin. When the fabric moves away from the skin at this high temperature, it will lose significant moisture to the ventilating dry air. Then, the fabric returns back towards the skin with a higher ability to adsorb moisture at contact, leading to a much higher latent heat loss over the ventilation cycle in the contact region compared to the case when no contact takes place.

Figures 9(*a*) and 9(*b*) show the 2-D ventilation model predictions as a function of the amplitude ratio ζ of (*a*) the time-space-averaged total air flow renewal (kg/m^2) in the microclimate and (*b*) the time-space-averaged sensible and latent heat loss at $f=25$, 40, and 60 rpm. The air renewal in the microclimate increases with the increase of the ventilation frequency and the corresponding sensible and latent heat losses increase with the increase in the ventilation frequency. However, at fixed ventilation frequency the air renewal rate and the total heat loss variation with the amplitude ratio are affected by the fabric-skin contact occurrence during the cycle. The maximum sensible heat loss occurs at $\zeta=1$ and decreases very slightly with increased contact period within the studied range.

Open Aperture Air Annulus Mass and Heat Transport Model Results. To investigate the effect of the presence of the open aperture on heat loss from the skin, simulations are performed for a domain of length $L=0.6$ m, and mean spacing $Y_m=2.6$ cm at three different frequencies of 25, 40, and 60 rpm and amplitudes corresponding to $\zeta=0.8$ and $\zeta=1.4$ for $R_f=6.5$ cm, $R_s=3.9$ cm, and $C_D=1$. The selection of the length is based on the realistic physical length of a sleeve. The ambient conditions are taken at 25°C and 50% RH and at an inner cylinder isothermal skin condition of 35°C and 100% relative humidity.

Introducing an aperture induces air renewal in the axial direction through the opening [1]. Figures 10(*a*) and 10(*b*) present a plot of (*a*) the total ventilation rate versus the amplitude ratio at different frequencies of motion and (*b*) the time- and θ-space-averaged radial flow rate variation in the axial direction at different amplitude ratios for $f=25$, 40, and 60 rpm at $\zeta=0.8$ and $\zeta=1.4$. The air renewal through the opening increases with amplitude ratio up to $\zeta=1$ when fabric-skin periodic contact takes place and then the change in the opening ventilation rate is negligible for $\zeta>1$ (Fig. 10(*a*)). At the opening ($x=0$), the radial ventilation rate approaches zero and a high gradient of radial flow rate occurs within the first 10% of the opening even when contact is present for $\zeta>1$. For most of the domain interior, negligible axial flow exists and the radial flow rate is constant. Figure 11 shows the variation of the steady periodic time- and angular-space-averaged (*a*) sensible and (*b*) latent heat loss as a function of the axial position x for the ventilation frequencies of 25, 40, and 60 rpm at $\zeta=0.8$ and $\zeta=1.4$. The maximum latent and sensible heat loss takes place at the opening and the enhancement of the local sensible heat loss at the open aperture compared to the closed end is 27.6%, 17.5%, and 15.1% at $f=25$, 40, and 60 rpm, respectively. The local latent heat loss at the opening increases by 17.4%, 12.7%, and 11.6% at $f=25$, 40, and 60 rpm, respectively, when

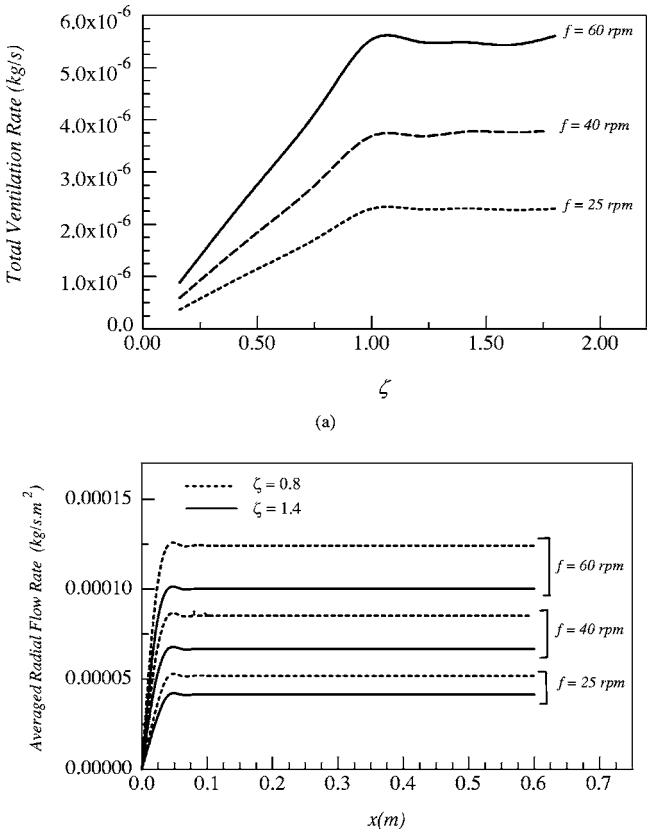

Fig. 10 A plot of (*a*) the total ventilation rate versus the amplitude ratio at different frequencies of motion and (*b*) the time- and θ-space-averaged radial flow rate variation in the axial direction at different amplitude ratios for $f=25$, 40, and 60 rpm at $\zeta=0.8$ and $\zeta=1.4$

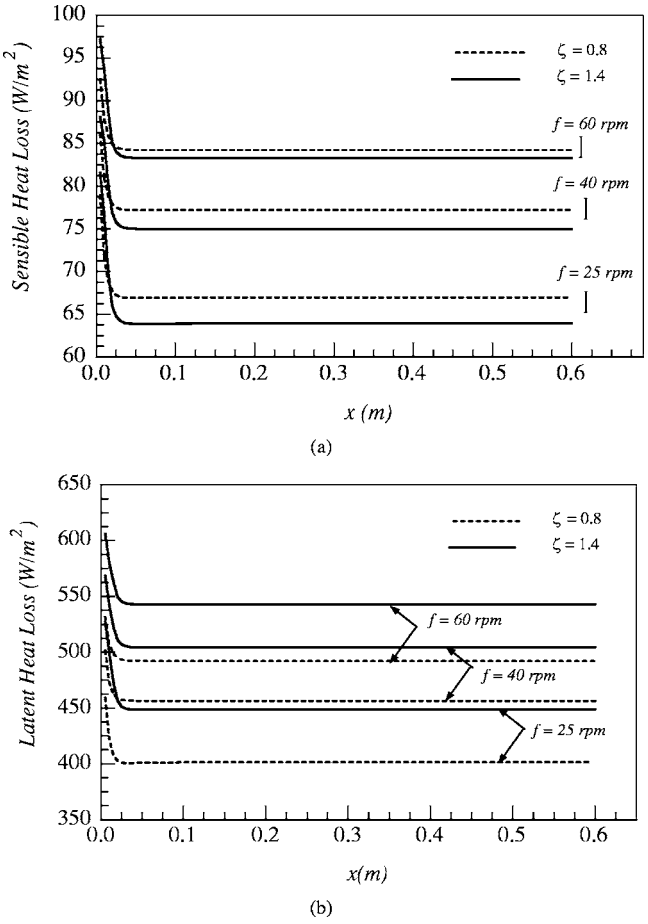

Fig. 11 The variation of the steady periodic time and angular-space-averaged (*a*) sensible and (*b*) latent heat loss as a function of the axial position x for the ventilation frequencies of 25, 40, and 60 rpm at $\zeta=0.8$ and $\zeta=1.4$

compared with latent loss at the closed end.

The presence of the opening has minimal effect on the overall time- and space-averaged heat loss due to the limited size of the region near the opening where substantial axial flow renewal occurs. For the open aperture system at $\zeta=1.4$, the overall total heat loss increase over closed apertures is 4.4%, 2.8%, and 2.2% at $f=25$, 40, and 60 rpm, respectively. Comparing the total heat loss for an open aperture system when no fabric-skin contact is present ($\zeta=0.8$) to the case when periodic contact occurs ($\zeta=1.4$), it is found that the contact increases the heat loss by 9.6%, 8.6%, and 8.5% at $f=25$, 40, and 60 rpm, respectively.

Conclusions

The coupled convection heat and moisture exchange within the clothing system subject to sinusoidal microclimate air layer thickness temporal variation is theoretically modeled to predict the heat losses from the skin due to ventilation with periodic fabric skin contact during the motion. Experimental results agree well with the model predictions of heat loss through the fabric during periodic localized contact and noncontact of the fabric cylinder with the skin cylinder. The presence of an open aperture in the system slightly increases the overall heat loss due to the limited effect of axial ventilation close to the opening. The effect of the opening on heat loss decreases as the ventilation frequency increases.

The current model approach is novel in its consideration of the periodic nature of air motion in the trapped layer between skin and fabric and the handling of the heat and moisture transport during the periodic fabric-skin contact and no contact regions. The model provides an effective and fast method of providing a solution derived from first principles at low computational cost by transforming a 3-D flow problem to a 2-D problem (the radial direction of the airflow is lumped). This makes the model attractive for integration with human body thermal models to better predict human response under dynamic conditions.

Acknowledgment

The authors would like to acknowledge the financial support of the University Research Board of the American University of Beirut. The environmental chamber lab facility is supported by the American School and Hospital Aid (ASHA) Grant No. AUB-FEA-793.

Nomenclature

A_f = area of the fabric (m^2)
C = specific heat ($J/kg\cdot K$)
D = water vapor diffusion coefficient in air (m^2/s)
e_c = eccentricity between the skin and fabric cylinders
e_f = fabric thickness (m)
f = frequency of oscillation of the inner cylinder in revolution per minute (rpm)
h_{fg} = heat of vaporization of water (J/kg)
h_{ad} = heat of adsorption (J/kg)
h_r = radiation heat transfer coefficient ($W/m^2\cdot K$)
H_{ci} = conduction heat transfer coefficient between inner node and outer node ($W/m^2\cdot K$)

H_{co} = convection heat transfer coefficient between outer node and air flowing through fabric ($W/m^2 \cdot K$)

$h_{c(f\text{-}\infty)}$ = heat transport coefficient from the fabric to the environment ($W/m^2 \cdot K$)

$h_{c(o\text{-air})}$ = heat transport coefficient from the fabric to the trapped air layer ($W/m^2 \cdot K$)

$h_{c(\text{skin-air})}$ = heat transport coefficient from the skin to the trapped air layer ($W/m^2 \cdot K$)

H_{mi} = diffusion mass transfer coefficient between inner node and outer node ($kg/m^2 \cdot kPa \cdot s$)

H_{mo} = mass transport coefficient between outer node and air void in the fabric ($kg/m^2 \cdot kPa \cdot s$)

$h_{m(f\text{-}\infty)}$ = mass transfer coefficient between the fabric and the environment ($kg/m^2 \cdot kPa \cdot s$)

$h_{m(o\text{-air})}$ = mass transfer coefficient between the fabric and the air ($kg/m^2 \cdot kPa \cdot s$)

$h_{m(\text{skin-air})}$ = mass transfer coefficient between the skin and the air layer ($kg/m^2 \cdot kPa \cdot s$)

k_a = thermal conductivity of air ($W/m \cdot K$)

L = fabric length in x direction (m)

$\dot{m}_{ay}$ = mass flow rate of air in y direction ($kg/m^2 \cdot s$)

$\dot{m}_{ax}$ = mass flow rate of air in x direction ($kg/m^2 \cdot s$)

$\dot{m}_{a\theta}$ = mass flow rate of air in θ direction ($kg/m^2 \cdot s$)

P_a = air vapor pressure (kPa)

P_i = vapor pressure of water vapor adsorbed in inner node (kPa)

P_o = vapor pressure of water vapor adsorbed in outer node (kPa)

P_{sk} = vapor pressure of water vapor at the skin (kPa)

R = total regain in fabric (kg of adsorbed H_2O/kg fiber)

R_D = fabric dry resistance ($m^2 \cdot K/W$)

R_E = fabric evaporative resistance ($m^2 \cdot kPa/W$)

R_f = fabric cylinder radius (m)

R_s = skin cylinder radius (m)

rpm = revolutions per minute

t = time (s)

T = temperature (°C)

w = humidity ratio (kg of water/kg of air)

$Y(\theta,t)$ = instantaneous air layer thickness (m)

Y_m = mean air layer thickness (m)

Greek Symbols

ε = fabric porosity

ρ = density of fabric (kg/m^3)

ΔY = amplitude of oscillation (m)

ω = angular frequency (rad/s)

ν = *kinematic* air viscosity (m^2/s)

τ = period of the oscillatory motion (s)

θ = angular coordinate

ζ = amplitude ratio

Subscripts

a = conditions of air in the spacing between skin and fabric

f = fabric

i = inner node

o = outer node

sk,s = conditions at the skin surface

$void$ = local air inside the void

∞ = environment condition

References

[1] Ghaddar, N., Ghali, K., Harathani, J., and Jaroudi, E., 2005, "Ventilation Rates of Micro-climate Air Annulus of the Clothing-skin System Under Periodic Motion," Int. J. Heat Mass Transfer, **48**(15), pp. 3151–3166.

[2] Ghaddar, N., Ghali, K., and Harathani, J., 2005, "Modulated Air Layer Heat and Moisture Transport by Ventilation and Diffusion From Clothing With Open Aperture," ASME J. Heat Transfer, **127**(3), pp. 287–297.

[3] Harter, K. L., Spivak, S. M., and Vigo, T. L., 1981, "Applications of the Trace Gas Technique in Clothing Comfort," Text. Res. J., **51**, pp. 345–355.

[4] Lotens, W., 1993, "Heat Transfer From Humans Wearing Clothing," doctoral thesis, TNO Institute for Perception, Soesterberg, The Netherlands, pp. 34–37.

[5] Danielsson, U., 1993, "Convection Coefficients in Clothing Air Layers," Ph.D. thesis, The Royal Institute of Technology, Stockholm.

[6] Havenith, G., Heus, R., and Lotens, W. A., 1990, "Resultant Clothing Insulation: a Function of Body Movement, Posture, Wind Clothing Fit and Ensemble Thickness," Ergonomics, **33**(1), pp. 67–84.

[7] Jones, B. W., Ito, M., and McCullough, E. A., 1990, "Transient Thermal Response Systems," *Proceedings of the 4th International Conference on Environmental Ergonomics*, Austin, TX, October 2–4, pp. 66–67.

[8] Jones, B. W., and McCullough, E. A., 1985, "Computer Modeling for Estimation of Clothing Insulation," *Proceedings of CLIMA 2000*, World Congress on Heating, Ventilating, and Air Conditioning, Copenhagen, Denmark, August 25–30, Vol. 4, pp. 1–5.

[9] Ghali, K., Ghaddar, N., and Jones, B., 2002, "Multi-Layer Three-Node Model of Convective Transport Within Cotton Fibrous Medium," J. Porous Media, **5**(1), pp. 17–31.

[10] Ghali, K., Ghaddar, N., and Jones, B., 2002, "Modeling of Heat and Moisture Transport by Periodic Ventilation of Thin Cotton Fibrous Media," Int. J. Heat Mass Transfer, **45**, pp. 3703–3714.

[11] Ghaddar, N., Ghali, K., and Harathani, J., 2005, "Modulated Air Layer Heat and Moisture Transport by Ventilation and Diffusion From Clothing With Open Aperture," ASME J. Heat Transfer, **127**(3), pp. 287–297.

[12] Womersley, J. R., 1955, "Oscillatory Motion of Viscous Liquid in Thin-walled Elastic Tube: I. The Linear Approximation for Long Waves," Philos. Mag., **46**, pp. 199–221.

[13] Lamoreux, L. W., 1971, "Kinematic Measurements in the Study of Human Walking," Bull. Prosthet. Res., pp. 3–86.

[14] Farnsworth, B., 1986, "A Numerical Model of Combined Diffusion of Heat and Water Vapor Through Clothing," Text. Res. J., **56**, pp. 653–655.

[15] Jones, B. W., and Ogawa, Y., 1992, "Transient Interaction Between the Human and the Thermal Environment," ASHRAE Trans., **98**(1), pp. 189–195.

[16] Hyland, R. W., and Wexler, A., 1983, "Formulations for the Thermodynamic Properties of the Saturated Phases of H_2O From 173.15 K to 473.15 K," ASHRAE Trans., **89**(2A), pp. 500–519.

[17] ASHRAE, 1993, *Handbook of Fundamentals*, American Society of Heating, Refrigerating and Air conditioning Engineers, Atlanta, GA.

[18] Kerslake, D. McK., 1972, *The Stress of Hot Environments*, Cambridge University Press, Cambridge.

[19] Mochida, T., 1970, "Convective and Radiative Heat Transfer Coefficients for the Human Body," *Bulletin of the Faculty of Engineering*, Hokkiado University, pp. 1–11.

[20] Ghaddar, N., Ghali, K., and Jones, B., 2003, "Integrated Human-Clothing System Model for Estimating the Effect of Walking on Clothing Insulation," Int. J. Therm. Sci., **42**(6), pp. 605–619.

Nanoscale Heat Conduction Across Metal-Dielectric Interfaces

Y. "Sungtaek" Ju[1]
e-mail: just@seas.ucla.edu

Ming-Tsung Hung

Takane Usui

Department of Mechanical and Aerospace Engineering,
University of California,
Los Angeles, CA 90095-1597

We report a theoretical study of heat conduction across metal-dielectric interfaces in devices and structures of practical interest. At cryogenic temperatures, the thermal interface resistance between electrodes and a substrate is responsible for substantial reduction in the maximum permissible peak power in Josephson junctions. The thermal interface resistance is much smaller at elevated temperatures but it still plays a critical role in nanoscale devices and structures, especially nanolaminates that consist of alternating metal and dielectric layers. A theoretical model is developed to elucidate the impact of spatial nonequilibrium between electrons and phonons on heat conduction across nanolaminates. The diffuse mismatch model is found to provide reasonable estimates of the intrinsic thermal interface resistance near room temperature as well as at cryogenic temperatures. [DOI: 10.1115/1.2241839]

Keywords: nanoscale heat transfer, thermal interface resistance, Josephson junctions, nanolaminates

Introduction

Heat conduction across interfaces is a critical consideration in a variety of scientific and engineering applications. This is especially true for micro- and nanoscale devices and structures whose thermal characteristics are strongly influenced by interface phenomena. Because the thermal interface resistance increases rapidly with decreasing temperature [1], its impact is most pronounced in cryoelectronic devices, such as superconducting Josephson junctions.

Near room temperature above, the thermal interface resistance between two solids is comparable to the thermal resistance of a few nanometer thick glass layer. As the minimum feature size of electronic and optical devices continues to scale down, even this relatively small interface resistance is becoming an important consideration. Examples of such devices include giant magnetoresistance sensors in data storage applications [2] and magnetic tunnel junctions in spintronic applications [3]. High density interfaces also strongly impede heat conduction across nanolaminates [4–6] and superlattices found in optoelectronic and thermoelectric devices [7]. Nanolaminates consisting of alternating layers of nanoscale metal and dielectric materials are promising as ultra-low thermal conductivity thermal barrier coatings.

The present manuscript reports a study of heat transport across metal-dielectric interfaces in microdevices and nanostructures of practical interest. Most previous studies of the interface resistance have focused on a simple generic interface formed between two full films or between a full film and a substrate. We study the thermal interface resistance at cryogenic temperatures by analyzing the thermal behavior of Josephson junctions in superconducting electronic circuits. The large thermal interface resistance is found to be responsible for substantial reduction in the maximum permissible peak power in Josephson junctions. Heat conduction across nanolaminates of alternating metal and dielectric materials is next studied using a two-fluid heat conduction model to examine the effects of the close proximity of interfaces and spatial electron-phonon nonequilibrium on heat conduction across interfaces. Our study suggests that the diffuse mismatch model provides reasonable estimates of the intrinsic interface resistance near room temperature as well as at cryogenic temperatures.

Heat Transfer in Josephson Junctions

Superconductor-normal metal-superconductor (SNS) Josephson junctions are key elements of superconducting electronic circuits. To ensure reliable operations of superconducting circuits, device-level thermal management is critical because Josephson junctions must be maintained below the critical temperature T_c of the electrodes to properly function. Figure 1 schematically shows an SNS junction that consists of superconducting electrodes, typically made of Niobium (Nb), and a normal-metal barrier layer. Heat generated in the junction is removed primarily by heat conduction across the bottom electrode-substrate interface.

At cryogenic temperatures, mismatch in lattice vibrational properties is often the main mechanism responsible for finite resistance to heat conduction across interfaces between two dissimilar solids [1]. The thermal interface resistance exhibits strong temperature dependence because phonons obey the Planck distribution. The net rate of heat transfer across an interface by phonons can be calculated by summing the contribution of all phonons incident on the interface per unit time. On the basis of the diffuse mismatch model of Swartz and Pohl [1], we write

$$\dot{Q}_{\text{net}} = \frac{\alpha_{12}}{4}\sum_j \int_0^{\omega_{1,\max}} N_{1j}\,\hbar\omega c_{1j}\,d\omega - \frac{\alpha_{21}}{4}\sum_j \int_0^{\omega_{2,\max}} N_{2j}\,\hbar\omega c_{2j}\,d\omega \tag{1}$$

The subscript j labels phonon modes, N is the phonon distribution function, ω is the phonon frequency, and c is the phonon velocity. The parameter α is the probability that phonons incident on the interface are transmitted. Equation (1) can be simplified under the Debye approximation:

$$\dot{Q}_{\text{net}} = \frac{\pi^2}{120}\left(\frac{k_B}{\hbar^3}\right)\frac{\left(\sum_j c_{i,j}^{-2}\right)\left(\sum_j c_{3-i,j}^{-2}\right)}{\sum_{i,j} c_{i,j}^{-2}}(T_1^4 - T_2^4) = \Psi(T_1^4 - T_2^4) \tag{2}$$

In the limit $(T_1 - T_2)/T_2 \ll 1$, the above equation can be linearized to define a constant thermal boundary resistance. This condition is

[1]Also with Biomedical Engineering Interdepartmental Program.

Contributed by the Heat Transfer Division of ASME for publication in the JOURNAL OF HEAT TRANSFER. Manuscript received July 22, 2005; final manuscript received March 1, 2006. Review conducted by Costas Grigoropoulos. Paper presented at the 2005 ASME Heat Transfer Summer Conference (HT2005), July 22, 2005, San Francisco, California, USA.

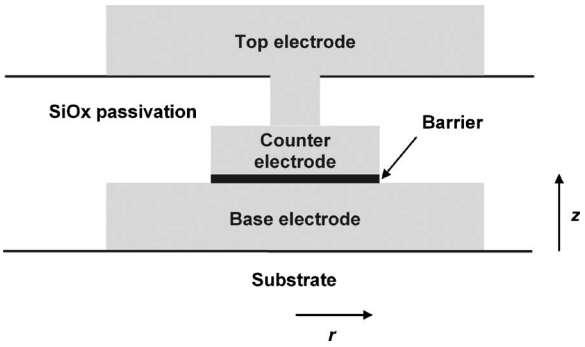

Fig. 1 Cross-sectional diagram of a superconductor-normal metal-superconductor Josephson junction. The electrodes are typically made of Nb, which become superconducting at temperatures below approximately 9 K. The barrier is a normal metal.

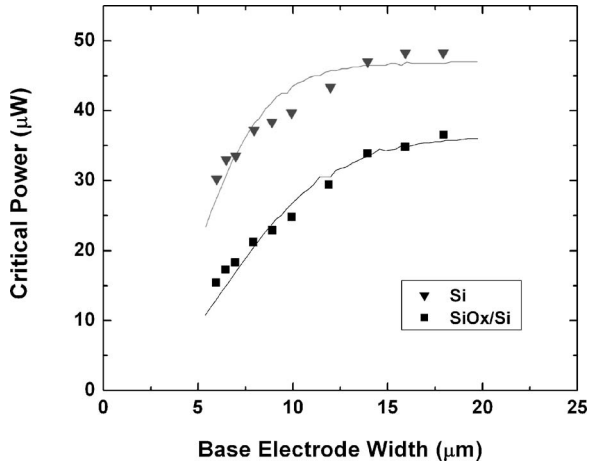

Fig. 2 Predicted and experimentally determined critical power of Nb-MoSi-Nb Josephson junctions. The data are from Chong et al. [9]. Two types of junctions with different bottom electrode-substrate interfaces are studied. The silicon substrates were maintained at 4 K.

not satisfied near the critical power condition of Josephson junctions where the electrodes undergo superconductor-normal metal transition. The critical temperature T_c of Nb thin films ($\sim$9 K) is substantially higher than the substrate temperature ($\sim$4 K). Chong et al. [8] and previous studies of self-heating in superconducting thin-film microbridges [9] severely underestimated the temperature dependence of the thermal interface resistance by using a linearized version of Eq. (2).

Since the electrical resistance of a Josephson junction increases abruptly when the local electrode temperature exceeds T_c, one can determine the critical power in each junction from its current-voltage characteristics. Chong et al. [8] reported such data on Nb-$MoSi_2$-Nb Josephson junctions. To facilitate the analysis of heat conduction in these junctions, we make a simplifying assumption that the temperature variation along the junction (z direction in Fig. 1) is negligible. The 1D approximation is consistent with the experimental observation that the critical power of devices with multiple stacked junctions is independent of the number of junctions and depends only on the total power dissipated within the entire stack. Our 2D simulations also confirm that heat generated within each junction is removed primarily by heat conduction along the base electrode and into the substrate due to the low thermal conductivity of the silicon dioxide passivation layers and the large thermal interface resistance between the electrode and the passivation layers.

By applying the energy conservation principle to a differential volume defined along the r-direction, we obtain the following governing equation:

$$\frac{1}{r}\frac{d}{dr}\left(ktr\frac{dT}{dr}\right) - \Psi(T^4 - T_{\text{bath}}^4) + q'' = 0 \tag{3}$$

The first term represents heat conduction along the electrodes, the second term heat conduction across the electrode-substrate interface, and the third term heat generation in the barrier. Here, the effective electrode thickness t is considered a step function of r to account for parallel heat conduction along the two electrodes and the barrier layer. Equation (3) is analogous to the heat conduction equation for an extended surface, which dissipates heat through radiation.

We discretize Eq. (3) using the finite volume method. The resulting system of nonlinear algebraic equations is solved iteratively to find the critical power at which the peak temperature is equal to the critical temperature of the niobium electrodes.

We anticipate that scattering of heat carriers at film surfaces strongly suppresses the thermal conductivity of 2–300 nm thick Nb films at cryogenic temperatures. To our knowledge no thermal conductivity data are available in the literature for such thin Nb films. Since the mean free path of phonons is expected to be limited by the film thickness and/or grain size, we expect the phonon thermal conductivity to follow the T^3 dependence of the lattice heat capacity. Heat conduction by electrons in superconducting metals is a complex phenomenon, which is beyond the scope of the present manuscript. Electrons that condense into Cooper pairs do not directly contribute to heat conduction, which leads to rapid decrease in electronic thermal conductivity with decreasing temperature.

We fit the experimental data of Chong et al. [9] with our model, taking the parameter Ψ and the thermal conductivity of the Nb films as adjustable parameters. The thermal conductivity of the Nb films is assumed to have a functional form k_0T^n with the exponent n set to be 3. While the actual temperature dependence can be more complicated, we find that the fitted values of Ψ, which are of primary interest here, do not depend sensitively on n.

Figure 2 shows the critical power of the Josephson junctions as a function of base electrode width. The symbols correspond to the data and the lines correspond to the best fits from the present model. The critical power increases rapidly with the base electrode width, which reflects efficient lateral heat spreading in the r direction. Once the electrode width becomes comparable to the thermal decay length, the critical power does not increase much further and reaches plateaus. The thermal decay length is the characteristic length along the r direction over which the temperature decays from the peak value down to the substrate temperature.

Figure 2 includes data obtained from the two types of junctions that have different electrode-substrate interfaces. In one type of junctions, the base electrode was separated from the substrate by a thin layer of SiOx. In the other type of junctions, a native SiOx layer was first etched away before the base electrode was deposited. The critical power is substantially higher for the second type of junctions because the extra interfaces and the SiOx layer add significant thermal resistance.

The diffuse mismatch model [1] allows us to predict the parameter Ψ in Eq. (3) using the phonon velocities as the only input parameters. For the Nb-Si interface, the diffuse mismatch model predicts $\Psi = 180\ \text{W/m}^2\,\text{K}^4$, which agrees well with our best fit result, $\Psi = 170\ \text{W/m}^2\,\text{K}^4$. For the Nb-SiOx-Si series interface, an extra term is added to Eq. (3) to account for the finite thermal resistance of the SiOx layer. The fit result of $\Psi = 80\ \text{W/m}^2\,\text{K}^4$ also compares well with the predicted value of $\Psi = 90\ \text{W/m}^2\,\text{K}^4$. Part of the discrepancy may be due to the fact that we approximate the "phonon" velocities in the highly disordered SiOx layer by the speeds of sound in quartz.

The above results demonstrate the significance of interface en-

gineering in the thermal management of superconducting electronics. Minimizing the number of interfaces plays an important role in increasing the critical power of SNS junctions. Our results also demonstrate that the diffuse mismatch model allows reasonable quantitative prediction of heat transfer rates across interfaces in Josephson junctions at cryogenic temperatures.

Heat Conduction Across Nanolaminates

Near room temperature and above, the magnitude of the thermal interface resistance predicted by the diffuse mismatch model is much smaller than that at cryogenic temperatures. More detailed studies of other physical mechanisms that may potentially affect heat transfer across interfaces are therefore warranted.

We analyze the thermal resistance of nanolaminates reported in the literature [5,6] to gain further insight into heat conduction across interfaces between metal and dielectric materials. Nanolaminates are very useful because their total thermal resistance represents the combined contribution of a large number of interfaces, making accurate measurements much easier.

We limit ourselves to nanolaminates consisting of metal and amorphous dielectric layers and assume that the continuum approximation is valid in describing heat conduction across the amorphous dielectric layers. This assumption is supported by a prevailing theory of heat conduction in highly disordered dielectrics [10], which concludes that the effective mean free path of heat carriers is of the order of interatomic spacing near room temperature and above. It is also consistent with the recent experimental observation that the thermal resistance is a linear function of thickness for AlOx films as thin as 2 nm [6]. We assume diffuse scattering of heat carriers at the interfaces and ignore quantum effects, such as coherent superposition of lattice waves reflected or transmitted by adjacent interfaces.

Heat Conduction Across Nanoscale Metal Films. One of the authors found in a recent study [11] that electron-phonon nonequilibrium has significant influence on conduction cooling of metallic nanoparticles subjected to pulsed laser heating. In the absence of significant inelastic scattering at the interface, electrons in the particle cannot interact directly with atomic vibrations in the surrounding dielectric medium. As a result, electrons must first exchange energy with phonons within the metal particle, which are then coupled with atomic vibrations in the dielectric material through interface bonds. This results in significant spatial nonequilibrium between electrons and phonons in the metal and ultimately extra thermal resistance.

We note that the impact of nonequilibrium among different types of heat carriers also needs to be considered at cryogenic temperatures. In fact, Yoo and Anderson [12] observed anomalous increase in the *apparent* thermal interface resistance near the normal metal-superconductor transition temperature and attributed it to nonequilibrium between conduction electrons and thermal phonons. The nonequilibrium effect, however, does not play a significant role in the Josephson junctions discussed in the preceding section because the intrinsic thermal interface resistance due to mismatch in lattice vibrational properties is so much larger.

We use the continuum two-fluid model to gain useful physical insight without introducing mathematical complexity of advanced transport models. A very brief discussion of the following analysis was first presented in [6]. A more rigorous study using the Boltzmann transport equation is also currently under way. The two-fluid model has been widely used to study ultra-fast pulsed laser heating of metals [13,14]. A similar approach was used to explain the temperature dependence of the thermal conductance across interfaces between TiN films and MgO substrates [15], but there is some doubt about the accuracy of the experimental data used in that study. While classical molecular dynamics simulations can readily simulate heat transport by phonons in nanostructures, the accuracy of such simulations has yet to be verified. Accurate modeling of interface phenomena and simultaneous treatment of phonon and electron transport, in fact, remain a significant challenge for atomistic simulations.

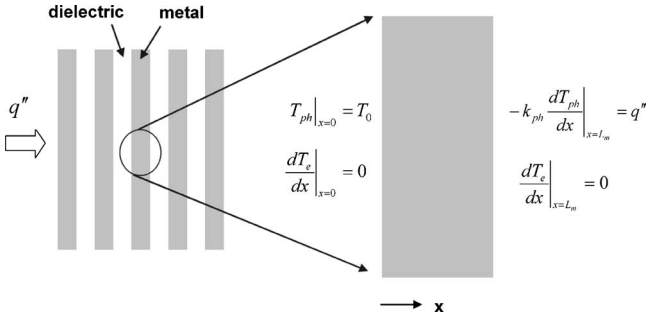

Fig. 3 Geometry and thermal boundary conditions used to analyze heat conduction across a metal layer sandwiched between two amorphous dielectric layers as part of a nanolaminate

The governing equations for the one-dimensional two-fluid heat conduction model are [14]

$$-\frac{d}{dx}\left(k_e\frac{dT_e}{dx}\right) = -G(T_e - T_{ph}) \tag{4a}$$

$$-\frac{d}{dx}\left(k_{ph}\frac{dT_{ph}}{dx}\right) = -G(T_e - T_{ph}) \tag{4b}$$

Subscripts *e* and *ph* are used to label quantities relevant to electrons and phonons, respectively. The electron-phonon coupling constant is denoted by G and the thermal conductivities by k.

We consider a metal film of thickness L_m that is sandwiched between two amorphous dielectric films and is subjected to uniform heat flux. The geometry considered is schematically illustrated in Fig. 3. The boundary conditions used in the present study are:

$$T_{ph}|_{x=0} = T_0, \quad -k_{ph}\left.\frac{dT_{ph}}{dx}\right|_{x=L_m} = q'', \quad \left.\frac{dT_e}{dx}\right|_{x=0,L_m} = 0 \tag{5}$$

Analytic solutions to Eqs. (4*a*), (4*b*), and (5) can be obtained if all the material parameters are assumed to be constant. Briefly, Eqs. (4*a*) and (4*b*) are added to form a homogeneous ordinary differential equation for $k_eT_e + k_{ph}T_{ph}$. The general solution of this homogeneous equation is then used to convert Eqs. (4*a*) and (4*b*) into separate second-order linear differential equations for T_e and T_{ph}. After solving the ODEs and applying the boundary conditions, we obtain

$$\frac{T_{ph} - T_0}{q''} = \left(\frac{\delta}{k_e + k_{ph}}\right)\left(\frac{1}{1 + \exp(L_m/\delta)}\right)\left(\frac{k_e}{k_{ph}}[\exp(L_m - x/\delta) - \exp(x/\delta) + 1 - \exp(L_m/\delta)] - \frac{1 + \exp(L_m/\delta)}{\delta/x}\right) \tag{6}$$

and

$$\frac{T_e - T_0}{q''} = \left(\frac{\delta}{k_e + k_{ph}}\right)\left(\frac{1}{1 + \exp(L_m/\delta)}\right)\left(\exp(x/\delta) - \exp(L_m - x/\delta) + \frac{k_e}{k_{ph}}[1 - \exp(L_m/\delta)] - \frac{1 + \exp(L_m/\delta)}{\delta/x}\right) \tag{7a}$$

An important parameter identified in Eq. (6) is the electron-phonon coupling length δ, which is defined as

$$\delta = \left(\frac{k_e k_{ph}}{G(k_e + k_{ph})} \right)^{1/2} \tag{7b}$$

It can be interpreted as the characteristic length of a region near the interface where electrons and phonons remain out of equilibrium with each other. Using the thermal conductivity ($k_e \sim 100$ W/m K, $k_{ph} \sim 5$ W/m K) and the electron-phonon coupling constant ($G \sim 10^{17}$ W/m^3 K) of typical metals [14], we estimate δ to be of the order of a few nanometers near room temperature. We note that a similar parameter was identified by Yoo and Anderson [12] in their study of superconductors and by Soviet researchers in their studies of electron-phonon drag and transport phenomena in semiconductors [16].

Figure 4 schematically shows the predicted phonon and electron temperature profiles across the metal film for three different values of L_m/δ. When the metal layer thickness L_m is comparable to the electron-phonon coupling length δ, the phonon and electron temperatures deviate from each other across the entire film. In the thick film limit, in contrast, the temperature deviation is confined to the vicinity of the interfaces and the two temperature profiles converge away from the interfaces.

The total thermal resistance of the metal film, defined in terms of phonon temperatures, is

$$R''_{\text{metal}} = \frac{T_{ph}|_{x=0} - T_{ph}|_{x=Lm}}{q''} = \frac{L_m}{k_{ph} + k_e} + 2\left(\frac{\delta}{k_{ph} + k_e} \right)\left(\frac{k_e}{k_{ph}} \right) \times \left(\frac{\exp(L_m/\delta) - 1}{\exp(L_m/\delta) + 1} \right) \tag{8}$$

The first term, proportional to the film thickness L_m, is identical to the solution of the conventional heat diffusion equation. The second term, to be labeled R''_{NE}, arises from spatial nonequilibrium between phonons and electrons near the interfaces and is a complex function of the thickness as well as the transport properties of the metal layer.

In the limit $L_m > \delta$, the nonequilibrium resistance R''_{NE} can be approximated as $2\delta/k_{ph}$, which is independent of the metal thickness L_m. This is equivalent to saying that heat conduction across a region of length δ from each interface is mediated only by phonons. Since the electron thermal conductivity is one or two orders of magnitude larger than the phonon thermal conductivity for typical metals, one can often neglect the first term of Eq. (8) and write $R''_{\text{metal}} = 2\delta/k_{ph} = \text{constant}$ (see Fig. 5).

In the opposite limit ($L_m \ll \delta$), the total thermal resistance of the metal layer can be approximated as $R''_{\text{metal}} \sim L_m/k_{ph}$. Note that the phonon thermal conductivity rather than the total thermal conductivity of the metal layer appears in the denominator. This shows that net heat conduction across an ultra-thin metal layer is mediated by phonons and not by electrons. This limiting behavior is consistent with the predicted temperature profiles shown in Fig. 4.

The present model is purely classical and does not take into account the quantum nature of electron transport. For electrons whose quantum wavelength is comparable to or larger than the thickness of a metal layer, the standing matter waves established across the layer may prevent any energy transport by electrons. This is consistent with the final result of the continuum model, but we caution the reader that the nature of electron-phonon coupling may not be rigorously captured in the two-fluid model in this limit.

The impact of the spatial electron-phonon nonequilibrium is most pronounced for noble metals, Au in particular, that have small electron-phonon coupling constants. Figure 5 shows the predicted R''_{metal} for metal films as a function of thickness using material parameters comparable to those of Au [11]. Studies of nanoparticles have shown that the electron-phonon coupling constant of Au does not exhibit significant size dependence. Since δ/k_{ph} is very large for Au, the two limiting behaviors of the thermal resistance discussed above can be readily recognized. At thickness below 20 nm, the thermal resistance increases rapidly with increasing thickness. In contrast, at thickness above 20 nm, the thermal resistance remains relatively constant. The conventional continuum heat conduction model predicts negligible thermal resistance for thin Au films.

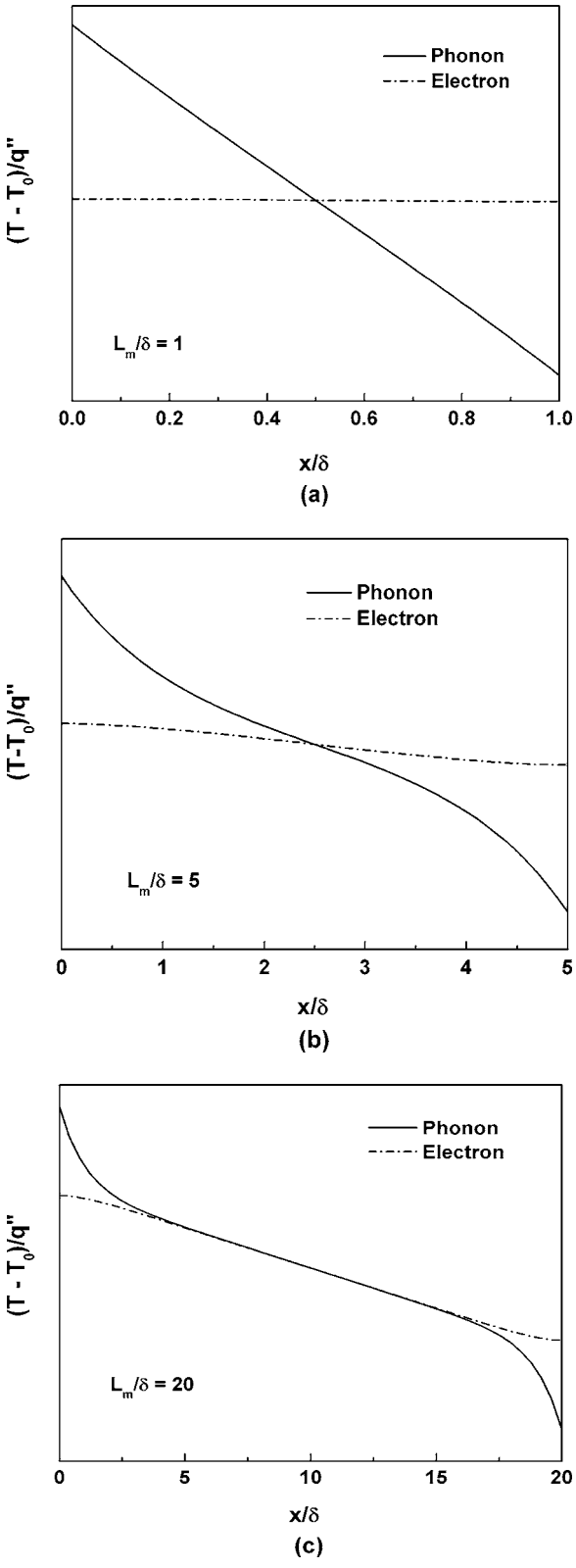

Fig. 4 Predicted electron and phonon temperature profiles in the metal layer for three cases with different values of L_m/δ

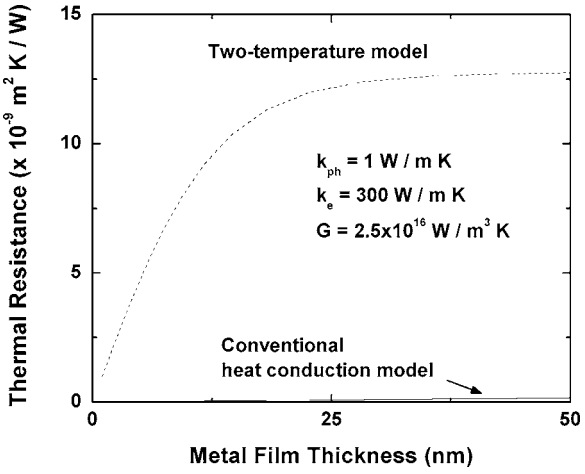

Fig. 5 Predicted out-of-plane thermal resistance of Au films sandwiched between two dielectric materials at room temperature. The dashed line is obtained using the present two-fluid heat conduction model and the sold line using the conventional heat conduction model.

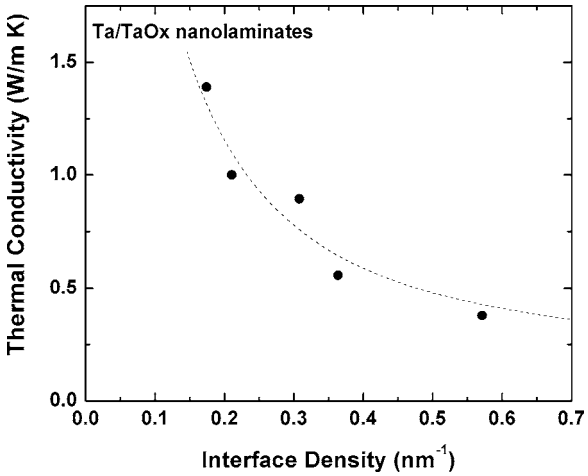

Fig. 6 The effective thermal conductivity of Ta/TaO*x* nanolaminates plotted as a function of interface density at room temperature. The symbols are experimental data [6] and the dotted line is the prediction of the present two-fluid model.

Thermal Resistance of Nanolaminates. The total thermal resistance per thickness of nanolaminates, or the inverse of the effective thermal conductivity, can be defined as

$$\frac{1}{k_{eff}} = \frac{L_d/k_d + R''_{\text{metal}} + R''_B}{L_m + L_d} \tag{9}$$

where k_d and L_d are the thermal conductivity and thickness of each dielectric layer, respectively, and R''_B is the *intrinsic* thermal boundary resistance.

Direct and independent measurements of k_{ph} and G of nanoscale metal films are very challenging and have not been reported in the literature. We examine instead whether the present model can explain trends observed in the existing data on nanolaminates of Ta/TaO*x* and W/AlO*x* [5,6] using a physically reasonable set of parameters. From the fact that the Ta and W films in these nanolaminates have electrical resistivities of approximately 100 $\mu\Omega$ cm, which is substantially higher than those of bulk metals, we anticipate that phonon scattering at defects and grain boundaries would result in very small phonon thermal conductivities. Even in bulk crystalline samples of pure Cu and Pt, the lattice conductivity is estimated to be only 5 W/m K at room temperature [17], which is two orders of magnitude smaller than the electronic thermal conductivity.

Figure 6 shows the effective thermal conductivity of the Ta/TaOx nanolaminates as a function of interface density, that is, the number of interfaces per unit thickness. The dotted line in Fig. 6 corresponds to the prediction of Eq. (9) with the following parameters: $k_{ph}=1$ W/m K, $R''_B=2\times10^{-9}$ m^2 K/W, $\delta=1$ nm. While this does not represent a unique set of parameters that can fit the data, it illustrates that the present model can explain the data using a physically reasonable set of model parameters. The TaOx layers in the laminates were produced using natural oxidation and we believe that difficulty in controlling the degree of Ta layer oxidation is responsible for the scatter in the data rather than the precision uncertainty in the experiments.

Figure 7 shows the thermal resistance per unit thickness of the W-AlOx nanolaminates [5] as a function of interface density. We choose to plot the inverse of the effective thermal conductivity for these nanolaminates to highlight the fact that, at high interface densities, the data deviate substantially from the linear behavior predicted by the conventional theory that does not take into account electron-phonon nonequilibrium. The interface resistance is obtained from a fit to the data at small interface densities and assumed to be constant. Because the extra thermal resistance R''_{NE} decreases with decreasing metal film thickness or increasing interface density, the conventional model overpredicts the total thermal resistance at high interface densities. The solid line in Fig. 7 corresponds to a fit obtained using Eq. (9) using a similar set of parameters as the Ta/TaOx nanolaminates.

While the fit is encouraging, we must also point out that there may be other physical mechanisms responsible for the observed deviation from the linear behavior. Pinholes in the ultra-thin AlOx layers, for example, can be filled with the metal, providing extra conduction paths for electrons. The electrical resistance of ultra-thin AlOx layers prepared using the nominally identical method, however, suggested that such conduction through pinholes would be negligible.

Another possibility is enhanced heat transfer between two metal layers via near-field radiative coupling. There are currently no experimentally confirmed quantitative model to predict energy transport via near-field radiative coupling. A heuristic model pro-

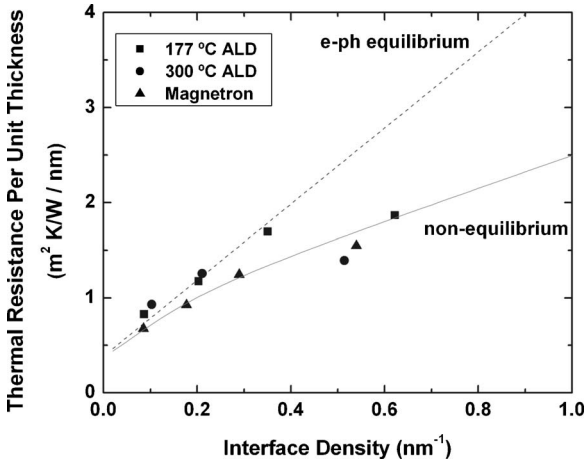

Fig. 7 The thermal resistance per unit thickness of W-AlO*x* nanolaminates at room temperature. The symbols are experimental data [5], the dotted line is the prediction of the conventional continuum heat conduction model, and the solid line is the prediction of the present two-fluid model. The nanolaminates were synthesized using the atomic layer deposition (ALD) technique at two different temperatures or using the magnetron sputtering technique (Magnetron) as described in [5].

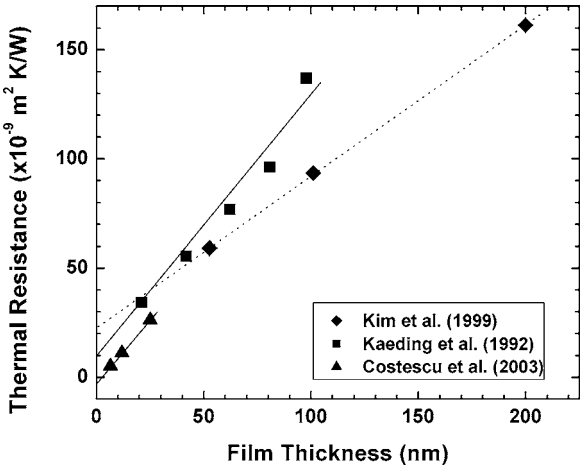

Fig. 8 The thermal resistance of SiO*x* films near room temperature reported in the literature [20,22,23] as a function of thickness. The *y* intercept is commonly interpreted as the thermal interface resistance.

posed by Xu et al. [18] predicts that the heat transfer rate would increase in inverse proportion to the cubic power of spacing between the metals and then reach a plateau when the spacing becomes comparable to the mean-free path of electrons. Our recent work [6], however, showed that the thermal resistance of nanoscale AlOx films sandwiched between two metallic films increases linearly with thickness and does not exhibit nonlinear dependence expected for near-field radiative coupling.

The thermal interface resistances we extract from both sets of the nanolaminate data are approximately 2×10^{-9} m^2 K/W. The present value is close to the prediction of the diffuse or acoustic mismatch model, but is significantly smaller than most previously reported values for interfaces between metal and amorphous dielectric materials [1,19]. The interface resistance between SiOx and Cr or Al thin films at room temperature, for example, was reported in some studies to be almost an order of magnitude larger [20,21].

It has been suggested that the presence of defects or contamination layers led to significant extrinsic thermal resistance, and large variations in the thermal resistance were reported even for comparable interfaces [20–24]. The nanolaminates we considered here were all synthesized in a controlled vacuum environment and much less likely to be affected by contaminations.

We should also point out significant challenges involved in accurate determination of the thermal interface resistance. Many previous studies estimated the thermal interface resistance by measuring the thermal resistance of dielectric films as a function of thickness and extrapolating the data to zero film thickness, as shown in Fig. 8. For films that are tens of nanometers thick, the interface resistance accounts for only a small fraction of the total resistance. Very precise measurements are therefore needed to extract the interface resistance. Uncertainties resulting from parasitic thermal resistance within samples, including that of the substrate, can also be appreciable. Our analysis of the previously reported thermal conductivity data of SiOx [24], for example, yielded a negative value for the thermal interface resistance. We believe that such an anomalous result is due to experimental bias errors rather than a real physical phenomenon.

Summary and Conclusions

The present manuscript reports a study of heat transport across metal-dielectric interfaces in micro- and nanoscale devices and structures of practical interest. Heat conduction in Josephson junctions is analyzed to illustrate the significance of thermal interface engineering in the thermal management of superconducting electronics. Minimizing the number of interfaces plays an important role in improving the critical power of SNS junctions. Experimental data also show that the diffuse mismatch model allows accurate quantitative prediction of the rate of heat transfer across interfaces in Josephson junctions at cryogenic temperatures.

The effective thermal conductivity of nanolaminates is analyzed to gain further insight into heat conduction across interfaces near room temperature. A theoretical model is presented to elucidate the effect of the close proximity of interfaces and electron-phonon nonequilibrium on heat conduction across metal-dielectric interfaces. The thermal interface resistance values extracted from Ta/TaOx and W/AlOx nanolaminates are significantly smaller than previously reported values for comparable metal-dielectric interfaces. The previous data may have been affected by the presence of contaminations layers or significant experimental uncertainties. The present results suggest that the diffuse mismatch model provides reasonable estimates of the thermal interface resistance even at elevated temperatures when these extrinsic effects are taken into account.

The present work does not explicitly consider any quantum mechanical effects, including coherent superposition of lattice waves reflected or transmitted by adjacent interfaces. While this might be reasonable for amorphous or highly defective thin films, more rigorous studies are needed to further elucidate quantum and ballistic effects not considered in the present work.

Nomenclature

c = phonon velocity, m/s
G = electron-phonon coupling constant, W/m^3 K
k = thermal conductivity, W/m K
k_B = Boltzmann constant, J/K
L = thickness of a layer, m
N = phonon distribution function, m^{-3} s
q'' = heat flux, W/m^2
r = radial coordinate, m
T = temperature, K
z = coordinate axis along nanolaminates, m
α = phonon transmission probability
δ = electron-phonon coupling length, m
h = Planck's constant, J s
ω = phonon frequency, rad/s
Ψ = ballistic energy transport coefficient, W/m^2 K^4

Subscripts

d = quantities pertaining to dielectric layers
e = quantities pertaining to electrons
m = quantities pertaining to metal layers
ph = quantities pertaining to phonons

References

[1] Swartz, E. T., and Pohl, R. O., 1989, "Thermal Boundary Resistance," Rev. Mod. Phys., **61**(3), pp. 605–668.
[2] Ju, Y. S., Lee, W.-Y., Cyrille, M.-C., Fontana, R. E., and Gurney, B. A., 2002, "Thermal Engineering of Giant Magnetoresistive (GMR) Sensors: Alternative Dielectric Gap," IEEE Trans. Magn., **38**(5), pp. 2259–2261.
[3] Ju, Y. S., 2006, "Nanoscale Thermal Phenomena in Tunnel Junctions for Spintronics Applications," ASME J. Electron. Packag., **128**(2), pp. 109–114.
[4] Ju, Y. S., and Lee, W. Y., 2003, US Patent No. 6,579,590.
[5] Costescu, R. M., Cahill, D. G., Fabreguette, F. H., Sechrist, Z. A., and George, S. M., 2004, "Ultra-Low Thermal Conductivity in W/Al2O3 Nanolaminates," Science, **303**(5660), pp. 989–990.
[6] Ju, Y. S., Hung, M.-T., Carey, M. J., Cyrille, M.-C., and Childress, J. R., 2005, "Nanoscale Heat Conduction across Tunnel Junctions," Appl. Phys. Lett., **86**, 203113.
[7] Chen, G., 1998, "Thermal Conductivity and Ballistic-Phonon Transport in the Cross-Plane Direction of Superlattices," Phys. Rev. B, **57**(23), pp. 14958–14973.
[8] Chong, Y., Dresselhaus, P. D., and Benz, S. P., 2003, "Thermal Transport in Stacked Superconductor-Normal Metal-Superconductor Josephson Junctions," Appl. Phys. Lett., **83**(9), pp. 1794–1796.
[9] Skocpol, W. J., Beasley, M. R., and Tinkham, M., 1974, "Self-Heating Hotspots in Superconducting Thin-film Microbridges," J. Appl. Phys., **45**, pp. 4054–4066.

[10] Klemens, P. G., 1958, "*Thermal Conductivity of Lattice Vibrational Modes*," Solid State Physics, Vol. 7, F. Seitz and D. Turnbull, eds., Academic, New York.
[11] Ju, Y. S., 2005 "Impact of Nonequilibrium between Electrons and Phonons on Heat Transfer in Metallic Nanoparticles Suspended in Dielectric Media," ASME J. Heat Transfer, **127**, pp. 1400–1403.
[12] Yoo, K.-H., and Anderson, A. C., 1986, "Thermal Impedance to Normal and Superconducting Metals," J. Low Temp. Phys., **63**, pp. 269–286.
[13] Anisimov, S. I., Kapeliovich, B. L., and Perelman, T. L., 1974, "Emission of Electrons from the Surface of Metals Induced by Ultrashort Laser Pulses," Zh. Eksp. Teor. Fiz., **66**(2), pp. 776–781.
[14] Qiu, T. Q., and Tien, C. L., 1993, "Heat-Transfer Mechanisms During Short-Pulse Laser-Heating of Metals," ASME J. Heat Transfer, **115**(4), pp. 835–841.
[15] Majumdar, A., and Reddy, P., 2004, "Role of Electron-Phonon Coupling in Thermal Conductance of Metal-Nonmetal Interfaces," Appl. Phys. Lett., **84**(23), pp. 4768–4770.
[16] Gurevich, Y. G., and Mashkevich, O. L., 1989, "The Electron-Phonon Drag and Transport Phenomena in Semiconductors," Phys. Rep., **191**(6), pp. 327–294.
[17] Berman, R., 1976, *Thermal Conduction In Solids*, Clarendon, Oxford.
[18] Xu, J.-B., Läuger, K., Möller, R., Dransfeld, K., and Wilson, I. H., 1994, "Heat Transfer Between Two Metallic Surfaces at Small Distances," J. Appl. Phys., **76**, pp. 7209–7216.
[19] Cahill, D. G., Ford, W. K., Goodson, K. E., Mahan, G. D., Majumdar, A., Maris, H. J., Merlin, R., and Phillpot, S. R., 2003, "Nanoscale Thermal Transport," J. Appl. Phys., **93**(2), pp. 793–818.
[20] Lee, S. M., and Cahill, D. G., 1997, "Heat Transport in Thin Dielectric Films," J. Appl. Phys., **81**(6), pp. 2590–2595.
[21] Kim, J. H., Feldman, A., and Novotny, D., 1999, "Application of the Three Omega Thermal Conductivity Measurement Method to a Film on a Substrate of Finite Thickness," J. Appl. Phys., **86**(7), pp. 3959–3963.
[22] Stoner, R. J., and Maris, H. J., 1993, "Kapitza Conductance and Heat-Flow Between Solids at Temperatures from 50 to 300 K," Phys. Rev. B, **48**(22), pp. 16373–16387.
[23] Kading, O. W., Skurk, H., and Goodson, K. E., 1994, "Thermal Conduction in Metallized Silicon-Dioxide Layers on Silicon," Appl. Phys. Lett., **65**(13), pp. 1629–1631.
[24] Costescu, R. M., Wall, M. A., and Cahill, D. G., 2003, "Thermal Conductance of Epitaxial Interfaces," Phys. Rev. B, **67**(5), 054302.

Energy Transport and Nanostructuring of Dielectrics by Femtosecond Laser Pulse Trains

Lan Jiang

Hai-Lung Tsai
e-mail: tsai@umr.edu

Laser-Based Manufacturing Laboratory,
Department of Mechanical and Aerospace Engineering,
University of Missouri-Rolla,
Rolla, MO 65409

This study analyzes single burst ablation of dielectrics by a femtosecond pulse train that consists of one or multiple pulses. It is found that (1) there exist constant-ablation-depth zones with respect to fluence for one or multiple pulses per train and (2) for the same total fluence per train, although the ablation depth decreases in multiple pulses as compared to that of a single pulse, the depth of the constant-ablation-depth zone decreases. In other words, repeatable structures at the desired smaller nanoscales can be achieved in dielectrics by using the femtosecond pulse train technology, even when the laser fluence is subject to fluctuations. The predicted trends are in agreement with published experimental data. [DOI: 10.1115/1.2241979]

Keywords: femtosecond laser, pulse train, quantum mechanics, nanostructure, dielectrics

1 Introduction

An ultrashort (<10 ps) laser pulse can fully ionize almost any solid material and greatly reduce recast, microcracks, and heat-affected zone. Hence, ultrashort lasers are very promising for the micro-/nano-fabrication of all types of materials, especially dielectrics [1–9]. Recent developments of nonlinear optical devices make it possible to obtain almost any arbitrary pulse shapes. Many studies have been reported regarding pulse shaping and its effects on laser-material interactions. For example, by using shaped pulse trains, (1) the ionization process can be controlled [10]; (2) atoms can be selectively ionized [11]; (3) the molecular ground-state rotational dynamics can be manipulated [12]; (4) chemical reactions can be controlled [13]; and (5) the x-ray line emission from plasmas under a femtosecond pulse can be significantly enhanced [14].

These aforementioned abilities of shaped pulse-trains are useful to control and improve micro-/nano-scale processing of dielectrics [3,15,16] and semiconductors [17,18]. Chowdhury et al. [3] conducted pump-probe experiments on femtosecond double-pulse ablation of fused silica through investigating the plasma dynamics at various pulse separation times [3]. Stoian et al. [16] demonstrated an improvement in the quality of femtosecond laser microstructuring of dielectrics by using temporally shaped pulse trains [15]. Stoian et al. [15] further presented the implementation of a self-learning loop on temporal shaping, which again illustrated that under certain excitation conditions, the material response can be guided [16]. The same group showed that this technology is also effective in laser silicon processing and suitable to generate controllable ion beams [17]. Similar work was reported by Choi et al. [18] as well.

Although some explanations were given for possible reasons leading to better ablation quality by pulse train technology, there is no theoretical analysis to directly support the results. As there are many process parameters, such as the pulse profile, pulse separation, number of pulses per train, and fluences, it is very difficult to optimize the process to achieve the best possible ablation quality without a fundamental understanding of the ablation mechanisms.

This study employs the plasma model recently developed by the authors [7–9] to investigate the pulse-train technology, in which quantum theories are employed to calculate the time and space dependent optical and thermal properties, including the electron heat capacity, electron relaxation time, electron conductivity, reflectivity, and absorption coefficient. This paper calculates the ablation of fused silica by a single pulse and pulse-trains consisting of multiple pulses. It is shown that there exist constant-ablation-depth zones with respect to fluence in the femtosecond pulse-train technology by which repeatable nanostructures can be obtained, even when the laser system is subject to fluctuations in fluence.

2 Theory

2.1 Assumptions. Energy transport in the ultrashort laser ablation process can be divided into two stages: (1) the photon energy absorption, mainly through free electron generation and heating, and (2) the redistribution of the absorbed energy to the lattice leading to material removal [4,9]. This stage separation is based on the assumption that free electron generation and heating are completed in such a short time that the lattice temperature remains unchanged within the duration of a femtosecond laser pulse ($\sim$120 fs). The present study is concerned with the first stage of the energy transport, while the lattice temperature remains unchanged in the subpicosecond time regime [7,8].

Building-up of free electrons is necessary to initiate the laser ablation process of dielectrics. It is widely assumed that the ablation starts when the free electron density reaches the critical density [1,6–8,19–22]. For femtosecond lasers, the critical density is selected as the free electron density at which the plasma oscillation frequency is equal to the laser frequency. Once the critical density is created, the originally transparent or semitransparent material becomes opaque, and a large percentage of the absorbed laser energy is deposited in a thin surface layer (tens to thousands of nanometers) within the femtosecond pulse duration [4,20,21]. This leads to the ablation of the thin layer, which starts a few to tens of picoseconds later [4,20–23]. Hence, laser threshold fluence can be considered as the minimal fluence that just creates the critical density [1,6–8,19–22]. Since the free electrons in the thin ablation layer are excited up to tens of electron volts, the Coulomb explosion, electrostatic ablation, or nonequilibrium thermal ablation, instead of melting, dominate after the ionization process [4,5,21]. Thus, under the irradiation of a femtosecond pulse or femtosecond pulse train with subpicosecond-or-shorter pulse

Contributed by the Heat Transfer Division of ASME for publication in the JOURNAL OF HEAT TRANSFER. Manuscript received December 21, 2005; final manuscript received May 2, 2006. Review conducted by Costas Grigoropoulos.

separation time, hydrodynamic (liquid phase) motion of a dielectric is generally negligible. As a result, comparing with long (>10 ps) pulses or pulse trains (including the pulse separation time), melting and recast are greatly reduced and negligible.

This paper investigates a single burst ablation of dielectrics by a femtosecond pulse train with subpicosecond pulse separation, in which a "burst" means the laser irradiation of the whole pulse train may consist of one or multiple pulses. Our calculations are within the single burst irradiation in the subpicosecond time scale before the change of lattice temperature actually happens. In the limit of negligible recast, ablation depth can be considered to be the maximum depth at which the free electron density is equal to the critical density in a given processing window [7,8,19,20]. Similarly, the ablation crater shape corresponds to the ionized region at which the free electron density is greater than or equal to the critical density [7,8,19,20].

2.2 Free Electron Generation: Ionization. The following expression derived from the Fokker-Planck equation is used to calculate the free electron generation [1,6,8,19,20], in which the electron decay term is also considered [1]:

$$\frac{\partial n_e(t,r,z)}{\partial t} = a_i I(t,r,z) n_e(t,r,z) + \delta_N (I(t,r,z))^N - \frac{n_e(t,r,z)}{\tau} \quad (1)$$

where t is the time; r is the distance to the Gaussian beam axis; z is the depth from the surface of the bulk material; τ is the decay time constant; $n_e(t,r,z)$ is the free electron density; a_i is the avalanche ionization constant; $I(t,r,z)$ is the laser intensity inside the bulk material; and δ_N is the cross section of N-photon absorption. Based on experimental measurements of the threshold fluences at the wavelength of 780 nm for fused silica, $a_i = 4 \pm 0.6$ cm^2/J, $\delta_6 = 6 \times 10^{8 \pm 0.9}$ cm^{-3} ps^{-1}(cm^2/TW)^6 [2], and $\tau = 60$ fs [1].

Since the model calculates the electron density distribution within hundreds of femtoseconds, this study ignores electron-lattice energy exchange that is on the order of picoseconds [19]. This assumption was well justified in Refs. [19,20] by experiments and comparison simulations. Also, our related work [24] shows that, for free electron generation in dielectrics, the contribution of electron-phonon interaction is at least two orders of magnitudes smaller than the contribution of ionizations within a femtosecond pulse duration, t_p. Further, the contribution of electron energy diffusion and the electron distribution change because of the Joule heating are, respectively, two and four orders of magnitudes smaller than the contribution of ionization within t_p [24]. Hence, the electron diffusion is also neglected in our model.

2.3 Laser-Plasma Interaction: Optical Properties. The original laser beam before it interacts with the material is assumed to be a Gaussian distribution in time and space. It is assumed that the laser focus point is at the material surface, $z = 0$. Considering time and space dependent optical properties, the laser intensities inside the bulk materials are expressed as [7,8]

$$I(t,r,z) = \frac{2F}{\sqrt{\pi/\ln 2}\, t_p}(1 - R(t,r)) \times \exp\left(- \frac{r^2}{r_0^2} - (4 \ln 2)\left(\frac{t}{t_p}\right)^2 - \int_0^z \alpha(t,r,z)dz \right) \quad (2)$$

where F is the laser fluence; t_p is the pulse duration; $R(t,r)$ is the reflectivity; r_0 is the radius of the laser beam that is defined as the distance from the center at which the intensity drops to $1/e^2$ of the maximum intensity; and $\alpha(t,r,z)$ is the absorption coefficient.

The laser intensity distribution inside the material can be determined if the time and space dependent reflectivity and absorption coefficient are obtained. The optical properties of the highly ionized dielectrics under a femtosecond pulse can be well determined by plasma properties [2]. In this study, the Drude model for the plasma in the metals and doped semiconductors is used to determine the optical properties of the ionized dielectrics. The spatial and temporal dependent dielectric function of the plasma is expressed as [25]

$$\boldsymbol{\epsilon}(t,r,z) = 1 + \left(\frac{n_e(t,r,z)e^2}{m_e \epsilon_0} \right) \left(\frac{-\tau_e^2(t,r,z) + i\tau_e(t,r,z)/\omega}{1 + \omega^2 \tau_e^2(t,r,z)} \right) \quad (3)$$

where e is the electron charge; m_e is the mass of electron; ϵ_0 is the electrical permittivity of free space; $\tau_e(t,r,z)$ is the free electron relaxation time; and ω is the laser frequency. The plasma frequency is defined by [26]

$$\omega_p(n_e) = \sqrt{\frac{n_e(t,r,z)e^2}{m_e \epsilon_0}} \quad (4)$$

At the critical electron density, n_{cr}, the plasma frequency is equal to the laser frequency. Hence,

$$n_{cr} = \frac{4\pi^2 c^2 m_e \epsilon_0}{\lambda^2 e^2} \quad (5)$$

where c is the scalar speed of light in vacuum and λ is the wavelength of the laser. The complex dielectric function can be split into the real and imaginary components as follows

$$\boldsymbol{\epsilon}(\mathrm{t,r,z}) = \epsilon_1(t,r,z) + i\epsilon_2(t,r,z) = \left(1 - \frac{\omega_p^2(n_e)\tau_e^2(t,r,z)}{1 + \omega^2 \tau_e^2(t,r,z)}\right) + i\left(\frac{\omega_p^2(n_e)\tau_e(t,r,z)}{\omega\left(1 + \omega^2 \tau_e^2(t,r,z)\right)} \right) \quad (6)$$

The relationship between the complex refractive index, **f**, and the complex dielectric function is given by

$$(\mathbf{c}/\mathbf{v}) = \mathbf{f} = (f_1 + if_2) = \sqrt{\boldsymbol{\epsilon}} = \sqrt{\epsilon_1 + i\epsilon_2} \quad (7)$$

where **c** is the velocity of light in vacuum; **v** is the velocity of light in the material; f_1 is the normal refractive index; and f_2 is the extinction coefficient. Thus, the f_1 and f_2 functions are

$$f_1(t,r,z) = \sqrt{\frac{\epsilon_1(t,r,z) + \sqrt{\epsilon_1^2(t,r,z) + \epsilon_2^2(t,r,z)}}{2}}$$
$$f_2(t,r,z) = \sqrt{\frac{-\epsilon_1(t,r,z) + \sqrt{\epsilon_1^2(t,r,z) + \epsilon_2^2(t,r,z)}}{2}} \quad (8)$$

The reflectivity of the ionized material is determined by the following Fresnel expression at the surface

$$R(t,r) = \frac{(f_1(t,r,0) - 1)^2 + f_2^2(t,r,0)}{(f_1(t,r,0) + 1)^2 + f_2^2(t,r,0)} \quad (9)$$

The absorption coefficient of laser intensity by the plasma via the free electron heating is calculated by

$$\alpha_h(t,r,z) = \frac{2\omega f_2(t,r,z)}{c} \quad (10)$$

Note that Eq. (10) represents only a part of the laser energy that is absorbed via free electron heating, and there is another part of absorption that is via ionization. The total absorption coefficient, α, accounting for both the free electron heating absorption and the absorption through avalanche ionization and multiphoton ionization is [7]

$$\alpha(t,r,z) = (a_i n_e(t,r,z) + \delta_N (I(t,r,z))^{N-1}) \times (\langle \boldsymbol{\epsilon}(t,r,z) \rangle + U_I) \quad (11)$$

where $\langle \boldsymbol{\epsilon}(t,r,z) \rangle$ is the average kinetic energy of free electrons and U_I is the band gap of materials. For fused silica, $U_I = 9$ eV. Note α in Eq. (11) is used in Eq. (2) in Sec. 2.3 for various pulse absorption mechanisms including free electron heating and generation (ionizations), while α_h in Eq. (10) is used for free electron heating which is explained in Sec. 2.4.

2.4 Free Electron Heating: Electron Relaxation Time. The free electron relaxation time in Eq. (3) is calculated by the following quantum estimation derived from the Boltzmann transport equation [27]

$$\tau_e(t,r,z) = \frac{1}{\nu_{ei}} = \frac{3\sqrt{m_e}(k_B T(t,r,z))^{3/2}}{2\sqrt{2}\pi(Z^*)^2 n_e(t,r,z)e^4 \ln\Lambda} \times (1+\exp(-\mu(n_e,T)/k_B T(t,r,z)))F_{1/2} \quad (12)$$

$$\ln\Lambda = \frac{1}{2}\ln\left(1+\left(\frac{b_{\max}}{b_{\min}}\right)^2\right) \quad (13)$$

where T is the electron temperature, k_B is the Boltzmann's constant, Z^* is the ionization state; μ is chemical potential; $F_{1/2}$ is the Fermi integral. The maximum ($b_{\max}$) and minimum ($b_{\min}$) collision parameters are given by [28]

$$b_{\max} = \frac{(k_B T/m_e)^{1/2}}{\max(\omega,\omega_p)}; \quad b_{\min} = \max\left(\frac{Z^* e^2}{k_B T}, \frac{h}{2\pi(m_e k_B T)^{1/2}}\right) \quad (14)$$

where h is the Planck constant.

However, at the very beginning of laser ablation, the electron kinetic energy is relatively low, and contributions to the free electron relaxation time from electron-phonon collisions could be important. Hence, in this study when the electron kinetic energy is lower than or comparable to the Fermi energy, the contributions of both electron-phonon and electron-ion collisions are considered, and the free electron relaxation time is determined by [28]

$$\tau_e = \frac{1}{\nu_e} = \frac{1}{\nu_{ei}} + \frac{1}{\nu_{ep}} \quad (15)$$

where ν_{ei} is the electron-ion collision frequency and ν_{ep} is the electron-phonon collision frequency determined by

$$\frac{1}{\nu_{ep}} = \left(\frac{M}{m_e}\right)^{1/2}\frac{\hbar}{U_{\rm IP}}\frac{T_D}{T_l}\left(\frac{n_e(t,r,z)}{n_{\rm cr}}\right)^{1/3} \quad (16)$$

where M is the atomic mass unit; $\hbar = h/2\pi$ is the reduced Planck constant; $U_{\rm IP}$ is the ionization potential that is 13.6 eV for fused silica [25]; T_D is the Debye temperature (290 K for fused silica); and T_l is the lattice temperature in K that is assumed to be a constant (300 K, room temperature) during the laser pulse duration. Equation (16) is derived for the plasma with a time-dependent electron density based on Refs. [21,27].

For free electrons modeled as "particle in a box," the chemical potential can be calculated by [26]

$$\mu(n_e,T) = \epsilon_F(n_e) \times \left[1 - \frac{\pi^2}{12}\left(\frac{k_B T(t,r,z)}{\epsilon_F(n_e)}\right)^2 + \frac{\pi^2}{80}\left(\frac{k_B T(t,r,z)}{\epsilon_F(n_e)}\right)^4\right] \quad (17)$$

where the higher order terms are neglected and ϵ_F is the Fermi energy that is determined by

$$\epsilon_F(n_e) = \left(\frac{(hc)^2}{8m_e c^2}\right)\left(\frac{3}{\pi}\right)^{2/3}(n_e(t,r,z))^{2/3} \quad (18)$$

where c is the scalar speed of light in vacuum. And the electron temperatures are determined by

$$c_e(T,n_e)n_e(t,r,z)\frac{\partial T(t,r,z)}{\partial t} = \alpha_h(t,r,z)I(t,r,z) \quad (19)$$

where c_e is the specific heat of free electrons which can be determined by

$$c_e(T_e) = \left(\frac{\partial\langle\epsilon\rangle}{\partial T_e}\right)_V \quad (20)$$

The average kinetic energy, $\langle\epsilon\rangle$, is determined by the Fermi-Dirac distribution

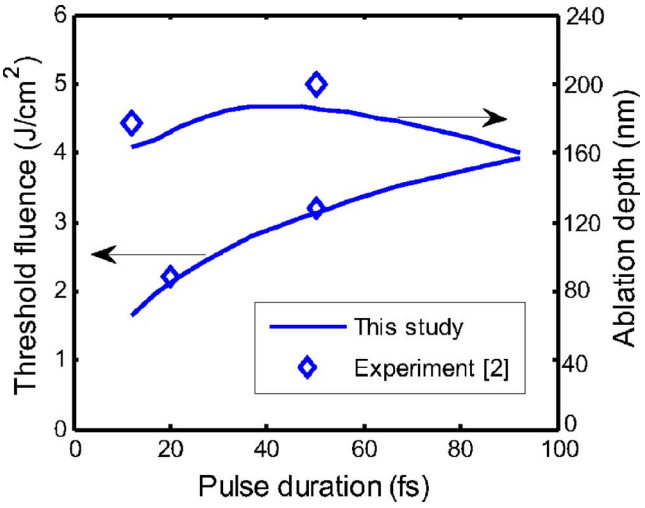

Fig. 1 The theoretical and experimental threshold fluences and ablation depths as a function of pulse duration by a single pulse at the fluence of 5 J/cm² and the wavelength of 780 nm

$$\langle\epsilon\rangle = \frac{\sum_k \langle n_k\rangle\epsilon_k}{N_e} = \frac{\int_0^\infty \frac{1}{e^{\beta(T)(\epsilon-\mu(n_e,T))}+1}\rho(\epsilon)\epsilon d\epsilon}{\int_0^\infty \frac{1}{e^{\beta(T)(\epsilon-\mu(n_e,T))}+1}\rho(\epsilon)d\epsilon} \quad (21)$$

where $\beta(T) = 1/k_B T(t,r,z)$ and $\rho(\epsilon)$ is the density of states given by

$$\rho(\epsilon) = \frac{8\sqrt{2}\pi m_e^{3/2}}{h^3}\sqrt{\epsilon} \quad (22)$$

It is assumed that a small volume of material is ablated if its free electron density is equal to or above the critical electron density. The aforementioned equations are solved by an iteration method detailed in Ref. [8].

3 Results and Discussion

3.1 Threshold Fluence, Ablation Depth, and Ablation Shape. Figure 1 shows the threshold fluence and ablation depth as a function of pulse duration for a pulse train consisting of one pulse (a single pulse can also be considered as multipulses with zero pulse separation) at the fluence of 5 J/cm² and the wavelength of 780 nm. It is seen that the predictions by the present study are in agreement with the available experimental results at different pulse durations [2]. The validation is not extended into a pulse duration range where the nominal ablation fluence is close to the threshold fluence (and hence the ablation depth is very sensitive to fluence fluctuations). On the other hand, our predictions of the ablation depth and threshold fluence for barium aluminum borosilicate (BBS) in the pulse duration range 40–800 fs are consistent with experimental data. However, due to the page limitation, the results of BBS are not included in this paper.

In our simulations, a train may consist of single or multiple pulses and all have the pulse duration of 50 fs and the wavelength of 780 nm. The pulses within a train have the same fluence. For a train consisting of one pulse, the ablation threshold fluence is found to be 3.3 J/cm². For double pulses per train, the ablation thresholds are found to be 1.8, 1.9, and 2.3 J/cm² per pulse, i.e., 3.6, 3.8, and 4.6 J/cm² per train, at the separation times of 50 fs, 100 fs, and 300 fs, respectively. The ablation shapes are shown in Fig. 2, in which the single pulse at 5 J/cm² is also considered as

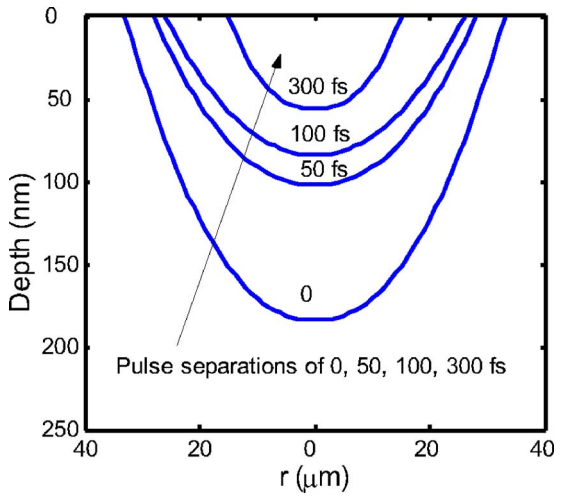

Fig. 2 Ablation crater shapes by pulse trains consisting of double pulses with the total fluence of 5 J/cm^2

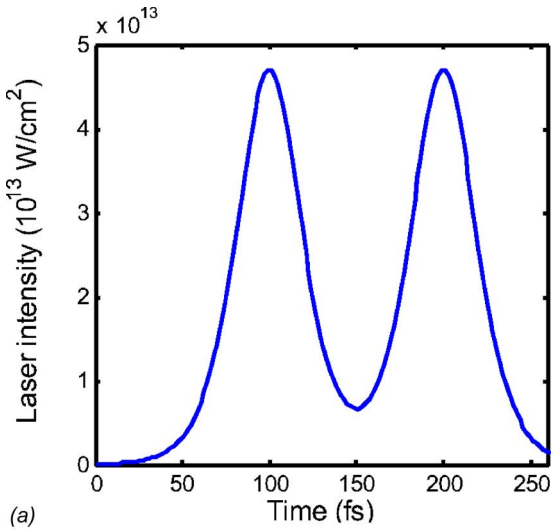

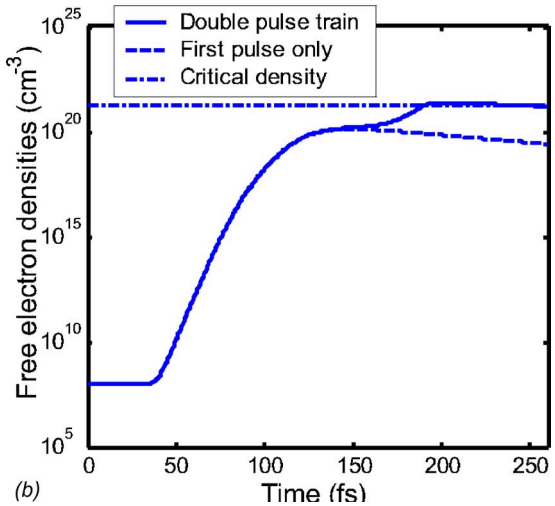

Fig. 3 (*a*) Laser intensity distribution and (*b*) electron density at $r=0$, $z=1$ nm for double-pulse train with the total fluence of 5 J/cm^2 and pulse separation of 100 fs

a train consisting of double pulses at 2.5 J/cm^2 per pulse with zero pulse separation. At the total fluence of 5 J/cm^2 and the beam spot size of 100 μm, by using the train consisting of double pulses, the ablation depths are 184, 102, 84, and 56 nm, at the pulse separations of 0, 50, 100, and 300 fs, respectively. The ablation depth decreases with the increases of pulse delay, which was also experimentally observed [3]. The corresponding ablation crater diameters for these four cases are 66, 56, 52, and 30 μm, respectively, using the laser beam with a spot size of 100 μm.

It is shown that at the same total fluence, the use of double pulses can obtain smaller structures, which also implies lower throughput as compared to the case of single pulse, which was also observed in experiments [3]. This is because of the lower free electron density as compared to single pulse per train at the same fluence. Specifically, the highest electron density decreases: 3.3×10^{21}, 2.7×10^{21}, 2.6×10^{21}, and 2.2×10^{21} cm^{-3} corresponding to the increases of pulse separation: 0, 50, 100, and 300 fs, respectively. This is due to: (1) the free electrons generated by multiphoton ionization are proportional to I^6 for fused silica at the laser wavelength of 780 nm; (2) the electron decay term in Eq. (1) becomes more significant as the pulse separation time increases; and (3) the surface-generated plasma by the previous pulse(s) interferes with the subsequent pulse(s).

3.2 Transient Localized Free Electron Distribution. The results in Sec. 3.1 demonstrate that it is possible to manipulate transient free electron density distributions inside the dielectrics by shaping pulse train to achieve better ablation quality. The manipulability of energy distribution by the pulse train technology makes it possible to control the transient (femtosecond time scale), localized (nanometer length scale) significantly varying free electron densities of the irradiation area which in turn determines the optical and thermal properties. This is an important reason leading to the advantages of the pulse train technique. As an example, Fig. 3 demonstrates the transient localized properties under a double-pulse burst with the fluence of 2.5 J/cm^2 per pulse and the pulse separation of 100 fs. The calculation starts at the $2t_p$, where t_p is the pulse duration (i.e., 50 fs), before the peak of the first pulse in a train.

The laser intensity distribution at $r=0$ is shown in Fig. 3(*a*). Under this double-pulse train, the free electron generation is dominated by the first pulse only until 150 fs at which the free electron density reaches about 1.3×10^{20} cm^{-3} as shown in Fig. 3(*b*). In contrast, the peak free electron density is 2.4×10^{21} cm^{-3}, which is about 18 times greater than the contribution of the first pulse alone. This is mainly due to the enhancement of avalanche ionization process at a higher free electron density [6–8,19,20], i.e., the building-up of free electrons by the first pulse greatly enhances the free electron generation through avalanche ionization during the second pulse. It is possible to achieve the desired electron dynamics (hence optical and thermal properties) by carefully adjusting the pulse train parameters, such as the pulse separation, number of pulses, and pulse fluence distribution, and among which the pulse separation time is convenient to change.

3.3 Pulse Separation Time. The effect of the pulse separation can be visualized through comparisons of the laser intensity distributions as shown in Fig. 4, in which the dashed line represents the original laser energy at $r=0$ before it interacts with the materials and the solid line represents the laser energy transmitted into the material at $r=0$. After the free electron density becomes comparable to the critical density, the original beam profile is strongly shaped by the generated plasma which can be quantified by the transient reflectivity as shown in Fig. 5(*a*). At $r=0$, the peak reflectivity is 0.95, 0.94, 0.93, and 0.84 for the pulse separations of 0, 50, 100, and 300 fs, respectively, due to lower free

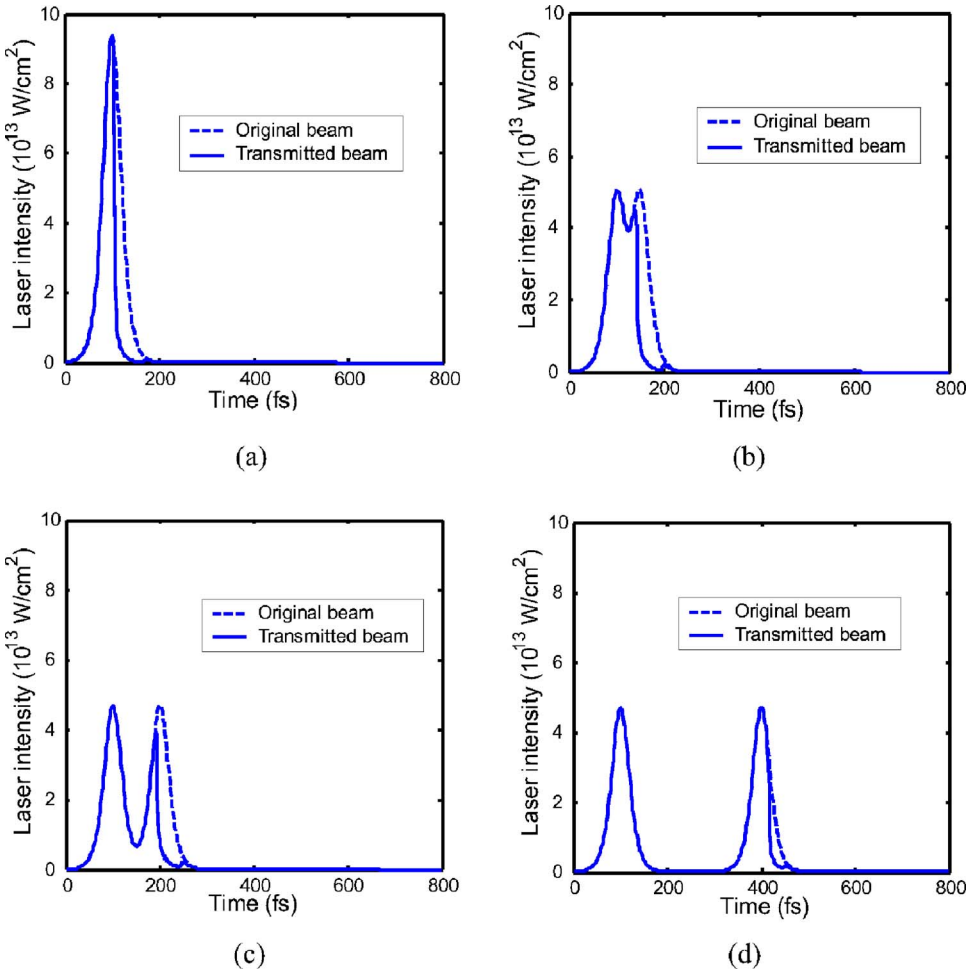

Fig. 4 Center ($r=0$) laser intensity distributions: (*a*) single pulse per train at 5 J/cm^2 per pulse (also considered as 2 pulses at 2.5 J/cm^2 with 0 pulse separation); (*b*) 2 pulses per train at 2.5 J/cm^2 per pulse (pulse separation is 50 fs); (*c*) 2 pulses per train at 2.5 J/cm^2 per pulse (pulse separation is 100 fs); (*d*) 2 pulses per train at 2.5 J/cm^2 per pulse (pulse separation is 300 fs)

electron density at a longer pulse separation. In contrast, the reflectivity of bulk fused silica is almost zero at the room temperature and the wavelength of 780 nm. Figure 5(*b*) shows the overall reflectivity integrated for the time period during the pulse irradiations. The overall reflectivity significantly decreases as the pulse separation increases. The highest overall reflectivity integrated for the time period during the pulse irradiations is 0.34, 0.29, 0.26, and 0.08 at the separations of 0, 50, 100, and 300 fs, respectively.

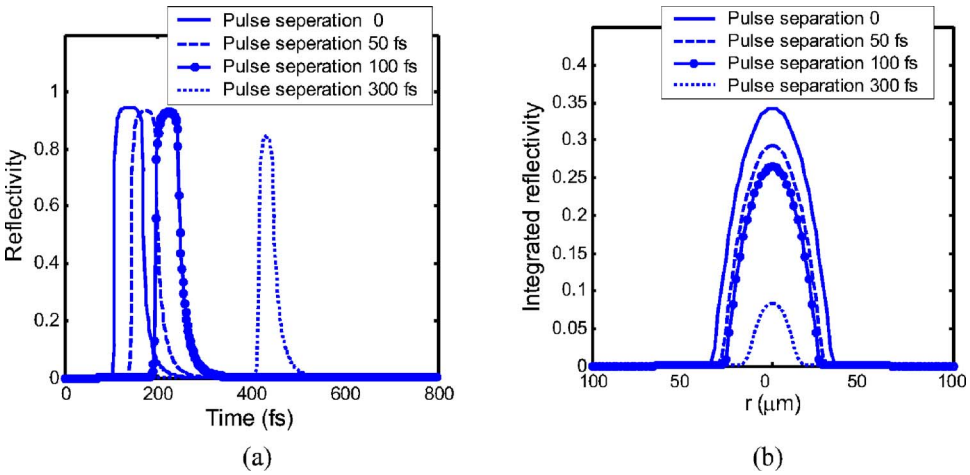

Fig. 5 The reflectivity at $r=0$ at different pulse separation times: (*a*) transient reflectivity and (*b*) integrated reflectivity

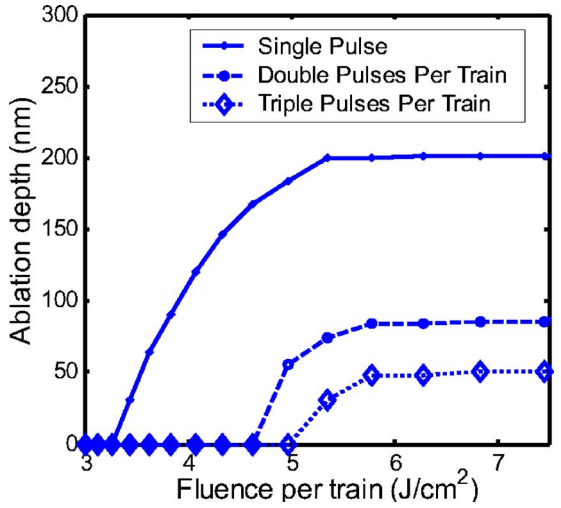

Fig. 6 The ablation depth as a function of total fluence per train; the separation time between pulses for double pulses is 300 fs and for triple pulses is 200 fs

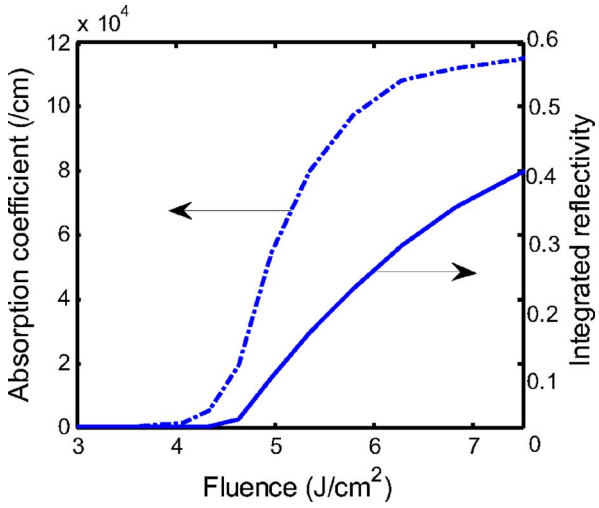

Fig. 7 Surface center integrated reflectivity and absorption coefficient at $t=425$ fs (the end of the second pulse) under the double-pulse train with separation time of 300 fs

3.4 Fluence. The ablation depth strongly depends on the fluence. For comparison purpose, the fluences in Fig. 6 are in terms of total fluence per train instead of per pulse. As shown in Fig. 6, there are constant-ablation-depth zones with respect to fluences, which are due to the fact that the overall reflectivity and absorption coefficient significantly increase with the increase of fluences [6–8,19,20]. If there exists a constant-ablation-depth zone with respect to fluences, in similar conditions, a flat-bottom crater would be formed under a Gaussian beam, which has been experimentally observed [3,29,30]. Also, a constant-ablation-depth zone with respect to fluences has been directly demonstrated in experiments [31,32]. Note a constant-ablation-depth zone with respect to fluences exists only in a limited fluence range, and the ablation depth may significantly increase if the fluence continues to increase [32,33].

A constant-ablation-depth zone with respect to fluences can be used to improve the repeatability in laser nano-/microfabrications. Laser pulse fluence is subject to fluctuations, which may lead to significant variations in ablation depth especially at fluences slightly above the ablation threshold. Hence, for the case of single pulse per train, it is difficult to control the accuracy for ablation depth below 200 nm as shown in Fig. 6. For example, the ablation depth at 4 ± 0.5 J/cm^2 by a single pulse per train would vary in the range of 47–157 nm. Hence, a slight variation in fluence will result in a large difference in ablation depth. This explains the poor repeatability in the femtosecond ablation of nanostructures using fluences slightly above the ablation threshold [34]. On the other hand, the ablation depth at 6.5 ± 0.5 J/cm^2 is quite stable and is around 200 nm, which is the theoretical limit of repeatable accuracy by the femtosecond single pulse per train for the process window employed in the present study. In contrast, using double pulses per train with the pulse separation time of 300 fs, the ablation depth can be accurately controlled to around 85 nm at 6.5 ± 0.5 J/cm^2, which provides a potential method to achieve repeatable nanostructures. Similarly, using triple pulses per train with the pulse separation time of 200 fs, the ablation depth can be controlled to around 49 nm at 6.5 ± 0.5 J/cm^2. Hence, by using the constant-ablation-depth zones with respect to fluences, repeatable nanostructures at the desired dimension can be obtained, even when the laser system is subject to fluctuations in fluences.

The existence of a constant-ablation-depth zone is caused mainly by the changes of optical properties. As shown in Fig. 7, under the double pulses with separation time of 300 fs, at $r=0$, and $t=425$ fs (the end of the second pulse), the absorption coefficients in the surface layer (numerically 1 nm) at the total fluence per train of 4, 5, and 7.5 J/cm^2 are, respectively, 1.6×10^3, 5.6×10^4, and 1.2×10^5 /cm, and the corresponding overall integrated reflectivity are 0.01, 0.08, and 0.4, respectively. Hence, as the total fluence increases, the percentage of the reflected energy increases, and the percentage of the absorbed laser energy deposited in a given thin surface layer also increases. The increase of both the overall reflectivity and the absorption coefficient tend to decrease and attenuate the laser intensity in the material and, as a result, decrease the ablation depth. Hence, roughly speaking, there exists a certain fluence range during which the "negative" effect on ablation depth due to the increases of reflectivity and absorption coefficient "offsets" the increase of the fluence, resulting in a constant-ablation-depth zone. The constant-ablation-depth zone of a pulse train is lower than that of a single pulse per train, as shown in Fig. 7, because for the same total fluence the ablation depth is lowered by a pulse train with multiple pulses.

4 Conclusions

This study employs the validated plasma model with quantum treatments to investigate the pulse-train ablation of dielectrics. The following major conclusions are made from the simulation results:

- The previous pulse has significant effects on the thermal and optical properties for the subsequent pulse within the same train. At the same total fluence, the overall reflectivity significantly decreases as the pulse separation increases.
- The pulse-train technology can obtain smaller structures, although its throughput is relatively low as compared to the case of single pulse at the same total fluence.
- By using constant-ablation-depth zones with respect to fluences in the femtosecond pulse-train technology, repeatable nanostructures at the desired dimension can be obtained, even when the laser system is subject to fluctuations in laser fluences. However, a constant- ablation-depth zone with respect to fluences exists only in a limited fluence range.
- The predicted trends are in agreement with published experimental observations.

Acknowledgment

This work was supported by the Air Force Research Laboratory under Contract No. FA8650-04-C-5704 and the National Science Foundation under Grant No. 0423233.

Nomenclature

a_i = avalanche ionization constant
$b_{\max}$ = maximum collision parameter, Eq. (14)
$b_{\min}$ = minimum collision parameter, Eq. (14)
c = scalar speed of light in vacuum
$\mathbf{c}$ = vector velocity of light in vacuum
c_e = average specific heat per electron
e = electron charge
$\mathbf{f}$ = complex refractive index
f_1 = normal refractive index
f_2 = extinction coefficient
F = laser fluence
h = Planck constant
$\hbar$ = reduced Planck constant
I = laser intensity
k_B = Boltzmann's constant
m_e = nonrelativistic mass of electron
M = atomic mass unit
n_{cr} = critical free electron density
n_e = free electron density
$\langle n_k \rangle$ = average number of electrons in energy state
N = number of photons required in multiphoton ionization
N_e = total number of free electrons
r = distance to the Gaussian beam axis
r_0 = radius of laser beam
R = reflectivity
t = time
t_p = pulse duration
T = free electron temperature
T_D = Debye temperature
T_F = Fermi temperature
T_l = lattice temperature
U_I = band gap energy
U_{IP} = ionization potential
$\mathbf{v}$ = velocity of light in material
z = depth from surface in bulk material
Z^* = charge state of ions

Greek symbols

α = absorption coefficient of free electrons
α_h = absorption coefficient via electron heating
$\rho(\epsilon)$ = the density of states in Eq. (22)
δ_N = cross section of N-photon ionization
ϵ_F = Fermi energy
ϵ_k = energy state
$\langle \epsilon \rangle$ = average electron kinetic energy
$\boldsymbol{\epsilon}$ = complex dielectric function
ϵ_0 = electrical permittivity of free space
ϵ_1 = real component of dielectric function
ϵ_2 = imaginary component of dielectric function
λ = laser wavelength
$\ln \Lambda$ = Coulomb logarithm, Eq. (13)
μ = chemical potential
ν_e = electron collision frequency
ν_{ei} = electron-ion collision frequency
ν_{ep} = electron-phonon collision frequency
ω = laser frequency
ω_p = plasma frequency
τ = electron decay time constant in Eq. (1)
τ_e = free electron relaxation time

References

[1] Li, M., Menon, S., Nibarger, J. P., and Gibson, G. N., 1999, "Ultrafast Electron Dynamics in Femtosecond Optical Breakdown of Dielectrics," Phys. Rev. Lett., **82**, pp. 2394–2397.
[2] Lenzner, M., Krüger, J., Sartania, S., Cheng, Z., Spielmann, C., Mourou, G., Kautek, W., and Krausz, F., 1998, "Femtosecond Optical Breakdown in Dielectrics," Phys. Rev. Lett., **80**, pp. 4076–4079.
[3] Chowdhury, I. H., Xu, X., and Weiner, A. M., 2005, "Ultrafast Double-Pulse Ablation of Fused Silica," Appl. Phys. Lett., **86**, p. 151110.
[4] Jiang, L., and Tsai, H. L., 2003, "Femtosecond Laser Ablation: Challenges and Opportunities," *Proceeding of NSF Workshop on Research Needs in Thermal, Aspects of Material Removal*, Stillwater, OK, pp. 163–177.
[5] Stoian, R., Ashkenasi, D., Rosenfeld, A., and Campbell, E. E. B., 2000, "Coulomb Explosion in Ultrashort Pulsed Laser Ablation of Al_2O_3," Phys. Rev. B, **62**, pp. 13167–13173.
[6] Perry, M. D., Stuart, B. C., Banks, P. S., Feit, M. D., Yanovsky, V., and Rubenchik, A. M., 1999, "Ultrashort-Pulse Laser Machining of Dielectric Materials," J. Appl. Phys., **85**, pp. 6803–6810.
[7] Jiang, L., and Tsai, H. L., 2004, "Prediction of Crater Shape in Femtosecond Laser Ablation of Dielectrics," J. Phys. D, **37**, pp. 1492–1496.
[8] Jiang, L., and Tsai, H. L., 2005, "Energy Transport and Material Removal during Femtosecond Laser Ablation of Wide Bandgap Materials," Int. J. Heat Mass Transfer, **48**, pp. 487–499.
[9] Jiang, L., and Tsai, H. L., 2005, "Improvements on Two-Temperature Models and Its Applications in Ultrashort Laser Damage of Metal Films," ASME J. Heat Transfer, **127**, pp. 1167–1173.
[10] Bartels, R., Backus, S., Zeek, E., Misoguti, L., Vdovin, G., Christov, I. P., Murnane, M. M., and Kapteyn, H. C., 2000, "Shaped-Pulse Optimization of Coherent Emission of High-Harmonic Soft X-rays," Nature (London), **406**, pp. 164–166.
[11] Lindinger, A., Lupulescu, C., Plewicki, M., Vetter, F., Merli, A., Weber, M. S., and Wöste, L., 2004, "Isotope Selective Ionization by Optimal Control Using Shaped Femtosecond Laser Pulses," Phys. Rev. Lett., **93**, p. 033001.
[12] Renard, M., Hertz, E., Lavorel, B., and Faucher, O., 2004, "Controlling Ground-State Rotational Dynamics of Molecules by Shaped Femtosecond Laser Pulses," Phys. Rev. A, **69**, p. 043401.
[13] Assion, A., Baumert, T., Bergt, M., Brixner, T., Kiefer, B., Seyfried, V. V., Strehle, M., and Gerber, G., 1998, "Control of Chemical Reactions by Feedback-Optimized Phase-Shaped Femtosecond Laser Pulses," Science, **282**, pp. 919–922.
[14] Andreev, A. A., Limpouch, J., Iskakov, A. B., and Nakano, H., 2002, "Enhancement of X- ray Line Emission from Plasmas Produced by Short High-Intensity Laser Double Pulses," Phys. Rev. E, **65**, p. 026403.
[15] Stoian, R., Mermillod-Blondin, A., Winkler, S., Rosenfeld, A., Hertel, I. V., Spyridaki, M., Koudoumas, E., Fotakis, C., Burakov, I. M., and Bulgakova, N. M., 2004, "Temporal Pulse Manipulation and Adaptive Optimization in Ultrafast Laser Processing of Materials," Proc. SPIE, **5662**, pp. 593–602.
[16] Stoian, R., Boyle, M., Thoss, A., Rosenfeld, A., Korn, G., Hertel, I. V., and Campbell, E. E. B., 2002, "Laser Ablation of Dielectrics With Temporally Shaped Femtosecond Pulses," Appl. Phys. Lett., **80**, pp. 353–355.
[17] Spyridaki, M., Koudoumas, E., Tzanetakis, P., Fotakis, C., Stoian, R., Rosenfeld, A., and Hertel, I. V., 2003, "Temporal Pulse Manipulation and Ion Generation in Ultrafast Laser Ablation of Silicon," Appl. Phys. Lett., **83**, pp. 1474–1476.
[18] Choi, T. Y., Hwang, D. J., and Grigoropoulos, C. P., 2002, "Femtosecond Laser Induced Ablation of Crystalline Silicon upon Double Beam Irradiation," Appl. Surf. Sci., **197-198**, pp. 720–725.
[19] Stuart, B. C., Feit, M. D., Herman, S., Rubenchik, A. M., Shore, B. W., and Perry, M. D., 1996, "Nanosecond-to-Femtosecond Laser-Induced Breakdown in Dielectrics," Phys. Rev. B, **53**, pp. 1749–1761.
[20] Stuart, B. C., Feit, M. D., Rubenchik, A. M., Shore, B. W., and Perry, M. D., 1995, "Laser-Induced Damage in Dielectrics With Nanosecond to Subpicosecond Pulses," Phys. Rev. Lett., **74**, pp. 2248–2251.
[21] Gamaly, E. G., Rode, A. V., Luther-Davies, B., and Tikhonchuk, V. T., 2002, "Ablation of Solids by Femtosecond Lasers: Ablation Mechanism and Ablation Thresholds for Metals and Dielectrics," Phys. Plasmas, **9**, pp. 949–957.
[22] Du, D., Liu, X., Korn, G., Squier, J., and Mourou, G., 1994, "Laser-Induced Breakdown by Impact Ionization in SiO_2 With Pulse Widths From 7 ns to 150 fs," Appl. Phys. Lett., **64**, pp. 3071–3074.
[23] Rethfeld, B., Kaiser, A., Vicanek, M., and Simon, G., 2002, "Ultrafast Dynamics of Nonequilibrium Electrons in Metals Under Femtosecond Laser Irradiation," Phys. Rev. B, **65**, p. 214303.
[24] Jiang, L., and Tsai, H. L., 2006, "Plasma Modeling for Femtosecond Laser Ablation of Dielectrics," J. Appl. Phys., **100**(2), p. 023116.
[25] Fox, M., 2001, *Optical Properties of Solids*, Oxford University Press, Oxford.
[26] Ashcroft, N. W., and Mermin, N. D., 1976, *Solid State Physics*, Holt, Rinehart.
[27] Lee, Y. T., and More, R. M., 1984, "An Electron Conductivity Model for Dense Plasma," Phys. Fluids, **27**(5), pp. 1273–1286.
[28] Eidmann, K., Meyer-ter-Vehn, J., Schlegel, T., and Hüller, S., 2000, "Hydrodynamic Simulation of Subpicosecond Laser Interaction With Solid-Density Matter," Phys. Rev. E, **62**, pp. 1202–1214.

[29] Wu, Z., Jiang, H., Zhang, Z., Sun, Q., Yang, H., and Gong, Q., 2002, "Morphological Investigation at the Front and Rear Surfaces of Fused Silica Processed With Femtosecond Laser Pulses in Air," Opt. Express, **10**, pp. 1244–1249.
[30] Bonse, J., Munz, M., and Sturm, H., 2004, "Scanning Force Microscopic Investigations of the Femtosecond Laser Pulse Irradiation of Indium Phosphide in Air," IEEE Trans. Nanotechnol., **3**, pp. 358–367.
[31] Nakamura, S., Hoshino, M., and Ito, Y., 2001, "Monitoring of CW YAG Laser Welding Using Optical and Acoustic Signals," *Proceedings of ICALEO*, Jacksonville, FL.
[32] Lapczyna, M., Chen, K. P., Herman, P. R., Tan, H. W., and Marjoribanks, R. S., 1999, "Ultra High Repetition Rate (133 MHz) Laser Ablation of Aluminum With 1:2-ps Pulses," Appl. Phys. A: Mater. Sci. Process., **69**, pp. S883–S886.
[33] Herman, P. R., Oettl, A., Chen, K. P., and Marjoribanks, R. S., 1999, "Laser Micromachining of 'Transparent' Fused Silica With 1-ps Pulses and Pulse Trains," Proc. SPIE, **3616**, pp. 148–155.
[34] Chichkov, B. N., Ostendorf, A., Korte, F., and Nolte, S., 2001, "Femtosecond Laser Ablation and Nanostructuring," *Proceedings of ICALEO*, Jacksonville, FL.

The Thickness of the Liquid Microlayer Between a Cap-Shaped Sliding Bubble and a Heated Wall: Experimental Measurements

Xin Li

D. Keith Hollingsworth

Larry C. Witte

Department of Mechanical Engineering,
University of Houston,
Houston, TX 77204-4006

A laser-based method has been developed to measure the thickness of the liquid microlayer between a cap-shaped sliding bubble and an inclined heated wall. Sliding vapor bubbles are known to create high heat transfer coefficients along the surfaces against which they slide. The details of this process remain unclear and depend on the evolution of the microlayer that forms between the bubble and the surface. Past experiments have used heat transfer measurements on uniform-heat-generation surfaces to infer the microlayer thickness through an energy balance. These studies have produced measurements of 20–100 μm for refrigerants and for water, but they have yet to be confirmed by a direct measurement that does not depend on a first-law closure. The results presented here are direct measurements of the microlayer thickness made from a reflectance-based fiber-optic laser probe. Details of the construction and calibration of the probe are presented. Data for saturated FC-87 and a uniform-temperature surface inclined at 2 deg to 15 deg from the horizontal are reported. Millimeter-sized spherical bubbles of FC-87 vapor were injected near the lower end of a uniformly heated aluminum plate. The laser probe yielded microlayer thicknesses of 22–55 μm for cap-shaped bubbles. Bubble Reynolds numbers range from 600 to 4800, Froude numbers from 0.9 to 1.7, and Weber numbers from 2.6 to 47. The microlayer thickness above cap-shaped bubbles was correlated to a function of inclination angle and a bubble shape factor. The successful correlation suggests that this data set can be used to validate the results of detailed models of the microlayer dynamics. [DOI: 10.1115/1.2241858]

Introduction

Boiling heat transfer occurs in a wide variety of engineering applications including energy conversion systems, manufacturing processes, and cooling of advanced electronic systems. Nucleate boiling provides an attractive means of cooling temperature-sensitive, high heat-flux devices because it can sustain a large heat flux over a small and relatively stable temperature difference. Modern developments in high-density computer chips and compact heat exchangers are requiring reliable predictions of the initiation of boiling and of the heat transfer rate that follows for a variety of surfaces and convective fields. Assuring that a surface designed to operate in boiling is in fact doing so is of extreme importance. For example, it is well known that boiling can be delayed on heat-flux-controlled surfaces so that damaging overshoots in surface temperature can occur. In addition to eliminating temperature overshoot, there is also a need for flows that combine single-phase convection and boiling so that heat transfer is enhanced beyond the rates that occur in boiling alone.

There are many convective situations where bubbles that have been formed at one place in a device will, after detachment, move along adjacent surfaces. This motion history has become known as the sliding bubble phenomenon. There is evidence that sliding bubbles can dramatically increase the local heat transfer rate from the surface on which they slide. One of the first devices in which sliding bubbles has been observed to enhance heat transfer is a shell-and-tube heat exchanger that experiences boiling over some or all of its tubes. Cornwell [1] produced a surprising result during a study of a tube bank. With all the tubes at the same heat flux, the upstream tubes were in nucleate flow-boiling while the downstream tubes experienced no boiling at all. Clearly the heat transfer coefficient on the downstream tubes had to be high enough to hold the surface temperature below that required for the onset of boiling—while supporting a heat flux that should have resulted in boiling. Cornwell postulated that the heat transfer coefficient on the downstream tubes resulted from heat transfer into bubbles that nucleate on the upstream tubes and slide around the walls of the downstream tubes. Furthermore, at higher heat flux levels, boiling initiated on the downstream tubes with no reported temperature overshoot. This observation implies that for higher fluxes, the downstream heat transfer coefficients are so high that little change is experienced once boiling initiates. Recent work has shown that the importance of the sliding-bubble phenomenon extends beyond the external-flow surfaces of heat exchangers and surfaces that experience pool boiling. For example, Thorncroft and Klausner [2] discussed sliding bubbles in the context of convective boiling inside tubes—a common industrial application that is not commonly associated with this mechanism.

A sliding bubble can induce at least three significant mechanisms that enhance heat transfer. Because the bubble displaces liquid and acts similar to a bluff body moving through the liquid, a local enhancement in convection around the bubble can occur. Also, it has been known for decades (Cooper and Lloyd [3] and Koffman and Plesset [4]) that sliding bubbles can create a thin liquid microlayer between the bubble and the surface on which it slides. As the bubble slides, the microlayer evaporates and is replenished by liquid trapped under the upstream edge of the bubble. This is much the same mechanism that occurs as bubbles

Contributed by the Heat Transfer Division of ASME for publication in the JOURNAL OF HEAT TRANSFER. Manuscript received September 13, 2005; final manuscript received February 3, 2006. Review conducted by Costas Grigoropoulos.

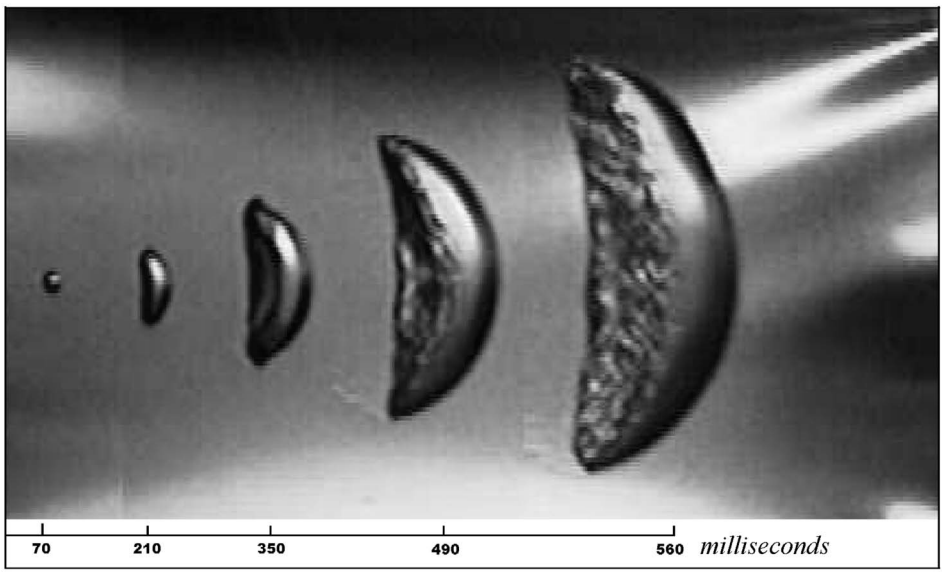

Fig. 1 Image collage from Bayazit et al. (16,17)

are nucleated and grow outward from a nucleation site. Finally, the bubble induces substantial mixing in its wake, and there is an attendant, and sustained, increase in surface heat flux behind the bubble.

Cornwell and co-workers [5–7] have examined the fluid dynamics of sliding bubbles and the accompanying heat transfer implications. They also investigated the velocity of bubbles as they rise under an inclined plate and the film thickness that separates the bubble from the surface. Kenning and co-workers [8,9] have also undertaken studies that seek to explain the enhancement mechanisms of sliding bubbles. Kenning was the first to apply liquid crystal thermography to the measurement of surface temperature fields that develop around sliding bubbles. Kenning et al. [10] mapped the surface temperature imprint from a bubble sliding through saturated water using liquid crystals. Because the liquid was saturated, the amount of heat transferred to the bubble could be estimated from the observed volume increase of the bubble. They were unable to determine the effect of the bubble wake on the overall enhancement of heat transfer from the surface.

Qui and Dhir [11] studied flow patterns and heat transfer for PF-5050 bubbles moving under a polished silicon surface inclined from 5 to 75 deg from horizontal. They found that bubbles change shape from near spherical to ellipsoidal as they grow during motion under the surface. They also performed flow visualization studies of the flow patterns around the bubble. Their results clearly show the formation and shedding of vortices behind the bubble that can contribute to enhancement of heat transfer during bubble passage. Their results also indicate that the bubble slides on a very thin liquid layer formed by the wedging action of the bubble as it encounters liquid. Film thicknesses were not measured directly.

Addlesee and Kew [12] produced a model of the microlayer dynamics by constructing an analogy to a falling liquid film on an inclined surface. They began with a boundary layer model for the induced flow near the solid surface produced by the passage of a hemispherical bubble. They assumed that the entire volumetric flow inside this boundary layer was introduced into the microlayer, and they constructed and solved a momentum integral description for the flow within the microlayer. Their model produces microlayer thicknesses that are several times those measured both in this laboratory for FC-87, and by Kenning et al. [10] for water. However, the Addlesee and Kew model gives results that are consistent with experiments if only some fraction of the volumetric flow in the upstream boundary layer is admitted to the microlayer. The *a priori* identification of this fraction remains an open question.

Nishikawa et al. [13] measured film thicknesses for air bubbles in water rising under an inclined heated surface using a resistance probe mounted in the surface. They used bubble volumes of 2, 4, and 8 cm^3 and inclination angles of 5 deg, 15 deg, 30 deg, and 60 deg from horizontal for a downward- facing surface. They used their experimental results as input for a theoretical model of low-flux, isolated bubble nucleate boiling. They found that bubble size has little influence on the thickness of the film separating the bubble from the surface, a result that agrees well with our measurements. They also found that film thickness increased with increasing angle, a result that is at odds with our measurements.

In summary, the sliding bubble phenomenon is an ubiquitous, yet poorly understood, mechanism in two-phase heat transfer. The outstanding issues are: (1) the dynamics of the microlayer, our ability to predict its thickness and the heat flux through it; (2) the relative importance of the energy flow through the microlayer in the context of bubble growth; and (3) the dynamics and surface energy flux associated with the wake.

Work in the UH Boiling and Phase Change Laboratory by Bayazit [14] and Figueroa [15] focused on measurements of the surface temperature depression and heat transfer rate into the microlayer and bubble wake. Results of this work are published in Bayazit et al. [16,17]. The real-time surface temperature distributions were measured using liquid crystal thermography and an electrically heated test surface built from 50-μm-thick stainless steel foil. The test fluid was FC-87, a perfluorocarbon fluid manufactured by the 3M Corporation. Figure 1 is a collage of images of the same bubble from a typical run along with the timing of the images. Here, a small spherical bubble quickly grows and changes into a cap-shaped bubble.

A contour plot of the reduction in surface temperature, T_w, caused by the passing of the bubble is shown in Fig. 2. The bubble location was determined by a collocation procedure between the bubble image as shown in Fig. 1 and the liquid crystal image of the surface. Figure 2 represents a typical cap-shaped bubble—between the second and third bubbles in Fig. 1. The maximum temperature depression is 5 °C, approximately one-third of the surface-to-bulk temperature difference typical of this location. The

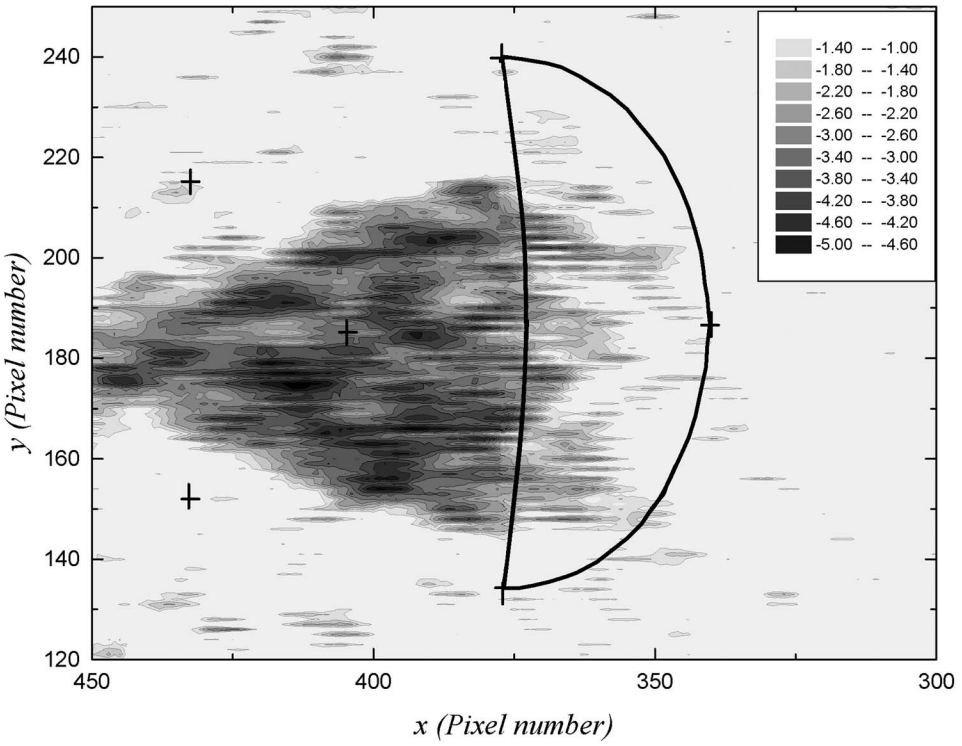

Fig. 2 Contour plot of the change in T_w caused by the bubble: $T_w(t=280\ \text{ms}) - T_w(t=0\ \text{ms})$. Bubble is moving from left to right. From Bayazit et al. (16,17).

depression in T_w starts beneath the bubble due to heat transfer through the microlayer and continues to form the triangular wake. The depression does not extend to the transverse extremities, and the lateral extremes of the wake are sharply defined. This observation may indicate that the bubble curves away from the wall toward its transverse end such that an effective microlayer does not form near the extremities.

A numerical model based on a first-law closure for the microlayer was developed by Bayazit using surface temperature data as shown in Fig. 2. That model gives microlayer thicknesses near the centerline of the bubble in the range 35 to 60 μm for cap-shaped FC-87 bubbles developing on a uniform-heat-generation surface inclined at 12 deg. These inferential results for microlayer thickness are similar to those of Kenning et al. [10], but they are no substitute for a direct measurement of this controlling length scale for the problem. To attempt such a direct measurement, perhaps the first of its kind for this problem, our laboratory employed a fiber-optic based laser reflectance method.

Fiber-optic techniques for the measurement of millimeter-thick liquid films were first considered by Ohba et al. [18] for conditions in which impedance (i.e., conductance and capacitance) probes cannot be used. Such conditions include the use of dielectric fluids, such as FC-87. Than et al. [19] reported the development of a theoretical model that accounts for interfacial refraction for probes using multiple fibers.

Experimental Apparatus and Procedure

Basic Facilities. Figure 3 shows the test chamber, a rectangular aluminum enclosure with dimensions of 394 mm by 203 mm by 191 mm. Space is provided at the top to collect vapor created as bubbles are introduced and grow as they slide under the plate. The chamber can be rotated around a pivot which allows the test surface to be positioned at different angles to the horizontal. The two sidewalls and the bottom wall are equipped with tempered glass windows for visualization and lighting of the chamber and test surface. Openings are provided to allow injection of the vapor, filling and draining of the system, suction and condensation of collected vapor, thermocouples and pressure transducer placement.

A 9.5-mm-thick 254 mm by 174 mm aluminum plate was used as the test surface. The bottom surface was polished to inhibit nucleation. Two thermofoil heaters (each 76.2 mm square) with an integral 1 Ω RTD in the center were attached on the top of the aluminum plate. The intended boundary condition for this high-conductivity surface was a uniform temperature as measured from the two RTDs. The four edges of the test surface were cooled to prevent nucleation where the surface clamped to the enclosure. Chilled water from an ice bath was circulated through copper tubing embedded into the edge of the aluminum plate. The fiber optic probe was mounted in a 1.7-mm-diam hole on the center of the test plate.

The test fluid was Flourinert FC-87, manufactured by 3M. It has a saturation temperature of 30 °C at atmospheric pressure. Single vapor bubbles were generated from a syringe-needle system located near the bottom of the test surface. The resulting initial bubble diameter was about 1 mm. Time was allowed between bubble injections for the test surface to return to an undisturbed (natural convection) operating condition. Only solitary bubbles (those where no additional bubbles formed or merged with the injected bubble) were considered.

Imaging System. Digital images at 1000 frames/s were acquired with an IDT X-Stream VISION XS-4 monochrome CMOS camera fitted with a Navitar 7000 lens. Two 100 W bulbs provided light at the side view window and a 75 W bulb mounted at the bottom view window provided light to the bubble in plan view. Two mirrors were mounted on the test surface at a 45 deg inclination to allow the camera to capture the side view and plan

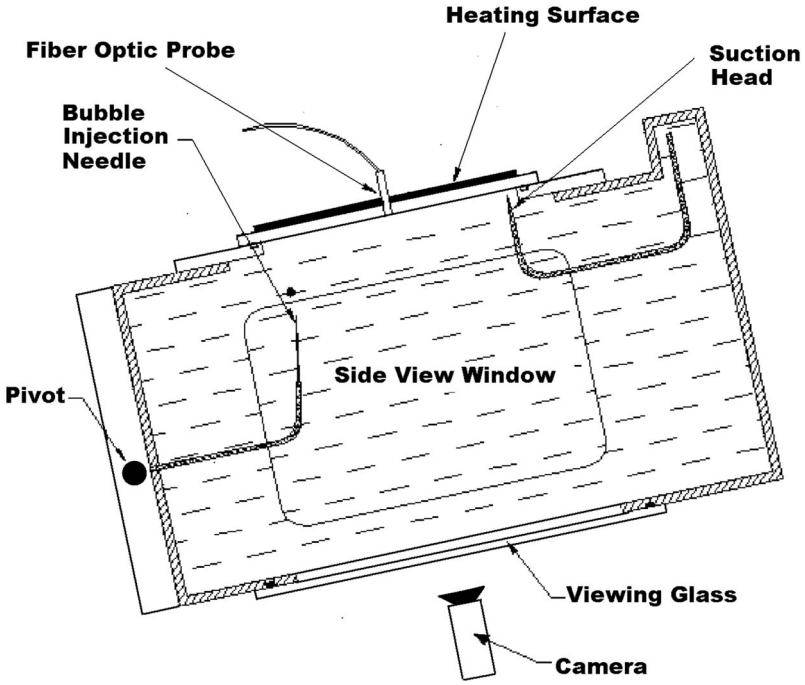

Fig. 3 Sketch of the test chamber

view images simultaneously. Figure 4 shows an example image collage, in which images at different times are shown together, for the test surface inclined at 15 deg. These image sequences allow measurements of bubble speed, acceleration, and size, but they do not resolve the microlayer itself. The images are the subject of a companion paper, and are used in this paper only to provide the dimensions of the bubbles when they pass the fiber optic probe that measures the microlayer thickness.

Fiber Optic Probe System. A schematic of the fiber optic sys-

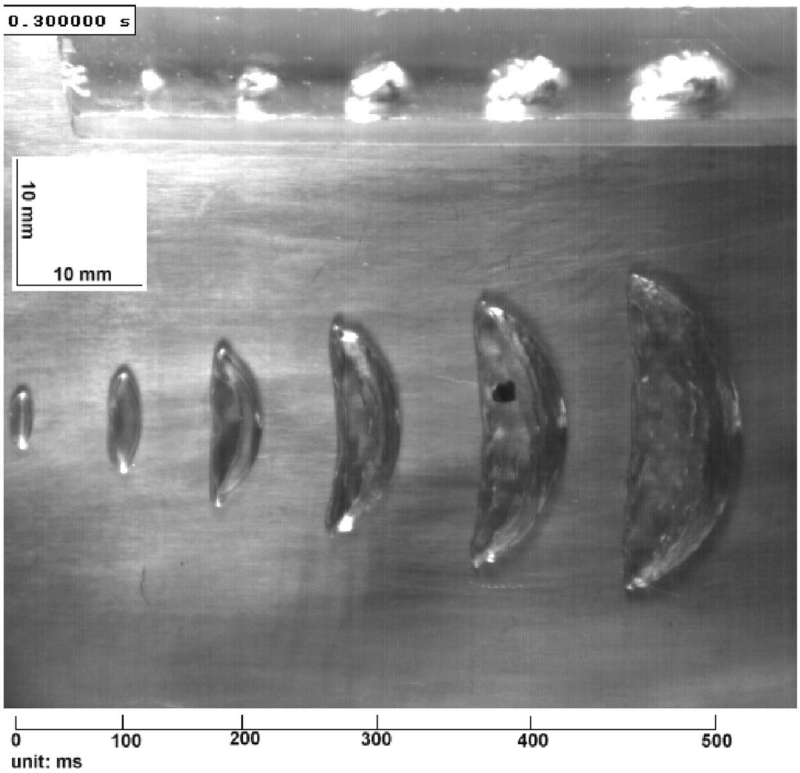

Fig. 4 A collage of bubble images showing plan and side views for a 15 deg inclination angle

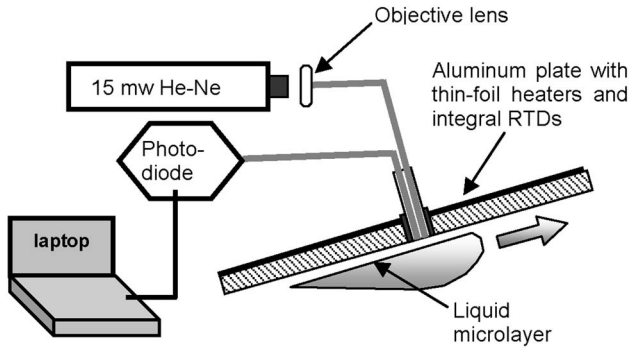

Fig. 5 Schematic of the two-fiber probe system

tem is shown in Fig. 5. A beam from a 15 mW helium-neon laser is routed through a transmitting fiber that is terminated and polished flush with the test surface. A similar receiving fiber directs reflected light back to a DET-110 high-speed photodiode that generates a voltage that is digitized by an IOtech DaqBook connected to a laptop computer. Probe resolution is limited by the properties of the optical fibers. Our extension of the technique to films that are tens of microns thick was made possible through recently available optical fibers with a core region of 200 μm and an overall diameter of 220 μm. Figure 6 shows the internal structure of the probe. The two optical fibers were attached side by side with epoxy in a 1.7-mm-diam glass tube such that the bubble crosses the probe in the direction shown relative to the two fibers. The second largest bubble in Fig. 4 is shown traversing the probe location, seen as a dark circle beneath the bubble. The probe is accurate only for flat liquid films. Any wave on the gas/liquid interface causes a distortion of the measurement due to the slope of the interface reflecting the light toward or away from the receiving fiber.

Probe Calibration. A schematic of the apparatus used for static calibration of the probe is shown in Fig. 7. The system included a glass container (178 mm inner diameter, 150 mm deep), two syringes, three micrometer heads with needles mounted on the top and a stainless steel platform sitting on the bottom of the container. The optical fiber probe was fixed in the center of the platform. The container rested in a leveling table with four adjustable legs and was sealed by an aluminum cover to reduce the evaporation of FC-87. Three digital micrometer heads were mounted

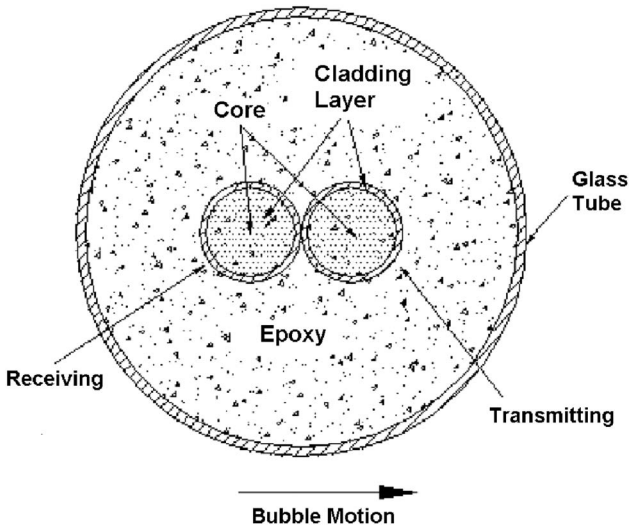

Fig. 6 End of the fiber optic probe

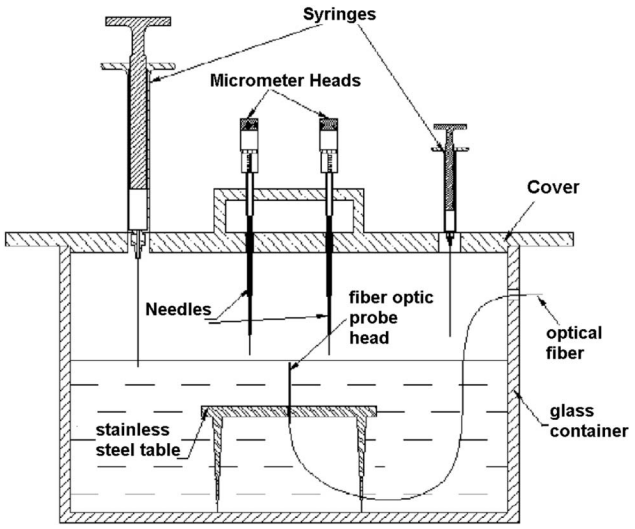

Fig. 7 Schematic of the calibration system

vertically and 120 arc deg apart in the aluminum cover. The precision of the micrometer heads was ±0.5 μm and the adjustable range was 0–25 mm. Three needles were mounted on the ends of the micrometers. Two syringes with volumes of 10 ml and 1 ml were mounted on the cover to adjust the height of the liquid surface. The smallest increment of surface height was 0.1 ml =4 μm using the smaller syringe. The container was surrounded by a coil of latex hose through which chilled water flowed in order to prevent evaporation of the test fluid.

Before use, the apparatus was cleaned with isopropyl alcohol, and the FC-87 was filtered. The glass container and the stainless platform were leveled. The fiber optic probe head was mounted into the center of the platform, FC-87 was added to a level above the probe, and the cover was installed. The three needle tips were adjusted to the same horizontal plane by bringing them in contact with the free surface, and the micrometers were set to zero. Fluid was extracted using the syringes so that the free surface fell in increments of a few microns. When the liquid surface was steady after each fluid withdrawal, the micrometers were adjusted to touch the surface and readings were recorded from the three micrometers. The room lights were turned off and the photodiode voltage was recorded. This process continued until the free surface was broken by the fiber optic probe head. Within about 20 μm of that event, the photodiode voltage ceased to change. The resulting calibration curve is shown in Fig. 8 for three calibration trials.

The uncertainty in the liquid film thickness arises from the agreement in the three micrometer heads at each reading, typically ±1 μm, and the identification of the free surface level when at the probe head. A conservative estimate of the uncertainty of the probe head level is given by assuming the level change at the step the probe was uncovered was produced by the volume of one division of the smaller syringe. If that entire volume is taken as the volume uncertainty, ±0.05 ml, and is divided by the cross-section area of the container, a position uncertainty of ±2.0 μm results. The final root-sum-square uncertainty for the film thickness is approximately ±2.5 μm. The observed noise in the photodiode and A/D system was ±0.9 mV. The system becomes insensitive to thickness changes below 20 μm, and above 100 μm there is a marked reduction in the slope of the system response. The lower limit is caused by the spacing between the emitting and the receiving fibers. If the liquid layer is too thin, below 20 μm, the receiving fiber is outside the cone of the reflected light. As the film thickens, light can be reflected into the receiving fiber, and the signal strength increases. There is an upper limit, however, when the layer thickness reaches a point, 100 μm in this case,

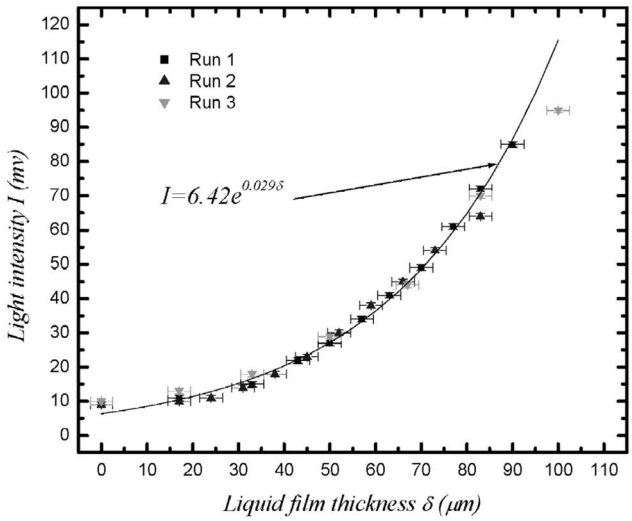

Fig. 8 Calibration curve for the fiber optic probe

where the signal begins to decrease because the reflected light is falling on an ever increasing area. Between these limits, the response is well-described by an exponential function

$$I = 6.420 \exp(0.029\delta) \quad (1)$$

where I is the voltage from the photodiode (mV), and δ is the liquid film thickness (μm). The standard estimate of error of the curve fit is ± 1.9 μm. After calibration, the probe was mounted in the test plate while viewed under a microscope to ensure a flush alignment with the test surface.

Experimental Results

Liquid Film Thickness. Only flat liquid films can be measured accurately by the probe, thus all the microlayer thickness measurements shown here are for cap-shaped bubbles which should have a relatively large interface bounding the microlayer. The four larger bubbles in Fig. 4 are examples. A total of 55 data sets for cap-shaped bubbles sliding at inclination angles, θ, of 2 deg to 15 deg were successfully collected in these experiments. Table 1 shows the experimental conditions for the 55 bubbles. For all the experiments, the bulk temperature, T_b, was held as close as possible to 25 °C, which is 5 °C below the saturation temperature at 1 atm. All the run numbers used in this section refer to Table 1.

Figures 9–12 show plots of representative data for microlayer thicknesses for $\theta=2$ deg, 5 deg, 10 deg, and 15 deg. All the signals have been converted through the calibration curve, Eq. (1), so that the results are shown as microlayer thickness, δ, versus the time required for the bubble to traverse the probe location. Figure 13 shows two example traces, one for Run 3 at 2 deg, and one for Run 47 at 15 deg. The probe was installed so that the bubble passed over the receiving fiber first. The spike at the right end of the signal is caused by the slope of the interface reflecting the light toward the receiving fiber at the end of the bubble. Light is also reflected preferentially away from the receiving fiber at the leading edge of the bubble. This produces a downward spike that is difficult to detect because it has the effect of delaying the rise in the signal. Given that the signal shape is not known, the delay tends to be masked except for bubbles at 2 deg. For these bubbles, the length of the curved leading edge is large enough to show a pronounced concave-up section at the beginning of the microlayer thickness trace.

The plateau in the center of the signal is a measure of the local microlayer thickness as the bubble slides past the probe. Spikes located within this plateau are interpreted as a response to the presence of waves on the interface bounding the microlayer and will be discussed later.

Only five traces were collected at $\theta=2$ deg because the weak natural convection environment made bubble nucleation on the test surface more difficult to eliminate and fewer single sliding bubbles were observed. Because the probe response was limited to a thickness of 20 μm, inclination angles greater than 15 deg were not attempted.

Referring to Fig. 9 for $\theta=2$ deg, the traces for the smaller bubbles (Runs 1–3) exhibit a smooth plateau near 50 μm. The

Table 1 Experimental conditions for microlayer thickness data sets: FC-87, 1 atm pressure, $T_{sat}=30$ °C

Run	Designation	θ (deg)	T_b (°C)	T_w (°C)
1	2 deg-1	2	25.0	31.6
2	2 deg-2	2	25.1	31.8
3	2 deg-3	2	25.1	31.9
4	2 deg-4	2	24.9	32.1
5	2 deg-5	2	25.1	32.2
6	5 deg-1	5	25.1	33.3
7	5 deg-2	5	25.0	33.4
8	5 deg-3	5	25.0	33.5
9	5 deg-4	5	25.0	33.5
10	5 deg-5	5	25.1	33.5
11	5 deg-6	5	25.0	33.6
12	5 deg-7	5	25.0	33.9
13	5 deg-8	5	25.1	34.0
14	5 deg-9	5	25.1	34.0
15	5 deg-10	5	25.2	34.1
16	5 deg-11	5	25.0	34.4
17	5 deg-12	5	25.1	34.4
18	5 deg-13	5	25.0	34.4
19	5 deg-14	5	25.1	34.5
20	5 deg-15	5	25.1	34.5
21	5 deg-16	5	24.9	34.5
22	5 deg-17	5	25.0	34.6
23	5 deg-18	5	25.0	34.9
24	10 deg-1	10	25.1	33.5
25	10 deg-2	10	25.0	33.9
26	10 deg-3	10	25.0	33.9
27	10 deg-4	10	25.1	34.0
28	10 deg-5	10	24.9	34.4
29	10 deg-6	10	24.8	34.4
30	10 deg-7	10	25.0	34.5
31	10 deg-8	10	25.1	34.9
32	10 deg-9	10	25.2	35.0
33	10 deg-10	10	25.0	35.0
34	10 deg-11	10	24.9	35.0
35	10 deg-12	10	24.9	35.1
36	10 deg-13	10	25.0	35.4
37	10 deg-14	10	25.0	35.5
38	10 deg-15	10	25.0	35.5
39	10 deg-16	10	25.1	35.5
40	10 deg-17	10	25.1	35.6
41	10 deg-18	10	25.1	35.8
42	15 deg-1	15	25.0	35.1
43	15 deg-2	15	25.1	35.4
44	15 deg-3	15	25.1	35.5
45	15 deg-4	15	25.1	33.6
46	15 deg-5	15	25.0	36.0
47	15 deg-6	15	24.9	36.1
48	15 deg-7	15	24.9	36.5
49	15 deg-8	15	25.0	36.5
50	15 deg-9	15	25.0	36.5
51	15 deg-10	15	25.1	36.6
52	15 deg-11	15	25.2	36.6
53	15 deg-12	15	25.1	36.6
54	15 deg-13	15	25.1	36.6
55	15 deg-14	15	25.0	36.8

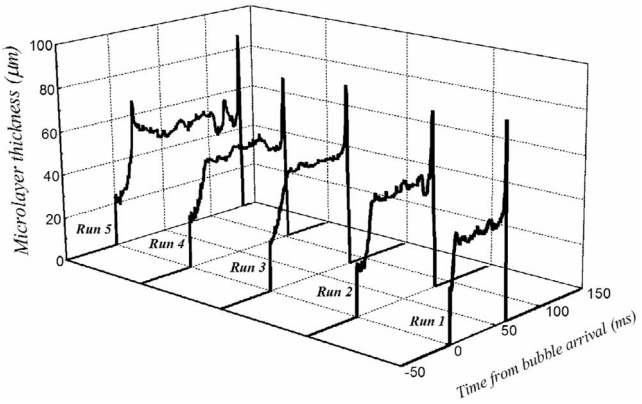

Fig. 9 Time history of bubble passage for a 2 deg inclination (Runs 1 to 5)

larger bubbles (Runs 4 and 5) produce a less-uniform plateau, perhaps indicating the onset of waves on the bounding interface. As waves establish on the bubble interface, the probe response becomes an unreliable measure of the thickness. Sharp upward spikes appear in the signal. Some downward displacement is also seen, but the upward spikes are far more evident. An optical model of the probe response to simple two-dimensional disturbances was developed; it showed that while upward and downward displacements in the signal are possible, the upward displacements can be much larger than downward displacements produced by interface disturbances of the same size. However, the

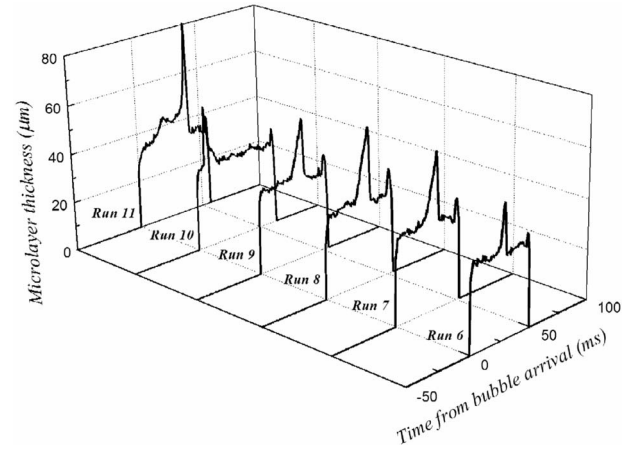

Fig. 10 Time history of bubble passage for a 2 deg inclination (Runs 6 to 11)

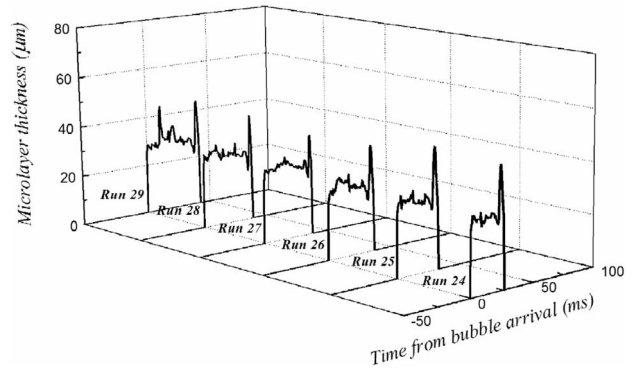

Fig. 11 Time history of bubble passage for a 2 deg inclination (Runs 24 to 29)

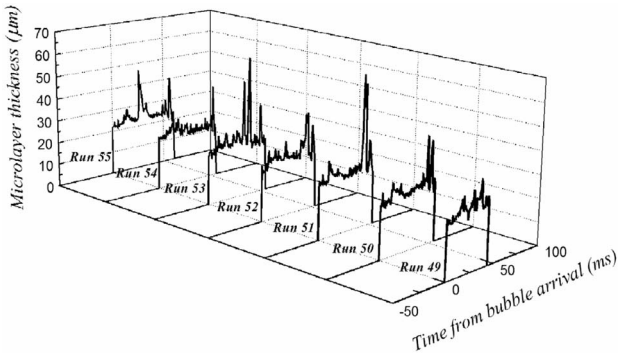

Fig. 12 Time history of bubble passage for a 2 deg inclination (Runs 49 to 55)

shape of the leading edge of bubbles at $\theta=2$ deg is evidence of a substantial signal response to interface curvature that reflects light away from the receiving fiber. A similar phenomenon can be observed occasionally at higher θ. For $\theta>2$ deg, when the bubble grows larger, the spikes in the signals have a tendency to grow larger and to occupy more of the bubble passage time. The tendency for the signal to exhibit spikes, interpreted here as evidence of a wavy interface, increases with both bubble size and inclination angle.

Dependence of Thickness on System Variables. We believe these to be the first detailed, noninferred measurements of the microlayer thickness for a cap-shaped sliding vapor bubble. The reduction in microlayer thickness with increasing inclination angle is readily evident, as shown by the average values shown in Table 2.

Bayazit [17] calculated film thicknesses in the 35–60 μm range for FC-87 for an inclination angle of 12 deg, based on an energy balance across the liquid microlayer. Kenning et al. [10] reported thicknesses of 50–70 μm for water bubbles under a 15 deg-inclined plate, again calculated on the basis of energy considerations. A modification by Li [20] of Addlessee and Kew's [12] boundary layer analysis, accounting for diversion of fluid away from the microlayer by bubble blockage, shows thicknesses on the order of 30–35 μm for 5 and 10 deg-inclined plates, in reasonably good agreement with our measurements. Nishikawa et al. [13] measured a thickness of 44 μm for water vapor bubbles

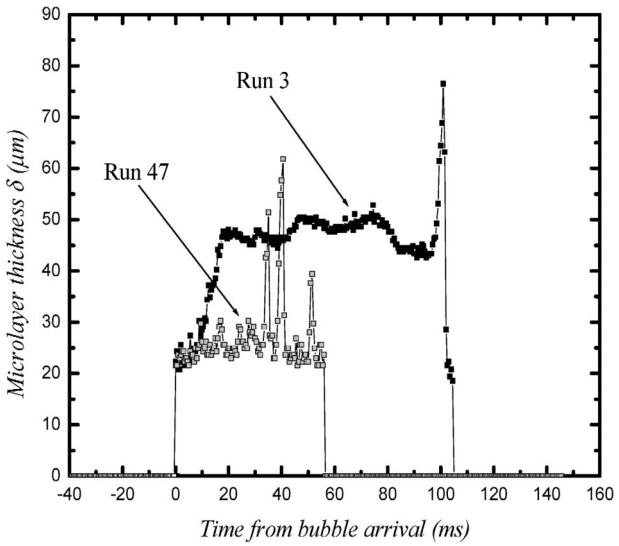

Fig. 13 Example traces of microlayer thickness: Run 3 at 2 deg, Run 47 at 15 deg

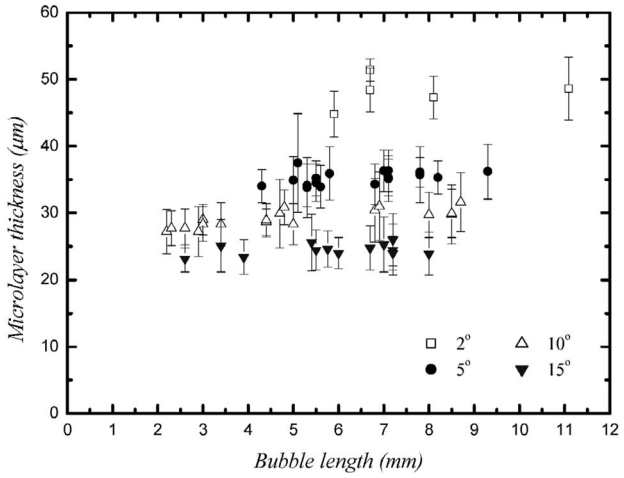

Fig. 14 Microlayer thickness versus bubble length

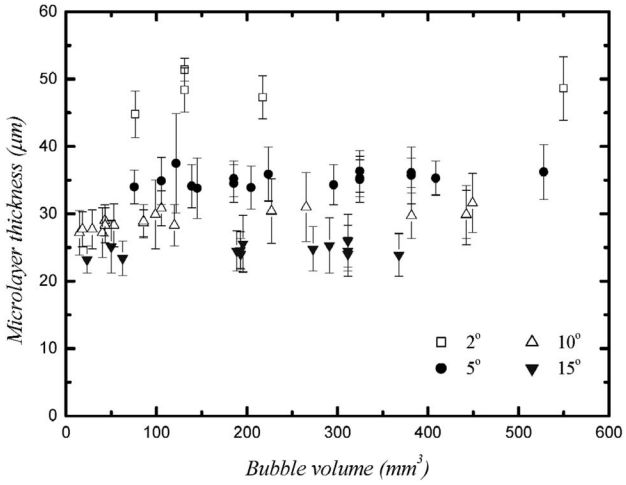

Fig. 16 Microlayer thickness versus bubble volume

moving under a 5 deg-inclined plate, in reasonable agreement with our results and those of Kenning. In contrast to our results, however, he found that liquid layer thickness increased with inclination angle, rather than decreasing, as was found in our study, and by the other investigators [10,12].

Figures 14–16 show microlayer thicknesses versus variables connected to the sliding bubble dimensions, namely, length (L), width (W), and volume (V). These data were produced by removing the leading and trailing spikes and filtering the plateau section to remove statistically outlying events that are interpreted as wave-generated spikes. The uncertainty bars indicate two standard deviations computed for the collection of points that survive the filtering process. More spikes appear in the signal with increasing θ so that the uncertainty increases somewhat as the scatter in the filtered plateau data increases.

Figure 17 shows how the dimensions were obtained from the bubble images such as those shown in Fig. 4. For cap-shaped bubbles, V was calculated from the two orthogonal views obtained from the high-speed images as

$$V = \frac{\pi}{6} WLH \tag{2}$$

as proposed by Maxworthy [21]. The bubble velocity, u_{bubble}, was defined as the distance traversed by the bubble nose position, NP, divided by Δt, the time between frames used in the computation.

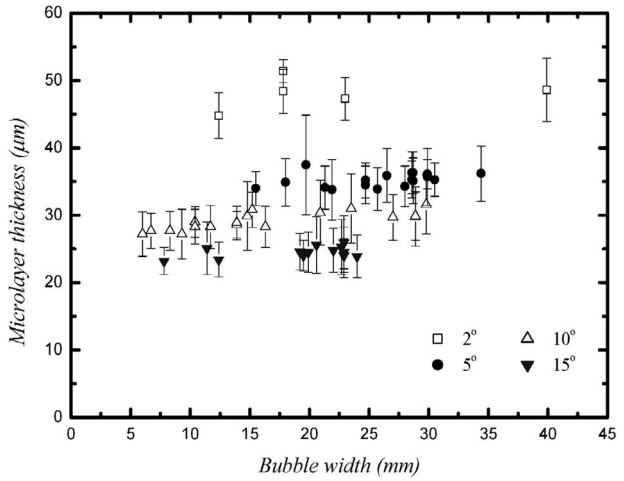

Fig. 15 Microlayer thickness versus bubble width

At 1000 fps, NP changes little between successive frames. Therefore, to lower the uncertainty of this calculation, every thirtieth frame was used ($\Delta t = 0.03$ s),

$$u_{\text{bubble}} = \frac{(\text{NP}_{i+30} - \text{NP}_i)}{\Delta t} \tag{3}$$

The uncertainty in velocity is estimated via root-sum-square combinations of observed uncertainties as

$$\Delta u_{\text{bubble}} = \left(2 \cdot \left(\pm 1 \text{ pixel} \cdot \frac{\text{ps}}{\Delta t}\right)^2 + \left(\frac{\Delta \text{ps}}{\text{ps}} \cdot u_{\text{bubble}}\right)^2\right)^{1/2} \tag{4}$$

where ps is the pixel size. Typical uncertainties in velocity are ±3.7 to ±5.2 mm/s, which corresponds to bubble velocities ranging from about 30 up to 160 mm/s.

Optical probe signals and sliding bubble images cannot be obtained simultaneously because the illumination for the imaging system had to be shut down when the fiber optic probe was operating. All the bubble dimensions and dimensionless numbers for the corresponding optical signal were acquired from bubbles that had the same passage time and experimental conditions as for the bubble image sequences.

Figures 14–16 show the microlayer thickness to be independent of bubble dimensions L, W, and V. This observation agrees with that of Nishikawa [13] who found that the liquid film thickness is independent of bubble size. Because the probe position is fixed in the test plate, the heated length from the bubble injector to the fiber optic probe is fixed. Large cap-shaped bubbles are easier to produce at smaller θ because the u_{bubble} is lower and the corresponding heating time is longer at the same wall superheat.

These figures show that θ essentially fixes the microlayer thickness, even though the bubble's size increases as it slides along the heated plate. The equivalent diameter, $D_{\text{eq}} \equiv (6V/\pi)^{1/3}$, was selected as a single characteristic length scale for the bubble. Because the bubble shape is not easily described, D_{eq} is the diameter of a sphere of equal volume. This choice follows Maxworthy [21],

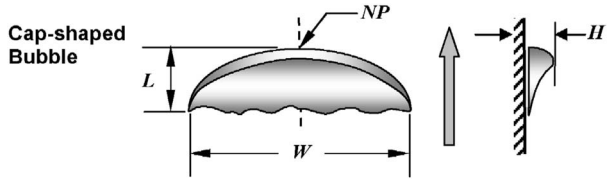

Fig. 17 Definition of bubble width (*W*), length (*L*), height (*H*), and nose position (NP)

Table 2 Averaged microlayer thickness at four inclination angles

Inclination angle, θ (deg)	Microlayer thickness, δ (μm)
2	48.1
5	35.2
10	29.1
15	25.4

in accordance with Eq. (2). The size of the bubble affects its buoyancy, which in turns affects its velocity. Dimensionless groups that depend on both velocity and size are the Reynolds number,

$$\mathrm{Re} \equiv \frac{u_{\mathrm{bubble}} \cdot D_{\mathrm{eq}}}{\nu} \tag{5}$$

the Weber number, We, a ratio of the inertial to surface tension forces acting on the bubble,

$$\mathrm{We} \equiv \frac{\rho u_{\mathrm{bubble}}^2 \cdot D_{\mathrm{eq}}}{\sigma} \tag{6}$$

and the Froude number, Fr, a ratio of the inertial to buoyancy forces acting on the bubble,

$$\mathrm{Fr} \equiv u_{\mathrm{bubble}}/(gD_{\mathrm{eq}} \sin \theta)^{0.5} \tag{7}$$

Figure 18 shows that δ does not depend on Re, only on the inclination. This observation of uniform δ for fixed θ is supported by values computed from first-law closure methods as reported by Monde [22] and Kenning et al. [10]. Figure 19 shows the microlayer thickness also to be independent of We. The maximum We produced by the facility increased with θ due to the increase in u_{bubble} with θ. Figure 20 shows that δ exhibits a strong increasing trend with Fr due to the direct relationship between Fr and θ.

Correlation of Microlayer Thickness and Bubble Dynamics. The dynamics of the sliding cap-shaped bubbles observed in this study appear to be dependent on surface inclination, bubble volume (represented here by D_{eq}), and fluid properties. The independence of bubble volume from inclination is accomplished by the possibility of varying the development length, bulk subcooling, and wall superheat. To construct a correlation of δ to macroscopic measurands, we start by modeling the flow in the microlayer as a laminar duct flow in which the pressure and viscous terms dominate. The momentum equation is

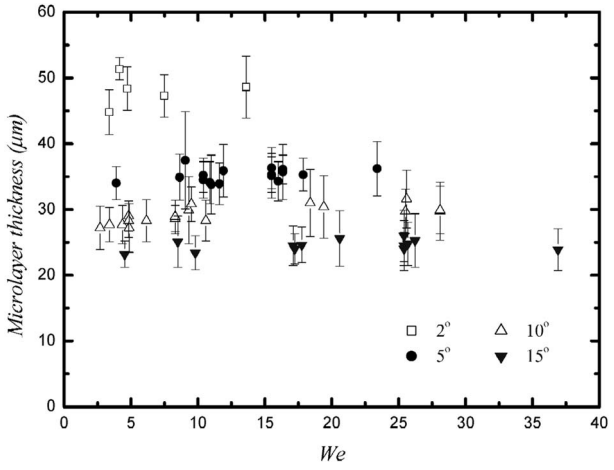

Fig. 19 Microlayer thickness versus Weber number

$$\frac{\partial p}{\partial x} = \mu \frac{\partial^2 u}{\partial y^2} \tag{8}$$

Equation (8) is made dimensionless by selecting δ as the length scale, and following the classical development for vertically rising bubbles, $U^* \equiv \sqrt{gD_{\mathrm{eq}}}$ is selected as the velocity scale. The pressure is scaled on the stress created by the buoyancy of the bubble acting normal to the microlayer, $\rho gV \cos \theta / WL$. Here the liquid density approximates the density difference between phases, and the plan area of the bubble is described by the product of bubble length and width. With these selections, Eq. (8) produces a pair of dimensionless groups: a microlayer Reynolds number,

$$\mathrm{Re}^* \equiv \frac{U^* \delta}{\nu} \tag{9}$$

and a group that includes the inclination dependence and a ratio that may be described as a bubble shape factor, $6/(\pi \cos \theta) \cdot WL/D_{\mathrm{eq}}^2$. Figure 21 shows that a reasonable correlation for the microlayer thickness can be obtained by plotting the measured data in these coordinates. A straight line captures the data to a mean deviation of 9.4% with most of the data lying inside ±20%:

$$\frac{U^* \delta}{\nu} = \frac{39.26}{\pi \cos \theta} \cdot \frac{WL}{D_{\mathrm{eq}}^2} \tag{10}$$

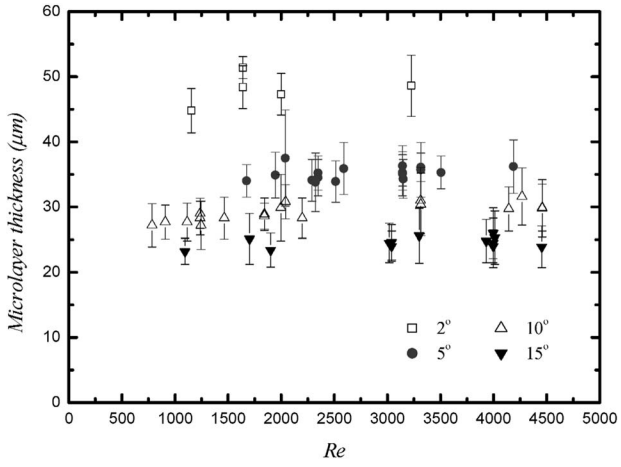

Fig. 18 Microlayer thickness versus Reynolds number

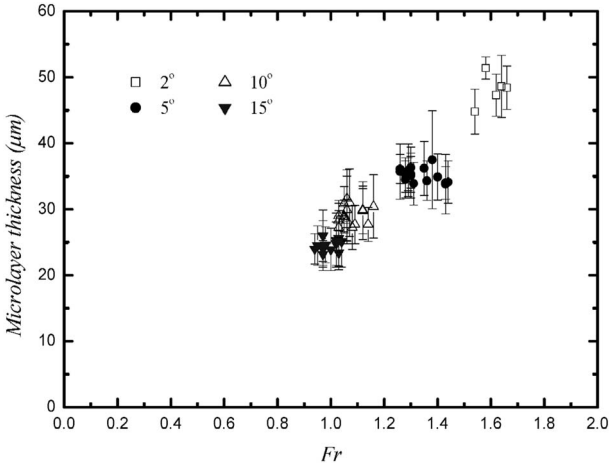

Fig. 20 Microlayer thickness versus Froude number

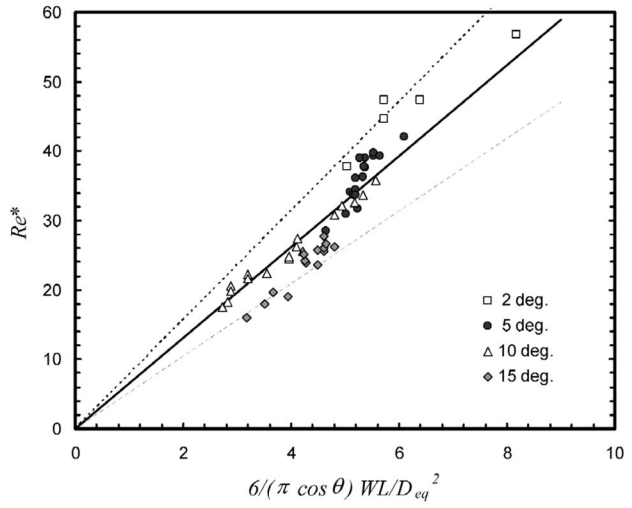

Fig. 21 Microlayer Reynolds number as given by Eq. (10)

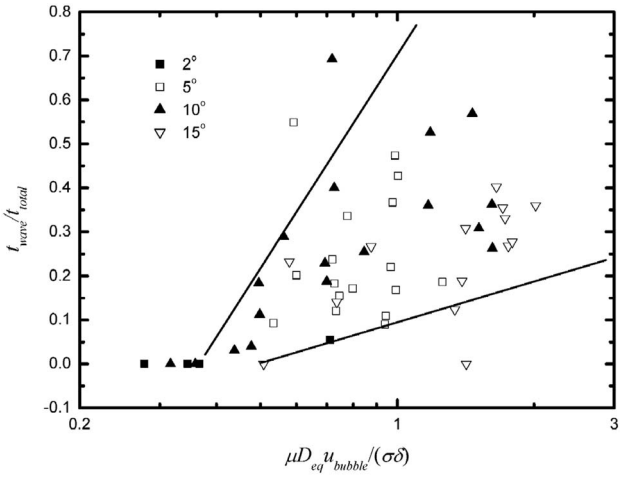

Fig. 23 t_{wave}/t_{total} versus $\mu D_{eq} u_{bubble}/(\sigma\delta)$

This result conforms to the expectation that the microlayer thickness correlates to the variables controlling bubble kinematics (θ, D_{eq}, and ν), but with the addition of a descriptor of bubble shape. For these data, WL/D_{eq}^2 varied from 1.5 to 4.3. If the form of this result is maintained, but the inclination dependence is generalized to a best-fit power function of θ, the result shown in Fig. 22 and given as Eq. (11) is obtained:

$$\frac{U^*\delta}{\nu} = \frac{31.85}{\pi} \cdot \frac{WL}{D_{eq}^2}\theta^{-0.10} \tag{11}$$

A straight line captures the data to a mean deviation of 5.5%, a value that challenges the uncertainty in the measurements.

Instability within the Microlayer. We have speculated that the spikes in the microlayer thickness traces are caused by waves on the interface that bounds the microlayer. These waves could be caused by disturbances external to the microlayer or by an instability in the liquid film itself. The external disturbances originate mainly as surface waves on the downward facing part of the bubble as high-speed images have shown. These waves appear to propagate around the bubble in both the streamwise and spanwise directions, and it is possible that they continue along the interface bounding the microlayer. If the waves are caused by an instability in the microlayer itself, a shear-driven mechanism is an obvious possibility. A dimensionless number which represents the magnitude of the shear stress in the microlayer versus the surface tension in the bubble interface bounding the microlayer is

$$\frac{\mu u_{bubble}}{\delta} \Big/ \frac{\sigma}{D_{eq}} = \mu u_{bubble} D_{eq}/(\sigma\delta) \tag{12}$$

where D_{eq} is used as the characteristic dimension for the bubble. To test the idea that the spikes are caused by surface waves, this dimensionless number was plotted against t_{wave}/t_{total}, the total length of time occupied by spikes in the optical signal (t_{wave}) over the total length of time required for the bubble to pass the fiber optic probe (t_{total}). This is a type of ergodic assumption, in which the time recorded for a particular event is representative of the spatial length over which the event is occurring.

Figure 23 shows that when $\mu u_{bubble} D_{eq}/(\sigma\delta) < 0.4$ no spikes are observed in the optical signal: the interface bounding the microlayer is smooth. When the value of this group is larger than 0.4, t_{wave}/t_{total} becomes significant and tends to increase as the value of $\mu u_{bubble} D_{eq}/(\sigma\delta)$ increases. The scatter is large and does not relate to inclination angle. This result is evidence that the appearance of spikes in the signal could be caused by the development of shear-driven interface waves such that $\mu u_{bubble} D_{eq}/(\sigma\delta) \approx 0.4$ is an indicator of the threshold for which waves can develop.

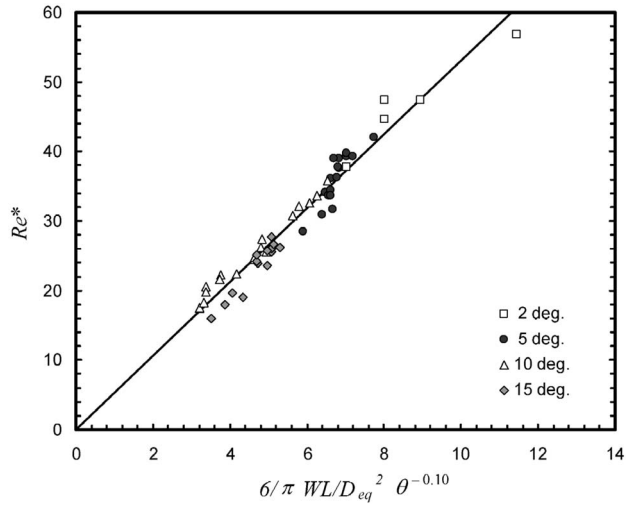

Fig. 22 Microlayer Reynolds number as given by Eq. (11)

Summary

The thickness of the liquid microlayer between a cap-shaped sliding bubble and an inclined heated wall was measured using a laser-based method. Data were reported for saturated FC-87 and a uniform-temperature surface inclined at 2 deg to 15 deg from the horizontal. A motion and shape analysis using image sequences at 1000 frames/s revealed details of the evolution of bubble shape. Bubble-averaged microlayer thickness for cap-shaped bubbles ranged from 25 to 48 μm and decreased with increasing inclination angle. The range of accessible inclination angles was limited by unwanted bubble nucleation below 2 deg and the minimum thickness, 20 μm, resolvable with the probe above 15 deg.

The microlayer thickness above cap-shaped bubbles in FC-87 is well-correlated to a function of inclination angle and a bubble shape factor. The successful correlation suggests that this data set can be used to validate the results of detailed models of the microlayer dynamics.

A relatively flat plateau in the microlayer thickness trace was identifiable for all cap-shaped bubbles; however, for larger inclination angles and Reynolds numbers, this plateau was interrupted by clusters of upward spikes. These spikes are thought to be the

nonlinear response of the probe to waves on the liquid/vapor interface that bounds the microlayer. The presence of this characteristic in the signal correlates well with the wavy structure seen in high-speed images of the phenomenon. Bubbles at inclinations of 2 deg tend to show no spikes and no waves on the interface facing the camera. A dimensionless grouping of variables representing the magnitude of the shear stress in the microlayer versus the surface tension in the bubble interface bounding the microlayer shows a threshold value beyond which disturbances appear in the microlayer trace.

Acknowledgment

This work was supported in part by a state of Texas Advanced Research Program Grant, ARP 003652-762.

Nomenclature

D_{eq} = equivalent diameter of bubble ($\equiv(6V/\pi)^{1/3}$)
Fr = Froude number ($\equiv u_{bubble}/(gD_{eq}\sin\theta)^{0.5}$)
g = gravitational acceleration, m/s^2
H = bubble height, mm
I = photodiode voltage, mV
L = bubble length, mm
NP = bubble nose position, mm
ps = pixel size, mm
R = radius of bubble, mm
Re = bubble Reynolds number ($\equiv u_{bubble}\cdot D_{eq}/\nu$)
Re^* = microlayer Reynolds number ($\equiv U^*\delta/\nu$)
T_w = wall temperature, °C
T_b = bulk liquid temperature, °C
t = time, s
t_{wave} = length of time signal affected by spikes, s
t_{total} = total time of bubble passage, s
U^* = characteristic velocity scale ($\equiv\sqrt{gD_{eq}}$), mm/s
u_{bubble} = bubble velocity, mm/s
V = bubble volume, mm^3
W = bubble width, mm
We = Weber number ($\equiv\rho u_{bubble}^2\cdot D_{eq}/\sigma$)

Greek

δ = microlayer thickness, μm
Δt = time between frames, s
μ = absolute viscosity, kg/s·m
ρ = density of the liquid phase, kg/m^3
ν = kinematic viscosity, m^2/s
θ = heating surface inclination angle, arc degrees
σ = surface tension, N/m

References

[1] Cornwell, K., 1991, "The Influence of Bubbly Flow on Boiling From a Tube Bundle," Int. J. Heat Mass Transfer, **33**, pp. 2579–2584.
[2] Thorncroft, G. E., and Klausner, J. F., 1999, "The Influence of Vapor Bubble Sliding on Forced Convection Boiling Heat Transfer," ASME J. Heat Transfer, **121**, pp. 73–80.
[3] Cooper, M. G., and Lloyd, A. J. P., 1969, "The Microlayer in Nucleate Pool Boiling," Int. J. Heat Mass Transfer, **12**, pp. 895–913.
[4] Koffman, L. D., and Plesset, M. S., 1983, "Experimental Observations of the Microlayer in Vapor Bubble Growth on a Heated Solid," ASME J. Heat Transfer, **105**, pp. 625–632.
[5] Addlesee, A. J., Cornwell, K., and Peace, D. G., 1989, "Fluid Dynamics of Sliding Bubbles and Heat Transfer Implications," *Proceedings Eurotherm Seminar 8*, "Pool Boiling," Paderborn, pp. 57–64.
[6] Addlesee, A. J., and Cornwell, K., 1997, "Liquid Film Thickness Above a Bubble Rising Under an Inclined Plate," Trans. IChemE, Part C, **75**, pp. 663–667.
[7] Addlesee, A. J., and Cornwell, K., 1999, "The Velocity of Bubbles Rising Under an Inclined Plate," *ImechE Conference Transactions, Sixth UK National Conference on Heat Transfer*, pp. 231–236.
[8] Yan, Y., and Kenning, D. B. R., 1994, "Heat Transfer Near Sliding Vapour Bubbles in Boiling," *Proceedings of the Tenth International Heat Transfer Conference*, pp. 195–200.
[9] Yan, Y., Kenning, D. B. R., Grant, I. A., and Cornwell, K., 1996, "Heat Transfer to Sliding Bubbles Under Plane and Curved Surfaces," *Fourth UK National Conference on Heat Transfer*, Manchester, IMechE, C510/118, pp. 295–299.
[10] Kenning, D. B. R., Bustnes, O. E., and Yan, Y., 2002, "Heat Transfer to a Sliding Vapor Bubble," Multiphase Sci. Technol., **14**, pp. 75–94.
[11] Qui, D., and Dhir, V. K., 2002, "Experimental Study of Flow Pattern and Heat Transfer Associated With a Bubble Sliding on Downward Facing Inclined Surfaces," Exp. Therm. Fluid Sci., **26**, pp. 605–616.
[12] Addlesee, A. J., and Kew, P. A., 2002, "Development of the Liquid Film Above a Sliding Bubble," Trans. IChemE, Part C, **80**, pp. 272–277.
[13] Nishikawa, N., Fujita, Y., Uchida, S., and Ohta, H., 1984, "Effect of Surface Configuration on Nucleate Boiling Heat Transfer," Int. J. Heat Mass Transfer, **27**, pp. 1559–1571.
[14] Bayazit, B. B., 2000, "A Thermographic Analysis of the Heat Transfer Mechanisms Generated by a Sliding Bubble," Masters thesis, University of Houston, Houston, TX.
[15] Figueroa, M., 2005, "The Evolution of the Microlayer Thickness Above a Sliding Vapor Bubble," Masters thesis, University of Houston, Houston TX, Fall, 2005.
[16] Bayazit, B. B., Hollingsworth, D. K., and Witte, L. C., 2001, "Heat Transfer Enhancement Caused by Sliding Bubbles," *Proceedings of the 35th National Heat Transfer Conference*, No. NHTC01-11651, Anaheim, CA, June, 2001.
[17] Bayazit, B. B., Hollingsworth, D. K., and Witte, L. C., 2003, "Heat Transfer Enhancement Caused by Sliding Bubbles," ASME J. Heat Transfer, **125**, pp. 503–509.
[18] Ohba, K., and Origuchi, T., 1985, "Multi-fiber Optic Liquid Film Sensor for Measurement of Two Phase Annular and Stratified Flow," *Proceedings of the International Symposium on Fluid Control and Measurement*, Tokyo, Japan, pp. 1–10.
[19] Than, C. F., Tee, K. C., Low, K. S., and Tso, C. P., 1993, "Optical Measurement of Slope, Thickness, and Velocity in Liquid Film Flow," Smart Mater. Struct., **2**, pp. 1–9.
[20] Li, X., 2005, "An Experimental Study of the Microlayer Thickness and the Kinematics of a Sliding Bubble, Ph.D. dissertation, Dept. of Mech. Engineering, University of Houston.
[21] Maxworthy, T., 1991, "Bubble Rise Under an Inclined Plate," J. Fluid Mech., **229**, pp. 659–673.
[22] Monde, M., 1990, "Measurement of Liquid Thickness During Passage of Bubbles in a Vertical Rectangular Channel," ASME J. Heat Transfer, **112**, pp. 255–258.

Methods to Accelerate Ray Tracing in the Monte Carlo Method for Surface-to-Surface Radiation Transport

Sandip Mazumder
Member ASME
Department of Mechanical Engineering,
The Ohio State University,
Columbus, OH 43202
e-mail: mazumder.2@osu.edu

Two different algorithms to accelerate ray tracing in surface-to-surface radiation Monte Carlo calculations are investigated. The first algorithm is the well-known binary spatial partitioning (BSP) algorithm, which recursively bisects the computational domain into a set of hierarchically linked boxes that are then made use of to narrow down the number of ray-surface intersection calculations. The second algorithm is the volume-by-volume advancement (VVA) algorithm. This algorithm is new and employs the volumetric mesh to advance the ray through the computational domain until a legitimate intersection point is found. The algorithms are tested for two classical problems, namely an open box, and a box in a box, in both two-dimensional (2D) and three-dimensional (3D) geometries with various mesh sizes. Both algorithms are found to result in orders of magnitude gains in computational efficiency over direct calculations that do not employ any acceleration strategy. For three-dimensional geometries, the VVA algorithm is found to be clearly superior to BSP, particularly for cases with obstructions within the computational domain. For two-dimensional geometries, the VVA algorithm is found to be superior to the BSP algorithm only when obstructions are present and are densely packed.
[DOI: 10.1115/1.2241978]

Keywords: thermal radiation, modeling, surface-to-surface, Monte Carlo, ray tracing, acceleration, BSP, volume-by-volume, computational efficiency

1 Introduction

In many applications, such as in chemical vapor deposition reactors used for rapid thermal processing of silicon wafers, direct surface-to-surface radiation exchange occurs between a hot source (e.g., tungsten lamps) and a target (e.g., the wafer) [1,2]. Often, the optical properties of the surfaces involved are strongly varying both spectrally and directionally [1,3]. The Monte Carlo method [4–6] is a proven powerful method for calculating radiation exchange in such scenarios mainly because of its ability to accurately account for directional surface properties. The disadvantage of the Monte Carlo method is that it is expensive compared to deterministic methods. In practical applications involving complex three-dimensional geometries and surfaces with complicated surface properties, a larger number of rays, usually exceeding several million, need to be traced to attain reasonable statistical accuracy [1,3,7–9]. In such scenarios, the tracing of the rays can become a major bottleneck for the overall computational procedure. Thus, efficient ray tracing is a prerequisite to the success of Monte Carlo methods for practical applications involving surface-to-surface radiation.

The central computational issue in a surface-to-surface Monte Carlo method is the determination of the intersection point between an infinite ray and the boundary, which is generally represented by a large set of discrete surface elements. If N rays are to be traced, and the computational domain boundary is comprised of M discrete surface elements (or faces), the number of intersection checks (or searches) that need to be performed are $N \times M$, since a traveling ray may potentially hit any surface element. Each intersection check requires solution of a system of 2×2 (in 2D) or 3×3 (in 3D) algebraic equations, in addition to several logical checks. Thus, the intersection calculations dominate the CPU budget if M is large.

The problem described in the preceding paragraph is often referred to as an $O(N^2)$ problem, since N and M are generally comparable. Such problems are prevalent in other applications as well, such as computer graphics applications in which ray tracing is used for surface rendering, shadowing, etc. Several well-known search algorithms are available, and have found prolific use within the computer graphics community to narrow down the search such that all M faces are not searched for each ray. Their use in thermal radiation Monte Carlo schemes, however, has been somewhat limited. The ultimate goal of such search algorithms is to reduce the $O(N^2)$ problem to a $O(N)$ problem. Although numerous methods to accelerate ray tracing have been reported in the literature, the underlying algorithms can be broadly categorized into the following types: (1) The bounding box (BB) algorithm [10–14], (2) the binary spatial partitioning (BSP) algorithm [15–18], (3) the uniform spatial division (USD) algorithm [12,13,19,20], and (4) the discrete function Monte Carlo (DFMC) algorithm [21]. Of the four, the first three algorithms share the common philosophy of narrowing the search using coarser entities, while the DFMC algorithm is fundamentally different from the other three.

In the BB algorithm [10–13], contiguous sets of boundary faces are enclosed within larger bounding boxes. Ray-box intersections, which are generally very efficient, are first performed to narrow down the search and are followed by detailed search of only those faces that are enclosed within the intersected boxes. In the multilevel version of the same algorithm, each box is dissected further into a set of hierarchically linked sub-boxes. The single-level version of the BB algorithm has been used in the past for surface-to-surface radiation Monte Carlo calculations by Mazumder and Kersch [14], and has been shown to result in substantial computational savings over the direct [or $O(N^2)$] method, although rarely

Contributed by the Heat Transfer Division of ASME for publication in the JOURNAL OF HEAT TRANSFER. Manuscript received November 15, 2005; final manuscript received February 9, 2006. Review conducted by Walter W. Yuen.

exceeding an order of magnitude. On an average, if L bounding boxes are used, in the single-level BB algorithm, the number of face searches will be $N \times M/L$. Thus, the computational time requirement will be $1/L$ times that required for direct calculations, assuming that the time spent in calculating ray-box intersections is negligible. As L becomes large, this will clearly not be the case. Also, in a domain with obstructions, since a given ray may intersect several boxes as it passes through, several boxes will have to be searched to guarantee that the nearest intersection point is found. All these factors slow down the BB algorithm. Its efficiency, although substantially superior to direct calculations, rarely scales as the number of bounding boxes used.

In the BSP algorithm [10–13,15–18], all faces within the computational domain are first placed in a large box (or voxel), whose planes are aligned to Cartesian planes. The box is then recursively bisected along the Cartesian directions, resulting in a set of hierarchical sub-boxes. The relationship between each parent box and its two children sub-boxes are stored in the form of a binary tree, along with information about their bounding planes and the enclosed faces. The bisection stops when a box has a minimum number of faces, typically decided through some trial runs. During ray tracing, ray-box intersections are first performed. As opposed to the BB algorithm, all boxes are not checked for intersection. Starting from the largest box, only pertinent sub-boxes are recursively checked by traversing the binary tree. In theory, the BSP algorithm requires only $O(N \times \log(M))$ intersection calculations. In practice, perfect logarithmic scaling is difficult to attain because of the possibility of the existence of the multiple intersection points, and lack of a perfectly balanced tree, i.e., the two children of a mother may not have an equal number of faces. Further details in this regard will be presented in the sections to follow. Despite these issues that may hamper the performance of the BSP algorithm, with careful construction of the binary tree, the algorithm is very efficient, and can result in orders of magnitude gains in computational efficiency, as will be demonstrated shortly. In general, as the number of faces, M, is increased, $\log(M)/M$ decreases exponentially, implying that the computational benefits of the BSP algorithm increase exponentially as the problem size increases. Thus, the BSP algorithm is particularly well-suited for practical applications involving large mesh sizes.

While the BSP algorithm is robust and efficient, its implementation in a computer program is not trivial: It requires adaptive data structures, and recursive procedures, among other complexities. The uniform spatial division (USD) algorithm [12,13,19,20] may be thought of as a variation of the BB algorithm, in which a uniform coarse Cartesian mesh is superposed on the computational domain, solely for the purpose of ray tracing. The mesh essentially breaks up the computational domain into a set of equal sized Cartesian boxes. Rays are then traced from box to box, and larger intersected boxes are subsequently searched in detail to locate intersection points. The algorithm has been used extensively by Burns and co-workers [19,20] in their code MONT3D. In recent years, particular emphasis has been placed on accelerating the process of identifying the "next" box as a ray exits a certain box [20]. The so-called "mailbox" technique has also been suggested (but not applied) to accelerate ray tracing by storing information about previously traced rays and using this information later. With all of these improvements in place, computational gain of a factor of 80 has been reported for complex 3D geometries by Zeeb et al. [20]. In general, the USD algorithm requires more memory than the BSP algorithm, and is not expected to result in logarithmic scaling of the efficiency with increase in the number of faces, even in theory. To the best of the author's knowledge, a formal analysis of its scaling properties has not been performed yet. Its advantage over the BSP algorithm is that it is relatively easy to implement.

The DFMC algorithm [21] is not an algorithm for acceleration of ray tracing *per se*. In this method, the core Monte Carlo algorithm is altered by sampling ray paths rather than ray directions. The method is particularly well-suited to scenarios in which a large number of strongly specular surfaces are present, and has been reported to result in computational savings of close to one order of magnitude. The DFMC algorithm appears to have been used only by the group by whom it was originally developed.

The BB, BSP, and USD algorithms share one common problem: The intersection search cannot be concluded once the first intersection point is found. The search has to be continued until all intersection points are determined, and has to be followed by a shortest distance check to determine the legitimate intersection point. Instead, if a ray is advanced little by little starting from its emission location, and its advancement terminated as soon as it hits another surface, the intersection point that will be found is guaranteed to be the nearest. The VVA algorithm is based upon this important realization. It is motivated by the fact that Monte Carlo radiation calculations are rarely performed without accompanying heat transfer calculations, in which case, a volumetric mesh already exists, and can be made use of for ray tracing. Another crucial advantage of the VVA concept is that the number of volumes (or cells) that a ray passes through, scales with the number of grid points only in one direction even for a 3D geometry, while the total number of boundary faces to be searched in other algorithms scales as the square of the number of grid points in one direction. For example, if a cube with 10 cells in each direction is considered, the number of cells, on an average, through which a ray will traverse to reach another boundary face is 10. Since each cell has six faces, on an average, 60 ray-quadrilateral intersection checks will be necessary in the VVA algorithm. For the other algorithms, $6 \times 10 \times 10 = 600$ boundary faces will have to be searched for intersection. If the mesh is doubled in each direction, in the VVA algorithm, $20 \times 6 = 120$ intersections will have to be computed, while in the other three algorithms $6 \times 20 \times 20 = 2400$ intersections will have to be computed. Thus, even for completely unobstructed geometries, the VVA algorithm is an $O(N \times M^{1/2})$ algorithm. For geometries with obstructions, as is the case in most practical applications, its performance is expected to be much better.

In this study, the VVA algorithm is explored for the first time. For comparison, the BSP algorithm is considered, since it appears to have the best combination of positive attributes among existing acceleration techniques for ray tracing. Since the BSP algorithm is relatively new to the heat transfer community, it is also discussed in significant detail in this article. While the descriptions to follow are general and apply to any arbitrary geometry, the algorithms are tested on simple but large (i.e., up to several tens of thousand faces) geometries so that the performance characteristics of the two algorithms can be understood and interpreted intuitively, and the results can be reproduced by future researchers in the area.

2 Algorithms for Acceleration of Ray Tracing

In the absence of a participating medium, the net radiative heat flux on any surface element i is a net sum of the incident radiation from all other patches and self-emission, and is mathematically written as [4,5]

$$Q_i = q_i A_i = \sum_{j=1}^{M} (\delta_{ij}\epsilon_j - R_{ij})\sigma T_j^4 A_j \tag{1}$$

where M is the total number of boundary surface elements (or faces), and A_j and T_j their surface areas, and temperatures, respectively. ϵ_j is the spectrally averaged emissivity of the jth face, and δ_{ij} is the Kronecker delta. R_{ij} is the so-called radiation exchange matrix, and represents the fraction of radiation emitted by face j and absorbed by face i after multiple events at boundaries. The Monte Carlo method is a statistical method, which, in essence, is used to compute R_{ij}. To obtain a statistically reliable estimate of R_{ij}, a large number of rays must be traced, and this section discusses two different algorithms for efficient tracing of the rays.

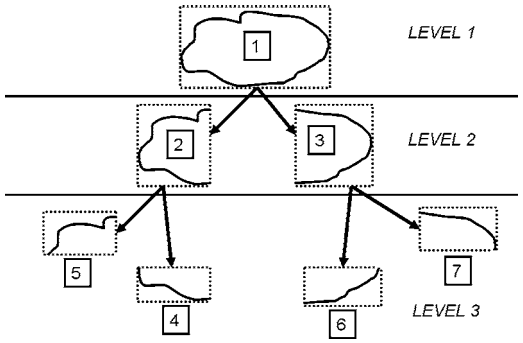

Fig. 1 Schematic representation of the bisection scheme in the BSP algorithm, the definition of "level," and the unique numbering pattern of the various boxes (or leaves)

2.1 Binary Spatial Partitioning (BSP). The BSP algorithm consists of a pre-processing step in which candidate faces for intersection are grouped within hierarchically linked boxes (or voxels). The process starts with a single box that includes all faces. This box is then bisected into two boxes along its central X plane. The two sub-boxes are then designated the two children of the original mother. In the next step the children boxes are bisected along their central Y planes, and the process is continued. The algorithm is schematically depicted for a 2D geometry in Fig. 1, in which only three levels are shown. After the creation of the two children, the faces of the mother box are also distributed among the two children. Often, a face may be shared by both children, and must be listed as belonging to both children in order to retain a water-tight geometry, as illustrated in Fig. 2. The bisection procedure can be terminated using a variety of criteria. One strategy is to simply set a maximum limit to the number of boxes (or entries) in the binary table, and terminate bisections as soon as that maximum limit is reached. The second strategy may be to set the minimum number of faces in a box. If bisection of a box results in fewer faces than the prescribed limit, the box is not bisected. It is then deemed the farthest "leaf" of the binary tree.

2.1.1 Creation of the BSP Tree. The algorithm for creation of the binary tree is as follows:

1. The coordinates of all vertices in the computational domain are scanned to determine the bounds of the computational domain. The binary table is initiated, and six real numbers, namely, $X_{\min}$, $X_{\max}$, $Y_{\min}$, $Y_{\max}$, $Z_{\min}$, and $Z_{\max}$ are stored for this first point. In addition, an integer list, consisting of all the face indices, is also stored.
2. The box is bisected along its central X, Y, or Z plane. The decision as to what direction the bisection should be performed in depends on the current level of the tree. The definition of "level" is as follows: The first entry corresponds to level 1, entries 2 and 3 in level 2, entries 4–7 in level 3, 8–15 in level 4, and so on. One approach to create an almost isotropic tree is to cycle the bisection directions with each level. If the box is bisected along the central X plane, for example, one of the children's $X_{\max}$ value will be replaced by $(X_{\min}+X_{\max})/2$ of its mother, while the $X_{\min}$ value of the other child will be replaced by $(X_{\min}+X_{\max})/2$ of its mother. All other bounds are set to that of their mother.
3. The two children are incrementally numbered, such that each entry (or box) in the table has a unique number (Fig. 1). For the mother, the entry numbers corresponding to her two children are stored, while for the children the entry number for their mother is stored.
4. The face list of the mother is distributed between the children after checking to see which faces lie within the bounding box of the children. This is done by scanning the coordinates of the individual face vertices. Faces that are shared by both children are assigned to both for reasons discussed earlier.
5. Steps 2–4 are repeated recursively until the prescribed termination criteria, discussed earlier, is reached.

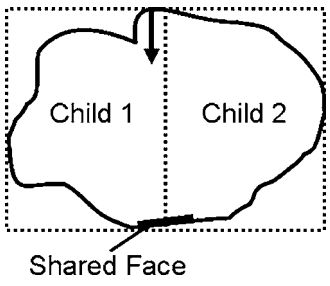

Fig. 2 Illustration of water tightness: In this example, if a ray-box intersection is performed with the bounding box of Child 2, an intersection is not found. This would suggest that the ray must hit something that belongs to Child 1. If the shared face belongs to Child 2 alone, the ray will never find an intersection and will escape though an artificially created hole.

In summary, for each entry (or box) in the table, the following data are stored: (a) Six real numbers defining the geometric bounds of the box, (b) the number of faces in each box, (c) an integer list of the global face indices, (d) the entry numbers of the two children (if they exist), and (e) the entry number of the mother.

It is worth mentioning at this point that the algorithm, just described, will result in a binary tree that may become severely unbalanced as the tree grows, i.e., the number of faces belonging to the two children of a certain mother may be dramatically different (or unbalanced). For example, if a cube is divided using the above algorithm, a box at the corner may have a significantly larger number of faces than one that is slightly away from the corner. It is well known that the use of unbalanced BSP trees can adversely affect the efficiency of ray tracing [15–18], as will also be evident from results shown later. Advanced techniques for balanced tree creation divide each mother adaptively so that both children receive an equal number of faces [15,16]. Other techniques such as rope trees [17], and stochastic sub-division [18] are also used to circumvent this problem. These advanced techniques require basic understanding of the BSP algorithm to begin with, and are not considered in this study for the sake of simplicity.

2.1.2 Traversing the BSP Tree. In most practical applications, since the mesh does not move, creation of the BSP tree is a one-time process. Once the BSP tree has been created, ray tracing can commence. As discussed earlier, the first step is to traverse the BSP tree in order to narrow down the search, and is performed using the following algorithm:

1. An integer array of size equal to the number of entries in the BSP tree is created and set to 0. This array denotes which boxes in the BSP tree are to be finally searched in detail. A zero indicates that detailed search is not necessary.
2. The search flag is set to 1 for the first entry in the tree (i.e., the supreme mother), and the traversing commences.
3. A loop cycling over all points in the table is initiated.
4. A check is performed to see if the search flag is equal to 1 for the running index of the loop. If not, the entry is not searched further. For the supreme mother, the flag has been already set to 1, and therefore, step 5 will be executed. For all other entries, the search flag will be determined after execution of steps 5–7.

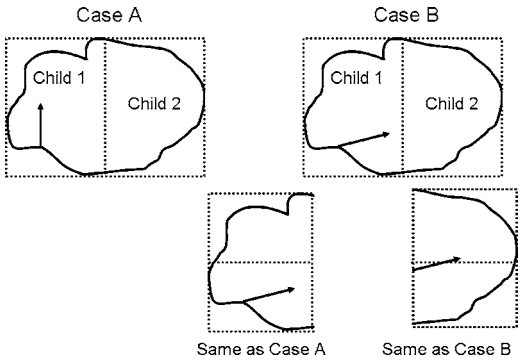

Fig. 3 Illustration of recursion in the BSP algorithm, showing that any scenario a child faces is what its mother has already encountered before, thereby allowing recursive procedures

5. Starting from the mother, the indices of the two children are obtained, if they exist. Nonexistent children can be denoted by setting their indices to a negative integer during the process of creation of the BSP tree. If the children do not exist, the traversing is terminated for that branch, implying that all faces belong to the mother and need to be searched in detail for possible intersection.
6. A check is performed to see if the originating point of the ray is within the geometric bounds of the first child. If so, then its search flag is immediately set to 1. At this point, there are two possibilities: The ray may pass through the second child (Case B of Fig. 3), or it may completely miss it (Case A of Fig. 3). A ray-box intersection is performed using the method of slabs, an extremely efficient method developed by Kay and Kajiya [22] that requires only twelve floating point operations to determine if a ray hits a box.
7. If the ray misses the second child, it need not be searched further. If the ray passes through the second child, its search flag is set to 1. In order to perform further search for the second child, the emission point of the ray is advanced to the point of intersection between the ray and the bounding box of the second child. The emission point for the first child remains as the original emission point. The idea is illustrated in Fig. 3, which also goes on to show that subsequent sub-divisions are recursive.
8. If the original emission point is found to be enclosed within the bounding box of the second child to begin with, the exact same procedure, described above in steps 6 and 7, is conducted, except that it commences with the second child.
9. The traversing of the BSP tree is complete once the loop over all the points in the table has been completely cycled. An example of the traversing process is shown in Fig. 4 for a simple 2D case with a four-level tree.
10. The final step is to reset the search flags of all entries, except those that do not have any children, to 0. For the example shown in Fig. 4, this implies that the search flag for boxes 1,2,3,4,6, and 7 will be reset to 0. This implies that only the farthest leaves will be finally searched.

The algorithm for traversing the BSP tree, just described, is the one that is used for the present study, and conforms to the data storage outlined earlier. It may not necessarily be the most effective way of traversing the BSP tree, although variations of it are expected to change the efficiency only marginally.

2.2 Volume-by-Volume Advancement (VVA). The VVA algorithm does not require any pre-processing steps. It is also equally applicable to scenarios in which the grid may move or

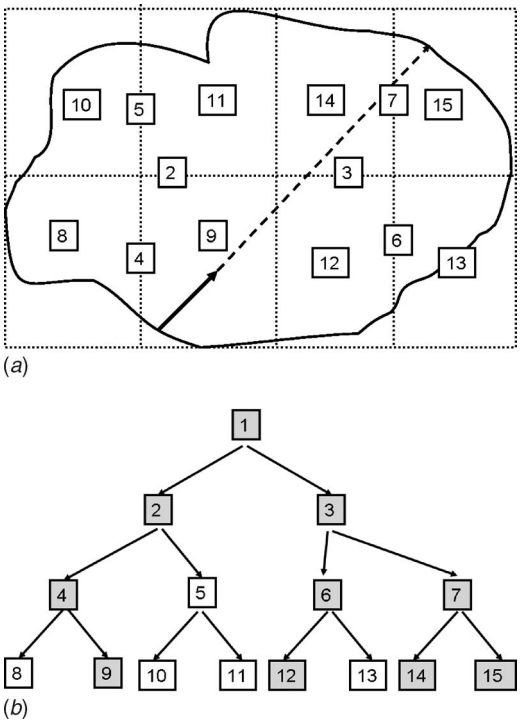

Fig. 4 An example illustrating the working mechanism of the BSP algorithm: (*a*) The geometry, the emitted ray, and the various boxes in its path, (*b*) the boxes and sub-boxes for which the search flag becomes 1 are shaded gray

deform after every time step. In that sense, it is more versatile than existing algorithms for acceleration of ray tracing. The VVA algorithm is also easier to program than the other algorithms, and requires the following steps:

1. Starting from the global face index corresponding to the emission location, the adjacent cell's global index is obtained from the grid connectivity information. It is to be noted that cell-to-face, face-to-cell, face-to-vertex, cell-to-vertex connectivity data are stored as part of any accompanying heat transfer and/or fluid flow calculations, and are, therefore, readily available for use in the VVA algorithm.
2. The face indices of the cell are then obtained from connectivity data. The exact number of faces of the cell will depend on the grid topology, and the algorithm can account for any topology as long as the cells are convex, which is usually the type created by most mesh generators, commercial or otherwise.
3. A loop is run over all faces, and the face number corresponding to the emission location is skipped. Within this loop, ray-face intersections are computed until an intersection is found. This point represents the exit point of the ray from the cell in question, and is designated the new emission location.
4. A check is performed to see if the face index corresponding to the intersection point is a boundary face. If so, the next legitimate intersection point has been found, and boundary conditions must be applied prior to further tracing.
5. If the intersected face is not a boundary face, from the face index, the cell indices of the two cells adjacent to the face are obtained from grid connectivity data. One of these indices will correspond to the cell at the back of the ray (i.e., the one from which it came), and is not considered. The other cell index (on the front of the ray) is

deemed the legitimate cell index for further advancement of the ray.

6. Steps 2–5 are repeated until a boundary face is intersected.

The implementation of the VVA algorithm, described above, requires no additional memory and only a few tens of lines of programming, irrespective of the programming language used.

3 Results and Discussion

Computations were performed using the two algorithms described in Sec. 2. In addition, direct calculations (i.e., without any acceleration of ray tracing) were performed to judge the efficiency of the two algorithms. Ray-line and ray-triangle intersection calculations were performed using parametric vector representation of surfaces. The procedures to do so are straightforward and available in detail elsewhere [4,10,13,14]. For 3D cases, even though planar quadrilateral surface elements were used for the test cases to be described shortly, in order to keep the algorithms general-purpose, the intersection calculations did not assume that the four points of the quadrilateral are on a single plane. Thus, each quadrilateral was divided into two triangles and ray-triangle intersections were computed rather than ray-quadrilateral intersections. Although procedures such as backface culling [10,13] are often recommended and used to narrow down the number of candidate faces for intersections, such procedures were not implemented here because the gains resulting from such procedures are highly geometry dependent, to the extent that sometimes backface culling can adversely affect the computational efficiency.

3.1 Verification of the Monte Carlo Code. Prior to efficiency studies, the Monte Carlo code was verified both for 2D and 3D geometries by comparing results against deterministic radiation exchange calculation results using analytically calculated view-factors [4,5]. This is an important step to ensure that the direction, location and frequency of the rays are being sampled correctly, and that boundary conditions are being properly implemented. The procedures for sampling of the rays are well documented in textbooks, such as in Chapter 20 of the one by Modest [4], and are not repeated here since no changes were made to these standard procedures. Furthermore, for the sake of brevity, only 2D results are presented here.

The test case considered here for verification is that of radiation transport in a square cavity with diffuse gray walls having emissivity equal to 0.5. The left wall is set at 1000 K, while the other three walls are held at a constant temperature of 300 K. Each wall is divided into 10 equal sized faces. Figure 5 shows the computed heat fluxes at the various walls. As expected, the accuracy of the results improves as more rays are traced, and the results agree almost perfectly with view-factor results when 10^6 rays are traced. Following verification of the basic Monte Carlo scheme, computations were also performed with the acceleration schemes in place, and the results compared against direct ray tracing results to ensure that the results matched number for number.

3.2 Efficiency Studies. Following verification of the core Monte Carlo scheme, studies were undertaken to judge the effectiveness of the two algorithms under investigation. For efficiency studies, all walls were assumed to be gray and diffuse with prescribed emissivity equal to 0.5, and were set to the same temperature, so that all faces emitted the same number of rays, and any directional bias in the ray tracing was eliminated. For the BSP algorithm, the maximum number of entries in the BSP table was set arbitrarily to $M/8$. A simple calculation will reveal that, on an average, this is expected to result in 16 faces in each farthest leaf if M is sufficiently large, and the tree is perfectly balanced. Both 2D and 3D calculations were performed, and two different geometries were considered: An open box (or rectangle in 2D), representative of a geometry without obstruction, and a box in a box, representative of a geometry with obstruction (Fig. 6). All calculations were performed on a 1.5 GHz Intel Pentium processor. In each case, a total of one million rays were traced.

The results of two-dimensional calculations are shown in Table 1. In this case, the number of faces is small even for the finest mesh considered, and thus, the performance of the individual algorithms is not obviously noticeable. In particular, the scaling of the CPU time with the number of faces is not clear with such a small number of faces. Nevertheless, a few important observations can be made from the data. First, both the VVA algorithm and the BSP algorithm result in computational gains, although the gains are only a factor of 2–5. For the BSP algorithm, the relative gain in computational efficiency increases as the number of faces increase. The VVA algorithm appears to be superior to the BSP algorithm in the case where obstructions are present in the geometry, while the BSP algorithm is superior in cases where the geometry is unobstructed. Since the VVA algorithm's CPU time consumption scales as the number of grid points in one direction only, for 2D problems, the VVA algorithm scales linearly with the number of boundary faces, as is evident from its data for an open rectangle. Thus, there is no great benefit in using the VVA algorithm for 2D geometries, unless obstructions are present.

Results of ray tracing in 3D geometries are shown in Table 2. For both the VVA and the BSP algorithms, the computational gains increase as the size of the problem is increased. Since the CPU consumption of the VVA algorithm is expected to scale as $M^{1/2}$, and that of the BSP algorithm is expected to scale as $\log M$, this nonlinear increase in computational gains with problem size is not surprising. For the largest case considered (the last entry in Table 2), the computational gain attained using the VVA algorithm is a factor of 334, while that using the BSP algorithm is 52. Thus, without doubt, both algorithms are tremendously beneficial for acceleration of ray tracing in large geometries with a large number of boundary faces. The VVA algorithm appears to be superior to the BSP algorithm for 3D geometries both with and without obstructions.

An important aspect of any algorithm of the type used here is its scaling properties with the problem size. Although, in theory, $M^{1/2}$ and $\log M$ scaling laws are expected to be obeyed by the VVA and BSP algorithms, respectively, whether such scaling is manifested in practice remains to be seen. In order to investigate the practical scaling characteristics of the two algorithms, the data in Table 2 was analyzed further.

Figure 7 shows a plot of the CPU consumed by the VVA algorithm as a function of the number of boundary faces, M. Also shown in the same figure are curve-fits to the data. It is interesting to note that separate scaling laws, $M^{0.54}$ and $M^{0.46}$, are manifested for cases with and without obstruction, respectively, even though the same algorithm is used in both cases. Regardless, the important conclusion to draw from this analysis is that the VVA algorithm scales roughly as $M^{1/2}$ even in practice, the worst performance being $M^{0.54}$, and the best depending on the topology and density of the obstructions within the computational domain.

As insinuated earlier, the performance of the BSP algorithm is greatly affected by how well balanced the BSP tree is. Figure 8 shows a plot of the CPU consumed for the BSP algorithm as a function of the number of boundary faces, M. A logarithmic curve $[=5.7 \log_2(M)]$ is also shown on the same figure. The factor 5.7 was chosen to match the curve to the first data point (i.e., 52 s for $M=600$). It is clear from the plot that in practice, logarithmic scaling is not manifested. The excess CPU may have been consumed due to a variety of reasons: (1) Overheads in creating the BSP tree, (2) overheads in traversing the BSP tree, (3) inclusion of multiple intersection points, and finally, (4) an unbalanced BSP tree. The most prolific symptom of an unbalanced BSP tree is that the CPU consumed scales linearly with an increase in the number of faces. This happens because the number of faces in the farthest leaves of the tree increases linearly when the tree is already severely unbalanced. Thus, if the total number of faces are doubled,

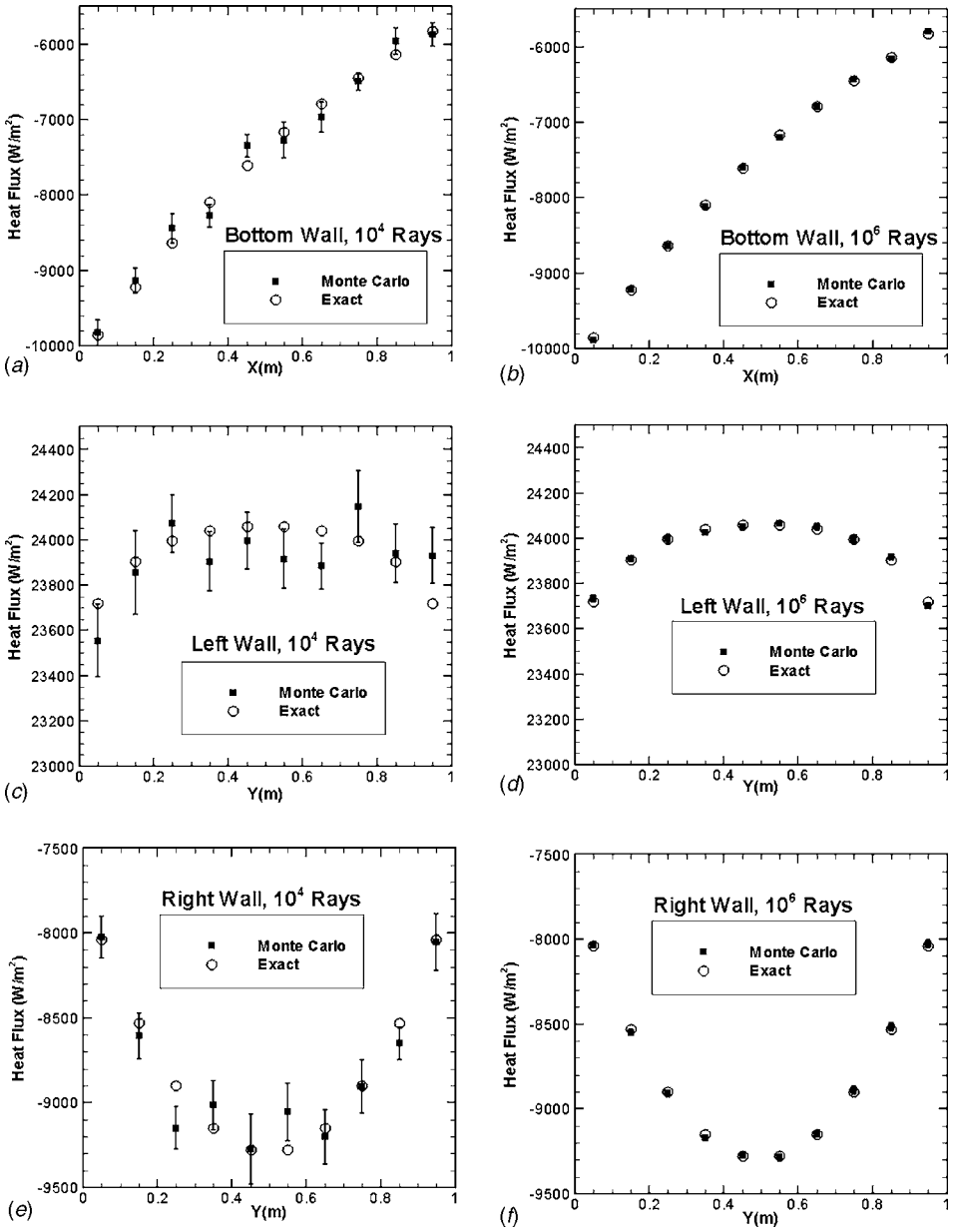

Fig. 5 Comparison of Monte Carlo results with results obtained using the view-factor method: The statistical errors were computed using 9 ensembles, and the error bars shown correspond to ± std. dev. The statistical errors for 10^6 rays are so small that they are not visible on the plots.

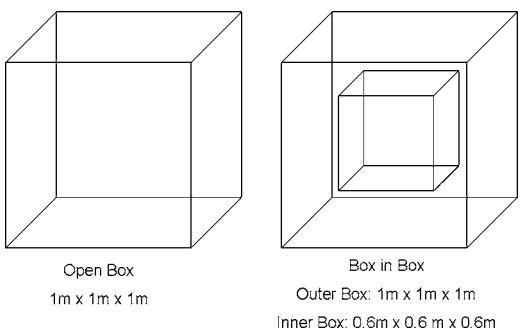

Fig. 6 Geometry used for the test cases considered in the present study

the number of detailed intersection searches that are finally performed, are also doubled. As discussed earlier, unbalanced trees will result if adaptive algorithms are not implemented to balance the tree. In the current study, since no such special algorithms were used, it is expected that the tree will become more and more unbalanced as it grows, and will be most severely unbalanced for the largest problem size. In order to test this hypothesis, a linear component (i.e., one that scales linearly with M) was added to the CPU curve, indicated by the dotted line in Fig. 8. It is observed that this new curve fits the raw data quite well, indicating that the tree is, indeed, unbalanced. Further probing of the code during execution revealed that the number of faces in the farthest leaves of the BSP tree increased almost linearly beyond 10,000 faces, with as many as 108 faces in many of the leaves, as opposed to the expected value of 16 faces. Thus, it can be concluded that although the BSP algorithm, in theory, has logarithmic scaling properties, logarithmic scaling, in practice, can only be achieved if

Table 1 Performance of various algorithms for tracing one million rays in 2D geometries

Grid points in one direction	Boundary Faces, M	CPU time (in seconds)		
		Open Box		
		Direct	VVA	BSP
10	40	6.7	4.5	7.3
20	80	12.5	8.8	10.3
40	160	24.5	16.9	14.4
80	320	48.2	35.6	19.8
		Box in Box		
Grid points in one direction[a]	Boundary Faces, M	CPU time (in seconds)		
		Direct	VVA	BSP
20 (12)	128	20	3.9	12.3
40 (24)	256	39.3	7.2	16.1
80 (48)	512	77.7	14.3	22.8

[a]The number in parenthesis denotes the number of grid points on the inner box.

special measures are adopted to balance the tree. Nevertheless, the present study shows that even with an unbalanced tree, the BSP algorithm can result in orders of magnitude gain in computational efficiency for large-scale problems in ray tracing. This is because the slope for the linear component due to overheads is still very small compared to the slope for direct calculations (0.02 versus 0.97 for the test case considered here).

4 Summary and Conclusions

Acceleration of ray tracing is imperative to enable use of the Monte Carlo method for radiation transport calculations in practical applications involving complex three-dimensional geometries. Two different algorithms for acceleration of ray tracing have been described, tested, and systematically analyzed in this study. One of these algorithms is the well-established binary spatial partitioning (BSP) algorithm. The other algorithm, named the volume-by-volume advancement (VVA) algorithm is new, and was explored for the first time. Based on the test cases considered here, the following conclusions may be drawn:

- Both the BSP and the VVA algorithm result in computational gains over the direct calculation method, irrespective of the geometry and dimensionality of the problem. The computational gains increase nonlinearly (or at least, super-linearly) for both algorithms, as the problem size increases. Thus, the power of such acceleration algorithms is truly manifested in large three-dimensional calculations.
- The performance of the VVA algorithm was found to be superior to the BSP algorithm, especially when obstructions were placed in the geometry. In addition, it is easy to implement in a computer program, requires no additional memory, requires no pre-processing, and is also applicable to transient scenarios where the grid may move or deform. In theory, the CPU time consumed by this algorithm scales as $M^{1/2}$, where M is the total number of boundary faces. In practice, this scaling law was also roughly observed, indicating that the algorithm has virtually no overheads associated with it. For the largest case considered in the present study, the computational gain using the VVA algorithm was found to be a factor of 334.
- The BSP algorithm has the potential of providing logarithmic scaling of performance with increase in problem size. However, in order to attain logarithmic scaling, the BSP tree needs to be adaptively constructed so that it is almost balanced. The core BSP algorithm, without any adaptation, will result in an unbalanced tree, which will hamper the efficiency as the problem size is increased. In such a scenario, the efficiency is more likely to scale

Table 2 Performance of various algorithms for tracing one million rays in 3D geometries

Grid points in one direction	Boundary Faces, M	CPU time (in seconds)		
		Open Box		
		Direct	VVA	BSP
10	600	239	15	52
20	2400	1316	44	102
40	9600	9120	130	245
80	38,400	37,871	290	1037
		Box in Box		
Grid points in one direction[a]	Boundary Faces, M	CPU time (in seconds)		
		Direct	VVA	BSP
10 (6)	816	326	9	60
20 (12)	3264	1764	22	119
40 (24)	13,056	12,358	66	292
80 (48)	52,224	50,229	150	975

[a]The number in parenthesis denotes the number of grid points on the inner box.

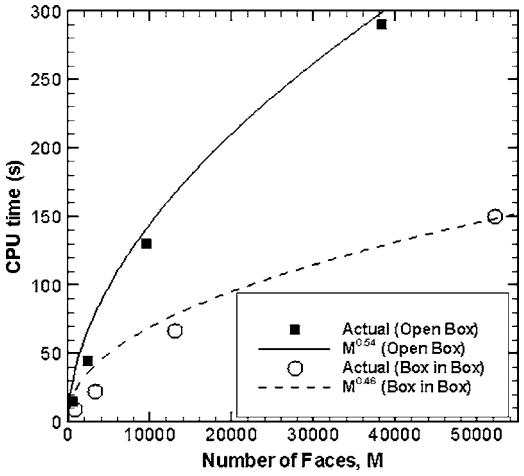

Fig. 7 Performance characteristics of the VVA algorithm in 3D geometries, and the scaling laws derived from them

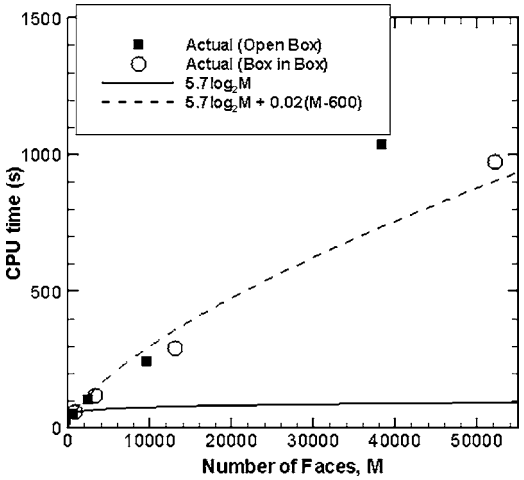

Fig. 8 Performance characteristics of the BSP algorithm in 3D geometries, and the scaling laws derived from them

super-linearly (i.e., linearly, but with a slope much larger than for direct calculations), rather than logarithmically. For the largest case considered in the present study, the computational gain using the BSP algorithm was found to be a factor of 52. From a programming viewpoint, the BSP algorithm is much more difficult to implement than the VVA algorithm, and also requires more memory.

Future research needs to be directed towards further refinement of these algorithms, and further testing for complex physical problems with real surface properties to elucidate additional subtle issues in the implementation and the working mechanisms of these algorithms for surface-to-surface radiative heat transfer applications.

Nomenclature

A = area of boundary face (m^2)
M = number of boundary faces
N = number of rays
Q = radiative heat transfer rate (W)
q = radiative heat flux (W/m^2)
R_{ij} = radiation exchange matrix (dimensionless)
T = temperature (K)

Greek

δ_{ij} = Kronecker delta
ϵ = emissivity (dimensionless)
σ = Stefan-Boltzmann constant ($=5.67\times10^{-8}\ Wm^{-2}\,K^{-4}$)

References

[1] Kersch, A., and Morokoff, W., 1995, *Transport Simulations in Microelectronics*, Birkhauser, Basel.
[2] Chatterjee, S., Trachtenberg, I., and Edgar, T. F., 1992, "Modeling of a Single Wafer Rapid Thermal Reactor," J. Electrochem. Soc., **139**, pp. 3682–3690.
[3] Mazumder, S., and Kersch, A., 1999, "Effect of Thin Films on Radiative Transport in Chemical Vapor Deposition Systems," International Mechanical Engineering Congress and Exposition, Nashville, TN, ASME-HTD, Vol. 364-3, pp. 9–13.
[4] Modest, M. F., 2003, *Radiative Heat Transfer*, 2nd ed., Academic, New York.
[5] Siegel, R., and Howell, J. R., 2001, *Thermal Radiation Heat Transfer*, 4th ed., Taylor and Francis-Hemisphere, London.
[6] Haji-Sheikh, A., 1988, "Monte Carlo Methods," in *Handbook of Numerical Heat Transfer*, W. J. Minkowycz, E. M. Sparrow, G. E. Schneider, and R. H. Pletcher, eds., Wiley, New York, Chap. 16.
[7] Maltby, J. D., and Burns, P. J., 1991, "Performance, Accuracy, and Convergence in a Three-Dimensional Monte Carlo Radiative Heat Transfer Simulation," Numer. Heat Transfer, Part B, **19**(2), pp. 191–209.
[8] Burns, P. J., and Pryor, D. V., 1999, "Surface Radiative Transport at Large Scales via Monte Carlo," in *Annual Review of Heat Transfer*, C. L. Tien, ed., Begell House, New York, Vol. 9, pp. 79–158.
[9] Burns, P. J., Maltby, J. D., and Christon, M. A., 1990, "Large-Scale Surface to Surface Transport for Photons and Electrons via Monte Carlo," Comput. Syst. Eng., **1**(1), pp. 75–99.
[10] Foley, J., Van Dam, A., Feiner, S., and Hughes, J., 1990, *Computer Graphics Principles and Practice*, Addison-Wesley, Reading, MA.
[11] Arvo, J., and Kirk, D., 1989, "A Survey of Ray Tracing Acceleration Techniques," in *An Introduction to Ray Tracing*, A. S. Glassner, ed., Academic Press, San Diego, CA, pp. 201–262.
[12] Glassner, A. S., 1984, "Space Subdivision for Fast Ray Tracing," IEEE Comput. Graphics Appl., **4**(10), pp. 15–22.
[13] Glassner, A. S., 1989, *An Introduction to Ray Tracing*, Academic, London.
[14] Mazumder, S., and Kersch, A., 2000, "A Fast Monte-Carlo Scheme for Thermal Radiation in Semiconductor Processing Applications," Numer. Heat Transfer, Part B, **37**(2), pp. 185–199.
[15] Sung, K., and Shirley, P., 1992, "Ray Tracing with a BSP Tree," in *Computer Graphics Gems III*, D. Kirk, ed., AP Professional, San Diego, CA, pp. 271–274.
[16] Chin, N., 1995, "A Walk Through BSP Trees," in *Computer Graphics Gems V*, A. W. Paeth, ed., AP Professional, San Diego, CA, pp. 121–138.
[17] MacDonald, J. D., and Booth, K. S., 1990, "Heuristics for Ray Tracing Using Space Subdivision," Visual Comput., **6**(3), pp. 153–166.
[18] Havran, V., Kopal, T., Bittner, J., and Zara, J., 1998, "Fast Robust BSP Tree Traversal Algorithm for Ray Tracing," Journal of Graphics Tools, **2**(4), pp. 15–23.
[19] Zeeb, C. N., Burns, P. J., Branner, K., and Dolaghan, J. S., 1999, User Manual for MONT3D–Version 2.4, Colorado State University, Fort Collins, CO, available online at www.colostate.edu/~pburns/monte/manual.html.
[20] Zeeb, C. N., Dolaghan, J. S., and Burns, P. J., 2001, "An Efficient Monte Carlo Particle Tracing Algorithm for Large, Arbitrary Geometries," Numer. Heat Transfer, Part B, **39**(4), pp. 325–344.
[21] Shaughnessy, B. M., and Newborough, M., 1998, "New Method for Tracking Radiative Paths in Monte Carlo Simulations," ASME J. Heat Transfer, **120**(3), pp. 792–795.
[22] Kay, T. L., and Kajiya, J. T., 1986, "Ray Tracing Complex Scenes," in Computer Graphics (SIGGRAPH '86 Proceedings), D. C. Evans and R. J. Athay, eds., Vol. 20, pp. 269–278.

Transient Response of Two-Phase Heat Exchanger With Varying Convection Coefficients

G. F. Naterer
University of Ontario Institute of Technology,
Oshawa, Ontario, Canada
e-mail: greg.naterer@uoit.ca

C. H. Lam
Honeywell Aerospace,
Mississauga, Ontario L1H 7K4, Canada
e-mail: chunho.lam@honeywell.com

Transient changes of fluid and wall temperatures in a two-phase heat exchanger are investigated in this article, particularly with respect to spatial and temporal effects of varying convection coefficients. The coupled energy equations for both sides of the heat exchanger are solved directly with an integral method. Varying convection coefficients are related to changes of vapor fraction between the inlet and outlet of the heat exchanger. Unlike past numerical studies encountering difficulties with instability, stiffness, and lack of convergence, the current integral formulation provides a reliable alternative and efficient procedure for transient response within the heat exchanger. Furthermore, complex inversion from a transformed domain is not needed, in contrast to conventional methods with Laplace transforms. In this article, past integral methods are extended to cases with varying convection coefficients, arising from changes of phase fraction on the two-phase side of the heat exchanger, as well a multiple step-changes of temperature. The predicted results show close agreement with past data, including numerical simulations with a dynamic simulator. [DOI: 10.1115/1.2241974]

1 Introduction

Log-mean and effectiveness-NTU solution methods [1–3] have been widely documented for steady-state heat exchanger analysis. Relatively less data and analysis are available for transient problems, such as transient temperature changes on the shell side or tube side of heat exchangers. Detailed analysis of such three-dimensional (3D) transient problems, including turbulence and phase transition, can be studied with CFD (computational fluid dynamics) [4]. However, such analysis usually comes at considerable cost (computational time and storage), so that it becomes infeasible for purposes of real-time control. In this article, a simplified analytical approach that retains the essential thermal physics of the problem, while keeping reasonable accuracy, is studied. This simplified method could be applied to control systems in aircraft heat exchangers, where fast system response to transient step-changes of temperature is needed.

The classical book by Kays and London [2] provides detailed correlations for friction factors and Colburn factors for various types of compact heat exchangers. These configurations include flat tube, circular tube and plate/fin configurations. Kakac, Shah, and Bergles [5] have provided comprehensive data for heat exchangers in low Reynolds number regimes. Na Ranong and Roetzel [6] have investigated transient behavior of heat exchangers coupled by a circulating freestream. The authors considered how the overall heat transfer coefficient depends on the mass flow rate of the circulating freestream. Laplace transforms and a method of finite differences were used to predict the system response to transient perturbations of the inlet temperature and mass flow rate. Flow perturbations were shown to affect transient changes of the outlet fluid temperature. In the steady state, it was shown that a certain heat capacity rate of the circulating freestream maximizes the temperature change of the external flow stream.

Dynamic behavior of plate heat exchangers with flow maldistribution from the port to channel was reported by Srihari et al. [7]. Fluid axial dispersion characterizes back mixing and other notable deviations from plug flow through the heat exchanger. Variations of the heat transfer coefficient, due to nonuniform distribution of fluid velocity throughout the channels, were also reported. Solutions were obtained with Laplace transforms and numerical inversion from the frequency domain. Predicted results show that the dynamic response and thermal performance deteriorates with flow maldistribution. Unlike Laplace transforms, this article develops an integral method for heat exchanger analysis.

Step changes of the heat transfer coefficient for a separating wall of a counter-current heat exchanger were documented by Siakavellas and Georgiou [8]. The predicted results show a significant influence of both delay time and Biot number on the thermal response of the flat plate within the heat exchanger. Under certain ranges of the Biot number, it was shown that the plate approaches a steady-state solution quickly, when a step change is applied. Two distinct zones of thermal stress were observed when the steady-state temperature perturbation becomes zero.

Unlike these past steady-state studies, this article considers transient operation of a heat exchanger. Yin and Jensen [9] have developed an integral method to predict transient temperature responses to step changes in fluid temperature and mass flow rates within a two-phase heat exchanger. Both single-phase fluid and wall temperatures were predicted analytically. The other side of the heat exchanger remains at a constant temperature. Nonlinear interfacial constraints are needed at the moving phase interface, whether it involves liquid/gas [10] or solid/liquid phase change [11]. Jang and Wang [12] have investigated the transient responses of crossflow heat exchangers, with one fluid mixed and the other fluid unmixed. Both step-changes of the mixed fluid and unmixed fluid streams were considered. The predicted transient response of the outlet temperature was observed to be identical in both cases for the unstepped fluid, but results for the stepped fluid were notably different.

Step, ramp, exponential, and sinusoidal excitations of the inlet heat exchanger temperature were investigated numerically with a finite element method by Rao et al. [13]. Both direct and fluid coupled indirect heat exchangers were considered with a forced convection loop. In addition, a thermally driven free convection loop was investigated. The predicted results have shown that a direct heat exchanger does not exhibit any time delay between the response and excitation function, while the phase difference between the response and sinusoidal excitation is lowest.

Abdelghani-Idrissi et al. [14] have applied a first-order response with a time constant to analyze transient step-changes of mass

Contributed by the Heat Transfer Division of ASME for publication in the JOURNAL OF HEAT TRANSFER. Manuscript received November 10, 2005; final manuscript received April 12, 2006. Review conducted by Bengt Sunden.

flow rates in a tubular counter-flow heat exchanger. A decreasing linear time constant arises with the hot fluid stream, while the cold fluid exhibits both linearly increasing and uniform time constants along the heat exchanger. A step-change of flow rate is applied to the hot fluid stream, but not the cold stream, thereby affecting the time constants. Analytical expressions for the time constants were derived for all cases. Although good agreement between predicted results and experimental data was achieved, the formulation requires a time lag and characteristic time constant, which depend on additional (unknown or unavailable) experimental or numerical data.

Gowda and co-workers [15] have applied a velocity correction procedure with finite element simulations to predict transient flow conditions in an in-line tube bank. The semi-implicit algorithm is solved for a Reynolds number of 100 and pitch-to-diameter ratios between 1.5 and 2.0. A Galerkin weighted residual formulation was adopted in the numerical simulations. The time evolution of streamlines, as well as Nusselt numbers, pressure and shear stress distributions were reported by the authors.

In the detailed design of heat exchangers, a common goal involves higher rates of heat exchange, without excessively raising the pressure drop throughout the system. Many thermal techniques, such as fins and baffles, are effective for enhancing the rate of heat exchange, but at the expense of excessive pressure losses. This tradeoff can be effectively expressed through a reduced rate of total entropy production [16,17]. Thus, combining CFD (computational fluid dynamics) with entropy generation predictions has useful benefits in heat exchanger analysis. These predictions can be well supplemented by measured data [18] involving local irreversibilities throughout the heat exchanger.

As discussed previously, past studies of transient responses within heat exchangers have generally involved numerical methods [19,20] or Laplace transforms [21]. Due to the complexity of simulating internal flows within heat exchangers, numerical solutions have exhibited difficulties with stiffness, instability and poor convergence. Also, solution inversion from the transformed domain has led to notable difficulties with analytical transform methods [21]. Jin and Jensen [9] have developed useful integral methods, but with limitations to cases of constant coefficients and single step-changes in temperature. This article extends those developments to cases with varying convection coefficients, due to changes of vapor fraction on the two-phase side of the heat exchanger, as well a multiple step-changes of temperature.

2 Problem Formulation

The quality of aircraft cabin air is important for comfort of long and short distance travelers. The air must be clean, pressurized, and kept at a comfortable temperature. At cruise altitudes, the outside air temperature and humidity are typically −56 C and 2%, respectively. Outside air and re-circulated internal air are passed through heat exchangers before supplying the cabin. Outside air flows through the compressor and becomes hotter and pressurized. A portion of air drawn off for the passenger cabin is first cooled by heat exchangers in the engine struts and then air conditioning units under the floor of the cabin. These heat exchangers (analyzed in this article) often use a refrigerant-based air conditioning process for cooling. A water separator removes moisture condensed during the refrigeration process. The cooled air is mixed with filtered air from the passenger cabin, which is then sent to the cabin and distributed through overhead outlets. Exiting air flows below the cabin floor into a lower lobe of the fuselage. The cabin has a high overall air-change rate. All cabin air is typically replaced by an incoming mixture of outside air and filtered air in intervals of about two to three minutes.

Consider transient heat transfer within a cross-flow heat exchanger, between a single-phase fluid (air) and an evaporating fluid (such as R134a). Several assumptions will be adopted in the following analysis: (i) constant mass flow rate of each fluid, (ii) constant specific heat of single-phase fluid through the heat exchanger, (iii) fluid temperatures are only functions of time (t) and position (x), (iv) longitudinal and transverse heat conduction within the wall and fluids are negligible, compared to convection, and (v) no chemical reactions within the fluid or wall. Yin and Jensen [9] have considered transient heat exchanger response under these assumptions. This article makes extensions to that model, particularly for varying convection coefficients (due to phase change in the secondary stream) and multiple step-changes in temperature.

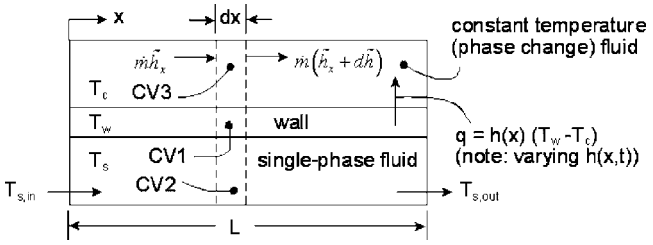

Fig. 1 Schematic of heat exchanger control volumes

Consider a differential control volume of thickness dx within the wall (see Fig. 1). In this control volume, the transient change of wall temperature balances the convective heat transfer from the single-phase fluid, minus convective heat transfer to the phase-change fluid, i.e.,

$$m_w c_{pw} \frac{\partial T_w}{\partial t} = h_s(x) A_c (T_s - T_w) - h_c(x) A_c (T_w - T_c) \tag{1}$$

Performing a similar energy balance within differential control volumes in the single-phase fluid and phase-change fluid, respectively,

$$m_s c_{ps} \frac{\partial T_s}{\partial t} + \dot{m}_s c_{ps} L \frac{\partial T_s}{\partial x} = h_s(x) A_s (T_w - T_s) \tag{2}$$

$$\dot{m}_c L h_{fg} \frac{\partial \lambda}{\partial x} = h_c(x) A_c (T_w - T_c) \tag{3}$$

where h_{fg} and λ refer to the latent heat of evaporation and vapor phase fraction, respectively. On the right side, the heat transfer coefficient, h_c, depends on the flow regime in two-phase conditions, i.e., slug flow, annular, transition, mist (see Fig. 2). Equation (3) represents an energy balance for a differential control volume encompassing the constant temperature fluid, which undergoes a change of phase (see Fig. 1). For a quasi-stationary approximation, the net enthalpy difference across streamwise edges of the control volume balances the convective heat transfer across the wall. This approximation assumes that streamwise heat transport throughout the fluid occurs rapidly, in comparison to the time scale associated with stabilized movement of the phase interface. As a result, a transient term appears in the heat balance at the phase interface, but it will be neglected relative to the heat convection term in Eq. (3).

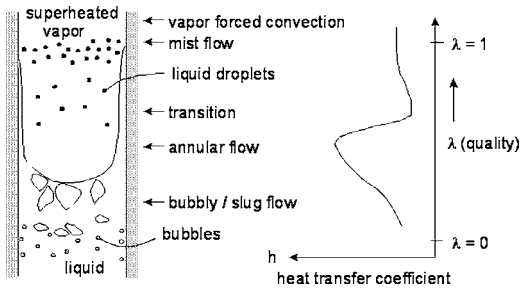

Fig. 2 Varying convective heat transfer coefficients

Under steady-state conditions, the heat transfer rate for a parallel flow heat exchanger in Fig. 1 must be multiplied by F (correction factor) to establish the heat transfer rate for a heat exchanger. The steady-state profiles for the fluid and wall temperatures must be modified accordingly. Thus, the convective heat flux in the previous energy balance is multiplied by the correction factor. It can be shown that equivalent results are obtained, except that $N_2 \rightarrow FN_2$, $N_3 \rightarrow FN_3$, and $NTU \rightarrow F(NTU)$ are replaced in the final temperature distributions. In the correction factor correlations and figures, an important observation is $F=1$ if $P=0$ or $R=0$, which can occur if the temperature change of either fluid stream is negligible (such as condensation or boiling). In the steady state, the heat exchanger characteristics become independent of the specific configuration, as one of the fluids undergoes phase change and its temperature change is negligible. Thus, the results for crossflow and parallel flow heat exchangers become equivalent, when the convection coefficients are uniform.

Define $x^*=x/L$ (nondimensional position), $t^*=t(\dot{m}_s/m_s)$ (nondimensional time), $T^*=(T/T_{s,\text{in}})/(T_{c,\infty}-T_{s,\text{in}})$ (nondimensional temperature) and the following additional non-dimensional variables:

$$N_1 = \frac{m_w c_{pw}}{m_s c_{ps}} \tag{4}$$

$$N_2(x) = \frac{h_c(x)A_c}{\dot{m}_s c_{ps}} \tag{5}$$

$$N_3(x) = \frac{h_s(x)A_s}{\dot{m}_s c_{ps}} \tag{6}$$

$$N_4 = \frac{\dot{m}_c}{\dot{m}_s Ja} \tag{7}$$

$$NTU = \frac{N_2 N_3}{N_2 + N_3} \tag{8}$$

where the Jacob number is $\text{Ja}=c_{ps}(T_w-T_s)/h_{fg}$. Using these nondimensional variables, the energy equations in both fluids and the wall become

$$N_1 \frac{\partial T_w^*}{\partial t^*} + N_2(x)(T_w^* - 1) + N_3(x)(T_w^* - T_s^*) = 0 \tag{9}$$

$$\frac{\partial T_s^*}{\partial t^*} + \frac{\partial T_s^*}{\partial x} = N_3(x)(T_w^* - T_s^*) \tag{10}$$

$$N_4 \frac{\partial \lambda}{\partial x^*} = N_2(x)(T_w^* - 1) \tag{11}$$

Integrating over the length of the heat exchanger $(x^*=0 \rightarrow 1)$, the governing equations become

$$N_1 \frac{\partial}{\partial t^*}\left(\int_0^1 T_w^* dx^*\right) + \int_0^1 N_2(T_w^* - 1)dx^* + N_3\left(\int_0^1 T_w^* dx^* - \int_0^1 T_s^* dx^*\right) = 0 \tag{12}$$

$$\frac{\partial}{\partial t^*}\left(\int_0^1 T_s^* dx^*\right) + T_s^*(1) - T_s^*(0) = N_3\left(\int_0^1 T_w^* dx^* - \int_0^1 T_s^* dx^*\right) \tag{13}$$

$$N_4(\lambda(1) - \lambda(0)) = \int_0^1 N_2(T_w^* - 1)dx^* \tag{14}$$

In order to evaluate the initial and steady-state temperatures, the previous governing equations can be solved without the transient terms, since the initial and steady-state conditions do not change during a specified time interval. This interval refers to the period between step-changes of fluid temperature. Initially, a step-change of fluid temperature $(T_c^0 \rightarrow T_c^\infty)$ is applied and the transient response of both fluid streams must be predicted. Furthermore, the time required to stabilize the outlet temperature will be calculated.

Using the steady-state and initial temperature profiles, it can be shown that the fluid and wall temperatures can be approximated in the following manner (see Appendix A):

$$T_s^* = (1 - e^{-NTUx^*})\tilde{f}(t^*) \tag{15}$$

$$T_w^* = \left(1 - \frac{NTU}{N_2}e^{-NTUx^*}\right)\tilde{g}(t^*) \tag{16}$$

where

$$\tilde{f}(t^*) = f(t^*) + T_c^{*0}(1 - f(t^*)) \tag{17}$$

$$\tilde{g}(t^*) = g(t^*) + T_c^{*0}(1 - g(t^*)) \tag{18}$$

Then, these profiles are substituted into the integral equations, which can be integrated from $x^*=0 \rightarrow 1$ to give

$$N_1 \frac{d\tilde{g}(t^*)}{dt^*}\left(1 + \frac{1}{N_2}e^{-NTU} - \frac{1}{N_2}\right) + N_2(\xi)\left[\tilde{g}(t^*)\left(1 + \frac{1}{N_2}e^{-NTU} - \frac{1}{N_2}\right) - 1\right] + N_3\tilde{g}(t^*)\left(1 + \frac{1}{N_2}e^{-NTU} - \frac{1}{N_2}\right) - N_3\tilde{f}(t^*)\left(1 + \frac{1}{NTU}e^{-NTU} - \frac{1}{NTU}\right) = 0 \tag{19}$$

$$\frac{d\tilde{f}(t^*)}{dt^*}\left(1 + \frac{1}{NTU}e^{-NTU} - \frac{1}{NTU}\right) - N_3\tilde{g}(t^*)\left(1 + \frac{1}{N_2}e^{-NTU} - \frac{1}{N_2}\right) + (1 - e^{-NTU})\tilde{f}(t^*) - N_3\tilde{f}(t^*)\left(1 + \frac{1}{NTU}e^{-NTU} - \frac{1}{NTU}\right) = 0 \tag{20}$$

Simplifying and re-arranging these equations

$$\frac{d\tilde{f}(t^*)}{dt^*} = C_1\tilde{f}(t^*) - C_1\tilde{g}(t^*) \tag{21}$$

$$\frac{d\tilde{g}(t^*)}{dt^*} = D_1\tilde{f}(t^*) + D_2\tilde{g}(t^*) + D_3 \tag{22}$$

where

$$C_1 = \frac{-N_3(NTU + e^{-NTU} - 1) - NTU(1 - e^{-NTU})}{NTU + e^{-NTU} - 1} \tag{23}$$

$$D_1 = \frac{N_3 + (N_3/NTU)e^{-NTU} - N_3/NTU}{N_1 + (N_1/N_2)e^{-NTU} - N_1/N_2} \tag{24}$$

$$D_2 = -\frac{N_2 + N_3}{N_1} \tag{25}$$

$$D_3 = \frac{N_2}{N_1 + (N_1/N_2)e^{-NTU} - N_1/N_2}m \tag{26}$$

Define the following modified function:

$$\hat{g}(t^*) = \tilde{g}(t^*) - \frac{C_1 D_3}{C_2 D_1 - C_1 D_2} \tag{27}$$

Then, combining the previous governing equations

$$\frac{d^2\hat{g}}{\partial t^{*2}} - \frac{d\hat{g}}{dt^*}(C_1 + D_2) - \hat{g}(C_2 D_1 - C_1 D_2) = 0 \tag{28}$$

Solving this equation and substituting into Eqs. (21) and (27) yields

$$\tilde{f}(t^*) = a\left(\frac{\beta_1 - D_2}{D_1}\right)e^{\beta_1 t^*} + b\left(\frac{\beta_2 - D_2}{D_1}\right)e^{\beta_2 t^*} - \frac{C_1 D_2 D_3}{D_1(C_2 D_1 - C_1 D_2)} - \frac{D_3}{D_1} \tag{29}$$

$$\tilde{g}(t^*) = ae^{\beta_1 t^*} + be^{\beta_2 t^*} + \frac{C_1 D_3}{C_2 D_1 - C_1 D_2} \tag{30}$$

The constants are obtained from the initial conditions, $\tilde{f}(t^*=0) = T_c^{*0} = \tilde{g}(t^*=0)$, i.e.,

$$a = \left(\frac{D_1 + D_2 - \beta_2}{\beta_1 - \beta_2}\right)T_c^{*0} + \frac{D_3(C_1\beta_2 - C_1 D_2 - C_2 D_1)}{(\beta_1 - \beta_2)(C_1 D_2 - C_2 D_1)} \tag{31}$$

$$b = -\left(\frac{D_1 + D_2 - \beta_1}{\beta_1 - \beta_2}\right)T_c^{*0} - \frac{D_3(C_1\beta_1 - C_1 D_2 - C_2 D_1)}{(\beta_1 - \beta_2)(C_1 D_2 - C_2 D_1)} \tag{32}$$

Also, the roots of the auxiliary equation are

$$\beta_{1,2} = \tfrac{1}{2}\left(C_1 + D_2 \pm \sqrt{(C_1 + D_2)^2 + 4(C_2 D_1 - C_1 D_2)}\right) \tag{33}$$

In the next section, cases with varying convection coefficients will be examined.

3 Formulation of Varying Convection Coefficient Model

From the mean value theorem of calculus, there exists ξ in $0 \leqslant \xi \leqslant 1$ for Eq. (14) where

$$\int_0^1 N_2(T_w^* - 1)dx^* = N_2(\xi)\int_0^1 (T_w^* - 1)dx^* \tag{34}$$

This approximation will be adopted and $N_2(\xi)$ will be evaluated after the spatial integrations can be completed from solutions in the previous section, i.e.,

$$N_2(\xi) = \frac{\displaystyle\int_0^1 N_2(T_w^* - 1)dx^*}{\displaystyle\int_0^1 (T_w^* - 1)dx^*} \tag{35}$$

In this way, both spatial and temporal variations of the convection coefficient are considered. Based on the solutions derived in the previous section and Eq. (35), the mean value of the varying convection coefficient can be determined from

$$N_2(\xi) = \frac{\displaystyle\int_0^1 N_2(T_w^* - 1)dx^*}{\displaystyle\int_0^1 (T_w^* - 1)dx^*} = \frac{N_4[\lambda(1) - \lambda(0)]}{\tilde{g}(t^*)(1 + e^{-NTU}/N_2 - 1/N_2) - 1} \tag{36}$$

This equation can be solved implicitly for N_2, but nonlinear iterations are required since the solution of $\tilde{g}(t^*)$ depends on N_2.

The mean value of N_2 is the value required to establish the given exit vapor quality, $\lambda(1)$. It does not refer to a mean value, but rather an integrated value that satisfies the overall energy balance in Eq. (14). The value of N_2 is a dimensionless group including the heat transfer coefficient, h_c. This coefficient varies with x (space) and t (time). The spatial distribution of N_2 in Eq. (14) is initially unknown, so the mean value theorem and temperature distribution from Eq. (16) are used to approximate its value in Eq. (35). Rather than serving as an average value, it represents the value required to satisfy the overall energy balance between latent heat absorbed by the phase change fluid and convective heat transfer across the wall. In a design process, the first step would determine the required value of N_2. The next step would provide a method from which a suitable mean heat transfer coefficient, h_c, can be calculated from given data, in order to find the required heat transfer surface area from the value of N_2. This paper analyses the first step of this design process, but not the second step.

Iteration is required to calculate N_2 in Eq. (36). It can be observed that N_2 appears on both left and right sides of Eq. (36). An initial constant convection coefficient is substituted in the denominator of the right side to predict a first-order "corrected value" of N_2. The converged value accommodates changes of the convection coefficient, due to varying flow regimes in the two-phase side of the heat exchanger. For example, (two-phase boiling flows), the convection coefficient rises rapidly in the slug/annular flow regimes, falls in the transition regime and rises moderately for mist flow and convection of pure vapor when the vapor fraction approaches $\lambda = 1$ at the outlet (see Fig. 2).

In the current formulation, the convection coefficient varies with both position (x^*) and time (t^*) within the heat exchanger, due to the step-change in temperature and varying modes of boiling between the inlet and outlet. In the previous derivation, the spatially varying portion of the convection coefficient was integrated from $x^* = 0 \rightarrow 1$, thereby yielding a mean value of $N_2(\xi)$ from the mean value theorem of calculus. This formulation will be called the VCC model (varying convection coefficient model).

A challenge in the heat exchanger analysis is the phase change process in the condenser/evaporator. When a fluid stream within the heat exchanger experiences a change of phase due to boiling/condensation, then it can be more helpful to evaluate enthalpy (rather than temperature) in the energy balances. Temperature is assumed to remain nearly constant during the phase change, even though heat is transferred between the fluid streams. Based on the enthalpy difference, the analysis must include both the latent and sensible heat portions of the energy transfer between different fluid streams in the heat exchanger.

Based on the definitions of the R and P factors in classical heat exchanger analysis [2], the P factor approaches zero when the fluid stream in the tube flow experiences no change of temperature. This situation arises in condensers and evaporators since the temperature remains approximately constant due to the change of phase. If the other fluid is the condensing or evaporating stream, then R approaches zero instead. Since the temperature of the fluid undergoing phase change does not appreciably change along the flow path, it may be interpreted in view of a single phase stream with a capacity rate, C, approaching an infinite value. For example, a single-phase stream would approach isothermal flow when its flow rate becomes large. Unlike single-phase flows in heat exchangers, a difficulty in the analysis of condensers and evaporators is the unknown phase change regimes experienced by the other fluid stream.

Since the heat transfer coefficient depends on the local phase fraction, which varies throughout the flow path, this heat transfer coefficient becomes position dependent. However, the phase distribution is typically unknown until the flow field solution is obtained. This suggests the importance of a systematic procedure for analyzing the heat transfer processes in condensers and evaporators. A proposed procedure for such analysis is summarized below.

(1) A boundary condition is applied at the heat exchanger inlet;
(2) a suitable forced convection correlation is used up to the point where phase change is first realized;
(3) the phase transition is identified when the mass fraction of the multiphase stream becomes nonzero. A change of phase fraction can be detected from the temperature (with respect to the phase change temperature) or enthalpy (with respect to an equation of state);
(4) at the first point experiencing phase change, the phase fraction can be computed and the appropriate flow region is identified. Then, the appropriate heat transfer correlation for that flow regime can be adopted based on suitable correlations;
(5) near the saturation points, a suitable convection correlation may be adopted with property values evaluated along the saturated liquid and vapor lines.

A similar procedure can be adopted for both types of two-phase flows, i.e., condensation or boiling. In boiling problems, a two-phase flow map may be needed to identify the flow regime based on the computed phase fraction. This two-phase flow mapping would distinguish between flow regimes, such as wavy, annular, and slug flow regimes. For example, if saturated liquid enters the tube, evaporation occurs initially by bubbles growing along the heating surface. As the vapor fraction increases, transition occurs to plug flow, followed by slug flow.

Since an integral method is adopted in the current analysis, only inlet and outlet values of the vapor phase fraction are needed. Once the mixture becomes saturated vapor, subsequent heat addition is transferred to the vapor in a superheated state. The average heat transfer coefficient is effectively computed as an arithmetic average of coefficients throughout the flow path.

4 Formulation of Second Step-Change of Temperature

After a time of $t^*=t_1^*$, consider another step-change in temperature, i.e., $T_c^\infty \rightarrow T_{c1}$. The previous procedure can be repeated, but the spatial temperature profile before the step-change is applied as the initial condition for the new period, i.e.,

$$T_s^{*0} = \tilde{f}(t_1^*)(1 - e^{-NTUx^*}) \tag{37}$$

$$T_w^{*0} = \tilde{f}(t_1^*)\left(1 - \frac{NTU}{N_2} e^{-NTUx^*}\right) \tag{38}$$

For the steady-state profiles

$$T_s^{*\infty} = T_{c1}^*(1 - e^{-NTUx^*}) \tag{39}$$

$$T_w^{*\infty} = T_{c1}^*\left(1 - \frac{NTU}{N_2} e^{-NTUx^*}\right) \tag{40}$$

Thus, the single-phase and wall temperatures become

$$T_s^* = (1 - e^{-NTUx^*})\tilde{F}(t^*) \tag{41}$$

$$T_w^* = \left(1 - \frac{NTU}{N_2} e^{-NTUx^*}\right)\tilde{G}(t^*) \tag{42}$$

The modified time functions ($\tilde{F}$ and $\tilde{G}$) are expressed as follows:

$$\tilde{F}(t^*) = T_{c1}^* F(t^*) + \tilde{f}(t_1^*)(1 - F(t^*)) \tag{43}$$

$$\tilde{G}(t^*) = T_{c1}^* G(t^*) + \tilde{f}(t_1^*)(1 - G(t^*)) \tag{44}$$

These time functions satisfy analogous governing equations and initial conditions in the transformed time coordinate ($\tilde{t}^* = t^* - t_1^*$,), i.e.,

$$\frac{d\tilde{F}(t^*)}{dt^*} = C_1\tilde{F}(t^*) - C_1\tilde{G}(t^*) \tag{45}$$

$$\frac{d\tilde{G}(t^*)}{dt^*} = D_1\tilde{F}(t^*) + D_2\tilde{G}(t^*) + D_3 \tag{46}$$

subject to $\tilde{F}(0)=\tilde{f}(0)=\tilde{G}(0)$. The solutions are

$$\tilde{F}(t^*) = a\left(\frac{\beta_1 - D_2}{D_1}\right)e^{\beta_1 t^*} + b\left(\frac{\beta_2 - D_2}{D_1}\right)e^{\beta_2 t^*} - \frac{C_1 D_2 D_3}{D_1(C_2 D_1 - C_1 D_2)} - \frac{D_3}{D_1} \tag{47}$$

$$\tilde{G}(t^*) = ae^{\beta_1 t^*} + be^{\beta_2 t^*} + \frac{C_1 D_3}{C_2 D_1 - C_1 D_2} \tag{48}$$

where the constants become

$$a = \left(\frac{D_1 + D_2 - \beta_2}{\beta_1 - \beta_2}\right)\tilde{f}(t_1^*) + \frac{D_3(C_1\beta_2 - C_1 D_2 - C_2 D_1)}{(\beta_1 - \beta_2)(C_1 D_2 - C_2 D_1)} \tag{49}$$

$$b = -\left(\frac{D_1 + D_2 - \beta_1}{\beta_1 - \beta_2}\right)f(t_1^*) - \frac{D_3(C_1\beta_1 - C_1 D_2 - C_2 D_1)}{(\beta_1 - \beta_2)(C_1 D_2 - C_2 D_1)} \tag{50}$$

Based on these solutions, the time required to stabilize back to T_c^0 for a case of $T_{c1}=T_c^0$ (case without step-change in temperature) can be predicted. For example, equating T_s^* with Eq. (15) and setting $x^*=1$ allows us to find the time required for the outlet temperature to re-stabilize after the step-change in temperature

$$T_c^{*0}(1 - e^{-NTU}) = (1 - e^{-NTU})[T_{c1}^* F(\tilde{t}^*) + \tilde{f}(t_1^*)(1 - F(\tilde{t}^*))] \tag{51}$$

Substituting the previous solution for T_s^*, this yields a nonlinear equation for the unknown time

$$\frac{T_c^{*0} - \tilde{f}(t_1^*)}{T_{c1}^{*0} - \tilde{f}(t_1^*)} = (\beta_2 e^{\beta_1\tilde{t}^*} - \beta_1 e^{\beta_2\tilde{t}^*})(1 - \tilde{f}(t_1^*)) + \beta_1 - \beta_2 \tag{52}$$

This can be solved for the nondimensional time to establish the required stabilization time.

Rather than a step-change in the upper temperature, consider another case of a step-change in the lower temperature $T_s^0 \rightarrow T_s^\infty$ at time $t=0$. In this case, the nondimensional temperature is redefined as

$$T^* = \frac{T - T_{c,\text{in}}}{T_s^\infty - T_{c,\text{in}}} \tag{53}$$

In this case, $T_c^* \rightarrow T_{s,\text{in}}^*$ can be replaced in the initial temperature profile and $T_s^{*\infty} \rightarrow 1$ can be approximated in the steady-state profile.

5 Results and Discussion

This work was motivated by a need to predict the transient response to step-wise temperature changes in an aircraft two-phase heat exchanger. The specific working fluids of interest are refrigerant (R134a) and air (see Appendix B). But in order to provide more generality to a range of flow conditions or other working fluids, the following results will be presented in nondimensional form. In this section, results from the following six test cases are presented: (i) Transient profiles with $N_2=1$, $N_3=1$ (Figs. 3 and 4), (ii) transient profiles with $N_2=10$, $N_3=1$ (Figs. 5 and 6), (iii) transient profiles with $N_2=10$, $N_3=10$ (Figs. 7 and 8), (iv) spatial profiles with $N_1=300$, $N_2=N_3=1$ (Figs. 9 and 10), (v) spatial profiles with $N_1=300$, $N_2=N_3=1$ (Fig. 11(*a*)) and (vi) spatial profiles with $N_1=300$, $N_2=N_3=10$ (Fig. 11(*b*)). In the numerical simulations, a steady state condition is reached throughout the

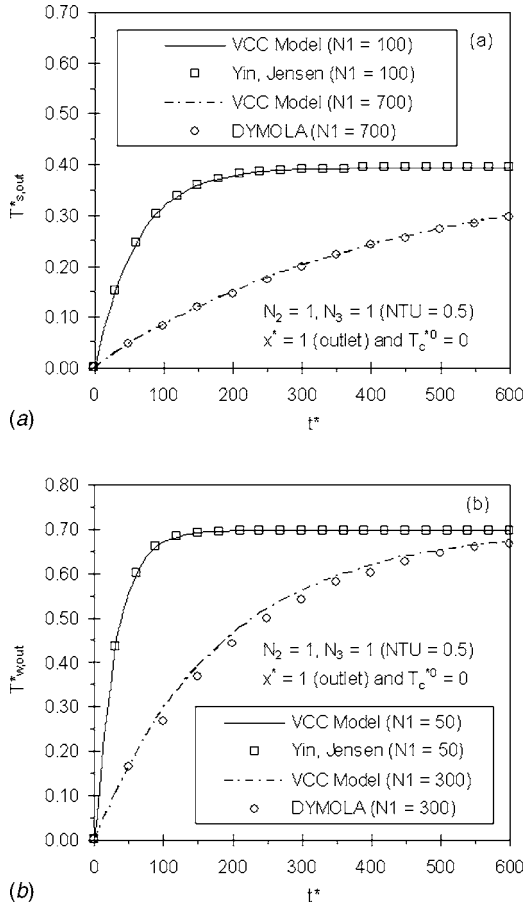

Fig. 3 Fluid and wall temperatures (Case 1)

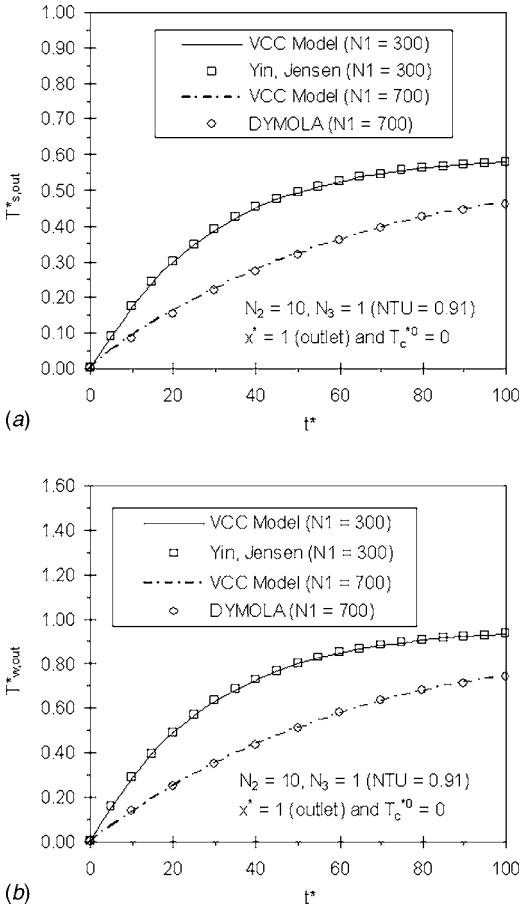

Fig. 5 Fluid and wall temperatures (Case 2)

entire system at time zero-minus. Then, the constant temperature fluid undergoes an instantaneous step change in temperature at time zero (from $T_c^0 \rightarrow T_c^\infty$). This creates spatial distributions of the single-phase fluid and wall temperature distributions, which are given by Eqs. (A5) and (A6) in the Appendix. These distributions represent the initial conditions for all six cases in this section. The boundary conditions for the six cases of single phase fluid at the inlet are given by $T_c^*(x^*=0)=0$ and (i) $\lambda(0)=1$, (ii) $\lambda(0)=1$, (iii) $\lambda(0)=0.1$, (iv) $\lambda(0)=0$, (v) $\lambda(0)=0$, and (vi) $\lambda(0)=0$, 0.2, and 0.4.

In the numerical results, a step-change of temperature is applied at the initial time ($t^*=0$) and subsequent transient responses of fluid and wall temperatures are predicted. In the legends, the acronyms refer to the varying convection coefficient model (VCC model) and numerical simulations with a dynamic Modelica simulator (DYMOLA [9]). Also, comparisons were made against data from Yin and Jensen [9]. The subscripts "out" refer to calculations at the outlet of the heat exchanger ($x^*=1$). In cases 1–3, $T_c^{*0}=0$ and the results are depicted at the outlet of the heat exchanger, while $T_c^{*0}=0.4$ in cases 4 and 5.

At the initial time ($t^*=0$), the fluid undergoes a step-change of inlet temperature and the fluid eventually stabilizes to a new asymptotic temperature after a sufficient period of time has

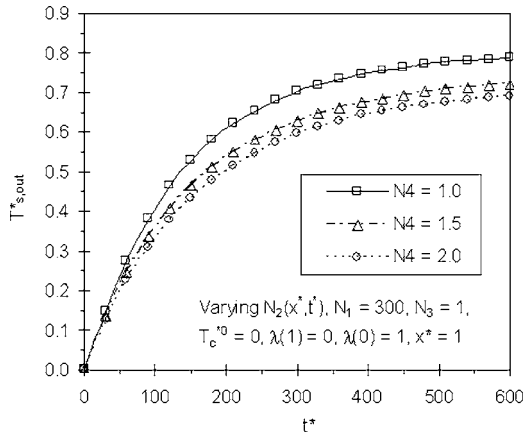

Fig. 4 Effects of varying convection coefficients (Case 1)

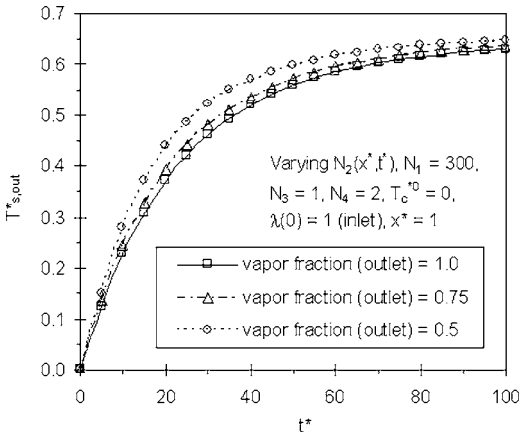

Fig. 6 Effects of varying convection coefficients (Case 2)

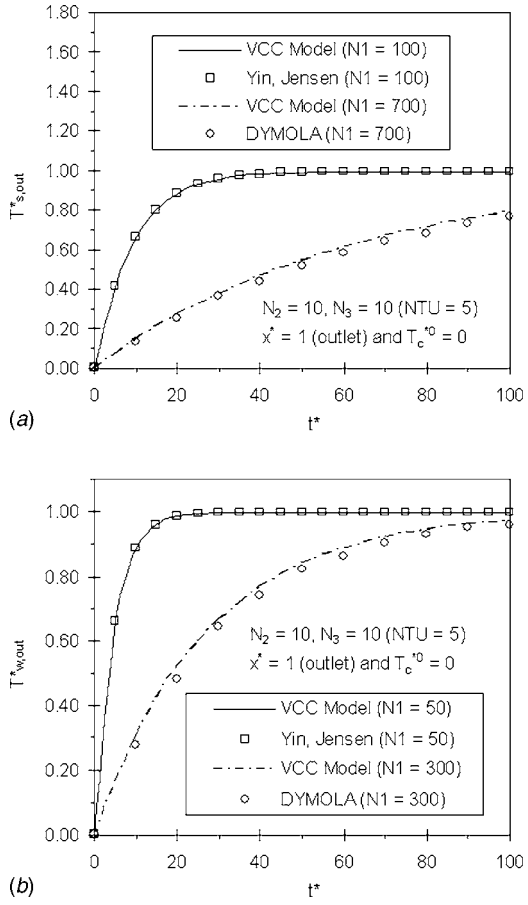

Fig. 7 Fluid and wall temperatures (Case 3)

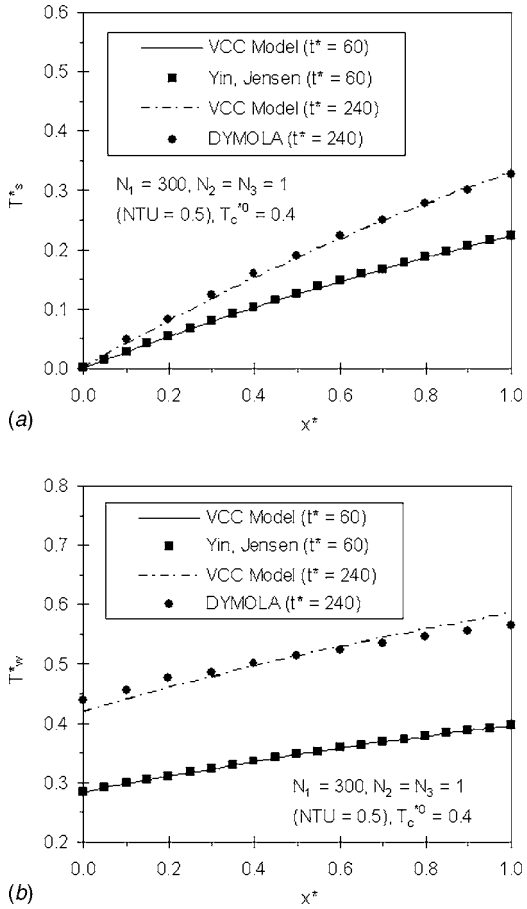

Fig. 9 Spatial variations of fluid and wall temperatures (Case 4)

elapsed. In Fig. 3, the transient responses of the outlet fluid and wall temperatures to this step-change are plotted at different values of N_1. Close agreement between the VCC model and past data, as well as numerical simulations with Modelica [9], can be observed. Both wall and fluid temperatures stabilize faster at lower values of N_1, since this entails lower thermal inertia of the wall. Also, a larger mass of fluid promotes heat exchange rapidly, either with a larger volume of heat exchanger or larger mass flow rates through the heat exchanger. These results represent transient profiles at the outlet, so lower stabilization times would be observed upstream, since a certain time is required for thermal disturbances to propagate downstream.

In Fig. 4, the latter case of Fig. 3(*b*) is re-considered (N_1=300), but accounting for varying convection coefficients. Pure liquid enters the two-phase heat exchanger, while vaporization leads to pure vapor with a vapor fraction of 1.0 at the outlet. Varying Jacob numbers are considered, as they represent a range of possible inlet saturation conditions leading to different values of the latent heat of vaporization. The coefficient N_4 increases at larger values of the latent heat of vaporization, or smaller temperature differences between fluid streams. In Fig. 4, it can be observed that similar time periods are needed for stabilized outlet fluid temperatures, but the fluid temperature becomes smaller at

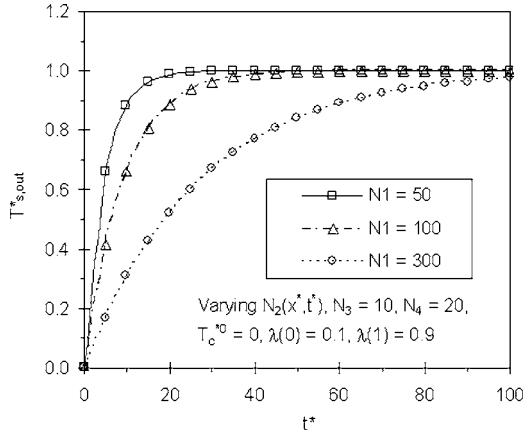

Fig. 8 Effects of varying convection coefficients (Case 3)

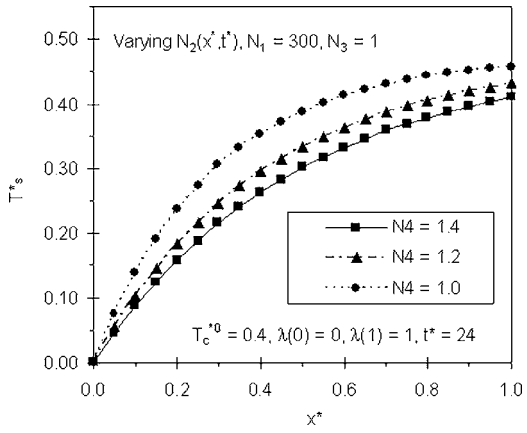

Fig. 10 Effects of varying convection coefficients (Case 4)

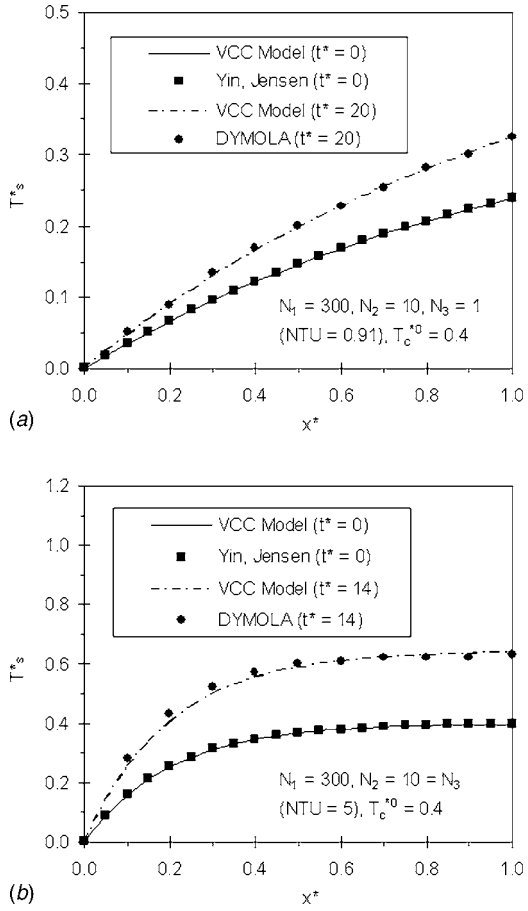

Fig. 11 Spatial temperature variations—(*a*) Case 5 and (*b*) Case 6

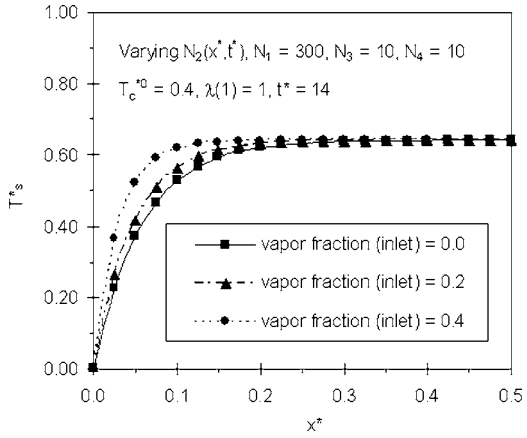

Fig. 12 Effects of varying convection coefficients (Case 6)

higher values of N_4. In those cases, the latent heat of vaporization is larger, so a longer heat exchanger is needed to vaporize a given flow stream from inlet liquid to outlet vapor conditions. As a result, additional heat exchange provides more cooling and lower outlet temperatures for the case of $N_4=2.0$.

In case 2 (Fig. 5), a higher value of $N_2=10$ is considered. Close agreement between predicted results (VCC Model), past data and numerical simulations can be observed. Comparing Figs. 5(*a*) and 5(*b*), similar periods of time are needed for stabilized outlet fluid and wall temperatures. In Fig. 6, changes of the convection coefficient occur with varying outlet phase fractions of vapor. At the inlet, the vapor phase fraction is 1.0, but outlet phase fractions of 1.0, 0.75, and 0.5 are considered. Either the Jacob number changes (due to a lower inlet saturation pressure) or the heat exchanger volume decreases, so the exiting fluid stream is not entirely vaporized in the latter two cases of Fig. 6. As a result, less heat exchange entails less cooling of the single-phase fluid stream and higher temperatures are observed when the outlet vapor fraction is 0.5. The value of N_2 varies throughout the heat exchanger in Fig. 6, due to varying flow regimes between inlet liquid and outlet conditions (see Fig. 2).

Figures 7 and 8 illustrate results for case 3. Comparisons of these results with previous cases (Figs. 3–6) show the sensitivity of the transient response to values of N_2 and N_3, at fixed values of N_1. For example, Figs. 5(*a*) and 7(*a*) show fluid temperature results for $N_1=700$, $N_2=10$, and different values of N_3. It appears that stabilized temperatures will be reached earlier at lower values of N_3, due to the larger heat transfer coefficient or heat exchanger volume in those cases. Figures 3(*a*) and 5(*a*) show fluid temperature results for $N_1=700$, $N_3=1$ and different values of N_2. Stabilized fluid temperatures are reached earlier in Fig. 5(*a*), since larger values of N_2. entail a larger heat transfer coefficient on the two-phase side of the heat exchanger. In Figs. 3(*b*) and 5(*b*), wall temperature results are shown for $N_1=300$, $N_3=1$ and different values of N_2. Similar trends for the wall temperatures are observed in this case, as well as Figs. 5(*b*) and 7(*b*), which show the wall temperature results for $N_1=300$, $N_2=1$ and different values of N_3.

Rather than assuming constant values of N_2 throughout the heat exchanger, Fig. 8 considers both spatial and temporal variations of N_2. In the solution procedure, these variations are integrated to the outlet of the heat exchanger. The inlet vapor fraction is 0.1 (bubble/slug flow regime) and the outlet vapor fraction is 0.9 (mist flow regime in Fig. 2). The fluid temperatures stabilize more rapidly at smaller values of N_1, since the larger mass of single-phase fluid entails a larger volume on that side of the heat exchanger. The results have been derived from the VCC Model, which was shown to exhibit close agreement with past data in Fig. 7 for the case of constant convection coefficients.

Spatial variations of both fluid and wall temperatures are illustrated in the remaining figures. In Fig. 9, close agreement between the VCC model and past data, including numerical simulations with Modelica [9] can be observed. Both fluid and wall temperatures rise nearly linearly from the inlet to the outlet. Departure from these linear profiles can be observed in Fig. 10, when the convection coefficient changes throughout the heat exchanger. Increasing linearity is observed for cases with higher values of N_4 (corresponding to smaller Jacob numbers and larger values of the latent heat of vaporization). Faster cooling of the single-phase stream occurs in those cases, as more heat is absorbed from the phase-change fluid for a fixed difference of phase fraction between the inlet and outlet.

Cases 5 and 6 with higher values of N_1 and N_2 are illustrated in Fig. 11. Unlike nearly linear profiles of fluid temperature in Fig. 11(*a*), the temperatures rise more rapidly to the outlet values in Fig. 11(*b*). The energy balance within the flow stream involves cross-stream conduction through the wall to the other side of the heat exchanger, as well as streamwise transport by convection. Larger values of N_3 correspond to higher convection coefficients or a larger cross-sectional area in the single-phase fluid side of the heat exchanger. Larger convective exchange implies that the fluid temperature rises more rapidly in the streamwise direction. In Fig. 11, close agreement can be observed between predicted results, numerical simulations and past data presented by Yin and Jensen [9].

In Fig. 12, Case 6 is re-considered, but with varying values of $N_2(x,t)$ throughout the heat exchanger, rather than constant values assumed in Fig. 11. The outlet vapor fraction is 1.0 and a single point in time ($t^*=14$) is shown. It can be observed that the fluid

temperature rises more rapidly to the outlet value in cases involving higher inlet vapor fractions. In order that the fluid stream is fully vaporized by the outlet, better heat exchange is required in the case with an inlet vapor fraction of 0. For refrigerative cooling in this application, it implies that better cooling is achieved in that case, thereby explaining why the case with $\lambda(0)=0$ yields colder temperatures than the other two cases in Fig. 12. These results exhibit realistic trends when considering changes of fluid temperature within a heat exchanger. For benchmark cases, close agreement between the VCC model, past data, and numerical simulations with a dynamical simulator has been demonstrated. As a result, the VCC model provides a useful design tool for predicting transient responses of both fluid and wall temperatures, including effects of varying convection coefficients, in a two-phase heat exchanger.

6 Conclusions

In this article, transient changes of fluid and wall temperatures in a two-phase heat exchanger were reported. Past integral methods were extended to cases involving varying convection coefficients, arising from changes of phase fraction on the single-temperature side of the heat exchanger, as well a multiple step-changes of temperature. In the newly formulated VCC model, varying convection coefficients are related to changes of vapor fraction between the inlet and outlet of the heat exchanger. The formulation was expressed in terms of nondimensional coefficients of N_1 (ratio of thermal capacities), N_2 (involving the varying convection coefficient), N_3 and N_4 (two-phase Jacob parameter). Both wall and fluid temperatures stabilize faster at lower values of N_1, since this entails lower thermal inertia of the wall. It was shown that the fluid temperatures stabilize more rapidly at smaller values of N_1, since the larger mass of single-phase fluid entails a larger volume on that side of the heat exchanger. Fluid temperatures become smaller at higher values of N_4. Departure from linear temperature profiles was observed when the convection coefficient changes throughout the heat exchanger. Increasing linearity was observed for cases with higher values of N_4, due to larger values of the latent heat of vaporization. Furthermore, it was shown that the fluid temperature rises more rapidly to the outlet value in cases involving higher inlet vapor fractions. Predicted results show close agreement with past data, including numerical simulations with a dynamic simulator.

Acknowledgment

Financial support of this research from Honeywell ASCa, Inc. and the Natural Sciences and Engineering Research Council of Canada is gratefully acknowledged.

Nomenclature

A = area (m^2)
A_x = cross-sectional flow area (m^2)
c_p = specific heat (kJ/kgK)
F,P,R = correction factor parameters for heat exchangers
h = heat transfer coefficient (W/m^2 K)
h_{fg} = latent heat of vaporization (J/kgK)
Ja = Jacob number, $Ja=c_{ps}(T_w-T_s)/h_{fg}$
L = heat exchanger length (m)
m = mass (kg)
$\dot{m}$ = mass flow rate (kg/s)
NTU = number of transfer units
N_1 = dimensionless group of $N_1=m_w c_{pw}/(m_s c_{ps})$
N_2 = dimensionless group of $N_2(x)=h_c(x)A_c/(\dot{m}_s c_{ps})$
N_3 = dimensionless group of $N_3(x)=h_s(x)A_s/(\dot{m}_s c_{ps})$
N_4 = dimensionless group of $N_4=\dot{m}_c/(\dot{m}_s Ja)$
t = time (s)
t_r = residence time (s)
T = temperature (K)
x = position (m)

Greek

β = root of auxiliary equation
λ = vapor phase fraction
ρ = density (kg/m^3)
ξ = nondimensional coordinate between 0 and 1

Subscripts

1,2 = point 1, 2 of a time period or function number (N1, N2)
c = constant temperature fluid
fg = fluid-gas
in = inlet
out = outlet
s = single-phase fluid
w = wall
∞ = final condition

Superscripts

0 = initial condition
∞ = final condition
* = dimensionless form

Appendix A: Initial and Steady-State Temperature Profiles

In the integral solution, streamwise profiles of temperature are needed to evaluate the integrals. The temperature distributions within the single-phase fluid and wall can be approximated by [9]

$$T_s^* = T_s^{*0} + (T_s^{*\infty} - T_s^{*0}) f(t^*) \tag{A1}$$

$$T_w^* = T_w^{*0} + (T_w^{*\infty} - T_w^{*0}) g(t^*) \tag{A2}$$

where the superscripts 0 and ∞ refer to the initial condition and steady state, respectively.

For the initial conditions, the wall temperature and single-phase fluid temperature equations become

$$T_w^{*0}(N_2+N_3) = N_3 T_s^{*0} + N_2 \tag{A3}$$

$$\frac{\partial T_s^{*0}}{\partial x^*} = N_3 \left[\frac{N_3 T_s^{*0} + N_2}{N_2+N_3} - \frac{(N_2+N_3)T_s^{*0}}{N_2+N_3} \right] \tag{A4}$$

Solving these equations subject to $T_s^{*0}(x^* \to \infty) = T_c^{*0}$ yields

$$T_s^{*0} = T_c^{*0}(1 - e^{-NTUx^*}) \tag{A5}$$

$$T_w^{*0} = T_c^{*0}\left(1 - \frac{NTU}{N_2} e^{-NTUx^*}\right) \tag{A6}$$

The same procedure is used for the steady-state profiles, except the simplified equations are solved subject to $T_s^{*\infty}(x^* \to \infty) = 1$, thereby yielding

$$T_s^{*\infty} = 1 - e^{-NTUx^*} \tag{A7}$$

$$T_w^{*\infty} = 1 - \frac{NTU}{N_2} e^{-NTUx^*} \tag{A8}$$

These results are used to establish the temperature profiles in Eqs. (15) and (16).

Appendix B: Thermophysical Properties of Working Fluids

For the specific applications of interest, typical operating conditions for the aircraft heat exchanger include a refrigerant saturation temperature and saturation pressure of −6 °C and 234.3 kPa, respectively. In the liquid phase, $\rho_l = 1314.3$ kg/m^3, $c_{vl} = 0.872$ kJ/kgK, $c_{pl} = 1.325$ kJ/kgK and $\mu_l = 2.88 \times 10^{-4}$ Pa s

and $k_1 = 0.095$ W/mK. The latent heat of vaporization is $h_{fg} = 203.1$ kJ/kg. In the vapor phase, $\rho_v = 11.65$ kg/m^3, $c_{vv} = 0.744$ kJ/kgK, $c_{pv} = 0.871$ kJ/kgK and $\mu_v = 1.05 \times 10^{-5}$ Pa s and $k_v = 0.011$ W/mK. The average incoming temperature of the air stream is 300 K, with properties of $\rho = 1.16$ kg/m^3, $c_p = 1.007$ kJ/kgK, $\mu_v = 1.846 \times 10^{-6}$ Pa s and $k = 0.0263$ W/mK.

References

[1] Bowman, R. A., Mueller, A. C., and Nagle, W. M., 1940, "Mean Temperature Difference in Design," Trans. ASME, **62**, pp. 283–294.

[2] Kays, W. M., and London, A. L., 1984, *Compact Heat Exchangers*, 3rd ed., McGraw-Hill, New York.

[3] Naterer, G. F., 2003, *Heat Transfer in Single and Multiphase Systems*, CRC Press, Boca Raton, FL.

[4] Patankar, S. V., 1980, *Numerical Heat Transfer and Fluid Flow*, Hemisphere, New York.

[5] Kakac, S., Shah, R. K., and Bergles, A. E., 1983, *Low Reynolds Number Flow Heat Exchangers*, Hemisphere, New York.

[6] Na Ranong, C., and Roetzel, W., 2002, "Steady-State and Transient Behavior of Two Heat Exchangers Coupled by a Circulating Freestream," Int. J. Therm. Sci., **41**(11), pp. 1029–1043.

[7] Srihari, N., Rao, B. P., Sunden, B., and Das, S. K., 2005, "Transient Response of Plate Heat Exchangers Considering Effect of Flow Maldistribution," Int. J. Heat Mass Transfer, **48**(15), pp. 3231–3243.

[8] Siakavellas, N. J., and Georgiou, D. P., 2005, "1D Heat Transfer Through a Flat Plate Submitted to Step Changes in Heat Transfer Coefficient," Int. J. Therm. Sci., **44**(5), pp. 452–464.

[9] Yin, J., and Jensen, M. K., 2003, "Analytic Model for Transient Heat Exchanger Response," Int. J. Heat Mass Transfer, **46**, pp. 3255–3264.

[10] Naterer, G. F., Hendradjit, W., Ahn, K. J., and Venart, J. E. S., 1998, "Near-Wall Microlayer Evaporation Analysis and Experimental Study of Nucleate Pool Boiling on Inclined Surfaces," ASME J. Heat Transfer, **120**(3), pp. 641–653.

[11] Naterer, G. F., 2001, "Establishing Heat—Entropy Analogies for Interface Tracking in Phase Change Heat Transfer With Fluid Flow," Int. J. Heat Mass Transfer, **44**(15), pp. 2903–2916.

[12] Jang, J. Y., and Wang, M. T., 1987, "Transient Response of Crossflow Heat Exchangers With One Fluid Mixed," Int. J. Heat Fluid Flow, **8**(3), pp. 182–186.

[13] Rao, N. M., Maiti, B., and Das, P. K., 2005, "Comparison of Dynamic Performance for Direct and Fluid Coupled Indirect Heat Exchange Systems," Int. J. Heat Mass Transfer, **48**(15), pp. 3244–3252.

[14] Abdelghani-Idrissi, M. A., Bagui, F., and Estel, L., 2001, "Analytical and Experimental Response Time to Flow Rate Step Change Along a Counter Flow Double Pipe," Int. J. Heat Mass Transfer, **44**(19), pp. 3721–3730.

[15] Gowda, Y. T., Patnaik, B. S., Narayana, P. A., and Seetharamu, K. N., 1998, "Finite Element Solution of Transient Laminar Flow and Heat Transfer Past an In-Line Tube Bank," Int. J. Heat Fluid Flow, **19**(1), pp. 49–55.

[16] Naterer, G. F., and Camberos, J. A., 2003, "Entropy and the Second Law in Fluid Flow and Heat Transfer Simulation," J. Thermophys. Heat Transfer, **17**(3), pp. 360–371.

[17] Naterer, G. F., 2005, "Embedded Converging Surface Microchannels for Minimized Friction and Thermal Irreversibilities," Int. J. Heat Mass Transfer, **48**(7), pp. 1225–1235.

[18] Adeyinka, O. B., and Naterer, G. F., 2005, "Experimental Uncertainty of Measured Entropy Production With Pulsed Laser PIV and Planar Laser Induced Fluorescence," Int. J. Heat Mass Transfer, **48**(8), pp. 1450–1461.

[19] Romie, F. E., 1984, "Transient Response of the Counterflow Heat Exchanger," Int. J. Heat Mass Transfer, **106**(3), pp. 620–626.

[20] Romie, F. E., 1985, "Transient Response of the Parallel-Flow Heat Exchanger," Int. J. Heat Mass Transfer, **107**(3), pp. 727–730.

[21] Roetzel, W., and Xuan, Y., 1992, "Transient Response of Parallel and Counterflow Heat Exchangers," Int. J. Heat Mass Transfer, **114**(2), pp. 510–512.

Journal of Heat Transfer

Technical Briefs

A Temperature Fourier Series Solution for a Hollow Sphere

Gholamali Atefi
e-mail: atefi@iust.ac.ir

Mahdi Moghimi

Department of Mechanical Engineering,
Iran University of Science and Technology,
Narmak, 16846-13114, Tehran, Iran

In this paper, we derive an analytical solution of a two-dimensional temperature field in a hollow sphere subjected to periodic boundary condition. The material is assumed to be homogeneous and isotropic with time-independent thermal properties. Because of the time-dependent term in the boundary condition, Duhamel's theorem is used to solve the problem for a periodic boundary condition. The boundary condition is decomposed by Fourier series. In order to check the validity of the results, the technique was also applied to a solid sphere under harmonic boundary condition for which theoretical results were available in the literature. The agreement between the results of the proposed method and those reported by others for this particular geometry under harmonic boundary condition was realized to be very good, confirming the applicability of the technique utilized in the present work. [DOI: 10.1115/1.2241914]

1 Introduction

There are several heat conduction problems that can be modeled by a sphere of constant properties, for example, food freezing and the hydrocooling of spherical fruits or vegetables [1]. The solution of some cases of heat conduction problems can be found in heat transfer literature. Heat conduction problems with periodic boundary condition have some applications in engineering such as penetration of the daily and annual temperature cycles into the earth's surface, heating up and cooling down phases in the Siemens Martin glass melting furnaces, wall temperature oscillation of internal combustion engines, experimental methods for specifying the thermal diffusivity of materials [2] and the temperature field [3,4], and also the thermal stresses caused by temperature distribution. Trostel calculated thermal stresses caused by thermal loads in a solid sphere [5]. Zubair and Chaudhry discussed the solution for temperature and heat flux in a semi-infinite solid subject to periodic-type surface heat fluxes [6]. The calculation of temperature distribution in a solid sphere under a periodic boundary condition is presented in [4] that is simulated by harmonic oscillation of the ambient temperature.

The purpose of this paper is to derive an analytical solution for a two-dimensional heat conduction in a hollow sphere, subjected to a periodic boundary condition. As for the validity of the results, a comparison between the temperature distribution in a solid sphere with the theoretical ones [4] is presented for the same boundary condition. The results can be used for approximation to the real problems with periodic boundary condition. They can also be utilized to verify the time consuming complex computer calculations.

2 Mathematical Model

The heat conduction equation in spherical coordinates for an isotropic material that has temperature and time-independent properties, and without heat source under axisymmetric condition, is:

$$a^2\frac{\partial\theta}{\partial t}=\frac{\partial^2\theta}{\partial r^2}+\frac{2}{r}\frac{\partial\theta}{\partial r}+\frac{1}{r^2}\left(\cot\psi\frac{\partial\theta}{\partial\psi}+\frac{\partial^2\theta}{\partial\psi^2}\right) \tag{1}$$

The initial temperature of the ambient and the hollow sphere are zero. The inner boundary condition is insulated and the outer one is assumed to be boundary condition of type 3:

$$h[\theta(r_o,\psi,t)-\theta_a(\psi,t)]=-k\left.\frac{\partial\theta}{\partial r}\right|_{r_o,\psi,t}$$
$$\left.\frac{\partial\theta}{\partial r}\right|_{r_i,\psi,t}=0 \tag{2}$$

We consider that $\theta_a(\psi,t)=f_o(\psi)g_o(t)$ where $g_o(t)$ is assumed to be a periodic function that is decomposed using Fourier series:

$$g_o(t)=\sum_{m=1}^{\infty}\theta_m\sin\left(2m\pi\frac{t}{p}\right) \tag{3}$$

and $f_o(\psi)$ is an arbitrary function.

3 Analytical Solution

The problem cannot be solved directly because of the dependency of nonhomogeneous term, $\theta_a(\psi,t)$, on time [5]. The solution of a heat-conduction problem with time-dependent boundary condition can be related to the solution of the same problem with time-independent boundary condition by means of Duhamel's theorem. Thus, first of all, the equation should be solved with the assumption that the boundary condition is time independent. In this situation the boundary and initial conditions are:

$$\theta(r_o,\psi,t)+\left.\frac{k}{h}\frac{\partial\theta}{\partial r}\right|_{r_o,\psi,t}=f_o(\psi)$$

Contributed by the Heat Transfer Division of ASME for publication in the JOURNAL OF HEAT TRANSFER. Manuscript received October 5, 2005; final manuscript received April 21, 2006. Review conducted by A. Haji-Sheikh.

$$\left.\frac{\partial\theta}{\partial r}\right|_{r_i,\psi,t} = 0 \tag{4}$$

$$\theta(r,\psi,0) = 0 \tag{5}$$

In this case, use was made of the superposition principle; the solution is the sum of a steady solution, $\theta_s(r,\psi)$, and a transient solution, $\theta_t(r,\psi,t)$. The differential heat conduction equation in steady form is:

$$\frac{\partial^2\theta_s}{\partial r^2} + \frac{2}{r}\frac{\partial\theta_s}{\partial r} + \frac{1}{r^2}\left(\cot\psi\frac{\partial\theta_s}{\partial\psi} + \frac{\partial^2\theta_s}{\partial\psi^2}\right) = 0 \tag{6}$$

where the boundary condition is given by Eq. (4). The transient differential equation is:

$$a^2\frac{\partial\theta_t}{\partial t} = \frac{\partial^2\theta_t}{\partial r^2} + \frac{2}{r}\frac{\partial\theta_t}{\partial r} + \frac{1}{r^2}\left(\cot\psi\frac{\partial\theta_t}{\partial\psi} + \frac{\partial^2\theta_t}{\partial\psi^2}\right) \tag{7}$$

and the following conditions must be satisfied:

$$\theta_t(r_o,\psi,t) + \frac{k}{h}\left.\frac{\partial\theta_t}{\partial r}\right|_{r_o,\psi,t} = 0$$

$$\left.\frac{\partial\theta_t}{\partial r}\right|_{r_i,\psi,t} = 0 \tag{8}$$

$$\theta_t(r,\psi,0) = -\theta_s(r,\psi) \tag{9}$$

3.1 Steady-State Problem. To solve Eq. (6), the method of separation of variables is used. Two differential equations are obtained, a Euler type and a Legendre type. Then, by applying Eq. (4), the solution of the steady state is:

$$\theta_s(r,\zeta) = \sum_{n=0}^{\infty} C_n\eta_n(r)P_n(\zeta); \quad \zeta = \cos(\psi) \tag{10}$$

where

$$\eta_n(r) = \frac{-(n+1)r_i^{-(n+2)}}{\Delta^{(n)}}r^n - \frac{nr_i^{(n-1)}}{\Delta^{(n)}}r^{-(n+1)} \tag{11}$$

$$\Delta^{(n)} = -(n+1)r_i^{-(n+2)}\left(r_o^n + n\frac{k}{h}r_o^{(n-1)}\right) - nr_i^{(n-1)}\left(r_o^{-(n+1)} - (n+1)\frac{k}{h}r_o^{-(n+2)}\right) \tag{12}$$

$$C_n = \frac{2n+1}{2}\int_{+1}^{-1} f_o(\zeta)P_n(\zeta)\,d\zeta \tag{13}$$

3.2 Transient Problem. Use was made of the method of separation of variables to solve Eq. (7). The boundary equation, Eq. (8), and Eq. (9) should be satisfied. When eigenvalues, ω_{kn}, are calculated, the final solution of the transient problem can be expressed as:

$$\theta_t(r,\psi,t) = -\sum_{k=0}^{\infty}\sum_{n=0}^{\infty}\frac{1}{\delta_{kn}}\Phi_n(\omega_{kn}r)P_n(\zeta)e^{-(\omega_{kn}/a)^2t} \times\int_{r_i}^{r_o} r^2C_n\eta_n(r)\Phi_n(\omega_{kn}r)dr \tag{14}$$

where

$$\delta_{kn} = \frac{r}{2\omega_{kn}}\{[\omega_{kn}^2r^2 - n(n+1)]\Phi_n^2 + \omega_{kn}r\Phi_n\Phi_n' + \omega_{kn}^2r^2\Phi_n'^2\}_{r_i}^{r_o} \tag{15}$$

$$\Phi_n(\omega_{kn}r) = \frac{1}{\sqrt{r}}\left\{\left[J_{-(n+1/2)}(\omega_{kn}r_o) + \frac{k}{2hr_o}\left(2\omega_{kn}r_oJ'_{-(n+1/2)}(\omega_{kn}r_o) - J_{-(n+1/2)}(\omega_{kn}r_o)\right)\right]J_{n+1/2}(\omega_{kn}r) - \left(J_{n+1/2}(\omega_{kn}r_o) + \frac{k}{2hr_o}2\omega_{kn}r_oJ'_{n+1/2}(\omega_{kn}r_o) - J_{n+1/2}(\omega_{kn}r_o)\right) \times J_{-(n+1/2)}(\omega_{kn}r)\right\} \tag{16}$$

3.3 Temperature Field Under Time Varying Boundary Condition. As we mentioned before, the temperature distribution under a constant boundary condition is the summation of steady and transient states:

$$\theta(r,\psi,t) = \sum_{n=0}^{\infty}\left(\eta_n(r) - \sum_{k=0}^{\infty}\frac{1}{\delta_{kn}}e^{-(\omega_{kn}/a)^2t}\Phi_n(\omega_{kn}r) \times\int_{r_i}^{r_o} r^2\eta_n(r)\Phi_n(\omega_{kn}r)\,dr\right)C_nP_n(\zeta) \tag{17}$$

Equation (17) expresses the temperature field under time-independent boundary condition. In the case, the boundary values depend on time; they have the variations in the forms:

$$dg_o = \frac{dg_o}{d\tau}d\tau$$

$$dC_n = \frac{dC_n}{d\tau}d\tau \tag{18}$$

It can be assumed that $dg_o/d\tau$, $dC_n/d\tau$ are constant at some time, τ. Therefore the temperature distribution after t-τ seconds after the beginning of the influences can be expressed in the form [7]:

$$\theta(r,\psi,t) = \sum_{n=0}^{\infty}\left(\eta_n(r) - \sum_{k=0}^{\infty}\frac{1}{\delta_{kn}}e^{-(\omega_{kn}/a)^2t}\Phi_n(\omega_{kn}r) \times\int_{r_i}^{r_o} r^2\eta_n(r)\Phi_n(\omega_{kn}r)\,dr\right)\frac{dC_n}{d\tau}P_n(\zeta) \tag{19}$$

Thus, the temperature field can be obtained by summation of dC_n during $d\tau$ and the influence of $C_n(0)$. The following equation is proven by the method of integration by parts:

$$C_n(0)e^{-(\omega_{kn}/a)^2t} + \int_{\tau=0}^{t} e^{-(\omega_{kn}/a)^2(t-\tau)}\frac{dC_n}{d\tau}\,d\tau = C_n(t) - \left(\frac{\omega_{kn}}{a}\right)^2\int_{\tau=0}^{t} C_n(\tau)e^{-(\omega_{kn}/a)^2(t-\tau)}\,d\tau \tag{20}$$

Making use of Eq. (20), the temperature field can be obtained in the simplified form:

$$\theta(r,\psi,t) = \sum_{n=0}^{\infty}\sum_{k=0}^{\infty}D_{kn}\Phi_n(\omega_{kn}r)P_n(\zeta)T_{kn}(t) \tag{21}$$

where,

$$D_{kn} = \frac{\omega_{kn}^2}{a^2\delta_{kn}} \tag{22}$$

$$T_{kn}(t) = \int_0^t \int_{r_i}^{r_o} r^2 \eta_n(r) \Phi_n(\omega_{kn} r) C_n(\tau) e^{-(\omega_{kn}/a)^2 (t-\tau)} \, dr \, d\tau \tag{23}$$

The heat flux of the outer surface of the sphere can be calculated by:

$$Q = -\int_0^{2\pi} \int_0^{\pi} \int_{r_i}^{r_o} \rho c \theta(r, \psi, t) r^2 dr \sin\psi \, d\psi \, d\varphi \tag{24}$$

Hence, the heat flux has the form:

$$Q = -2\pi\rho c \sum_{n=0}^{\infty} \sum_{k=0}^{\infty} D_{kn} \int_{r_i}^{r_o} r^2 \Phi_n(\omega_{kn} r) \, dr \int_{-1}^{1} P_n(\zeta) \, d\zeta T_{kn}(t) \tag{25}$$

By defining the dimensionless radius and time as,

$$\overline{r} = \frac{r}{r_o}, \quad \overline{t} = \frac{t}{p} \tag{26}$$

Eq. (21) can be rewritten in terms of Biot and Fourier numbers;

$$\mathrm{Bi} = \frac{h r_o}{k}, \quad \mathrm{Fo} = \frac{p}{a^2 r_o^2} \tag{27}$$

Since $f_o(\psi)$ is an arbitrary function, for example, we considered:

$$f_o(\psi) = 1 + \sin^2 \psi \tag{28}$$

With the assumption of,

$$\gamma_{kn} = \int_{\overline{r_i}}^{1} \overline{r^2} \eta_n(\overline{r}) \Phi_n(\omega_{kn} \overline{r}) \, d\overline{r} \tag{29}$$

and considering Eqs. (23) and (29), $T_{kn}(\overline{t})$ can be obtained:

$$T_{kn}(\overline{t}) = \gamma_{kn} \left(\frac{2n+1}{2} \right) \int_{-1}^{1} (2 - \zeta^2) P_n(\zeta) \, d\zeta \int_{\tau=0}^{\overline{t}} \sum_{m=1}^{\infty} \theta_m \sin(2m\pi\overline{t}) e^{-\omega_{kn}^2 \mathrm{Fo}(\overline{t}-\tau)} \, d\tau \tag{30}$$

As $\overline{t} \to \infty$ all exponential terms should vanish, hence $T_{kn}(\overline{t})$ takes the form:

$$T_{kn}(\overline{t}) = \frac{\gamma_{kn}}{\mathrm{Fo}\omega_{kn}^2} \times \left(\frac{2n+1}{2} \right) \int_{-1}^{1} (2 - \zeta^2) P_n(\zeta) \, d\zeta \times \left(\sum_{m=1}^{\infty} \frac{\theta}{\sqrt{1 + (2mM^2/\omega_{kn}^2)^2}} \sin(2m\pi\overline{t} + \phi_{kn}) \right) \tag{31}$$

where the dimensionless quantities M and ϕ_{kn} are defined as:

$$M = \sqrt{\frac{\pi}{\mathrm{Fo}}} \tag{32}$$

$$\phi_{kn} = \arctan\left(-\frac{2mM^2}{\omega_{kn}^2} \right) \tag{33}$$

Thus, the temperature distribution in a hollow sphere for a periodic boundary condition when the inner boundary is insulated and the outer one dissipates heat into the ambient can be expressed in the form:

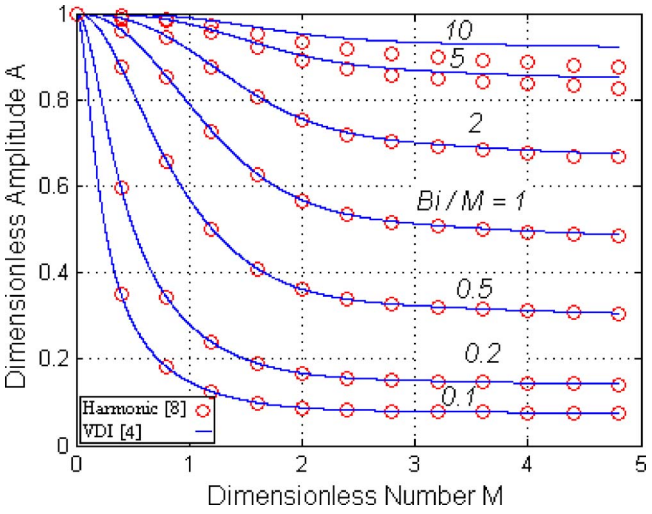

Fig. 1 Comparison between the result of the amplitude of a one-dimensional temperature field of a solid sphere [8] and the results for a solid sphere presented in [4] under the same boundary condition

$$\overline{\theta}(\overline{r}, \psi, \overline{t}) = \sum_{n=0}^{\infty} \sum_{k=0}^{\infty} \left(\frac{2n+1}{2} \right) \left(\frac{\gamma_{kn} \Phi_n(\omega_{kn}\overline{r})}{\delta_{kn}} \right) P_n(\zeta) \times \int_{-1}^{1} (2 - \zeta^2) P_n(\zeta) \, d\zeta \left(\sum_{m=1}^{\infty} \frac{\theta_m}{\sqrt{1 + (2mM^2/\omega_{kn}^2)^2}} \times \sin(2m\pi\overline{t} + \phi_{kn}) \right) \tag{34}$$

Substituting the eigenvalues into Eq. (34), the temperature distribution at the outer surface can be obtained in the form:

$$\overline{\theta}(1, \psi, \overline{t}) = \sum_{m=1}^{\infty} A_m \theta_m \sin(2m\pi\overline{t} + \phi_{kn}) \tag{35}$$

where A_m is the ratio of the oscillation amplitude of temperature distribution in the sphere and the ambient temperature with the same frequency and ϕ_{kn} is the phase difference. By calculating and plotting Eq. (35), the maximum amplitude of summation of harmonic waves and the phase difference can be obtained.

4 Results and Discussion

To check our series solution, as a special case, we solved the problem of a solid sphere with a harmonic boundary condition with our method and compared the results with the corresponding ones in the literature [5]. As presented in Figs. 1 and 2, they are in excellent agreement.

It is evident from Figs. 1 and 2 that for small values of M (slow oscillations of the outer ambient temperature), the dimensionless amplitude A is almost 1 and the phase difference ϕ is approximately zero. For the large values of M (fast oscillations of the outer ambient temperature), values of A decrease from its maximum at the outer boundary to its minimum at the inner boundary and the phase difference values are negative. For the large enough values of M, only a thin boundary region of the sphere follows the ambient temperature oscillation. For increasing $\overline{r_i}$ at constant Bi/M, the minimum of the phase difference decreases and occurs at larger M.

Figures 3–8 show the oscillation amplitude and the phase difference for the hollow sphere under a periodic boundary condition, which is decomposed using Fourier series with different radii and polar angles.

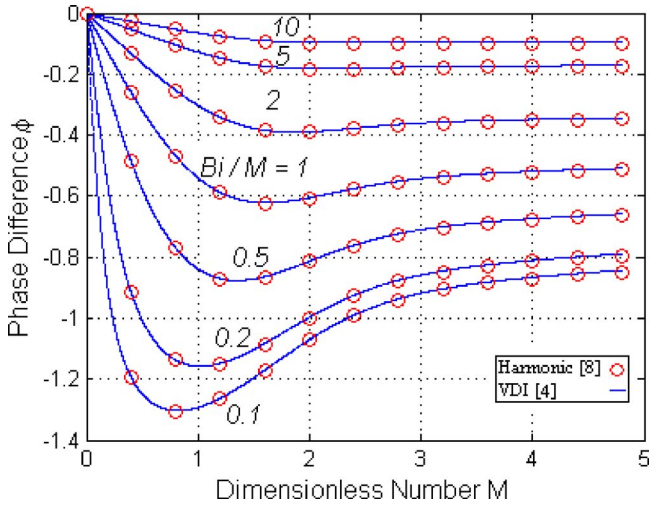

Fig. 2 Comparison between the result of the phase difference of a one-dimensional temperature field of a solid sphere [8] and the results for a solid sphere presented in [4] under the same boundary condition

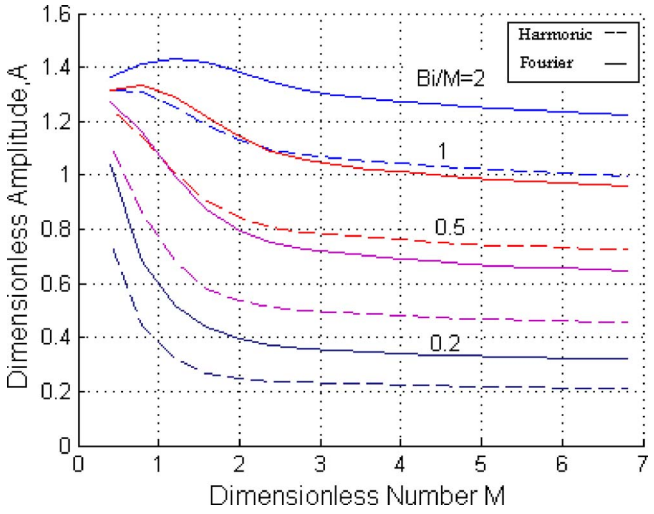

Fig. 5 Dimensionless amplitude, A, when $\bar{r}_i$=0.2, ψ=30

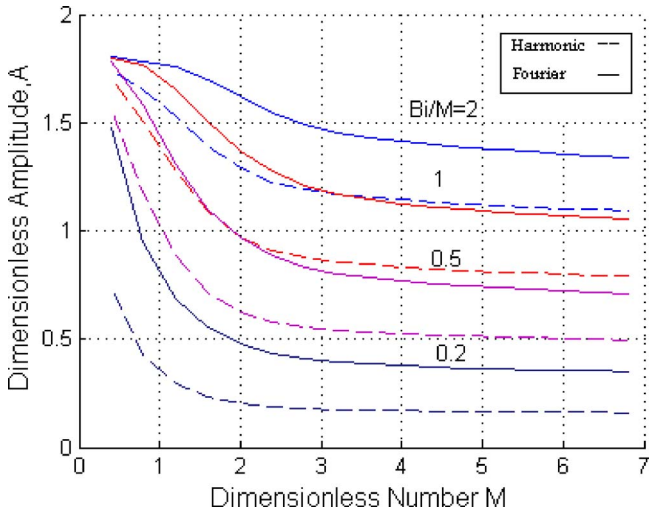

Fig. 3 Dimensionless amplitude, A, when $\bar{r}_i$=0.2, ψ=60

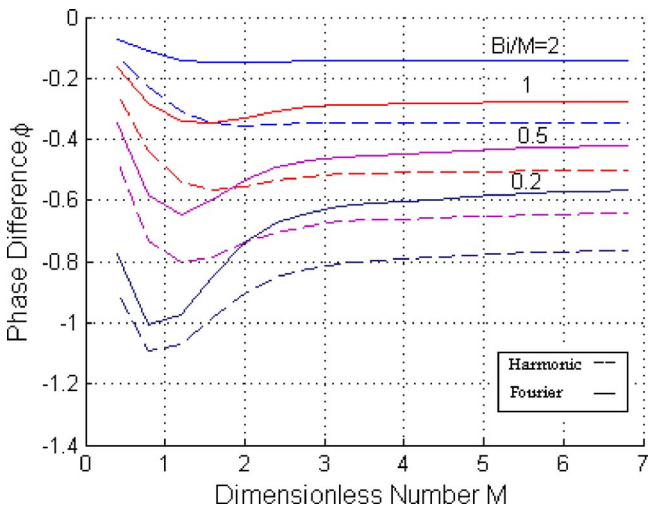

Fig. 6 Dimensionless phase difference, ϕ, when $\bar{r}_i$=0.2, ψ=30

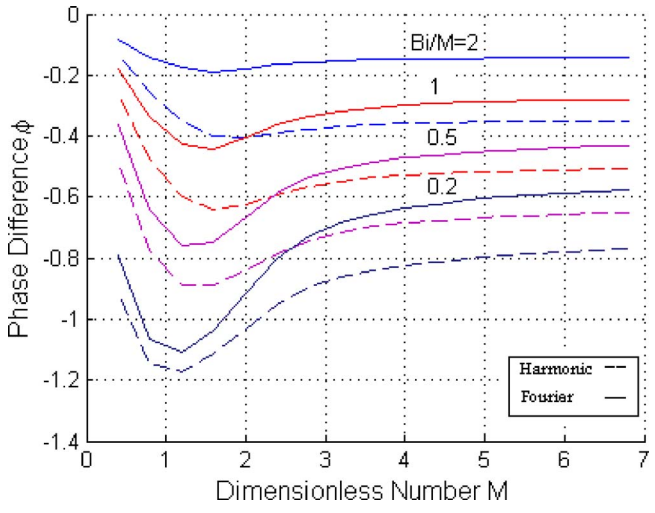

Fig. 4 Dimensionless phase difference, ϕ, when $\bar{r}_i$=0.2, ψ=60

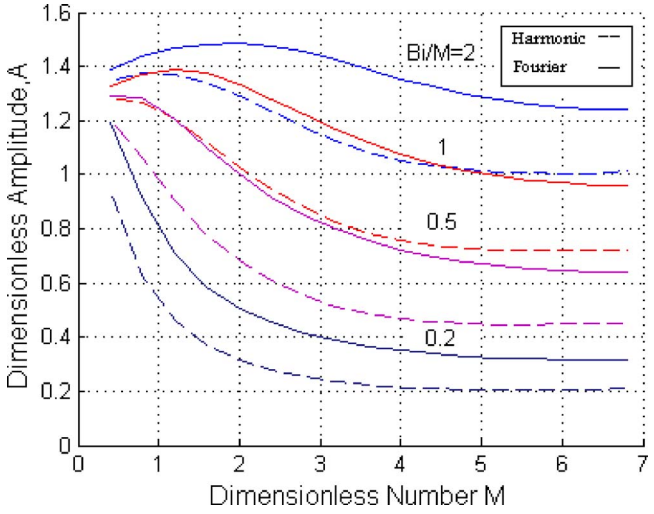

Fig. 7 Dimensionless amplitude, A, when $\bar{r}_i$=0.7, ψ=30

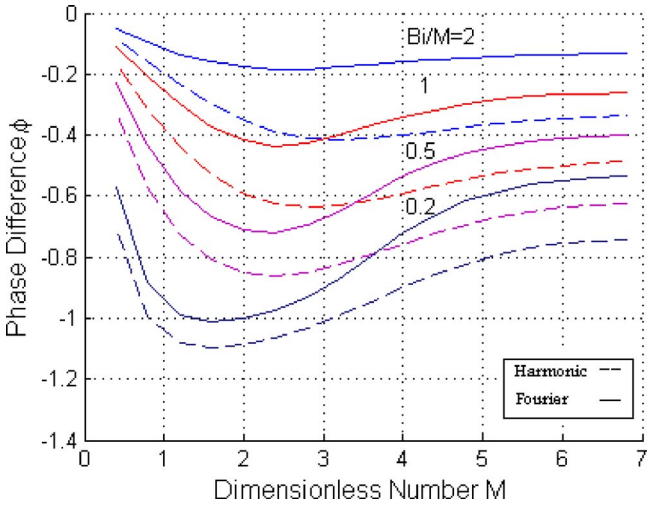

Fig. 8 Dimensionless phase difference, ϕ, when $\overline{r_i}$=0.7, ψ=30

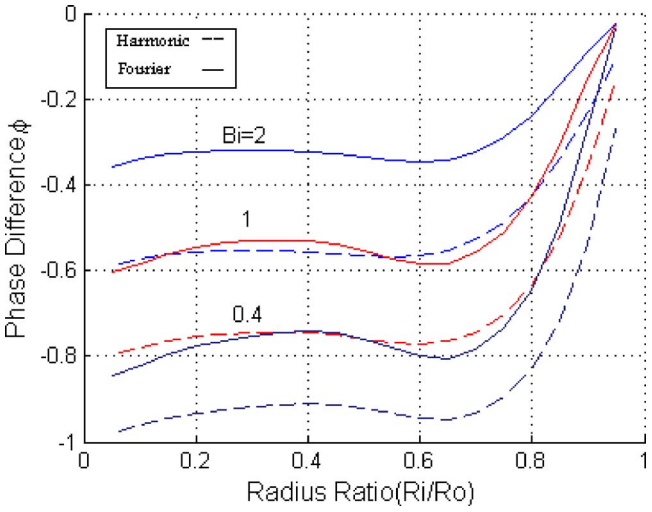

Fig. 10 Dimensionless phase difference, ϕ, when M=2, ψ=30

Figures 9 and 10 show the effect of $\overline{r_i}$ on the variations of A and ϕ for the different values of M. For $\overline{r_i}<0.5$, A and ϕ variations are not considerable but for $\overline{r_i}>0.5$, the effect of $\overline{r_i}$ is significant. When $\overline{r_i}$ tends to 1, A and ϕ tend to 1 and 0, respectively. One can observe from Figs. 9 and 10 that with increasing $\overline{r_i}$, A and ϕ do not increase necessarily, but for some values of $\overline{r_i}$ they decrease.

Figure 11 shows the effect of Biot number on the variation of $Q(t)/Q(p)$ for M=2, $\overline{r_i}$=0.5 under the periodic boundary condition. When the Biot number increases, the heat flux becomes larger and its value is positive in a half of a period and negative in another half. Figure 12 shows the effect of $\overline{r_i}$ on the variation of $Q(t)/Q(p)$ for M=2, Bi=1 under the periodic boundary condition. As Fig. 12 shows, when the thickness of the sphere decreases, the heat flux from the outer surface increases.

Nomenclature

a^2 = inverse of thermal diffusivity, s/m^2
c = specific heat capacity, J/kg.K
h = convection heat transfer coefficient, $W/m^2.K$
k = thermal conductivity, W/m.K
p = period of the ambient temperature, s
r = radius, m

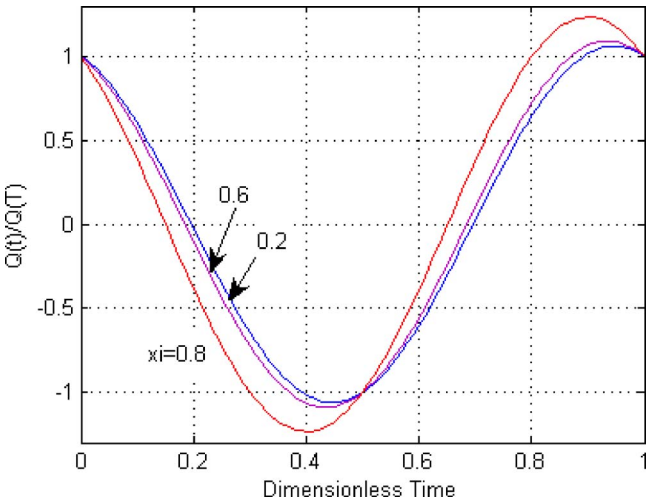

Fig. 11 $Q(t)/Q(p)$ when M=2, Bi=1 under periodic boundary condition

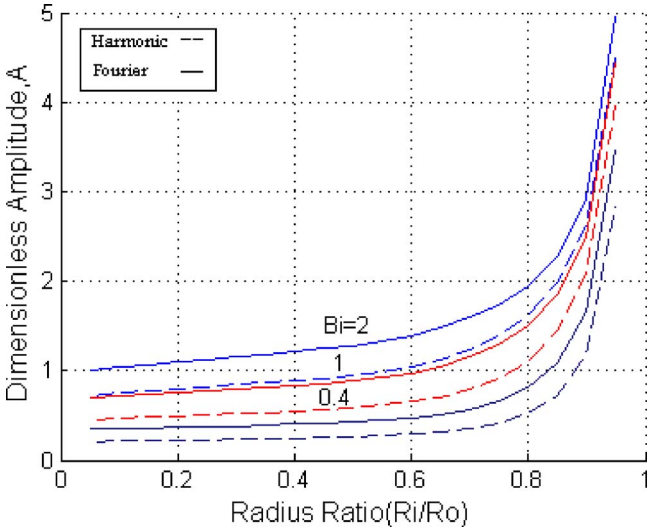

Fig. 9 Dimensionless amplitude, A, when M=2, ψ=30

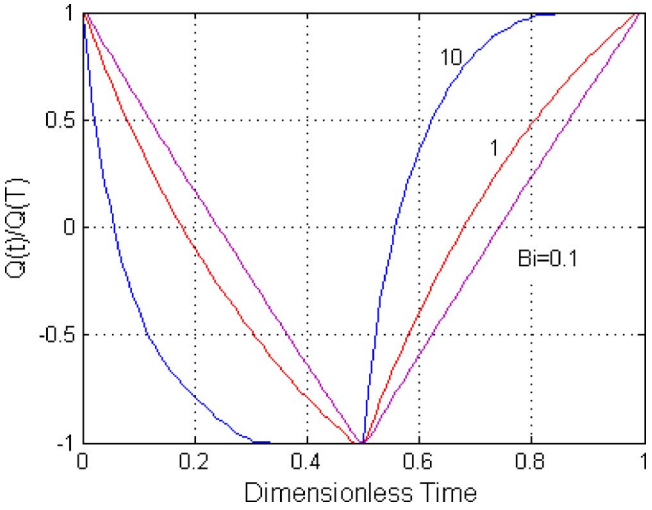

Fig. 12 $Q(t)/Q(p)$ when M=2 under periodic boundary condition

t = time, s
A = dimensionless amplitude
Bi = Biot number
Fo = Fourier number
M = defined by Eq. (32)
Q = heat flux, W
V = volume of the hollow sphere, m^3

Greek letters

θ = temperature, K
ω = eigenvalue
ϕ = phase difference, rad
r, φ, ψ = spherical coordinate
ρ = density, kg/m^3
ζ = defined by Eq. (10)
η = function defined by Eq. (12)
Φ = eigenfunction

Subscripts

a = ambient
i = inner
o = outer
s = steady state
t = transient

Superscript

- (overbar) = dimensionless quantity

References

[1] Dincer, I., 1995, "Estimation of Dimensionless Temperature Distributions in Spherical Products During Hydrocooling," Int. Commun. Heat Mass Transfer, **22**(1), pp. 123–131.
[2] Khedari, J., Benigni, P., Rogez, J., and Mathieu, J. C., 1995, "New Apparatus for Thermal Diffusivity of Refractory Solid Materials by the Periodic Stationary Method," Rev. Sci. Instrum., **66**(1), pp. 193–198.
[3] Khedari, J., Csurks, G., and Hirunlabh, J., 1998, "General Analytical Modeling of Heat Transfer in Isotropic Solid Materials Under Periodic Steady Regime," *Proceedings of the International Conference on Contribution of Cognition to Modeling (CCM'98)*, Lyon-Villeurbanne, France, pp. 9.10–9.13.
[4] Verein Deutscher Ingenieure-Wärmeatlas. Hrsgeg vom Verein Deutscher Ingenieure, 2003, Ed 14-17, Düsseldorf.
[5] Trostel, R., 1956, "Instationäre Wärmespannungen in einer Hohlkugel," Ing.-Arch., **24**, pp. 373–391.
[6] Zubair, S. M., and Chaudhry, M. A., 1995, "Heat Conduction in a Semi-infinite Solid Subject to Steady and Non-steady Periodic-Type Surface Heat Fluxes," Int. J. Heat Mass Transfer, **38**(18), pp. 3393–3399.
[7] Özisik, M. N., 1993, *Heat Conduction*, 2nd ed., Wiley, New York, pp. 195–201.
[8] Atefi, G., and Shirmohammadi, R., 2003, "Analytical Solution of One-Dimensional Temperature fField in Solid Sphere Under Harmonic Boundary Condition," *The 4th Iranian Aerospace Society Conference*, Amirkabir University of Technology, Vol. 2, pp. 466–476.

Drag Coefficient and Stanton Number Behavior in Fluid Flow Across a Bundle of Wing-Shaped Tubes

Andrej Horvat

Borut Mavko

Jožef Stefan Institute,
Reactor Engineering Division,
Jamova 39, SI 1001,
Ljubljana, Slovenia

Transient numerical simulations of fluid and heat flow were performed for eight heat exchanger segments with cylindrical and wing-shaped tubes in staggered arrangement. Their hydraulic diameters d_h were from 0.5824 to 3.899 cm *for the cylindrical tubes, and from 0.5413 to* 3.594 cm *for the wing-shaped tubes. Based on the recorded time distributions of velocity $u_f(t)$ and temperature $T_f(t)$, time average Reynolds number* $\overline{\mathrm{Re}}$*, drag coefficient* $\overline{C_d}$*, and Stanton number* $\overline{\mathrm{St}}$ *were calculated. In general, the drag coefficient and the Stanton number are smaller for the wing-shaped tubes than for the cylindrical tubes. However, with an increasing hydraulic diameter, these differences between both forms of tubes diminish. The time average values were further used to construct the drag coefficient and the Stanton number as polynomial functions* $\overline{C_d}(d_h, \overline{\mathrm{Re}})$ *and* $\overline{\mathrm{St}}(d_h, \overline{\mathrm{Re}})$.
[DOI: 10.1115/1.2241746]

Keywords: heat exchanger, tube shape, drag coefficient, Stanton number, numerical analysis

1 Introduction

Assessing drag and heat transfer between fluid flow and a structure in a heat exchanger is crucial to determine its operational parameters and performance already at the design stage. The assessment can be done by experimental testing (e.g., [1–4]) and by numerical calculations (e.g., [5–8]). Due to the nature of experimental work, an experimental investigation of all prototype geometries is not feasible. As an affordable substitute, numerical approaches and methods have been increasingly employed to simulate processes in heat exchangers in order to find new designs for emerging technological needs. Nevertheless, the direct numerical simulations of heat transfer processes in heat exchangers are still computationally too demanding. Therefore, significant simplifications, especially in the turbulence modeling and the wall effect treatment, are necessary.

Horvat and Mavko [9] proposed an alternative approach based on hierarchic modeling, in which the model and its computation are split onto two distinct levels. On the first level, transient three-dimensional numerical simulations of fluid and heat flow for geometry similar to a heat exchanger segment are performed. Based on the calculated three-dimensional velocity and temperature distributions, local values of the drag coefficient and of the heat transfer coefficient are determined. On the second level, an integral model [10], which uses the calculated local coefficients as input parameters, is applied to simulate heat transfer over a whole heat exchanger. As the computationally most demanding terms of momentum and heat transport are determined on a separate level, the integral code is fast running, but still capable to accurately predict the heat flow for a whole heat exchanger.

Seeking an optimal geometry of heat exchanger tubes, we performed numerical simulations of fluid and heat flow for a larger number of heat exchanger segments with a different form of tubes. In this article, we would like to present computational results for wing-shaped tubes based on a NACA profile in a staggered arrangement. For comparison, the results of numerical simulations performed for cylindrical tubes are also presented. The numerical simulations cover laminar, transitional, as well as turbulent flow regime.

To adequately model fluid and heat flow phenomena in the heat exchanger segments, transient numerical simulations with a special near-wall treatment were performed. These calculations were used to obtain the time average values of the drag coefficient and Stanton number. Based on these values, we constructed $\overline{C_d}$ and $\overline{\mathrm{St}}$ as polynomial functions of the Reynolds number and a geometrical parameter. For the most appropriate geometrical parameter, the hydraulic diameter d_h was chosen.

2 Geometrical Considerations

The numerical calculations were performed for a representative elementary volume (REV) of a tube bundle with staggered arrangement. The REV is colored grey in Fig. 1. The size and the shape of REV were selected after a fair amount of testing. We took under consideration errors arising from limiting the simulation domain, overall flow dynamics in the simulation domain, and needed computational resources. Based on the performed tests, it was concluded that in order to get representative data, it is more important to simulate longer time intervals than to enlarge the simulation domain.

In the case of cylindrical tubes, the diameter was 3/8 in. (9.525 mm). The calculations were performed for four geometries with different diagonal pitch-to-diameter ratio: $p/d=1.125$, 1.25, 1.5, and 2.0. For each geometry, the REV height h was equal to the diagonal pitch p. The analysis was limited to the bundle arrangements where the pitch in the x-direction p_x is equal to the pitch in the y-direction p_y.

The geometries with the wing form of tubes were based on the NACA four-digit-series of profiles e.g., NACA0020, where the last two digits represent the thickness-to-chord ratio t/c [11]. In general, the NACA profile coordinates are calculated as

$$\frac{y}{c} = a_0\left(\frac{x}{c}\right)^{1/2} + a_1\left(\frac{x}{c}\right) + a_2\left(\frac{x}{c}\right)^2 + a_3\left(\frac{x}{c}\right)^3 + a_4\left(\frac{x}{c}\right)^4 \tag{1}$$

For $t/c=1/5$, the coefficients are given by Ladson et al. [11]

$$a_0 = 0.2969, \quad a_1 = -0.126, \quad a_2 = -0.3516$$
$$a_3 = 0.2843, \quad a_4 = -0.1015 \tag{2}$$

To obtain a segment with the same fractions of the fluid phase and the solid structure as in the case of cylindrical tubes

$$V_{f,\mathrm{cyl}} = V_{f,\mathrm{wing}} \quad \text{and} \quad V_{s,\mathrm{cyl}} = V_{s,\mathrm{wing}}, \tag{3}$$

t/c was increased to 2/3. Therefore, the ordinates y in function (1) were multiplied by (2/3)/(1/5). Finally, the length of the chord c, and consequently, the size of the REV were determined from the requirement (3).

3 Simulation Details

The CFX 5.7 commercial code (ANSYS, Inc. [12]) was used to perform three-dimensional transient numerical simulations of air flow and heat transfer in REV. The tube walls in REV were treated as isothermal with the temperature $T_{\mathrm{wall}}=35°\mathrm{C}$. To allow disturbances to propagate over the geometrical limits of the simulation domain, the periodic boundary conditions were assigned in all three directions for all other boundaries. In order to consistently

Contributed by the Heat Transfer Division of ASME for publication in the JOURNAL OF HEAT TRANSFER. Manuscript received April 16, 2005; final manuscript received March 5, 2006. Review conducted by Sumanta Acharya.

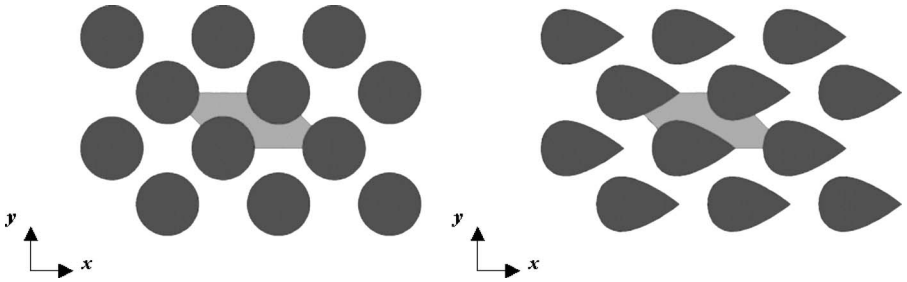

Fig. 1 Geometrical arrangement of heat exchanger structure for $p/d=1.25$; cylindrical (left) and wing (right) form

model the flow, periodicity had to be imposed on the transport equations in the streamwise direction.

As numerical results can be grid dependent, special care was taken to construct the numerical grids with sufficient resolution and uniformity. A basic criterion was the maximum nondimensional wall distance y^+ of the first layer of nodes. During the simulations, the maximum y^+ did not exceed the value of 2.0. The timestep for the transient calculations was based on an average time interval needed for a flow particle to pass the simulation domain

$$t_{\text{scale}} = \frac{2p_x}{u_f} \quad \text{and} \quad dt \leqslant \frac{t_{\text{scale}}}{80} \tag{4}$$

The details of the mathematical model and the validation of the numerical approach can be found in Horvat and Mavko [9].

4 Results

The transient numerical simulations of fluid and heat flow in REV were performed for the cylindrical and the wing-shaped tubes in the staggered arrangement (Fig. 1) with four different pitch-to-diameter ratios.

In order to extract relevant statistical values of physical variables, the volumetric average velocity

$$u_f(t) = \frac{1}{V_f}\int_{\hat{V}_f} u(t,x_i)dV \tag{5}$$

and the temperature

$$T_f(t) = \frac{1}{u_f(t)V_f}\int_{\hat{V}_f} u(t,x_i)T(t,x_i)dV \tag{6}$$

were recorded at each timestep after statistical steady-state flow conditions were reached. The length of the recording interval was set on a case-by-case basis, and it was at least 150 times longer that the time required for an average flow particle to travel the length of the simulation domain (4).

Using the obtained velocity distributions $u_f(t)$ and the temperature distributions $T_f(t)$, the Reynolds number

$$\text{Re}(t) = \frac{\rho u_f(t) d_h}{\mu} \tag{7}$$

the drag coefficient

$$C_d(t) = \frac{2\Delta p}{\rho u_f^2(t)}\left(\frac{A_f}{A_o}\right) \tag{8}$$

and the Stanton number

$$\text{St}(t) = \frac{\Delta T}{T_{\text{wall}} - T_f(t)}\left(\frac{A_f}{A_o}\right) \tag{9}$$

time distributions were calculated for each case. Further on, their time averages $\overline{\text{Re}}$, $\overline{C_d}$, and $\overline{\text{St}}$, and their standard deviations S_{Re}, S_{Cd}, and S_{St} were determined.

4.1 Drag Coefficient Functions. The time distributions of Reynolds number $\text{Re}(t)$ and drag coefficient $C_d(t)$ were obtained for both forms of tube cross sections. From the time distributions $\text{Re}(t)$ and $C_d(t)$, the statistical average values $\overline{\text{Re}}$ and $\overline{C_d}$ were calculated. Using the least-squares approximation, the calculated values enabled us to construct $\overline{C_d}$ for each form of tube cross sections as a polynomial function of Reynolds number $\overline{\text{Re}}$ and hydraulic diameter d_h. For the cylindrical form of tube cross sections, the function

$$\overline{C_d}(d_h,\overline{\text{Re}}) = 0.2353 + 3.222\cdot 10^{-10} d_h^{-4} + 1.348 d_h^{1/2} + 64.47\overline{\text{Re}}^{-1} - 1.855\cdot 10^{-5}\overline{\text{Re}} - 2.118\cdot 10^{-9}\overline{\text{Re}}^2 \tag{10}$$

was obtained. For the wing form of tube cross sections, we calculated the following function:

$$\overline{C_d}(d_h,\overline{\text{Re}}) = -0.3020 + 1.825\cdot 10^{-10} d_h^{-4} + 3.854 d_h^{1/2} + 2.875\overline{\text{Re}}^{-1} - 6.518\cdot 10^{-7}\overline{\text{Re}} - 7.158\cdot 10^{-13}\overline{\text{Re}}^3 \tag{11}$$

Figure 2 presents contour plots of the drag coefficient polynomials for the cylindrical (10) and for the wing (11) form of tube cross sections.

The comparison of the contour plots in Fig. 2 shows that the $\overline{C_d}$ function is much steeper for the wing form than for the cylindrical form of tube cross sections. For a given d_h, $\overline{C_d}$ monotonically decreases with $\overline{\text{Re}}$. If a value of $\overline{\text{Re}}$ is set, $\overline{C_d}$ has its minimum for a unique value of d_h. This value of the hydraulic diameter d_h is higher for the cylindrical form ($\sim$0.012 m) than for the wing form ($\sim$0.0075 m) of tube cross sections.

In Fig. 3, the drag coefficient functions (10) and (11) for the $p/d=1.125$, 1.25, 1.5, and 2.0 are compared with the discrete values of $\overline{C_d}$ that were obtained from the time distributions (8). In general, the constructed polynomial functions (10) and (11), give a good approximation of the discrete values. Larger discrepancies exist only for $p/d=1.5$ at higher values of $\overline{\text{Re}}$.

In the laminar region, where the Reynolds numbers are a few hundred, the flow reaches steady-state conditions. Furthermore, $\overline{C_d}$ decreases with increasing $\overline{\text{Re}}$ much faster than in the turbulent region. The transition is usually marked with strong oscillations, where the flow periodically changes the direction and the spanwise motion of the fluid becomes important. As a consequence, $\overline{C_d}$ increases. The increase of $\overline{C_d}$ (Fig. 3) indicates that the transition to turbulence occurs at slightly lower $\overline{\text{Re}}$ for the cylindrical form

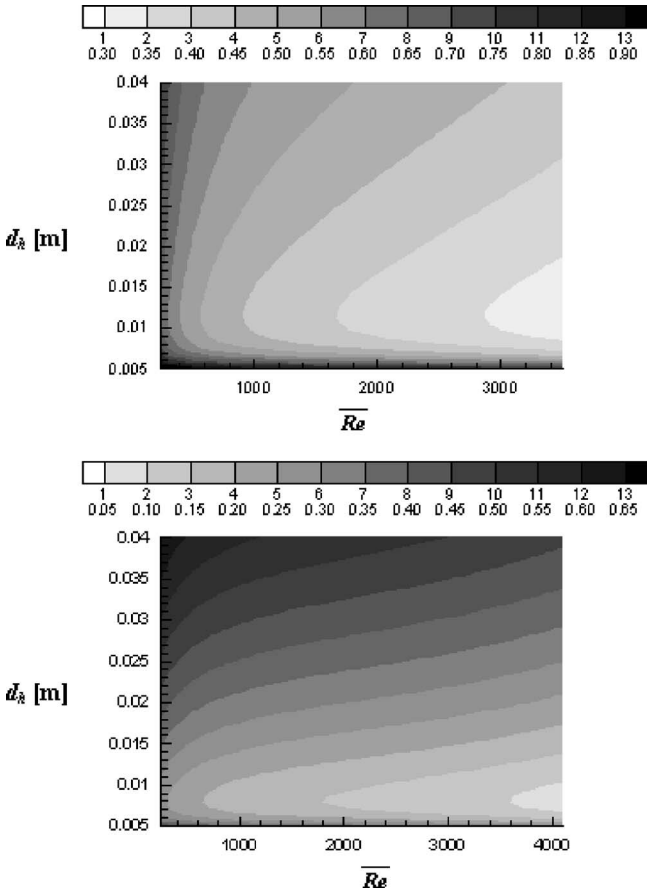

Fig. 2 Drag coefficient approximation functions (10) and (11) for (*a*) the cylindrical form and (*b*) the wing form

than for the wing form of tube cross sections. In the turbulent regime, $\overline{C_d}$ changes at a much slower rate. Although, $\overline{C_d}$ for the cylindrical form is in general larger than $\overline{C_d}$ for the wing form, the difference with increasing d_h becomes negligible at the pitch-to-diameter ratio $p/d=2.0$ especially for larger values of $\overline{\mathrm{Re}}$.

Large oscillations were observed in the tube bundle with the wing form of tube cross sections at $p/d=1.5$. These oscillations are characterized by a separation of the boundary layer on the tube walls. The location of the separation triggers strong unsteady spanwise streams that increase $\overline{C_d}$. Similar behavior of the drag coefficient distributions can also be observed in the diagrams of the experimental data for the ellipsoidal form of tube cross sections recorded by Kays and London [2].

4.2 Stanton Number Functions. Using the recorded time distributions of Stanton number $\mathrm{St}(t)$, the time averages $\overline{\mathrm{St}}$ were calculated for both forms of tube cross sections. From the calculated averages, the Stanton number approximation functions were determined with the least-squares method.

For the cylindrical tube cross sections, the function

$$\overline{\mathrm{St}}(d_h,\overline{\mathrm{Re}}) = -0.02388 + 6.774\cdot 10^{-12}d_h^{-4} - 0.01714d_h^{1/2} + 6.553(d_h/\overline{\mathrm{Re}})^{1/2} + 2.090\cdot 10^{-7}\overline{\mathrm{Re}}^{-3} + 1.271\overline{\mathrm{Re}}^{-1/2} + 7.999\cdot 10^{-6}\overline{\mathrm{Re}} - 2.945\cdot 10^{-13}\overline{\mathrm{Re}}^{3} \quad (12)$$

was obtained, whereas for the wing form of tube cross sections the following function was calculated:

$$\overline{\mathrm{St}}(d_h,\overline{\mathrm{Re}}) = -0.01863 + 1.331\cdot 10^{-11}d_h^{-4} + 0.1185d_h^{1/2} + 9.180(d_h/\overline{\mathrm{Re}})^{1/2} + 0.2078\overline{\mathrm{Re}}^{-1/2} + 3.271\cdot 10^{-7}\overline{\mathrm{Re}} - 2.530\cdot 10^{-15}\overline{\mathrm{Re}}^{3} \quad (13)$$

Figure 4 presents contour plots of the Stanton number polynomials for the cylindrical form (12) and for the wing form (13) of tube cross sections. For the range of $\overline{\mathrm{Re}}$ under consideration, the amount of heat transfer crucially depends on the momentum transfer from the fluid flow to the structure walls. Therefore, the $\overline{\mathrm{St}}$

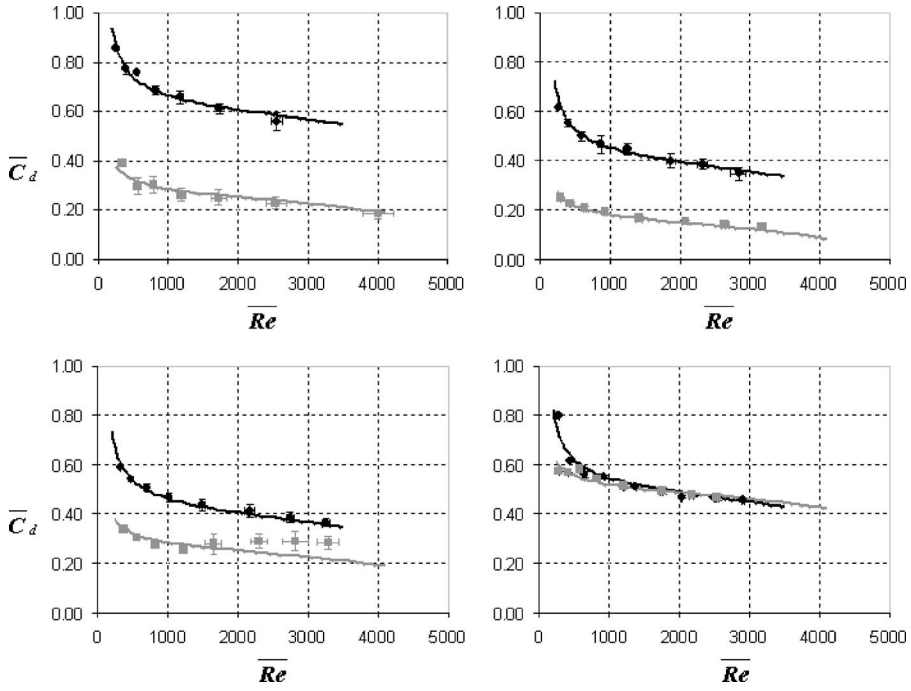

Fig. 3 Drag coefficient distribution for the cylindrical form (♦) and the wing form (■); (*a*) *p*/*d*=1.125, (*b*) *p*/*d*=1.25, (*c*) *p*/*d*=1.5, and (*d*) *p*/*d*=2.0

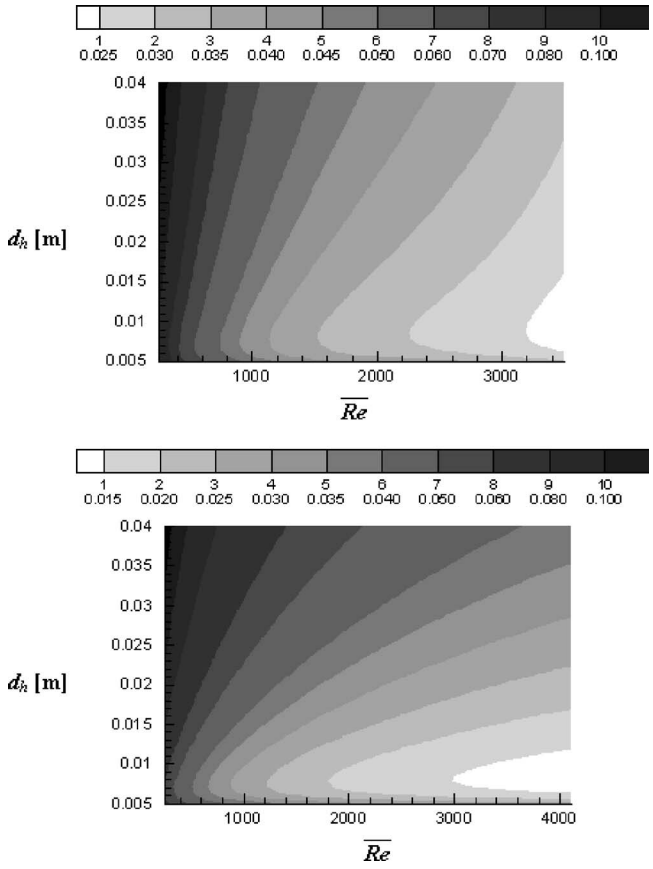

Fig. 4 Stanton number approximation functions (12) and (13) for (*a*) the cylindrical form and (*b*) the wing form

functions (Fig. 4) are similar to the $\overline{C_d}$ functions (Fig. 2). The Stanton number monotonically decreases with increasing $\overline{\mathrm{Re}}$ for any given d_h. This means that the flow velocity increases faster than the convective heat transfer from the isothermal walls to the fluid. Therefore, also the temperature $T_f(t)$ as defined by (6) decreases with increasing $\overline{\mathrm{Re}}$. The contour plots (Fig. 4) also show that if $\overline{\mathrm{Re}}$ is set, $\overline{\mathrm{St}}$ rapidly drops at small values of d_h and then gradually increases with the raising values of d_h.

In Fig. 5, the Stanton number functions (12) and (13) for the $p/d=1.125$, 1.25, 1.5, and 2.0 are compared with the discrete values of $\overline{\mathrm{St}}$. The constructed polynomial functions (12) and (13) give a satisfactory approximation of the discrete values. Larger discrepancies can only be observed for the wing form of tube cross section at $p/d=1.5$ where the flow oscillations occur. In the laminar region, $\overline{\mathrm{St}}$ decreases faster with increasing $\overline{\mathrm{Re}}$ than in the turbulent region. The transitional behavior that is evident from the calculated values of $\overline{C_d}$ (Fig. 3) shows almost no influence on the $\overline{\mathrm{St}}$ values. Figure 5 shows that $\overline{\mathrm{St}}$ is larger for the cylindrical than for the wing form of tube cross sections. Although, the difference is large for small d_h, it disappears at larger values of d_h.

5 Conclusions

Transient numerical simulations of heat transfer were performed for eight heat exchanger segments with the cylindrical and the wing-shaped tubes in the staggered arrangement. Their hydraulic diameters d_h were from 0.5824 to 3.899 cm for the cylindrical tubes, and from 0.5413 to 3.594 cm for the wing-shaped tubes. Based on the calculated results, the time distributions of Reynolds number $\mathrm{Re}(t)$, drag coefficient $C_d(t)$, and Stanton number $\mathrm{St}(t)$ were obtained. It is important to mention that we encounter much more complex physical behavior than it was reported in the available literature (e.g., [13–15]). Large flow oscillations and semi-stochastic motion of the flow in the spanwise direction were observed as the flow regime changes from laminar to turbulent.

Based on the recorded time distributions of velocity $u_f(t)$ and temperature $T_f(t)$, time average Reynolds number $\overline{\mathrm{Re}}$, drag coef-

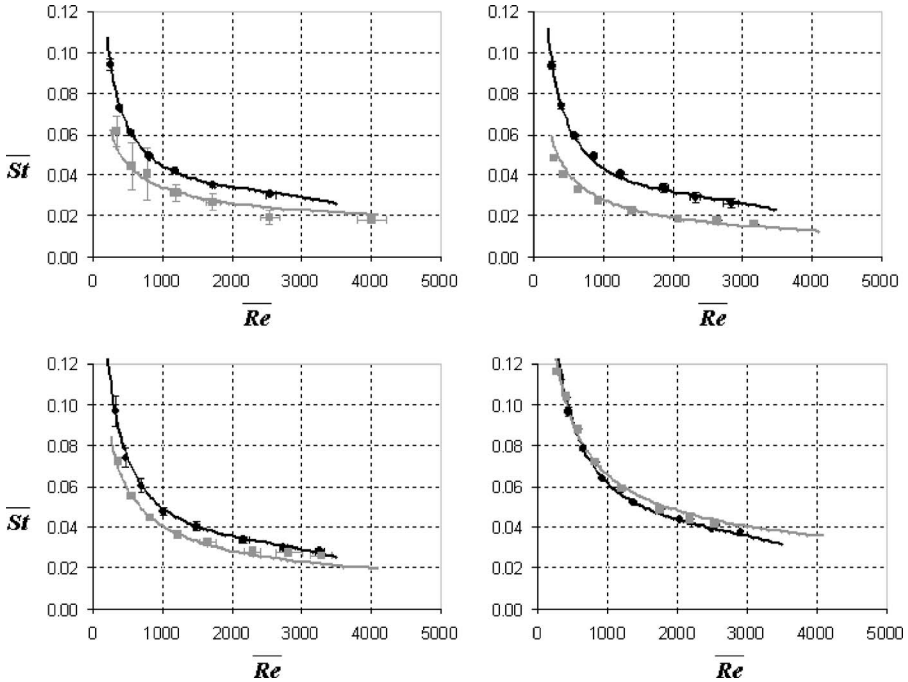

Fig. 5 Stanton number distribution for the cylindrical form (♦) and the wing form (■); (*a*) $p/d=1.125$, (*b*) $p/d=1.25$, (*c*) $p/d=1.5$, and (*d*) $p/d=2.0$

ficient $\overline{C_d}$, and Stanton number $\overline{\mathrm{St}}$ were calculated. The time average values $\overline{\mathrm{Re}}$, $\overline{C_d}$, and $\overline{\mathrm{St}}$ were further used to construct the polynomial functions $\overline{C_d}(d_h, \overline{\mathrm{Re}})$ and $\overline{\mathrm{St}}(d_h, \overline{\mathrm{Re}})$ for the cylindrical and the wing-shaped tubes. These polynomial functions are to be applied as input correlations in the integral model of a whole heat exchanger [10].

The calculated time average values $\overline{\mathrm{Re}}$, $\overline{C_d}$, and $\overline{\mathrm{St}}$ also enabled us to draw some conclusions on the thermal performance of the cylindrical form and the wing form of tube cross sections. The drag coefficient $\overline{C_d}$ as well as the Stanton number $\overline{\mathrm{St}}$ monotonically decrease with increasing $\overline{\mathrm{Re}}$ for any hydraulic diameter d_h. On the contrary, $\overline{C_d}$ and $\overline{\mathrm{St}}$ exhibit minimum at a certain value of d_h for any given $\overline{\mathrm{Re}}$. The minimum $\overline{C_d}$ of the cylindrical form was found at $d_h \sim 0.012$ m, whereas for the wing form of tube cross sections the minimum $\overline{C_d}$ was observed at $d_h \sim 0.0075$ m. In addition, the minimum value of $\overline{\mathrm{St}}$ was obtained at $d_h \sim 0.0075$ m for both sets of tested forms.

In general, the values of $\overline{C_d}$ and $\overline{\mathrm{St}}$ are lower for the wing form in comparison to the cylindrical form of tube cross sections. Although, the differences are large at small d_h, they practically disappear at larger values of d_h. This allows us to conclude that the influence of different forms of bounding surfaces diminishes with increasing d_h.

Acknowledgment

A. Horvat gratefully acknowledges the financial support received from the Ministry of Higher Education, Science and Technology of the Republic of Slovenia for the project "Determination of morphological parameters for optimization of heat exchanger surfaces."

Nomenclature

A_f = $V_f/2p_x$, fluid flow cross section
A_o = wetted surface
a_i = coefficients of the NACA wing polynomial
C_d = $2\Delta p/\rho u_f^2\ (A_f/A_o)$, drag coefficient
c = speed of sound, NACA wing chord length
d = diameter
d_h = $4V_f/A_o$, hydraulic diameter
dt = timestep
h = height of REV
Pr = Prandtl number
p = pitch between tubes, pressure
Re = $\rho u_f d_h/\mu$, Reynolds number
REV = representative elementary volume
St = $\Delta T/(T_{\mathrm{wall}} - T_f)\ (A_f/A_o)$, Stanton number
T = temperature
t = time, NACA wing thickness
t_{scale} = $2p_x/u_f$, average time needed for a flow particle to pass the simulation domain
u = streamwise velocity
V = volume
V_f = fluid volume in REV
y^+ = nondimensional wall distance

Greek

μ = dynamic viscosity
ρ = density
λ = thermal conductivity

Subscript/Superscript

f = fluid phase
s = solid phase
t = turbulence model variable
wall = wall conditions
x = streamwise direction
y = horizontal spanwise direction

References

[1] Zhukauskas, A., 1987, "Convective Heat Transfer in Cross Flow," *Handbook of Single-Phase Convective Heat Transfer*, Wiley, New York.
[2] Kays, W. S., and London, A. L., 1998, *Compact Heat Exchangers*, 3rd ed., Krieger, Malabar, Florida.
[3] Kakac, S., 1985, *Heat Exchangers: Thermo-Hydraulic Fundamentals and Design*, 2nd ed., Hemisphere, New York.
[4] Aiba, S., Tsuchida, H., and Ota, T., 1982, "Heat Transfer Around Tubes in In-Line Tube Banks," Bull. JSME, **25**, pp. 919–926.
[5] Launder, B. E., and Massey, T. H., 1978, "The Numerical Prediction of Viscous Flow and Heat Transfer in Tube Banks," ASME J. Heat Transfer, **100**, pp. 565–571.
[6] Antonopoulos, K. A., 1979, "Prediction of Flow and Heat Transfer in Rod Bundles," Ph.D. thesis, Mechanical Engineering Department, Imperial College, London, UK.
[7] Beale, S. B., and Spalding, D. B., 1999, "A Numerical Study of Unsteady Fluid Flow in In-Line and Staggered Tube Banks," J. Fluids Struct., **13**, pp. 723–754.
[8] Barsamian, H. R., and Hassan, Y. A., 1997, "Large Eddy Simulation of Turbulent Crossflow in Tube Bundles," Nucl. Eng. Des., **172**, pp. 103–122.
[9] Horvat, A., and Mavko, B., 2005, "Hierarchic Modeling of Heat Transfer Processes in Heat Exchangers," Int. J. Heat Mass Transfer, **48**, pp. 361–371.
[10] Horvat, A., and Catton, I., 2003, "Numerical Technique for Modeling Conjugate Heat Transfer in an Electronic Device Heat Sink," Int. J. Heat Mass Transfer, **46**, pp. 2155–2168.
[11] Ladson, C. L., Brooks, C. W., Jr., and Hill, A. S., 1996, "Computer Program to Obtain Ordinates for NACA Airfoils," NASA TM 4741, Langley Research Center, Hampton, VA.
[12] ANSYS, Inc., 2004, "ANSYS CFX 5.7.1 Documentation," www-waterloo.ansys.com/community/products.
[13] Bejan, A., 1995, *Convection Heat Transfer*, 2nd ed., Wiley, New York.
[14] Stanescu, G., Fowler, A. J., and Bejan, A., 1996, "The Optimal Spacing of Cylinders in Free-Stream Cross-Flow Forced Convection," Int. J. Heat Fluid Flow, **39**, pp. 311–317.
[15] Matos, R. S., Vergas, J. V. C., Laursen, T. A., and Bejan, A., 2004, "Optimally Staggered Finned Circular and Elliptic Tubes in Forced Convection," Int. J. Heat Fluid Flow, **47**, pp. 1347–1359.

Journal of Heat Transfer

Erratum

The title for the August special issue should have been, “Special Issue for the Heat Transfer Photogallery”.

